



HAL
open science

Chemical heterogeneity of atmospheric particles in urbanized and industrialized environments during pollution events.

Soulemane Halif Ngagine

► **To cite this version:**

Soulemane Halif Ngagine. Chemical heterogeneity of atmospheric particles in urbanized and industrialized environments during pollution events.. Ocean, Atmosphere. Université du Littoral Côte d'Opale, 2022. English. NNT : 2022DUNK0617 . tel-03773350

HAL Id: tel-03773350

<https://theses.hal.science/tel-03773350v1>

Submitted on 9 Sep 2022

HAL is a multi-disciplinary open access archive for the deposit and dissemination of scientific research documents, whether they are published or not. The documents may come from teaching and research institutions in France or abroad, or from public or private research centers.

L'archive ouverte pluridisciplinaire **HAL**, est destinée au dépôt et à la diffusion de documents scientifiques de niveau recherche, publiés ou non, émanant des établissements d'enseignement et de recherche français ou étrangers, des laboratoires publics ou privés.



Thèse de Doctorat

Discipline : Sciences de la Terre, de l'Univers, de l'Espace
Spécialité : Terre, Enveloppes Fluides

présentée à l'École Doctorale en Sciences Technologie et Santé (ED 585)

de l'Université du Littoral Côte d'Opale

par

Soulemane Halif NGAGINE

pour obtenir le grade de Docteur de l'Université du Littoral Côte d'Opale

***Chemical Heterogeneity of Atmospheric Particles in
Urbanized and Industrialized Environments during Pollution
Events.***

Soutenue le 01^{er} avril 2022 après avis des rapporteurs, devant le jury d'examen :

M. Petitprez Denis, Professeur, Université de Lille

M. Kajii Yoshizumi, Professeur, Kyoto University

M^{me} Liu Yao, Chargée de Recherche HDR, Université Gustave Eiffel

M^{me} Uzu Gaëlle, Directrice de Recherche, Université Grenoble-Alpes

**M^{me} Perdrix Esperanza, Maître Assistante,
Institut Mines-Telecom Nord Europe,**

**M^{me} Deboudt Karine, Professeur,
Université du Littoral Côte d'Opale**

**M Flament Pascal, Professeur,
Université du Littoral Côte d'Opale**

Président

Rapporteur

Rapporteur

Examinatrice

Membre Invité

Directrice de thèse

Co-Directeur



To my parents

Mariama Nboutpouen Dignigni and Ndoumkain Ousmane.

“When there are many laws, people cannot be wise”

Sultan Ibrahim Njoya,

Saan'gam, 1921

Acknowledgments

Cet important travail n'aurait pas été réalisé sans l'aide et le soutien de certaines personnes qui m'ont permis de le mener à bien.

Je tiens tout d'abord à remercier mes directeurs de thèse, Karine Deboudt et Pascal Flament. Deux personnes exceptionnelles dont je suis fier d'avoir croisé le chemin. Vous m'avez donné l'opportunité de travailler sur ce sujet qui interpelle une grande communauté scientifique et dont dépend les vies de millions de personnes chaque année. Vous m'avez fourni les conditions matérielles et techniques et surtout avez toujours été présent quand tout n'allait pas. Je ne saurais trouver les mots justes pour décrire la disponibilité et la réactivité dont vous avez fait preuve durant mes travaux. La dimension de mon apprentissage est inestimable et ceci grâce à votre écoute et nos échanges durant ces trois années et demie.

Je voudrais ensuite remercier M. Gaël Mouret, Directeur du Laboratoire de Physico-Chimie de l'Atmosphère pour m'avoir accueilli au sein du laboratoire durant toutes ces années et fourni les conditions pour mener à bien ces recherches intenses.

Je tiens également à remercier particulièrement les membres de mon jury : Denis Petitprez, Yoshizumi Kajii, Yao Liu, Gaëlle Uzu d'avoir accepté de réviser mon travail et d'avoir fait le déplacement pour ma soutenance. J'aurai aussi pu être l'étudiant de Kajii Sensei ou Denis car si je suis là aujourd'hui c'est aussi en partie grâce à leurs contributions. Denis m'a permis de rejoindre le Labex Cappa et Kajii Sensei fait partie de mes mentors.

Une reconnaissance particulière à Esperanza Perdrix et Davy Rousset pour leurs avis, recommandations et soutient tout au long de cette thèse lors des comités de suivi individuels.

Merci aussi à la Région Hauts-de-France et au Pôle Métropolitain de la Côte d'Opale d'avoir soutenu financièrement ce travail de thèse, ainsi qu'à ATMO Hauts de France pour la fourniture des données nécessaires à la conduite d'une partie importante de ce travail.

Je souhaite adresser des remerciements tout particuliers à Bo'o Soukoudjou Tamekouong, un deuxième papa pour moi, qui est la première personne à m'appeler Dr Ngagine alors que je n'étais encore qu'en classe de 5^{ième} au lycée. Il a toujours cru en moi et aura mérité que cette thèse lui soit dédié.

Je remercie également tous mes collègues qui ont permis à ce travail d'être correctement accompli. Pierre Kulinski, Fabien Marteel et Antoine Vaillant pour leurs contributions inestimables dans le développement et la mise en fonctionnement du TRAPS et de la campagne MIXTAPE. Fabrice Cazier et Dorothee Dewaelée qui ont mis à ma disposition les analyseurs et qui ont été disponible tout au long de la campagne MIXTAPE surtout lorsqu'il y'avait les problèmes. Ensuite Hervé Delbarre, Patrick Augustin, Elsa Dieudonné et Marc Fourmentin pour la collaboration lors de ces trois années en plus des données de dynamique et de météorologie mises à ma disposition. Eric F., Weidong C. et Ghoufrane A. pour les travaux sur la PAS. Et enfin, avec la plus grande reconnaissance, Romain Dufour pour son aide technique tant pour la campagne terrain que pour le traitement de données.

Je souhaite adresser des remerciements tout particuliers à Fatma Ozturk pour m'avoir encouragée à continuer dans la recherche. J'ai beaucoup appris auprès de toi lorsque j'étais encore ton étudiant en cycle Bachelor. Si j'ai réussi à en arriver là aujourd'hui, c'est aussi grâce à toi. Merci beaucoup !

Un merci spécial à Anh Bao Phung Ngoc, Willy Ayissi., Césaire Fotsing., Amadou Petouchi., Nina Reijrink, Roukaya Njoya et Rizky Amalia qui m'ont aidé pour la programmation sur python, les cartes et à relire certaines parties du travail. Vous m'avez fait gagner un temps précieux !

Je remercie également tous mes collègues amis Bastien W. Corantin M., Wilfried B., Hamed K. Salimata T., Amina S., Fatima A. Jonas D., Minh N., Ioannis C, Khaoula K., Boutheina A., Stephanie, Nur J., Layal F.,

Pendant ces trois années j'ai eu l'honneur de diriger l'association des étudiants Camerounais de Lille et le réseau de jeunes Panafricains The Cowry Network que j'ai fondé avec d'autres jeunes Africains. Je tiens à témoigner ma gratitude aux personnes suivantes qui sont ma famille à Lille et ailleurs pour leur soutien, leur confiance, leur présence. Boubacar A., Boukar Y., Moustapha M., Mouncharou M., Issah Ngouon, Adamou Y., Peouonchi Amadou, Fatime Ousman., Nabilah Pemi., Frédéric N., Leyla Sani, Philémon N., Ingrid E., Boris T., Parfait B., Jeanne B, Borel T., Yvan N., Billy., Steeve M., Stella N., Maximilienne N., Danielle K., Aissata K., Maleki A., Mery T., Ibrahima T., Boris O., Thérèse N., Adele Ngole., Obaa Akua., Abdulaziz Shan, Soyab A., Kamga M.n Fodop Y., Thépé F., Nkouakep D., Kouenda S., Ngouanet M., Kodikong F., Kanmegne D., Mounbagna Y., Mounpain A.. J'en ai forcément oublié car vous êtes très nombreux(ses).

Une attention particulière à la famille Karadeniz ; Ayhan, Derya, Nehir, Mustapha, et surtout ma princesse Elif.

Enfin, je tiens à remercier tout particulièrement ma merveilleuse famille de m'avoir toujours soutenu et accompagné pour mener à bien mes études Alim K., Mohamed M., Balkiss M. Rachidetou M. Saretou N. (ma jumelle), Rahinatou N., Adamou M., Ibrahim M. d'une part et à quelques membres très particuliers de ma famille Amidou Mbouandi., et Poukone Abdou pour leurs conseils et accompagnements.

Et surtout merci à toi, Maman qui a su me soutenir dans toutes les étapes de ma vie en général, bonnes comme mauvaises. Tu as toujours trouvé les mots pour me remonter le moral et me rassurer que je pouvais y arriver, surtout quand j'en avais le plus besoin.

FOREWORD

These thesis works began in October 2018 and were therefore scheduled to be completed by the end of 2021. They were to be supported in the second part of the thesis by a field campaign in the Dunkirk metropolitan area, intended to monitor a significant number of fine particle pollution episodes, allowing the most exhaustive description possible of the factors driving these episodes and their influence on the chemical composition of particles. The development of the COVID 19 epidemic having led to a quasi-complete confinement of the population, in France, in spring and autumn 2020, this field campaign was postponed several times and could thus only start in spring 2021 and end in November 2021, so with one year of delay. Soulemane NGAGINE obtained a six-month extension of his funding (until March 2022), which allowed him to complete this work and in particular the samples analysis, the exploitation of the results of the field campaign and the writing of his thesis manuscript. These time constraints did not allow him to consider the publication of these results on the field campaign, as it had been initially planned. This publication should be completed in the next few months.

Table of contents

Acknowledgments	7
FOREWORD	10
Table of contents	12
List of Figures	16
List of Tables	24
Abbreviations	26
Résumé de la thèse en français	27
Introduction	46
1. Atmospheric Aerosols	53
1.1. Physical characteristics of atmospheric aerosols.....	53
1.1.1. Size of aerosols	53
1.1.2. Aerosols life cycle.....	54
1.2. Sources of atmospheric aerosols	56
1.2.1. Anthropogenic sources	57
1.2.1.1. Traffic	57
1.2.1.2. Industrial activities	59
1.2.1.3. Coal and biomass burning	59
1.2.2. Natural sources.....	60
1.2.2.1. Mineral dust	60
1.2.2.2. Sea spray	61
1.2.2.3. Volcanic eruptions.....	61
1.2.2.4. Biogenic aerosols.....	62
1.3. Impacts of aerosols on climate and human health	62
1.3.1. Aerosols and climate.....	62
1.3.2. Aerosols and health	63
1.4. Chemical composition of atmospheric aerosols	66
1.4.1. Organic Aerosols (OA)	66
1.4.2. Secondary Inorganic Aerosols (SIA)	68
1.4.2.1. Ammonium sulphate and nitrate	68
1.4.2.2. Formation mechanisms of secondary inorganic aerosols	71
1.4.3. Black Carbon (BC)	73

1.4.5. Mineral dust	74
1.4.6. Sea-salt particles.....	75
1.4.7. Metals.....	76
1.5. Previous studies in the Great Dunkirk Area	77
1.6. Mixing state	79
1.6.1 Definition and importance of the study of the mixing state of aerosol particles	79
1.6.2. Characterisation of the chemical mixing state	81
1.6.3 Studies using the mixing state index, χ	86
2. Materials and Methods	90
2.1. Study area: Air quality in the Hauts de France Region (HDF) and in the Great Dunkirk Agglomeration (GDA).....	90
2.2. The MIXTAPE campaign.....	94
2.2.1. Sampling site	94
2.2.2. Meteorology	95
2.2.3. Forecasting PM pollution episodes	98
2.2.4. Instrumentation and measurements rationale.....	99
2.3. Individual particles characterisation during MIXTAPE.....	101
2.3.1. Particles sampling using the TRAPS	101
2.3.2. Individual particle analysis by TSEM-EDX.....	106
2.3.3. Identified particle types	113
2.4. Computation of the Mixing State Index χ	117
2.5. Other measurements.....	120
2.5.1. PM _{2.5} mass concentration	120
2.5.2. Aethalometer, SMPS and OPC.....	120
2.5.3. Meteorology and Atmospheric dynamics	124
3. Methodology of physico-chemical characterization of atmospheric particles	127
3.1. Time-resolved cascade impactors in the literature	127
3.2. Description and Theoretical Considerations.....	131
3.2.1. Description of the TRAPS	131
3.2.2. Theoretical Calculations and TRAPS Design	135
3.3. Materials and Methods	137
3.3.1. Experimental Setups for Laboratory Experiments	137
3.3.2. Experimental Setup for Atmospheric Applications.....	141

3.4. Results and Discussion	141
3.4.1. Experimental Determination of the Cut-Off Diameters	141
3.4.2. Observation and Analysis of Collected Particles.....	145
3.4.3. Application to Fine-Particle Pollution Event Monitoring	150
3.5. Conclusion.....	153
4. Analysis and evaluation of typical PM₁₀ pollution days in the Great Dunkirk Area	155
4.1. Data availability.....	155
4.2. Overview of air pollution days in the GDA.....	157
4.2.1. Compliance with air quality standards	158
4.2.2. Monthly variability	159
4.3. Classification of PM ₁₀ pollution days in the GDA	160
4.3.1. Local vs regional polluted days	163
4.3.2. Local episodes.....	164
4.3.3. Pollution events.....	166
4.4. Hourly description of few typical PM ₁₀ pollution events	167
4.4.1. PM evolution and meteorology.....	168
4.4.2. Sources of PM during PE-A.....	174
4.4.3. Sources of PM during PE-B and PE-C	177
4.4.4. Sources of PM during PE-D	178
4.5. Conclusion.....	182
5. Physico-chemical characterization of coarse and fine individual particles during pollution events in the Great Dunkirk Area.	184
5.1. MIXTAPE campaign overview.....	184
5.2. Overview of individual particle composition and mixing state during MIXTAPE	190
5.2.1. Evaluation of the accuracy of TSEM-EDX data	190
5.2.2. Individual particle composition and mixing state during MIXTAPE.....	192
5.3. Impact of environmental factors on the composition and mixing state of fine particles	195
5.3.1. Influence of pollution level.....	195
5.3.2. Influence of the local wind sector	197
5.3.3. Influence of the pollution type.....	199
5.4. Temporal variability of particulate pollution at the hourly scale.....	201
5.4.1. Evolution of individual particle composition and mixing state	204
5.4.2. Evolution of particles mixing state according to their particle type.....	209

5.5. Conclusion.....	211
General Conclusion	213
References.....	217
Annex.....	239
Communications	242

List of Figures

Figure 0-1. Basic scheme of the life cycle of aerosols, including emissions from their natural and anthropogenic sources, their transformations and their removal in the atmosphere.....	46
Figure 0-2. Evolution of aerosol mixing state of an aerosol that is transported in the atmosphere. The line graph (top) illustrates how aerosol mixing state changes qualitatively between a more or less internally mixed state and how different aerosol processes contribute to that change. Adding new types of aerosol particles makes the population more externally mixed (steps 2 and 4), while aerosol aging processes (step 3) or the addition of one dominate particle type (step 5) moves the population toward a more internally mixed state. DMS = dimethyl sulfide (Riemer et al., 2019).....	47
Figure 1-1. Representation of aerosol size distribution and the main formation and removal processes that influence aerosols composition and concentration in the atmosphere (Adachi and Buseck, 2008).	55
Figure 1-2. Regional deposition of particles in the human respiratory track and names of the different locations: the extrathoracic airway (ET), the tracheobronchial airway (TB), and the alveolar interstitium (AI) (adapted from Swuste et al., 1995).....	65
Figure 1-3. SOA formation from BVOCs reactions under low and high NO _x concentration.....	67
Figure 1-4. PM _{2.5} relative average composition at different European sites (Putaud et al., 2004).....	69
Figure 1-5. Annual average PM ₁ relative chemical composition across Europe. In panels (top and bottom), percentages (%) are the ranges of the annual averages and figures in italics are the number of sites for each category. (Bressi et al., 2021).....	70
Figure 1-6. TEM images showing morphology of soot-bearing aerosol particles: (a) fresh chain-like soot aggregates with no visible coating; (b) partially embedded soot (c) fully embedded soot (d) a subtype of fully embedded soot: individual soot particles were only embedded in the organic coating on a sulphur-rich particle (Xu et al., 2020).	74
Figure 1-7. Example of SEM images of mineral particles during haze episodes in Jinan City (North China). Mineral particles coated by Ca(NO ₃) ₂ (left), mixture of aggregation of many regular CaSO ₄ rods and minerals together coated by Ca(NO ₃) ₂ (middle) and irregular mineral particle (right). (adapted from (W. Li et al., 2016))	75
Figure 1-8. TEM images and EDS spectra of the typical fresh, partially aged and fully aged SSA. The main anionic elements are shown in the square brackets (Xu et al., 2021).	76

Figure 1-9. Morphology and composition of metal particles in East Asia. (a) one Pb-S bar mixed with Zn-rich coating, with minor S. (b) one regular Pb-S and two Fe-rich (Fe oxides) spheres mixed within S-rich aggregates. (d) one aggregate of many Fe-rich spheres with Zn-rich coating. (c) one Fe-rich sphere mixed within S-rich coating. (Adapted from (W. Li et al., 2016)	77
Figure 1-10. Diagram showing a fully externally mixed (a), a fully internally mixed (b) aerosol populations and an intermediate internal mixture (c), close to reality, with three different chemical species, symbolized by the colours blue, green and orange (adapted from Guilbaud, 2018).	80
Figure 1-11. Illustration of the relationship between $D\alpha$, $D\gamma$ and χ for representatives aerosol populations (Riemer and West, 2013)	85
Figure 1-12. Summary of the categories of chemical measurements used for mixing state and the type of information provided (Riemer et al., 2019).....	86
Figure 2-1. Localisation of the Great Dunkirk Area (GDA) (b), in the Hauts-de-France Region (a), located on the North Sea coast of France, close to Belgium and England. Principal land occupation includes industrial areas (purple), urban (brown), the North Sea (blue), farmlands (green) and road network (black). U, I, I2, S and R represent the different air quality monitoring stations, mainly of the air quality monitoring network ATMO-HdF (www.atmo-hdf.fr). M is the MIXTAPE sampling site hosting the meteorological station and presented later.....	91
Figure 2-2. Major pollutant emissions according to different sectors of activity in the Hauts de France region in 2018 (adapted from the report “Bilan de la qualité de l'air en 2018”,(ATMO HdF, 2018)	92
Figure 2-3. Number of days of PM ₁₀ levels exceedance of the daily EU limit in Northern France from 2014 to 2020 (ATMO HdF, 2020).....	93
Figure 2-4. Location of the MIXTAPE sampling site on the map of the Great Dunkirk Area (a.), external view of the shelter (b.) into which the instruments for PM sampling and pollutants monitoring are installed (c.). The meteorological station can also be seen on the rooftop of the nearby building in (b.).	95
Figure 2-5. Daily profiles of principal meteorological parameters (a): temperature (T), relative humidity (RH), wind speed (WS), pressure (P) and principal winds (b) observed at the M station in 2019.....	96
Figure 2-6. View of the shelter in which all the instruments are installed for monitoring. The sampling heads used respectively for the TRAPS, the Beta gauge “MP101” are shown together with the meteorological station. (Credit: Marc Fourmentin).	99

Figure 2-7. Schematic representation of impaction principle (a), a view of a multistage cascade impactor (b) and a collection efficiency curve for stage characterization (c) (Hinds, 2012)..... 102

Figure 2-8. Image showing the instruments used for in-situ characterisation of particles during the MIXTAPE campaign. The TRAPS is set inside a fridge (+4°C). Other instruments installed in the shelter such as the SMPS (TSI Inc.), the Optical Particle Counter (OPC) Mini-Wras (Grimm TM) and the aethalometer AE55 (Mc Gee Scientific) were connected to the same sampling line. (Credit: Marc Fourmentin)..... 103

Figure 2-9. View of a TRAPS impaction plate (Stage 2) onto which TEM grids are stacked on the polycarbonate membrane. The rotation of the plate in clockwise favouring collection of samples in a chronological order from T20 the initial sample at position zero to maximum T210 as shown here. 104

Figure 2-10. Illustration of a scanning electron microscope. Source: Liberal Dictionary (<https://www.tekportal.net/scanning-electron-microscope/>)..... 107

Figure 2-11. Image of the FEG-SEM model JEOL JSM-7100F located inside the IRENE-ULCO research building. (Credit: Marc Fourmentin)..... 108

Figure 2-12. Electron matter interactions at different sample depths and derived techniques of analysis (Sharga et al., 2021) 109

Figure 2-13. SEM images of individual particles collected during the MIXTAPE campaign (a) OM particle coated with N and S, (b) soot particles, (c and g) fresh and aged sea salts particles, (d and h) Ammonium sulphate and internally mixed sulphate particles with OM and soot, (e and i) particles rich in Si, Al, (e, f and j) metal-bearing particles and particularly iron oxides spheres and (k and l) particles mainly composed of Ca..... 114

Figure 2-14. mean EDX spectra of the main individual particle types (a and b) Carbonaceous, (c and g) Na-rich, (d and h) S-rich, (e) Si, Al-rich, (f) Metal-rich, (k and l) Ca-rich and (i) Unclassified type. (j) SEM image of the mixed particle composed of soot and silicates. The colours of the spectra are those used to represent each particle in the figures in chapter 5. The Cu-lines are due to the support of the carbon film (Cu-grids). 115

Figure 2-15. External view of the rooftop of the shelter into which the instruments are installed. 121

Figure 2-16. Schematic view of a Differential Mobility Analyzer 123

Figure 2-17. Schematic cross-section and operating principle of a Condensation Particle Counter 124

Figure 3-1. Rotating drum impactor (RDI) with PM10 inlet (left picture), nozzles for RDI stages A–C (middle), RDI sampling wheel with a stage C (0.1–1 μm) sample (right picture) (Bukowiecki et al., 2009)..... 129

Figure 3-2. Working principle of the Streaker (a) and a view of a typical particles sample on a 82 mm polycarbonate membrane with streaks readily visible (b) (<http://www.pixeintl.com/Streaker.asp>) 130

Figure 3-3. Internal view of the TRAPS impactor (a) and scheme of the acceleration nozzles with their dimensions and internal views (A-A cross-sectional drawing), for the coarse (b,d) and fine (c,e) stages. 132

Figure 3-4. Photographs of (a) the fully assembled TRAPS and its command board, (b) TRAPS parts (credit photo: Marc Fourmentin)..... 132

Figure 3-5. Output file extracted at the end of each TRAPS sampling series. Main information in the colored frames include: 1. date and time of the introduction of the SD card in the command board; 2. sample's (impact) start and end date and time; 3. sample number; 4. sampling duration; 5. rotation of the PM1 stage; 6. rotation of the fine stage; 7. example of the 3rd out of 12 possible samples. 134

Figure 3-6. Schematic view of the experimental setup for determining the fine stage collection efficiency using nebulized monodisperse silica spheres. 138

Figure 3-7. Image of the experimental set-up in the laboratory (LPCA-Dunkerque). 139

Figure 3-8. Schematic representation of the experimental setup for determining the coarse stage collection efficiency using vortex shaking of powders of monodisperse silica spheres. 140

Figure 3-9. Schematic representation of the four configurations used for the experimental determination of the collection efficiency. The nozzles of the coarse and fine stages are represented, respectively, in red and yellow. The motors and plates were removed in configurations (B, D), while the stages were fully assembled (with all their nozzles, motors and collection plates) in configurations (A, C). 142

Figure 3-10. Theoretical (blue dotted line) and experimental (black line) collection efficiency curves for the coarse (a) and fine (b) stages (Error bars = 1 S.D with n = 5 for the coarse stage and 3 S.D with n = 5 for the fine stage). 143

Figure 3-11. TSEM images (magnification: 50 \times , accelerating voltage: 15 kV) of the fine stage samples showing sodium chloride particles (a) and silica nanospheres (b) collected for 1 and 5 min, respectively. 146

Figure 3-12. TSEM images (Magnification: 25×, Accelerating voltage: 15 kV) of the coarse stage samples showing silica microspheres collected for 6 min.	147
Figure 3-13. Mean particle mass size distribution obtained using an optical particle counter (MiniWRAS model 1371 Grimm™) on June 13 th 2021 from 08:00 to 10:00 UTC.....	148
Figure 3-14. Image of the TEM grid (fine stage) used to evaluate the homogeneity of the repartition of impacted particles. The width of the impaction trace is marked by 2 horizontal lines and the nozzle width by 2 dotted lines. Green, blue and purple rectangles represent the analysed areas.	149
Figure 3-15. Distribution of the 6 particle types over the analysed areas identified in Figure 7. Each point represents a particle and each colour a particle type. A total of 405, 763 and 567 particles are observed in the green, blue and purple areas, respectively.....	150
Figure 3-16. Time series evolution of PM _{2.5} mass concentration at our sampling site. Coloured rectangles represent the TRAPS sampling periods, where P1 and P5 (cyan) are the analysed samples whose results are discussed in the paper.	151
Figure 3-17. Relative contribution of different particle types during P1 and P5, respectively, for the TRAPS fine fraction ((a) coarse stage) and ultrafine fraction ((b) fine stage).	151
Figure 3-18. 72 hours backtrajectories calculations arriving at 500 m altitude at the sampling site respectively on April 20 th and April 21 st at 08:00 UTC.....	153
Figure 4-1. Map of the Great Dunkirk Area located in the Northern-France Region. Seasonal variation of wind speed and direction in 2019. The industrial installations (purple), urban settlements (brown), agricultural and forest areas (green), main roads (black) are also represented, together with the different measurement stations of the ATMO HDF air quality monitoring network (AQMS) and the meteorological station M.	156
Figure 4-2. Seasonal variability of PM ₁₀ polluted days (PD) recorded at at least one of the 3 GDA stations (U, S and I) in 2018 (black), 2019 (dark blue) and 2020 (light blue).	159
Figure 4-3. Seasonal variation of the total rainfall that was recorded in the GDA from 2018 to 2020.	160
Figure 4-4. Flowchart for the classification of PM ₁₀ pollution episodes in the GDA. U, S, I and R refer to the Urban, Sub-urban, Industrial and Remote AQMS. WS refer to the wind speed recorded at the M station.	161
Figure 4-5. Repartition of the 91 PD recorded in 2018-2020, according to the plume extent (local or regional) and atmospheric condition (stationary or dispersion condition).	163

Figure 4-6. Monthly variation of local scale and regional polluted days in the GDA from 2018 to 2020	164
Figure 4-7. Number of stations impacted by the PM ₁₀ pollution plume during the local PD recorded from 2018-2020.....	165
Figure 4-8. Proportion of single pollution days compared to pollution events for 2018-2020.	167
Figure 4-9. Evolution of the PM _{2.5} /PM ₁₀ ratio according to PM ₁₀ concentrations (in µg/m ³) at the urban site (U).	168
Figure 4-10. Evolution of PM, precursor gases and meteorological parameters during PEA	169
Figure 4-11. Evolution of PM, precursor gases and meteorological parameters during PE-B and PE- C.....	172
Figure 4-12. Evolution of PM ₁₀ , precursor gases and meteorological parameters during PE-D.....	173
Figure 4-13. Location of the main land occupation map in the GDA together with pollution roses of urban PM _{2.5} (a) and industrial NO ₂ (b) concentrations during PEA (both PDA-1 and PDA-2). Urban (brown) and industrial (purple) areas can be identified in the south-western direction using the urban station (U) as a reference.	175
Figure 4-14. 3 days backward trajectories simulation showing air masses crossing the UK before arriving at 500 m altitude in the GDA during 2 pollution peaks recorded during PE-B and PE-C using the web-based version of HYSPLIT (https://www.ready.noaa.gov/).....	178
Figure 4-15. Daily cycle of PM ₁₀ , O ₃ , NO ₂ and SO ₂ concentrations during PED for remote (orange), sub-urban (green), industrial (purple) and urban (brown).	181
Figure 5-1. Map showing the Mixtape sampling site (M) and air quality monitoring stations (U, I and S) of the Atmo-HdF (www.atmo-hdf.fr) network. Industrial (purple) and urban (brown) areas, farmlands (green), northern sea (blue) as well as the road network (black lines) characteristics of the GDA are also presented. 4 main wind sectors influencing the M site are also represented: the marine, industrial-marine, industrial urban and urban sectors. MP: Metallurgy plant, EP: energy plant, R: Oil Refinery, CP: Chemical plant, AZ: Astra Zeneca, ESP: Electrical steel plant are among the main industrial installations across the study area.	185
Figure 5-2. Monthly temperature variation from 2018 to 2021 (a.) and seasonal variation of wind speed and direction (b) in 2021 in the Great Dunkerque Area (GDA). Error bars = ±1 S.D.....	186

Figure 5-3. Temporal variation of daily PM _{2.5} concentrations at the M and U stations from January to September 2021. Cyan rectangles highlight the studied pollution events where particle samples were collected.	187
Figure 5-4. Relative error associated to D α , D γ and χ for the different samples (S1 to S29) of fine particle fraction.	191
Figure 5-5. Atmospheric concentration (in cm ⁻³ , 1-10 μ m range) (top), D α , D γ and χ (middle), and relative abundance of individual particles (bottom) for all the samples collected on the coarse stage (1-10 μ m) during this MIXTAPE campaign. Error bars plotted together with χ values. The number of analyzed particles is indicated above the sample number.	193
Figure 5-6. Atmospheric concentration (in cm ⁻³ , 0.1- 0.7 μ m range) (top), D α , D γ and χ (middle) and relative abundance of individual particles (bottom) collected on the fine stage (0.1-1 μ m) for all the samples collected during the MIXTAPE campaign. Error bars plotted together with χ values. The number of analyzed particles is indicated above the sample number (Sx).....	194
Figure 5-7. Atmospheric concentration (in cm ⁻³ , 0.1- 0.7 μ m range) (top), D α , D γ and χ (middle) and relative abundance of individual particles (bottom) collected on the fine stage (0.1-1 μ m) during clean days (left) and polluted days (right) for samples S1 to S29.	197
Figure 5-8. Atmospheric concentration (in cm ⁻³ , 0.1- 0.7 μ m range) (top), D α , D γ and χ (middle) and relative abundance of individual particles (bottom) collected on the fine stage (0.1-1 μ m) under blowing winds from sectors Marine, Urban, Industrial (Industrial-urban and Industrial-Marine) sectors....	198
Figure 5-9. Atmospheric concentration (in cm ⁻³ , 0.1- 0.7 μ m range) (top), D α , D γ and χ (middle) and relative abundance of individual particles (bottom) collected on the fine stage (0.1-1 μ m) for each type of polluted day. Results of the samples collected when only PM _{2.5} levels exceedance were observed are also presented.....	200
Figure 5-10. Linear regression between hourly Mixtape PM _{2.5} and urban PM _{2.5} data.....	202
Figure 5-11. Time series evolution of PM _{2.5} at the U station (darkcyan) and meteorological parameters: WS (red), WD (black), T(orange), RH (blue), SR (filled dark cyan). Colored rectangles in cyan represent TRAPS sampling periods.	203
Figure 5-12. Time-height cross-sections of horizontal wind speeds and wind direction (top) and vertical wind dispersion (bottom) measured by the Doppler Lidar on March 31 th and April 1 st . Rectangles in red represent particle sampling periods.....	204

Figure 5-13. Evolution of $D\alpha$, $D\gamma$ and χ (top) and relative abundance of coarse (1-10 μm) individual particles for all the samples collected during PE1 from S1 to S7. Error bars plotted together with χ values. 206

Figure 5-14. Atmospheric concentration (in cm^{-3} , 0.1- 0.7 μm range) (top), $D\alpha$, $D\gamma$ and χ (middle) and relative abundance of individual particles (bottom) collected on the fine stage (0.1-1 μm) for all the samples collected during PE1 from S1 to S7. Error bars plotted together with χ values. The evolution of particle number concentration (100-750 nm) is also plotted on the top..... 207

Figure 5-15. Three-day back trajectories of continental air (left) arriving in Dunkirk from the W-SW direction in March 21st, 2021 and both continental and marine air arriving in Dunkirk from NE direction in April 1st, 2021 at 12:00. In the second day both continental pollutants from the great Paris region and the English Channel and marine pollutants can be transported to Dunkirk..... 209

Figure 5-16. Evolution of D_a , D_y and X of (a) carbonaceous particles and (b) Na-rich particles for each sample from S1 to S7. 210

List of Tables

Table 1-1. Global emission estimates for major aerosol classes (Fan et al., 2022; IPCC, 2013; Klimont et al., 2017; Seinfeld and Pandis, 2006)	56
Table 1-2. Different types of non-exhaust traffic emissions (adapted from (OECD, 2020))	58
Table 1-3. Aerosol mass definitions and notations. N is the number of particles in the population, and the number of species is A.	82
Table 1-4. Aerosol mass fraction definitions and notations. N is the number of particles in the population, and the number of species is A.	83
Table 1-5. Definitions of aerosol mixing entropies and particle diversity.	84
Table 1-6. Definitions of particle diversities (D_α , D_γ , D_β).	84
Table 1-7. Field studies that used individual particle data to determine the mixing state index, χ	88
Table 2-1. Main potential sources and local activities over the GDA, according to wind sectors, with a focus on possible PM emissions (OC = Organic Carbon, i.e. functionalised; EC = Elemental Carbon, i.e. soot, tar balls,)	97
Table 2-2. TRAPS sampling plan implemented during the first studied pollution event (PE1). As a maximum of 12 samples (i.e. impaction traces: see Chapter 3) can be collected per impaction plate, T10 represent the grid position of the first sample: i.e T (for Trace), 1 (for the coarse stage S1 or 2 in case of stage 2 see below) and 0 (for the sample 0) (see figure 2-10). The time necessary to rotate from one position to another is 60 seconds.	105
Table 2-3. Main parameters applied with Jeol FEG-SEM images and Bruker ESPRIT 2.2 Software to carry out analyses of MIXTAPE samples	110
Table 2-4. Chemical characteristics and possible sources of different types of individual particles.	112
Table 2-5. Specific masses of pure compounds used in the calculation of the particle masses.....	118
Table 3-1. Technical characteristics of the TRAPS.	133
Table 3-2. Theoretical calculations of the stage parameters of the TRAPS at $T = 293\text{K}$ and $p = 101.3\text{ kPa}$	136
Table 4-1. Data availability in each of the U, S, I, R and M stations for the 3-years studied period (2018-2020). The count is the number of daily data for this period, SD is for standard deviation.	157
Table 4-2. Number of polluted days (PD) at the U, S, I or R stations for WHO, US-EPA and EU standards for the 2018-2020 period.	158

Table 4-3. Average wind speed, pressure and PM ₁₀ concentration at the industrial, urban, suburban and remote stations for each class of the most represented local pollution days.	165
Table 4-4. Summary of the daily mean values of PM ₁₀ (U, S, I and R), PM _{2.5} (U), wind speed (WS), and atmospheric pressure (P) associated to the different types of PD comprising the studied PE.	167
Table 4-5. Determination of the correlation factors between PM ₁₀ , PM _{2.5} , O ₃ , NO ₂ , SO ₂ , T°, RH, WS and WD at the Urban, Industrial, Sub-urban or Remote stations during PEA in the GDA.	176
Table 4-6. Determination of the correlation factors between PM ₁₀ , PM _{2.5} , O ₃ , NO ₂ , SO ₂ , T°, RH, WS and WD at the Urban, Industrial, Sub-urban or Remote stations during PED in the GDA.	180
Table 5-1. Classification of the pollution days (PD) investigated during MIXTAPE. Daily mean PM ₁₀ , PM _{2.5} and BC concentrations are given in µg/m ³	188
Table 5-2. Sample ID and collection starting time	189
Table 5-3. Relative number percentage of individual particles for clean samples (CS), PM ₁₀ and PM _{2.5} polluted samples (PS). NS is the number of samples, NP the number of analyzed particles and PC the mean Particle Concentration (in #.cm ⁻³) for the fine (0.1-1µm) size fraction.....	196
Table 5-4. Relative number percentage of individual particles calculated for each PD type based on hourly PM ₁₀ concentrations (NP = number of analyzed particles, NS = number of analyzed samples)	199
Table 5-5. Relative number percentage of individual particles collected using the TRAPS coarse (Stage 1) and fine (Stage 2) stages per pollution day type during PE1.....	205

Abbreviations

ATOFMS	Aerosol time-of-flight mass spectrometry
BC	Black carbon
CCN	Cloud Condensation Nuclei
CCSEM/EDX	Computer-controlled scanning electron microscopy/energy dispersive X-ray spectroscopy
EEA	European Environmental Agency
GDA	Great Dunkirk Area
HCPC	Hierarchical clustering on principal components
MIXTAPE	MIXing sTate of Atmospheric Particles during pollution Events
OPC	Optical particle counter
PCA	Principal components analysis
PD	Pollution day
PE	Pollution events
PM	Particulate matter
PMF	Positive matrix factorization
SEM	Scanning electron microscopy
SEM/EDX	Scanning electron microscopy/energy dispersive X-ray spectroscopy
SMPS	Scanning Mobility particle sizer
STXM/NEXAFS	Scanning transmission X-ray microscopy/near edge X-ray absorption fine structure spectroscopy
TEM	Transmission electron microscopy
TRAPS	Time-Resolved Atmospheric Particle Sampler
VOC	Volatile organic compounds
WHO	World health organization

Résumé de la thèse en français

Malgré une diminution significative des concentrations des polluants atmosphériques réglementés (excepté pour l'ozone) lors de ces 10 dernières années en France, les dépassements des seuils Européens annuels ($25 \mu\text{g}\cdot\text{m}^{-3}$ pour les particules PM_{10} et $\text{PM}_{2.5}$) sont fréquemment observés, comme l'indique l'Agence Européenne de l'Environnement dans son rapport de 2019. Ces dépassements annuels sont le résultat des multiples dépassements de seuils journaliers enregistrés principalement dans les sites urbains et industriels, sites caractérisés par une multitude de sources de polluants. Lorsque ces sites sont situés à proximité des côtes, les conditions météorologiques singulières rendent complexe l'analyse des mécanismes physico-chimiques et dynamiques donnant lieu aux dépassement des seuils journaliers en PM.

L'objectif de cette thèse est de proposer une méthodologie pour étudier l'hétérogénéité chimique des particules atmosphériques lors des événements de pollution sur le site industriel et urbain du Grand Dunkerque. La méthodologie proposée doit pouvoir permettre de renseigner sur la composition chimique et l'état de mélange des particules, avec une haute résolution temporelle, mais aussi à un coût supportable et avec des temps d'analyse raisonnables.

Chapitre 1. Généralités sur les particules atmosphériques

Dans la première partie de cette thèse, un état des connaissances sur les aérosols atmosphériques a été établi. Des connaissances sur les sources et émissions (naturelles et anthropiques), la composition chimique globale (PM_{10} , $\text{PM}_{2.5}$ et PM_i) et individuelle, les processus de formation (Aérosols organiques et inorganiques), les effets sanitaires et climatiques, ainsi que de l'état de mélange des particules atmosphériques, ont pu être fournis. La complexité inhérente à l'étude des aérosols, notamment en raison de la forte variabilité spatio-temporelle de leur concentration et la nécessité de mieux suivre leur évolution lors de leur dispersion en milieu urbain a été illustrée, permettant ainsi de mieux comprendre leur comportement. Un état de l'art des travaux effectués sur le Dunkerquois a également été fourni. Dans la dernière partie de ce chapitre, l'incompatibilité entre d'une part la plupart des instruments disponibles sur le marché pour l'échantillonnage des particules à haute résolution temporelle et d'autre part la poursuite des objectifs de cette thèse, a été mise en évidence. Cela a permis de démontrer la nécessité de développer un instrument d'échantillonnage basé sur le principe de l'impaction en cascade et capable de fournir, en temps opportun et à moindre coût, des échantillons adaptés à l'observation et l'analyse individuelle des particules, incluant la Microscopie Electronique à Balayage (MEB). La

recherche de la meilleure résolution temporelle possible lors de l'échantillonnage nous a conduit à développer un impacteur à plateaux rotatifs, compatible avec les contraintes de l'analyse individuelle de particules.

Chapitre 2 : Méthodologie de caractérisation physico-chimique des particules et détermination de leur état de mélange

La campagne de 9 mois portant sur l'étude des particules atmosphériques lors des événements de pollution (MIXTAPE), conçue pour atteindre les objectifs de cette thèse, est présentée dans ce chapitre. Le site d'étude choisi est la zone du « Grand Dunkerque » (Communauté Urbaine), une agglomération faisant partie des Hauts-de-France et située sur la côte de la Mer du Nord. C'est un site multi-influencé caractérisé par une importante activité industrielle, facilitée notamment par la présence du troisième plus grand port commercial de France, à laquelle est greffé un réseau routier dense permettant de connecter la ville aux principales métropoles comme Paris, Londres, Bruxelles, Amsterdam, etc... Des installations urbaines côtoient les sites industriels et sont circonscrits par de vastes terres agricoles. La position côtière du site l'expose par ailleurs aux émissions de particules marines, en plus de celles provenant des sources anthropiques incluant le transport, le chauffage résidentiel et les émissions industrielles. Un ensemble d'instruments (**Figure 1**) permettant à la fois l'échantillonnage (impacteur en cascade) et la mesure des particules (Jauge beta MP101, SMPS TSI et Grimm) et la surveillance des conditions météorologiques et de dynamique atmosphérique (Lidar WLS 100) a été déployé durant la campagne MIXTAPE.

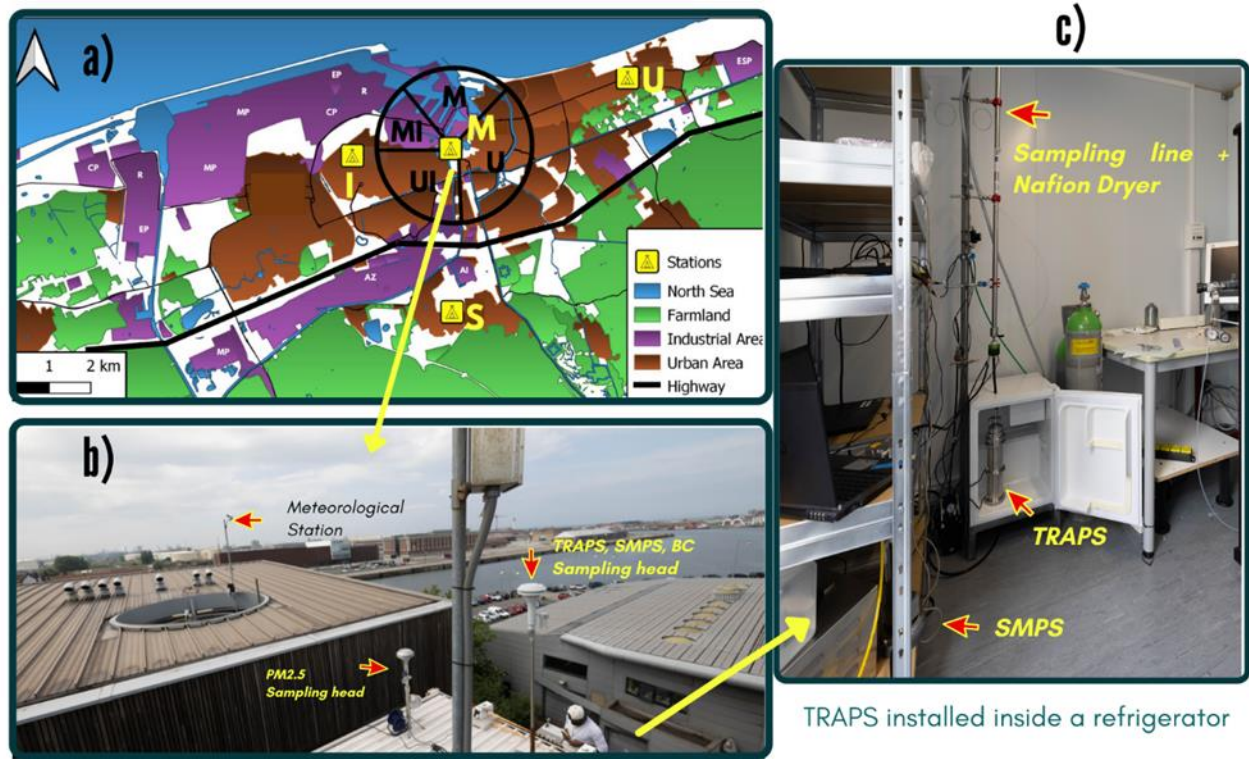


Figure 1. Localisation du site d'échantillonnage MIXTAPE sur la carte du Grand Dunkerque (a.), vue extérieure de l'abri (b.) dans lequel sont installés les instruments d'échantillonnage des particules et de suivi des polluants (c.). La station météorologique est également visible sur le toit du bâtiment voisin (b.).

Les particules prélevées par impaction en cascade ont été analysées par microscopie électronique à balayage, couplée à la spectrométrie d'émission des rayons X en mode automatisé (MEB-EDX). Les données de composition chimique élémentaire fournies par le MEB-EDX sont ensuite traitées par classification hiérarchique ascendante, couplée à l'analyse en composantes principales. Les principaux types de particules sont ainsi identifiés et classés dans 7 groupes : particules carbonées, riches en Na, riches en Ca, riches en Si-Al, riches en S, particules métalliques et « Autres ».

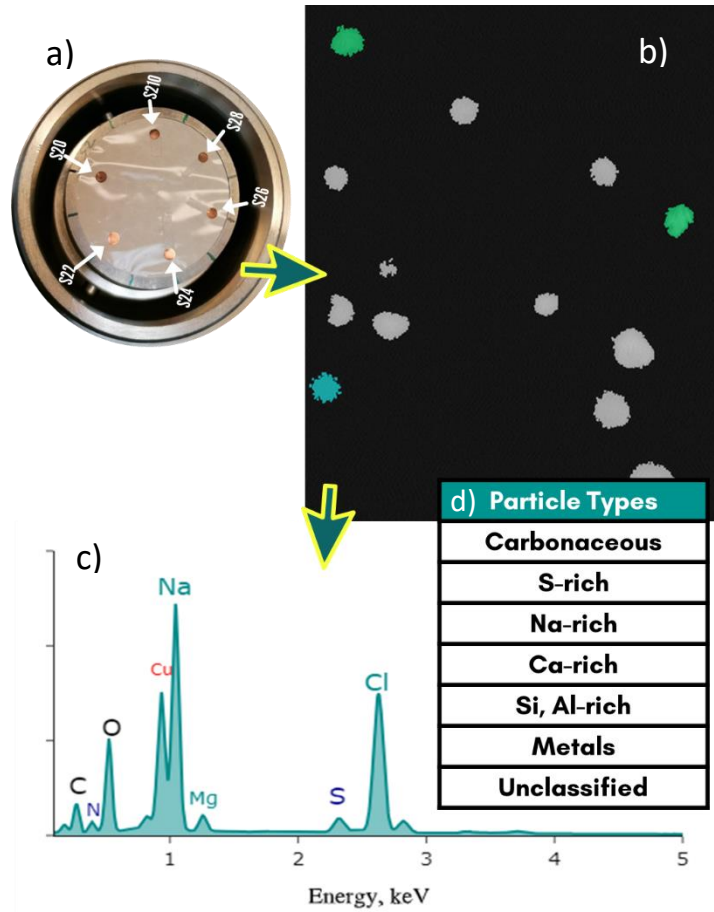


Figure 2. Les échantillons de particules à haute résolution temporelle sont collectés sur des grilles TEM à l'aide du TRAPS(a). Ils sont ensuite analysés par MEB-EDX en mode automatisé. On obtient une image binaire finale (b) permettant l'identification automatique des particules et l'acquisition d'un spectre par particule. Après classification, un spectre EDX (c) moyen des particules est calculé (exemple de particules riches en sodium présenté ici) pour chacun des 7 types de particules (d).

Une fois les principaux types de particules identifiés et leur composition élémentaire établie, un indice d'état de mélange est calculé ($\chi = (D\alpha - 1) / (D\gamma - 1)$) pour l'ensemble des particules de chaque échantillon. Il découle de la diversité intra-particulaire ($D\alpha$), définie comme le nombre moyen effectif d'éléments chimiques présent dans une particule, et la diversité globale ($D\gamma$) représentant le nombre moyen effectif d'éléments présents à l'échelle de l'ensemble des particules analysées. Cet indice χ est proche de 0 lorsque les particules sont essentiellement en mélange externe, et s'approche de 1 lorsqu'elles sont en mélange interne.

Considérant le nombre important de groupe de particules (7) et le nombre d'échantillons à analyser (29) on obtient 203 jeux de données pour lesquels l'indice de l'état de mélange doit être calculé. Il devient inenvisageable de procéder à un calcul manuel chronophage pour chaque échantillon. Dans le but de réduire le temps de calcul et surtout les potentielles erreurs, le calcul de l'indice d'état de mélange a été codée en langage python en utilisant l'interface Jupyter Notebook. Le code généré a ensuite été appliqué à tous les échantillons collectés lors de cette étude.

Chapitre 3. Développement et caractérisation du TRAPS

La conception du TRAPS (**T**ime **R**esolved **A**tmospheric **P**article **S**ampler), la détermination des diamètres de coupure des deux étages d'impaction, ainsi que des caractéristiques de la dynamique de dépôt des particules échantillonnées, sont présentées et discutées dans le chapitre 3. Après avoir décrit le TRAPS (**Figure 3.**), une présentation de la méthode d'estimation des diamètres de coupure théorique à l'aide du logiciel « @aerocalc »[®] a été effectuée.

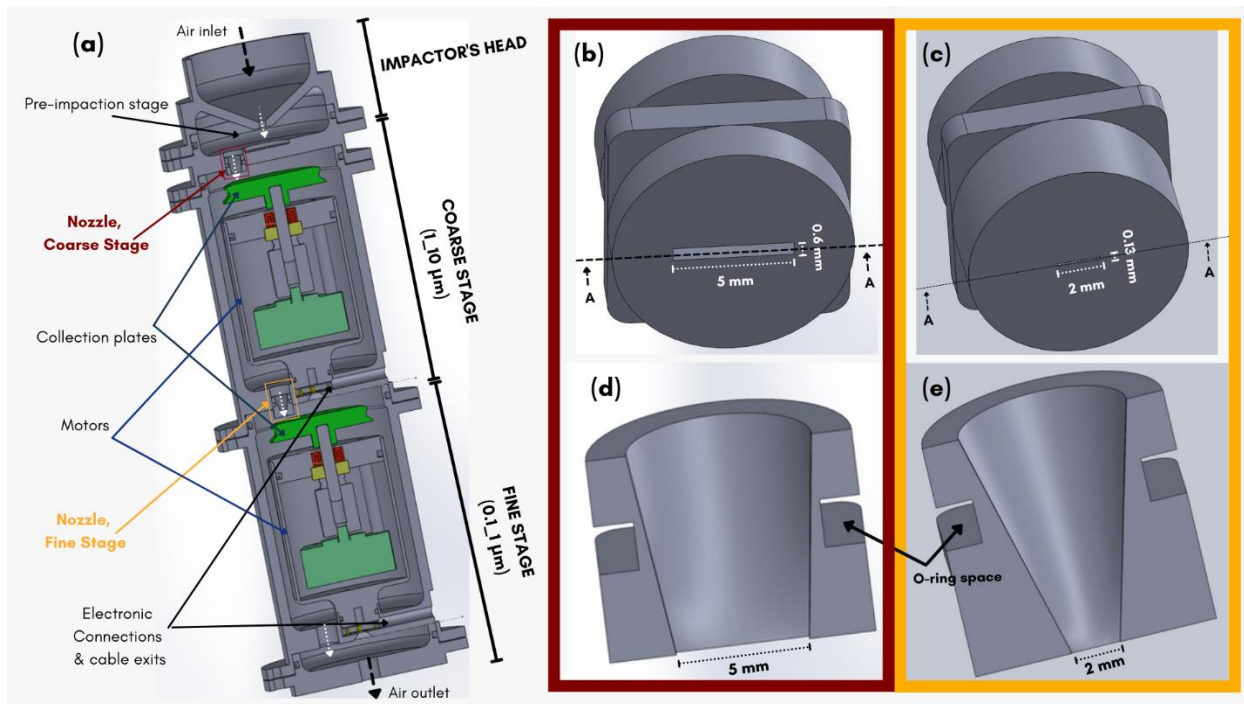


Figure 3. Vue interne de l'impacteur TRAPS (a) et schéma des buses d'accélération avec leurs dimensions et vues internes (dessin en coupe A-A), pour les étages grossier (b,d) et fin (c,e).

Il a ainsi été possible d'estimer théoriquement qu'avec des billes de silice de masse volumique $\rho = 1,80 \text{ g.cm}^{-3}$, une efficacité de collecte de 50% est obtenue pour des particules de diamètre aérodynamique $1.30 \mu\text{m}$ et $0.15 \mu\text{m}$, respectivement pour l'étage grossier et fin. Des expériences conduites en laboratoire, dans lesquels 2 bancs ont été montés respectivement pour l'étage fin et pour l'étage grossier (**Figure 4**), ont permis d'obtenir des diamètres de coupure expérimentaux de 1.32 et $0.13 \mu\text{m}$ et de confirmer que les conditions de fonctionnement du TRAPS sont en accord avec les estimations effectuées lors de sa conception (**Figure 5**).

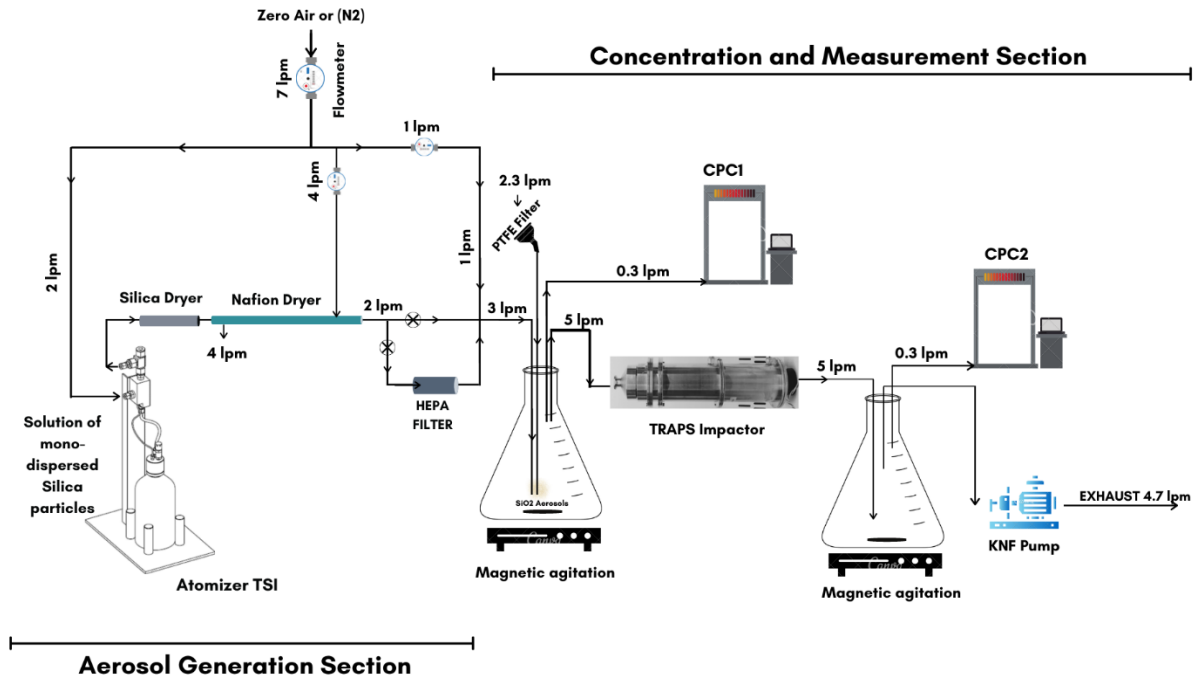


Figure 4. Vue schématique du montage expérimental permettant de déterminer l'efficacité de la collecte de l'étage fin en utilisant des sphères de silice monodispersées nébulisées.

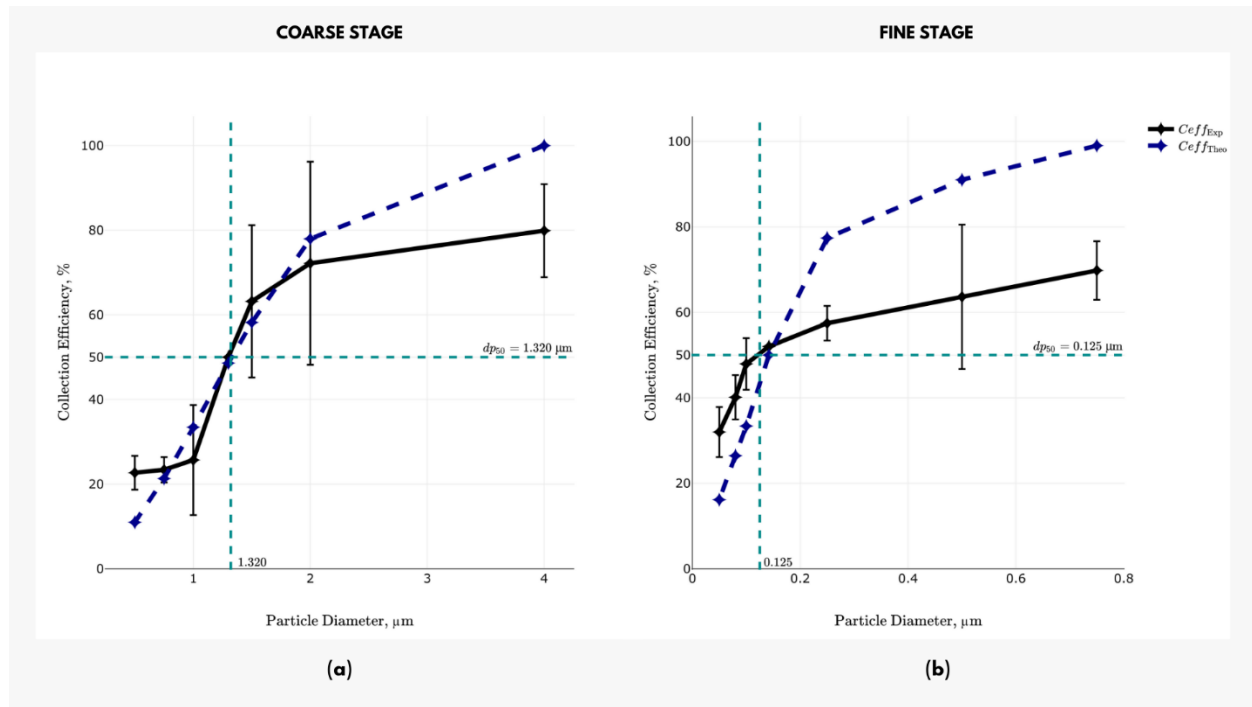


Figure 5. Courbes d'efficacité de collecte théoriques (ligne pointillée bleue) et expérimentales (ligne noire) pour les étages grossier (a) et fin (b) (barres d'erreur = 1 S.D avec $n = 5$ pour l'étage grossier et 3 S.D avec $n = 5$ pour l'étage fin).

Comme il est important qu'un dépôt de particules individualisées soit obtenu afin de faciliter leur analyse par MEB-EDX, l'aspect des traces d'impaction a été étudié au microscope. Cette étude nous a permis :

1) d'estimer l'ampleur de l'effet des rebonds de particule après impaction, et du recouvrement entre deux traces successives à l'intérieur du TRAPS. Des expériences en laboratoire ont permis de montrer que pour un angle de rotation de 28.8° , la distance séparant deux traces d'impaction était suffisante pour éviter le recouvrement.

2) de constater l'influence de la nature et par conséquent de la morphologie des particules, sur la forme des traces d'impaction obtenues. On montre ainsi que les particules de NaCl cristallisé, du fait de leur forme angulaire, se déplacent moins facilement sur le substrat après impaction et par conséquent présentent une forme de dépôt moins dispersé, de morphologie et de taille comparables à celles de la

buse, contrairement aux billes de silice parfaitement sphériques qui se dispersent beaucoup plus sur le substrat de collection.

3) de déterminer, pour un dépôt donné, la distribution spatiale des grands types de particules analysées et de mettre en évidence un dépôt homogène de ces différents types de particules sur les traces d'impaction (**Figure 6**). Ce facteur est crucial pour réduire considérablement les temps d'analyse en MEB par l'observation d'une partie limitée de la trace d'impaction, surtout lorsqu'on est en possession d'un nombre important d'échantillons (58 étages d'impaction dans notre cas, pour les 29 échantillons collectés).

4) d'estimer les temps d'échantillonnage nécessaires pour obtenir des particules individualisées. Les deux derniers objectifs ont été atteints en organisant deux campagnes tests de mesure pour l'échantillonnage des aérosols ambiants.

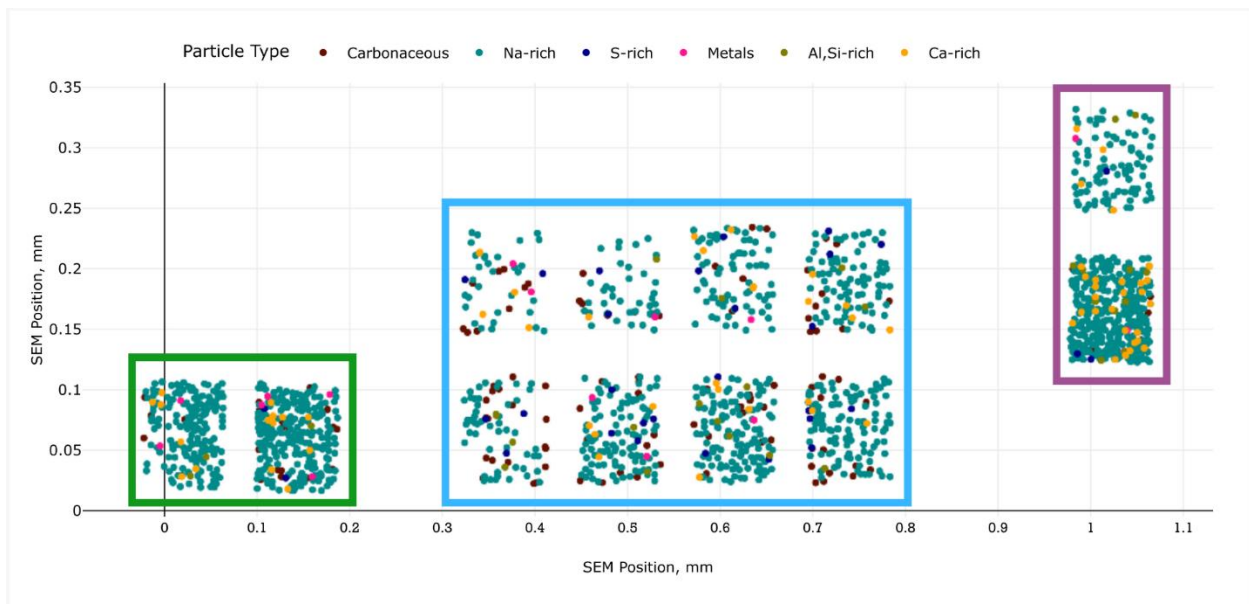


Figure 6. *Distribution des 6 types de particules sur les zones des traces d'impaction analysées par MEB-EDX. Chaque point représente une particule et chaque couleur un type de particule. Un total de 405, 763 et 567 particules sont observées dans les zones vertes, bleues et violettes, respectivement.*

Chapitre 4 : Caractéristiques des épisodes de pollution sur le Dunkerquois

Plusieurs articles ont montré l'influence des conditions météorologiques, notamment les conditions synoptiques et de la direction du vent local sur les concentrations des polluants particuliers mesurés à Dunkerque. A l'échelle Européenne, des travaux ont permis de mettre en évidence l'existence d'une saisonnalité des épisodes de pollution. Ces travaux ont permis d'attribuer des caractéristiques particulières aux différents épisodes. Dans ce chapitre, en utilisant les données de PM₁₀ et PM_{2.5} issues du réseau de surveillance de la qualité de l'air ATMO-Hauts de France, ainsi que la vitesse du vent, une classification des jours de pollution a pu être effectuée. Cette classification se base sur les données fournies par 3 stations locales (Urbaine (U), Industrielle (I) et Sub-urbaine (S)) et une station éloignée des sources (R).

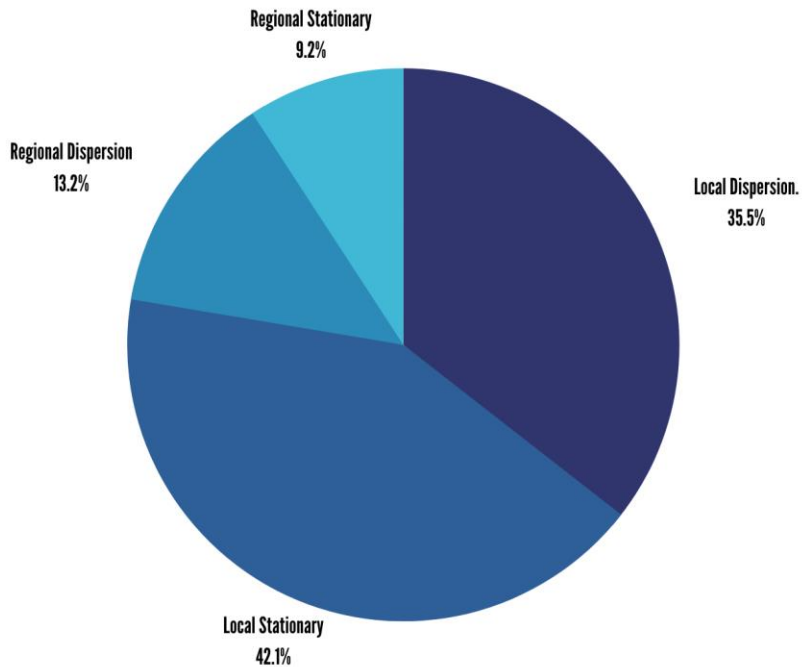


Figure 7. Répartition des 91 jours de pollution enregistrés en 2018-2020, selon l'étendue du panache (local ou régional) et la condition atmosphérique (condition stationnaire ou de dispersion).

L'analyse des 76 jours de pollution aux PM₁₀ (Pollution Days = PD) définis sur la base du seuil journalier maximum recommandé par l'OMS (45 µg/m³) et enregistrés entre 2018 et 2020, permet de montrer que les jours de pollution locale (identifiés dans l'une des trois stations U, I ou S) représentent 77.6% de tous les PD, le reste ayant une ampleur régionale (impliquant un dépassement simultané à la station R) (**Figure 7**). Ces PD sont principalement identifiés vers la fin de l'hiver et au printemps, le mois d'avril étant le plus représenté avec 22 PD. En s'intéressant à l'étendue spatiale de ces jours de

pollution à l'échelle locale (les plus abondants), on constate que la majorité de ceux-ci (plus de 50%) sont très localisés et ne concernent qu'une seule station (soit U, I ou S) et principalement la station industrielle (I). Ceci nous permet d'affirmer qu'en contrôlant précisément ces sources locales, il est possible de réduire considérablement le nombre de jours de dépassement aux PM_{10} sur le dunkerquois. Lorsqu'on s'intéresse au temps de résidence des panaches, on constate que seul 25% des jours de dépassement durent en moyenne 24 heures. Le reste est défini comme étant un événement de pollution (Pollution Event = PE), période pendant laquelle le dépassement des seuils journaliers des PM_{10} dure au moins 2 jours. Leur importance est critique notamment lorsqu'on s'intéresse à leurs effets sur la santé publique, car cela impacte le niveau de sévérité de l'événement, du fait de sa persistance. Quatre évènements de pollution typiques enregistrés entre 2018 et 2020 ont ensuite été finement étudiés, afin de compléter cette classification des jours de pollution par une description temporelle plus fine (horaire) des phénomènes pouvant permettre d'identifier les sources d'aérosols de pollution lors de ces évènements.

Chapitre 5 : Composition et état de mélange des particules atmosphériques lors des évènements de pollution sur la zone du Grand Dunkerque

Cinq évènements de pollution (PE) comprenant 11 jours de pollution (PD) ont été étudiés lors de la campagne MIXTAPE. Cette campagne a duré de janvier 2021 à octobre 2021. Dans ce chapitre, une vue d'ensemble des résultats de l'analyse des 28 000 particules obtenues à partir de 29 échantillons collectés est fournie. L'erreur associée au calcul de l'indice d'état de mélange pour chacun des échantillons collectés (**Figure 8** pour la fraction fine - 0.1-1 μ m) a été estimée à partir des travaux de Gasparik et al., (2020) qui ont montré que cette erreur est proportionnelle à l'erreur de comptage, c'est à dire proportionnelle à $\frac{1}{\sqrt{N}}$, N étant le nombre de particules analysées pour un échantillon donné. Un faible nombre de particules (moins de 1000 par échantillon) causerait une surestimation de la diversité particulaire moyenne ($D\alpha$) et une sous-estimation de la diversité globale ($D\gamma$), entraînant ainsi une surestimation de l'indice d'état de mélange (χ).

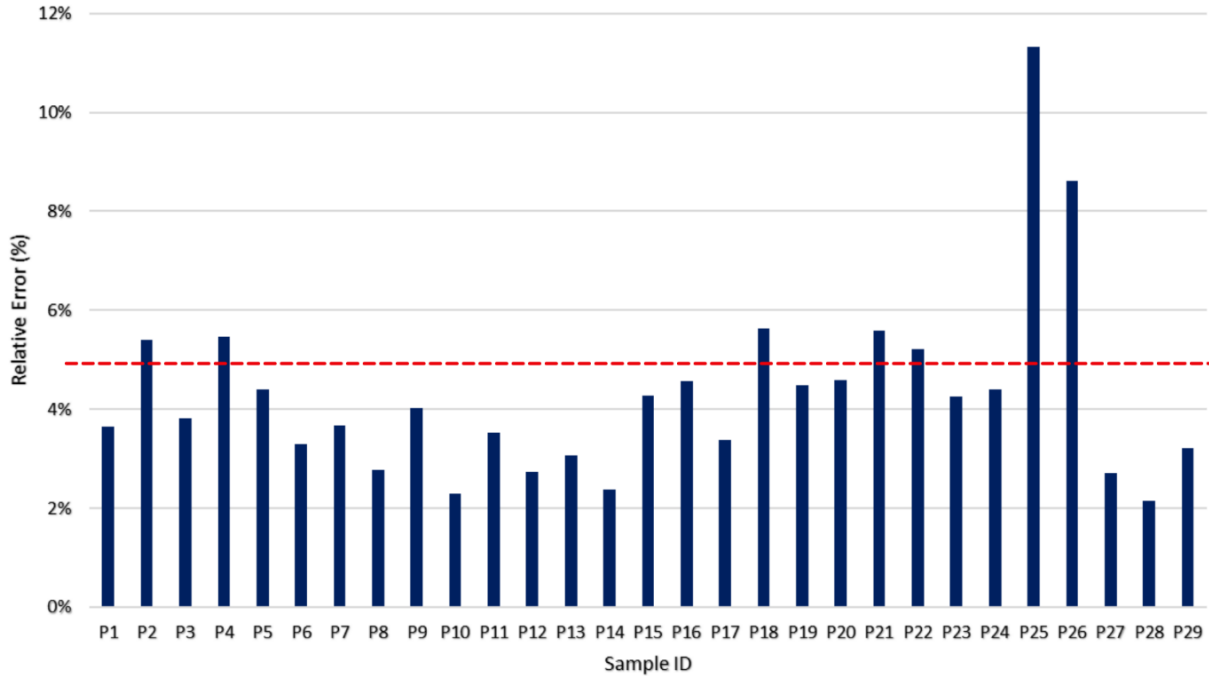


Figure 8. Erreur relative associée à D_a , D_γ et χ pour les différents échantillons (S1 à S29) pour la fraction fine ($0.1-1\mu m$)

On constate (Fig.8) que l'erreur relative est <5% pour 77% des échantillons analysés et inférieure à 10% pour 97% des échantillons. Cela nous amène à estimer que nos résultats sont fiables et peuvent être comparés à d'autres travaux dans la littérature.

L'évolution de la composition chimique et de l'indice d'état de mélange de l'ensemble des particules collectées durant MIXTAPE (29 échantillons ; Figure 9) sont discutés dans cette partie, à la fois pour la fraction fine et pour la fraction grossière des échantillons collectés avec le TRAPS. On constate, d'une manière générale, une forte variabilité dans la composition élémentaire, avec des échantillons composés des 6 types de particules identifiés précédemment par clustering, quand d'autres sont dominés par un seul type, en majorité des particules riches en sodium et des particules carbonées (Figure 9).

Si on s'intéresse plus particulièrement à certains échantillons, on constate que ceux présentant des compositions élémentaires pouvant apparaître comme similaires peuvent présenter en réalité des indices d'état de mélange différents. Par exemple, pour les échantillons S7 et S14 (Figure 9), on constate que l'échantillon S14, avec 8 éléments présents en moyenne (Tableau 1), est *A Priori* plus complexe chimiquement que l'échantillon S7 qui en compte 5. Ce qui de prime abord suggère une

diversité chimique plus importante pour l'échantillon S14. On constate cependant que S7, avec un $D\gamma$ de 5 éléments effectifs, est en fait plus complexe chimiquement que S14 ($D\gamma = 4.5$ éléments). Ceci s'explique par le fait que les 5 éléments effectifs (O, C, Cl, Na et S) de S7 sont à la fois présents au sein de la population et également au sein de chaque particule, ce qui conduit à un indice d'état de mélange de 0,92, contrairement à l'échantillon S14, dont l'indice n'est que de 0,77, car les 8 éléments présents ne le sont pas systématiquement dans chacune des particules analysées.

S7	S14
O(27.2%), C(25.3%), Cl(22.0%), Na (21.4%) and S (1.6%)	O(48.7%), Na(18.5%), C(12.8%), N(11.4%) And Cl(4.28%), Ca(1.1%), S(1.1%), Mg(1.0%)

Tableau 1. Composition élémentaire moyenne des échantillons S7 et S14 obtenue par TSEM-EDX.

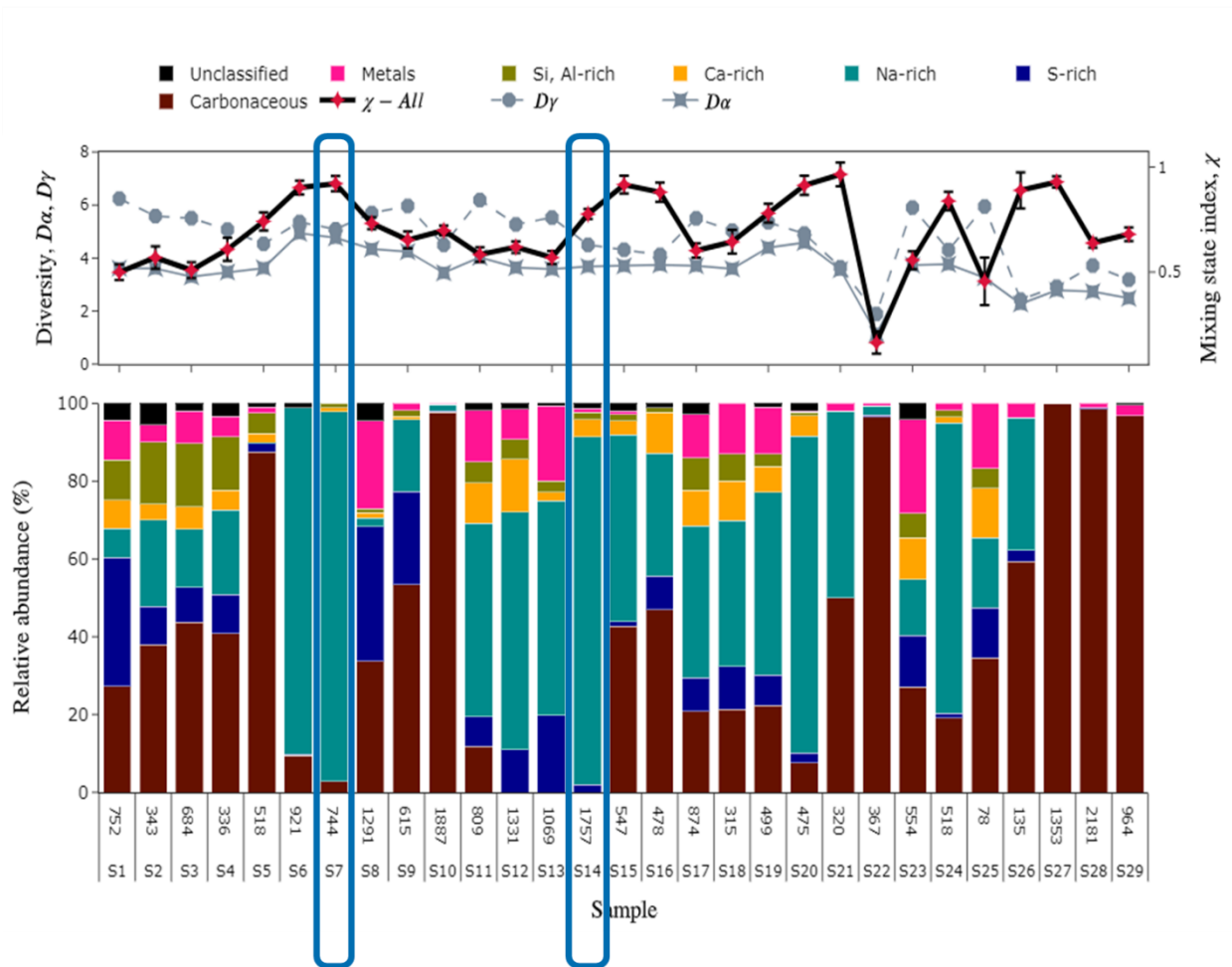


Figure 9. Evolution du $D\alpha$, $D\gamma$ et χ (en haut) et de l'abondance relative des particules individuelles (en bas) collectées sur l'étage fin ($0,1-1 \mu m$) pour tous les échantillons (S1 à S29) de la campagne MIXTAPE. Les barres

d'erreur sont estimées pour les valeurs de χ de chaque échantillon sur la base du nombre de particules analysées indiqué au-dessus du numéro de l'échantillon (S_x).

L'indice d'état de mélange chimique pour l'ensemble de la campagne MIXTAPE est proche de 0,30 soit une population de particules individuelles plus proche d'un mélange externe qu'interne. Mais cette valeur cache des disparités importantes selon les échantillons (Fig. 9) ce qui signifie que l'exploitation environnementale de l'indice de l'état de mélange chimique n'est possible qu'en considérant les conditions atmosphériques propres à chaque échantillon. La deuxième partie de ce chapitre s'est donc intéressée aux facteurs environnementaux pouvant expliquer les évolutions observées sur la composition élémentaire et l'indice d'état de mélange. Pour cela 3 paramètres sont examinés :

- 1) Le niveau de pollution lors de l'échantillonnage en comparant les échantillons collectés lorsque les concentrations des PM_{10} sont en-dessous (CD : *Clean Samples*) et au-dessus (PS : *Polluted Samples*) des seuils de l'OMS
- 2) L'origine des vents locaux (vents provenant du secteur industriel, marin ou urbain) et
- 3) L'étendue des panaches de pollution au moment de l'échantillonnage (local vs. régional, c'est à dire en conditions atmosphériques stagnantes ou de dispersion).

Les résultats obtenus nous ont permis de mettre en évidence que les variations de la composition chimique élémentaire des particules et notamment la distribution des éléments au sein de celles-ci ne dépend pas de ces trois paramètres examinés.

Afin d'identifier les paramètres clés pouvant expliquer les différences d'état de mélange observées, l'évolution horaire de la composition élémentaire et de l'indice d'état de mélange des particules lors d'un évènement de pollution (PE) a été examinée dans des conditions atmosphériques marquées par un changement rapide des caractéristiques des masses d'air échantillonnées. L'évènement en question a été enregistré entre le 31 mars et le 01^{er} avril 2021 (**Figure 10 haut**). Sur la base de la classification établie au Chapitre 4, le jour de pollution (PD) du 31/03/2021 a été classé comme « Local » (dépassements des seuils de PM_{10} uniquement enregistrés sur les stations locales : U, I et S), contrairement au 01/04/2021 pour lequel le dépassement du seuil, en plus des stations locales, est enregistré à la station « R » (= Remote), éloignée de toute source locale de PM et permettant de classer cet évènement comme d'amplitude régionale. La cohérence de cette classification est perceptible sur la

carte des moyennes journalière observées des PM₁₀ allant du 30/03 au 01/04/2021 présentée sur la **Figure 10 bas**.

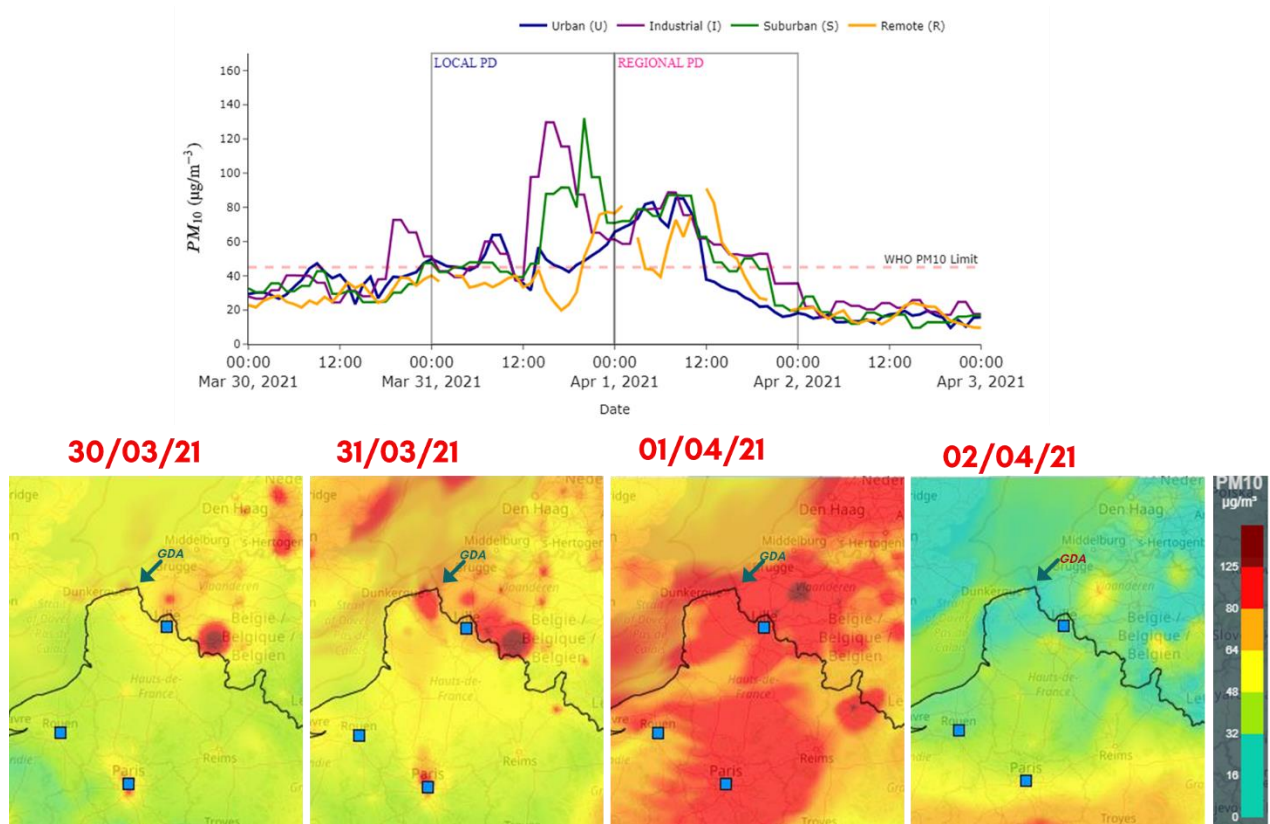


Figure 10. Evolution de la concentration en PM₁₀ sur les Stations U, I, S et R (haut) et carte des concentrations moyennes journalière des PM₁₀ observées (<http://www2.prevoir.org/>) entre le 30 mars et le 02 avril 2021. On ne constate pas d'épisode de pollution le 30 mars et le 02 avril pendant que l'épisode a une étendue spatiale locale le 31 mars et régionale le 01^{er} avril.

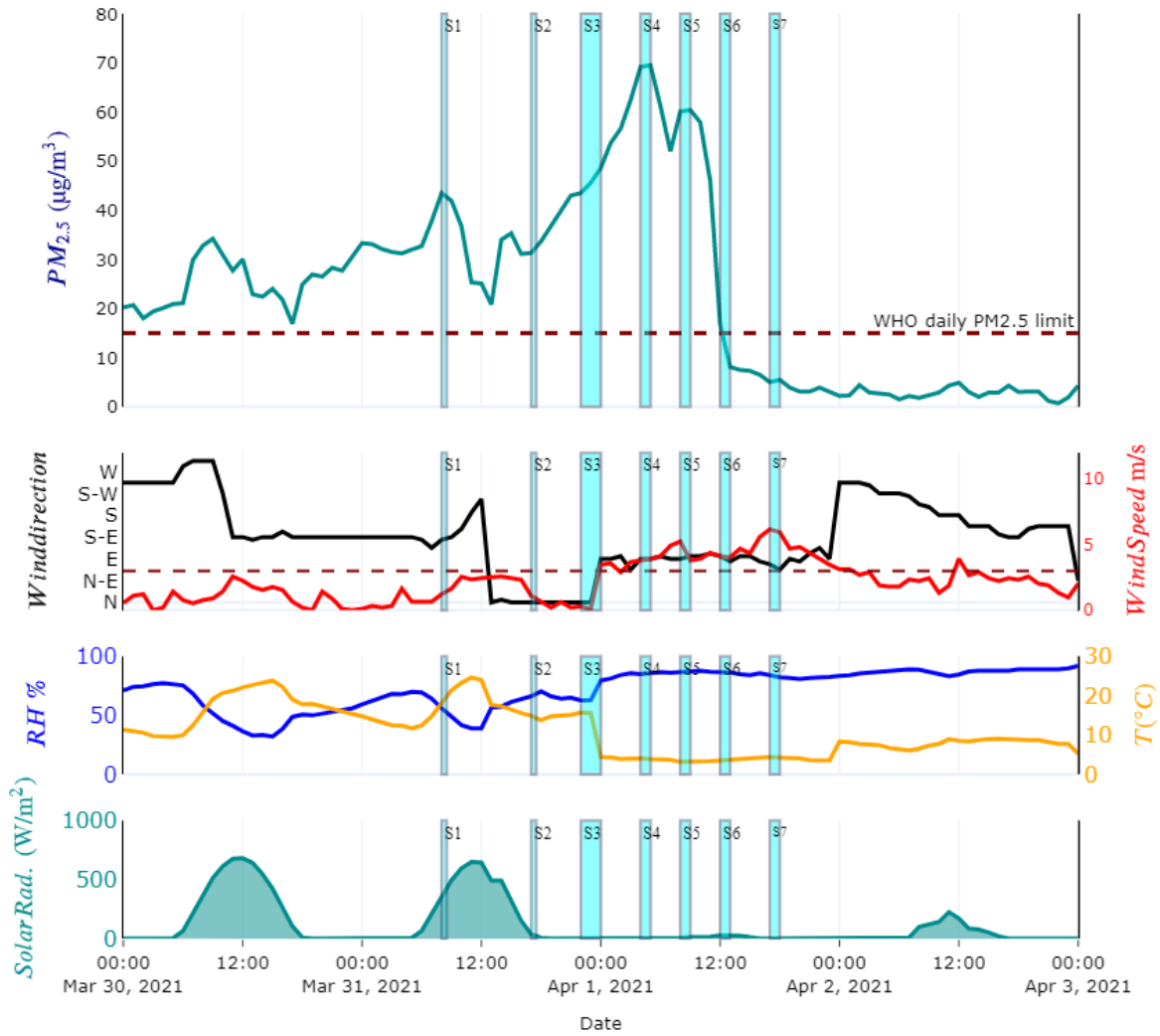


Figure 11. Evolution de la série temporelle des $PM_{2.5}$ à la station U (cyan foncé) et des paramètres météorologiques : Vitesse du vent (rouge) et Direction du vent (noir), Température (orange), humidité relative (bleu), Radiation solaire (cyan foncé rempli). Les rectangles colorés en cyan représentent les périodes d'échantillonnage TRAPS.

Durant ces deux jours, 7 échantillons (S1 à S7) ont été prélevés (**Figure 11**). Les échantillons S1, S2 et S3 ont été prélevés le 31/03/2021, pendant que S4, S5, S6 et S7 ont été prélevés le deuxième jour (1^{er} avril 2021).

Pour les échantillons du 31/03/2021 (S1, S2, S3) dits « locaux », différents types de particules ont été observés (**Figure 12**), à la fois pour la fraction grossière (1-10 μm) et la fraction fine (0.1-1 μm). Pour les échantillons dits « de couverture régionale » (S4, S5, S6, S7) (**Figure 12**), une fraction très élevée de particules carbonées et riches en Na est observée principalement entre S5 et S7 pour les 2 classes de taille. L'échantillon S4 présente quant à lui une composition élémentaire diverse dans la fraction fine et dominée par les particules carbonées dans la fraction grossière. Cette évolution temporelle des caractéristiques des particules peut s'expliquer par une évolution des conditions de dynamique atmosphérique à partir de l'échantillonnage de S4 (augmentation de la turbulence verticale favorisant le mélange des polluants ; observations réalisées à l'aide d'un Lidar, non présentées ici).

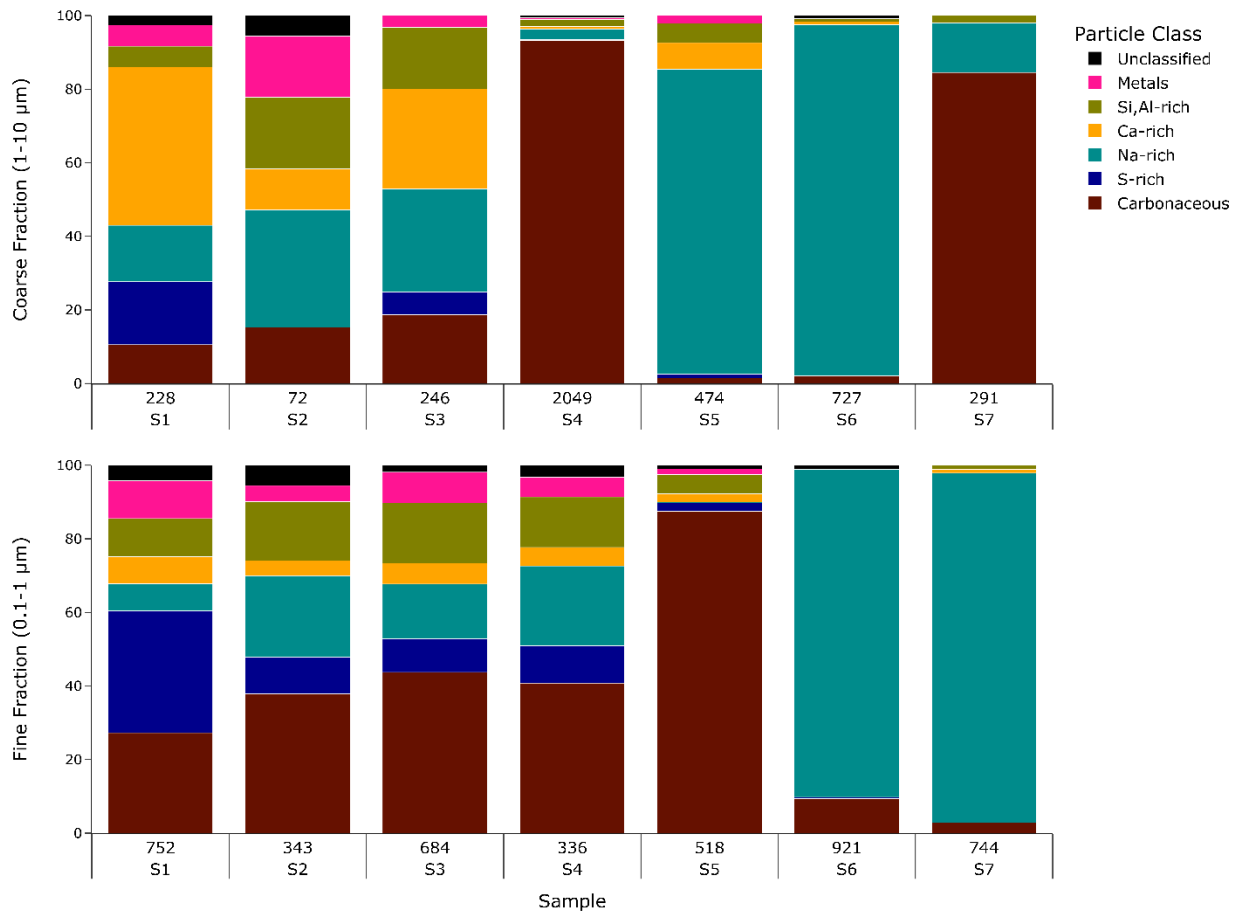


Figure 12. Evolution de l'abondance relative des particules individuelles pour les échantillons (S1 à S7) des fractions grossière (1-10 μm en haut) et fine (0.1-1 μm en bas) du TRAPS collectées lors de l'évènement de pollution allant du 31 mars au 01^{er} avril 2021.

Concernant l'évolution des diversités et de l'indice de l'état de mélange, d'une manière générale, on observe que la diversité chimique élémentaire des particules individuelles est plus importante lors que l'évènement a une couverture locale contrairement aux populations homogènes qui sont obtenus lorsque l'épisode a une couverture régionale.

Le 31/03/2021, le panache de pollution a une couverture locale. Cela signifie que les masses d'air stagnent ce jour-là et qu'il y a une accumulation des polluants locaux, provenant de sources variées, ce qui favorise l'introduction continue de nouvelles particules le temps que dure cet épisode. Ceci entraîne une augmentation de la diversité globale (D_γ : en moyenne 5 éléments sont présents dans l'ensemble des particules) pendant que la diversité à l'échelle de la particule individuelle (D_α) reste basse (3 éléments présents, en moyenne). Ceci s'explique par le fait que les particules, émises localement, n'ont pas eu le temps d'évoluer, mais la diversité des sources présentes à Dunkerque se traduit par une population globalement hétérogène, ce dont rend compte l'indice d'état de mélange chimique χ , proche de 0,50. **(Figure 13).**

Le 01/04/2021, le panache a une couverture régionale, comme on peut le constater sur la Figure 10. La proportion de particules transportées étant supérieure à celle localement émises, on obtient des populations de particules plus homogènes, ayant eu le temps d'évoluer au sein du compartiment troposphérique. Elles sont ici principalement composées de particules carbonées et d'origine marine (riches en Na). Les diversités globale (D_γ) et individuelle (D_α) en rendent compte, avec, dans les deux cas, un nombre effectif d'éléments chimiques présents compris entre 4.5 et 5.0. Cela conduit naturellement à des indices d'état de mélange élevés ($\chi > 0.8$) traduisant une population globalement en mélange interne **(Figure 13).**

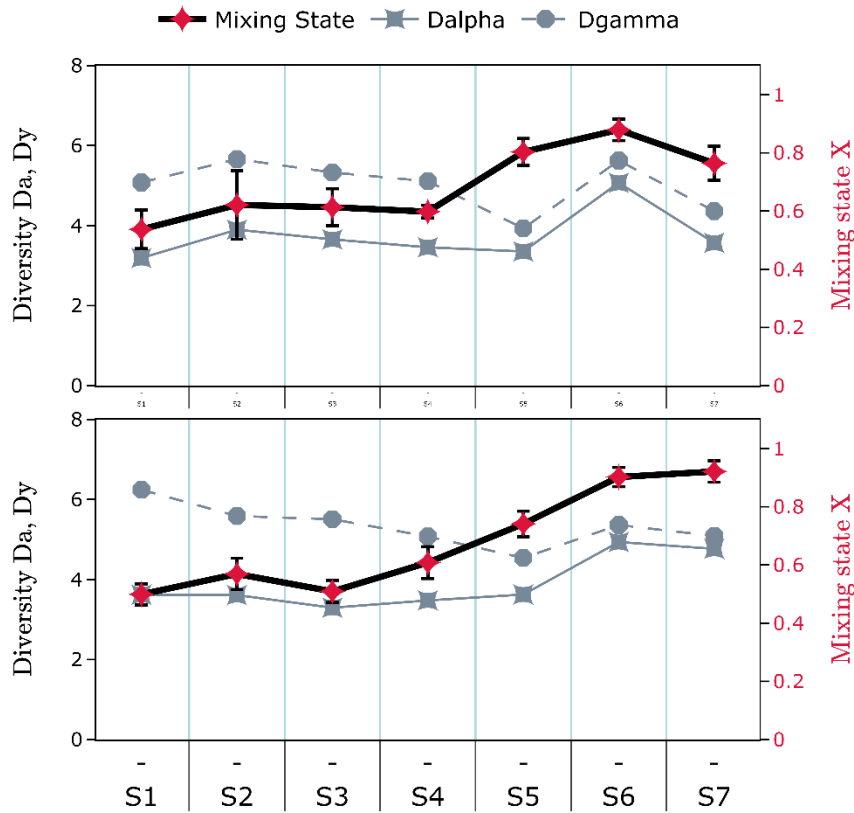


Figure 13. Evolution du D_a , D_y et χ des échantillons des particules individuelles (S1 à S7) de la fraction grossière (1-10 μm en haut) et fine (0.1-1 μm en bas) du TRAPS collectés lors de l'évènement de pollution allant du 31 mars au 01^{er} avril 2021.

On peut donc conclure que la couverture, locale ou régionale, des panaches de pollution influence significativement la composition chimique élémentaire et l'indice d'état de mélange des particules lors de ces évènements. Cela se traduit notamment par une augmentation de l'indice d'état de mélange avec l'augmentation du temps de résidence des particules dans l'atmosphère.

En résumé, lors de ce travail de thèse de Doctorat, un impacteur en cascade séquentiel, capable de fournir des échantillons de particules atmosphériques grossières (1-10 μm) et fines (0.1-1 μm) à haute résolution temporelle (TRAPS) a été développé et caractérisé en laboratoire et sur le terrain. Son

effectivité et opérationnalité dans la fourniture d'échantillons analysables par des techniques diverses de microscopie électronique a été démontré. Le TRAPS a été déployé lors de la campagne MIXTAPE dont le but était d'étudier la composition individuelle et l'état de mélange des particules atmosphériques lors d'évènements de pollution sur la zone du Grand Dunkerque. Une analyse statistique des jours de dépassement survenus entre 2018 et 2020 a permis de mieux classer ceux-ci en différents types et de constater qu'ils étaient plus nombreux en hiver et au printemps. Ils sont essentiellement liés aux émissions industrielles et sont en majorité d'une durée moyenne de 2 jours, ce qui correspond à notre définition de « l'évènement de pollution ». Les résultats d'analyse des particules échantillonnées lors de ces évènements ont permis de mettre notamment en évidence l'absence de lien direct entre l'hétérogénéité chimique des particules d'aérosol de pollution et l'origine des vents locaux. En s'intéressant aux facteurs qui pourraient influencer la composition chimique de ces particules et l'indice d'état de mélange qui en découle, il a été nécessaire de s'arrêter à une description horaire de l'évolution dans le temps d'un évènement de pollution. On a alors pu constater pour l'évènement de pollution étudié que c'est l'étendue, locale ou régionale, du panache de pollution qui explique principalement l'évolution de l'état de mélange chimique des particules. Les résultats de cette thèse pourraient être exploitables dans le cadre d'une amélioration des stratégies d'atténuation des effets de la pollution, notamment en matière de santé humaine.

Introduction

Aerosols are ubiquitous in the atmosphere and encompass groups of airborne solid or liquid particles of a small enough size to remain suspended during a time period from few minutes to tens of hours (Raes et al., 2000). They can be emitted directly from natural sources such as desert dust, volcanic ashes and sea salts or emitted from anthropogenic activities (road traffic, industries, domestic heating, etc.), for example very tiny soot or metal-bearing particles (Boucher, 2015). They can also result from transformations and reactions of gaseous pollutants in the atmosphere (VOC, sulphur- and nitrogen-compounds, ozone, hydroxyl radicals, etc.). Aerosols produced in this way are called secondary aerosols. They can be removed from the atmosphere, either through chemical processing, dry deposition or wet deposition in the form of rain (Raes et al., 2000).

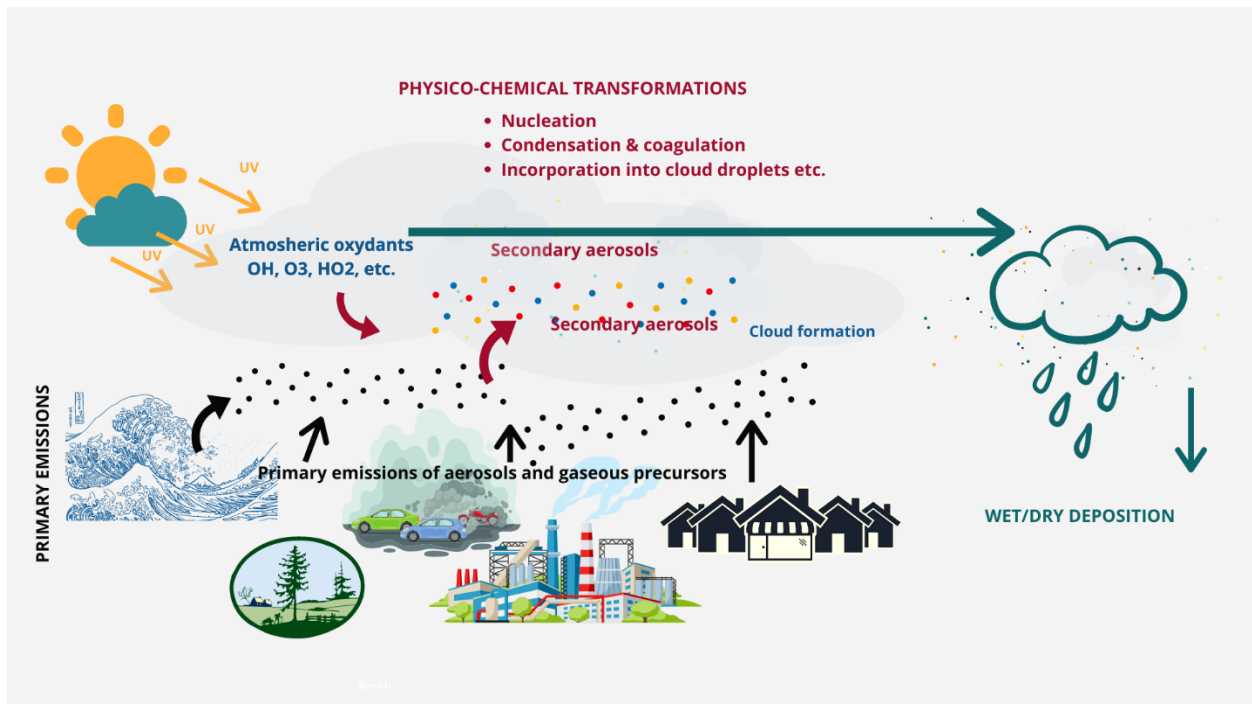


Figure 0-1. Basic scheme of the life cycle of aerosols, including emissions from their natural and anthropogenic sources, their transformations and their removal in the atmosphere

During the transport of a plume across an urban site (Figure 0-1 and 0-2), particle populations can undergo complex evolutions, including local emissions from the different sources, gas to particle formation, coagulation, and condensation, that can influence their composition, therefore, resulting in the formation of complex mixtures during the aging processes (Riemer et al., 2019). This can lead

Introduction

to various physicochemical and morphological changes at the particle level, resulting in considerable implications for health and climate (Ching et al., 2017; Ching and Kajino, 2018). The concept of the mixing state of aerosols was first introduced by Winkler (1973) as a way to account for differences in chemical composition across an aerosol. This definition was upgraded to characterize the distribution of chemical elements across individual particles within the particle populations of an aerosol (Riemer and West, 2013).

In Figure 0-2 the evolution of the mixing state from an internal mixing where all particles have the same composition as in the population, to an external mixing where each particle is unique is presented. We can see that with increasing residence time in the atmosphere, particles tend to become more internally mixed as generally low-volatility compounds, such as sulfates, nitrates and organic matter, can condense onto them, and as the particle coagulate with each other (Via et al., 2021). This has significant implications for health as well as for climate (Ching et al., 2019).

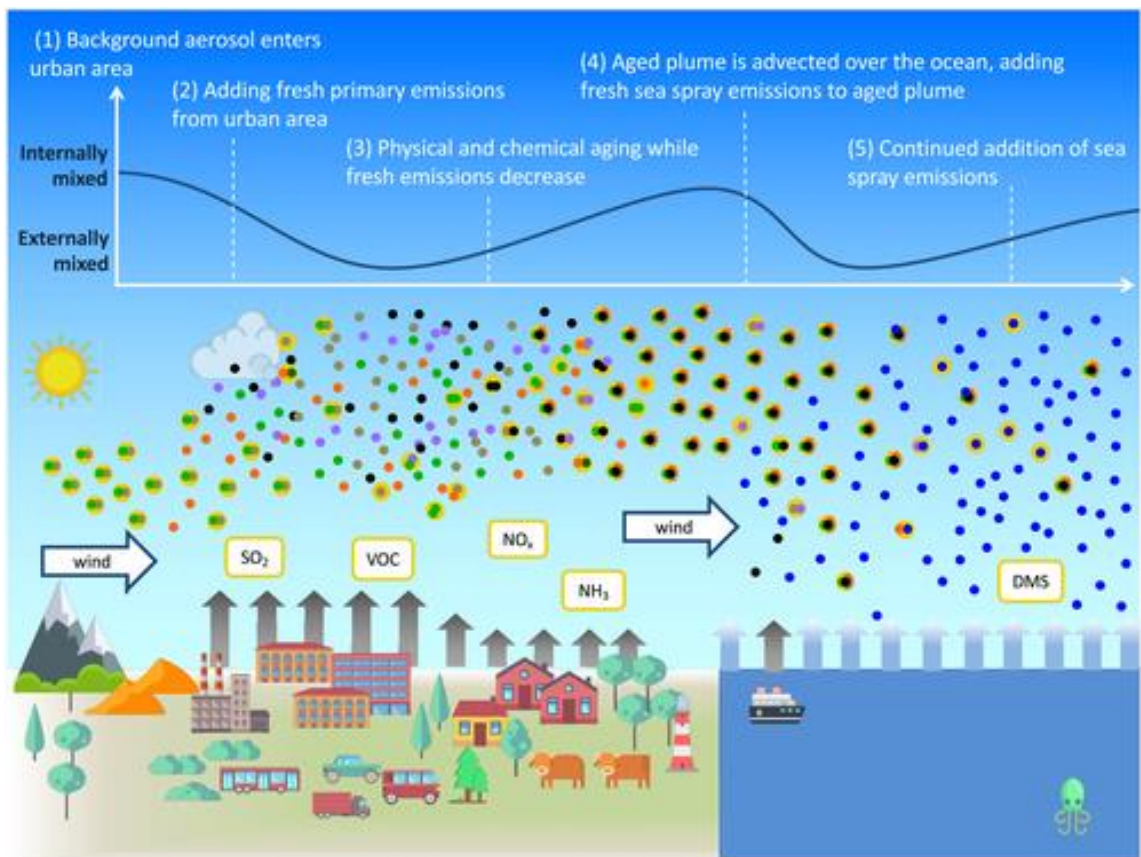


Figure 0-2. Evolution of aerosol mixing state of an aerosol that is transported in the atmosphere. The line graph (top) illustrates how aerosol mixing state changes qualitatively between a more or less internally mixed state and how

Introduction

different aerosol processes contribute to that change. Adding new types of aerosol particles makes the population more externally mixed (steps 2 and 4), while aerosol aging processes (step 3) or the addition of one dominate particle type (step 5) moves the population toward a more internally mixed state. DMS = dimethyl sulfide (Riemer et al., 2019).

For example, modifications of the hygroscopic properties of newly emitted soot particles, induced by the changes in their mixing state have been evidenced to influence the deposition of these particles in the respiratory tract (Ching and Kajino, 2018). From the climatic perspective, aging of soot particles results in the alteration of their radiative properties and in their ability to activate to form clouds by acquiring coating (Ching et al., 2017; Wang et al., 2010). The main implication is the difficulty to quantify the impact of these particles on climate as most models assume an internal mixing state for all particles (Bondy et al., 2018; Stevens and Dastoor, 2019).

A significant fraction of European citizens (77% in 2017), living nearby industrial and urban areas, are frequently exposed to high levels of Particulate Matter above the threshold of $45 \mu\text{g}\cdot\text{m}^{-3}$, as recommended by WHO for PM_{10} , i.e. particles with an aerodynamic diameter below $10 \mu\text{m}$ (WHO, 2021). It is also the case for the Great Dunkirk Area (GDA), a highly industrialized site located on the seacoast of Northern France, where the number of daily PM_{10} exceedances is still important over the years (ATMO HdF, 2020). As many industrial areas in the world, the GDA is influenced by pollutants originating from different local sources, including industrial, traffic, urban residential, agricultural and marine, as well as from regional or long-range transport (LRT) (Favez et al., 2021; Zhang et al., 2021). In this context, the main objective of this thesis is to study the evolution of individual particle composition and mixing state during pollution events in a multi-influenced atmospheric environment, such as the GDA.

The GDA has been widely studied in term of PM concentrations, chemical composition and sources using both continuous monitoring through online techniques or through offline methods that require sampling and further laboratory characterization of the pollutants (Arndt et al., 2021; Crenn et al., 2017; Ledoux et al., 2017; Mbengue et al., 2017; Setyan et al., 2019). Crenn et al. showed that combining both online and offline methods to provide chemical composition of aerosols at high temporal resolution could help to identify the sources and improve the understanding of air pollution events, especially in sites influenced by various anthropogenic emissions.

Introduction

Highly time-resolved chemical speciation of particulate matter using online techniques is already available and widely used in northern France (Crenn et al., 2017; Roig Rodelas et al., 2019; Zhang et al., 2021).

Using the Monitor for AeRosols and Gases in ambient Air (MARGA) during a 1-year campaign of hourly observations of PM_{2.5} at the suburban site of Douai (DO), it was possible to identify their sources and composition (Roig Rodelas, 2018). The results of this study showed that secondary inorganic aerosols, mainly nitrates (28%), sulfates (13%) and ammonium (10%) accounted for nearly half the mass of PM_{2.5} (Roig Rodelas, 2018). Along the same lines, by conducting a short campaign of one month at both the Douai suburban site and a second site (Grand Synthe, GS) located in the industrialized city of Dunkirk, (Crenn et al., 2017) reported a variation between 20.5 µg/m⁻³ and 32.6 µg/m⁻³ in DO and between 10.6 µg/m⁻³ and 29.9 µg/m⁻³ in GS during summer and winter, respectively, showing the seasonal variability to be mainly attributed to increased biomass burning emissions associated with residential heating in winter.

Using a High Resolution Time-of-Flight Aerosol Mass Spectrometer, non-refractory submicron aerosols (NR-PM₁) were characterized both at the same suburban site of Douai, but also at the industrial sites of Grande Synthe and nearby industrial installations in the eastern part of the Dunkirk Harbor (Crenn et al., 2017; Zhang et al., 2021). It was shown that total NR-PM₁ concentrations were lower by a factor of 4 (for DO) and 10 (for GS) in summer than those observed in winter. Organics and nitrates dominated the NR-PM₁ in DO for both seasons and during winter in GS, while sulfates and nitrates were the most dominant species in summer in GS. Due to the proximity of industrial installations, the amount of freshly emitted aerosols was more important in GS than in DO in winter (Crenn et al., 2017).

In the GDA, the chemical speciation of NR-PM₁ was studied during a campaign that lasted more than one-year (Zhang et al., 2021). Results showed a variation of the chemical composition according to the local aerosol emission sectors. In addition, one of the main findings of this work resides in that it allows associating a Positive Matrix Factorization (PMF) factor with ship emissions, revealing that ships are responsible for more than 50% of the OA emissions during short periods of time at the Dunkirk harbor. More specifically, the conversion of gaseous sulfur dioxide (SO₂) to particulate sulfates (-SO₄) is favored in the presence of high relative humidity (>70%), associated with low vertical

Introduction

turbulence, typically a vertical wind speed fluctuation of less than 0.5 m s^{-1} , and a wind speed not exceeding 2 m s^{-1} (Zhang et al., 2021).

Beside online methods, the use of electron microscopy together with energy dispersive spectrometry has been shown to be a technique of choice for the characterization of airborne particles. By providing direct information on the physical and chemical characteristics of individual particles collected at different altitudes using Transmission Electron Microscopy (TEM), (W. Wang et al., 2021) were able to perform vertical comparisons of morphologies and mixing state of particles collected in winter in Beijing and their results indicate that coal combustion activities significantly contributed to the large fractions of airborne particles above the boundary layer and in surface when mixing of polluted air occurred. SEM-EDX has been used in the GDA and allowed, for example, to identify specific particle types associated with different emissions sources from an iron-manganese alloy plant. The identified particles could thus serve as tracers of industrial activities in source apportionment studies (Arndt et al., 2016).

However, the current available offline techniques, such as cascade impaction, although they are less expensive and can easily cover large study areas, are limited in term of providing highly time resolved samples. This is due to the time required to change the aerosol collection substrate between two samplings and before laboratory analysis. Consequently, this limits their ability to investigate rapid changes in particle composition and mixing state, especially in the vicinity of industrial areas, where the repeated passage of emission plumes can lead to rapid changes in air quality in nearby urban areas is limited (Guilbaud, 2018; Marris et al., 2012a; Riffault et al., 2015; Setyan et al., 2019; Zhang et al., 2021).

In order to overcome these challenges, the first part of this thesis consisted in developing and characterizing a homemade Time-Resolved Atmospheric Particle Sampler (TRAPS), used to provide individual particle samples suitable for a wide range of single particle analysis techniques such as SEM, TEM and Raman at high time resolution.

The TRAPS was developed and deployed in the second part of this thesis, to study the **MIXing sTate of Atmospheric Particles during pollutions Events**, during the **MIXTAPE** campaign that lasted nine months. The sampling site was located in an urban area nearby the Dunkirk harbor, and time-resolved particle sampling was followed by individual particle analysis using TSEM-EDX.

Introduction

This manuscript is divided into 5 main chapters. The first chapter presents an overview on the current knowledge about tropospheric aerosols, including their composition, sources and effects, with a specific focus on aerosol mixing state (including the calculation of the mixing state index). In the second chapter (Materials and Methods), the MIXTAPE campaign, the GDA and the analytical- and sampling methodology are presented. In the third chapter, the development of TRAPS, the determination of its size segregation characteristics and particle deposition pattern through laboratory and field experiments are described. A classification of PM₁₀ pollution days that occurred from 2018 to 2020 in the GDA, as well as a presentation of typical PM₁₀ pollution events are presented in Chapter 4. The fifth and last chapter is dedicated to the presentation of the evolution of individual particle compositions, chemical diversity and mixing state during the five pollution events investigated during the MIXTAPE campaign, before a general conclusion on this work is provided.

CHAPTER 1.
ATMOSPHERIC AEROSOLS

1. Atmospheric Aerosols

In this first chapter, a state of the art of the knowledge of the physico-chemistry of atmospheric aerosols, their climatic, environmental and sanitary impacts as well as the study of the mixing state is presented.

1.1. Physical characteristics of atmospheric aerosols

In atmospheric sciences, aerosols or particulate matter (PM) are defined as a suspension of airborne solid or liquid particles residing in the atmosphere for at least several hours, excluding hydrometeors such as cloud and rain droplets or ice crystals (Mészáros, 1999). The size of PM ranges from a few nanometres up to several micrometres (Figure 1-1) and can influence their behaviour into the atmosphere.

1.1.1. Size of aerosols

In order to determine their size, the shape of particles is generally assumed to be spherical. The equivalent aerodynamic diameter is the diameter of a sphere of density 1 g.cm^{-3} with the same settling velocity as the particle of interest (Renoux and Boulaud, 1998). Particles can be classified according to their aerodynamic diameter (d_a). The terms PM_{10} , $\text{PM}_{2.5}$ and PM_1 (PM for “Particulate Matter”) are commonly used and respectively stand for particles having an aerodynamic diameter of less than or equal to $10 \text{ }\mu\text{m}$, $2.5 \text{ }\mu\text{m}$ and $1 \text{ }\mu\text{m}$. Among these particulate mass fractions, those with smaller aerodynamic diameters have a high probability of reaching deeper regions of our respiratory track (Adamson et al., 1999)

Another classification also distinguishes between coarse, fine and ultrafine aerosols, for which the size ranges are greater than $1 \text{ }\mu\text{m}$, between $1 \text{ }\mu\text{m}$ and $0.1 \text{ }\mu\text{m}$, and smaller than $0.1 \text{ }\mu\text{m}$, respectively. The distinction between coarse and fine aerosols is fundamental in aerosol studies. As they origin from different sources (see section 1.2.), their formation, transformation and removal processes are also different. Differences in their chemical composition as well as their health effects are also observed (section 1.3.) (Baldauf et al., 2001).

Chapter 1. Atmospheric Aerosols

1.1.2. Aerosols life cycle

Throughout their life cycle, particles encounter different phenomena that influence their size, their shape, their composition and physical and optical properties. The differentiation of particles in modes, i.e. different size ranges, often helps having a clear apprehension on these phenomena. Ultrafine and fine particles are generally formed due to condensation of gases and coagulation of smaller particles, although they can also be emitted directly by natural and anthropogenic sources. A more detailed classification into three to four size modes (Figure 1-1) is usually made in order to study different processes and properties that do not affect all fine particles in the same manner (Raes et al., 2000 ; Adachi and Buseck, 2008).

The nucleation or nuclei mode, formed by **gas-to-particle** conversion or nucleation, is stated as the production and growth of particles in the presence of condensable vapours (Hidy, 1984). They are mostly formed via chemical or photochemical reactions from gaseous compounds such as SO₂, NO_x (NO₂ + NO), NH₃ and VOC. The particle diameters range up to 10 nm with the lower limit not strictly defined. Their loss is induced by coagulation with bigger particles or condensational growth to give place to particles of **the Aitken mode**, which gathers particles with sizes comprised between 10 nm and 100 nm (0.1 µm) in diameter. Those are coming from the "condensation nuclei" of inorganic or organic compounds, whose "clusters" have grown as indicated just before, either by condensation of additional molecules or by coagulation with other clusters. The nucleation and Aitken modes account for the majority of particles by number, due to their small size however, are hardly representative of the total particle mass.

The accumulation mode refers to particle with size ranges from 0.1 to 1.0 µm. Particles in this mode are primary particles (directly emitted in the atmosphere) or they originate from the coagulation of particles from the nuclei and Aitken modes and from condensation of hot vapors onto pre-existing particles, making them grow into this size range. The accumulation of particles here is also favoured by the reduced efficiency of particle removal mechanisms (dry and wet deposition) in this regime (Figure 1-1).

The coarse mode comprises particles with diameter greater than 1-2 µm, mainly formed by mechanical processes and having various sources which can be human-made or natural. They are characterized by their large settling velocities, making their residence time in the atmosphere relatively short. The natural sources of coarse particles include sea spray, soil and rock debris, biomass burning,

Chapter 1. Atmospheric Aerosols

volcanic ashes and terrestrial biological organic particles. In the other hand, anthropogenic coarse particles can originate from different sources grouped as: Industrial processes, fuel combustion, non-industrial fugitive source (roadway dust, construction, etc.) and emissions from transport.

A synthesized and combined microphysical and dynamical picture of the global evolution of tropospheric aerosols is presented in Figure 1-1. This figure sums up the production and the removal processes that lead to changes in airborne aerosol concentrations.

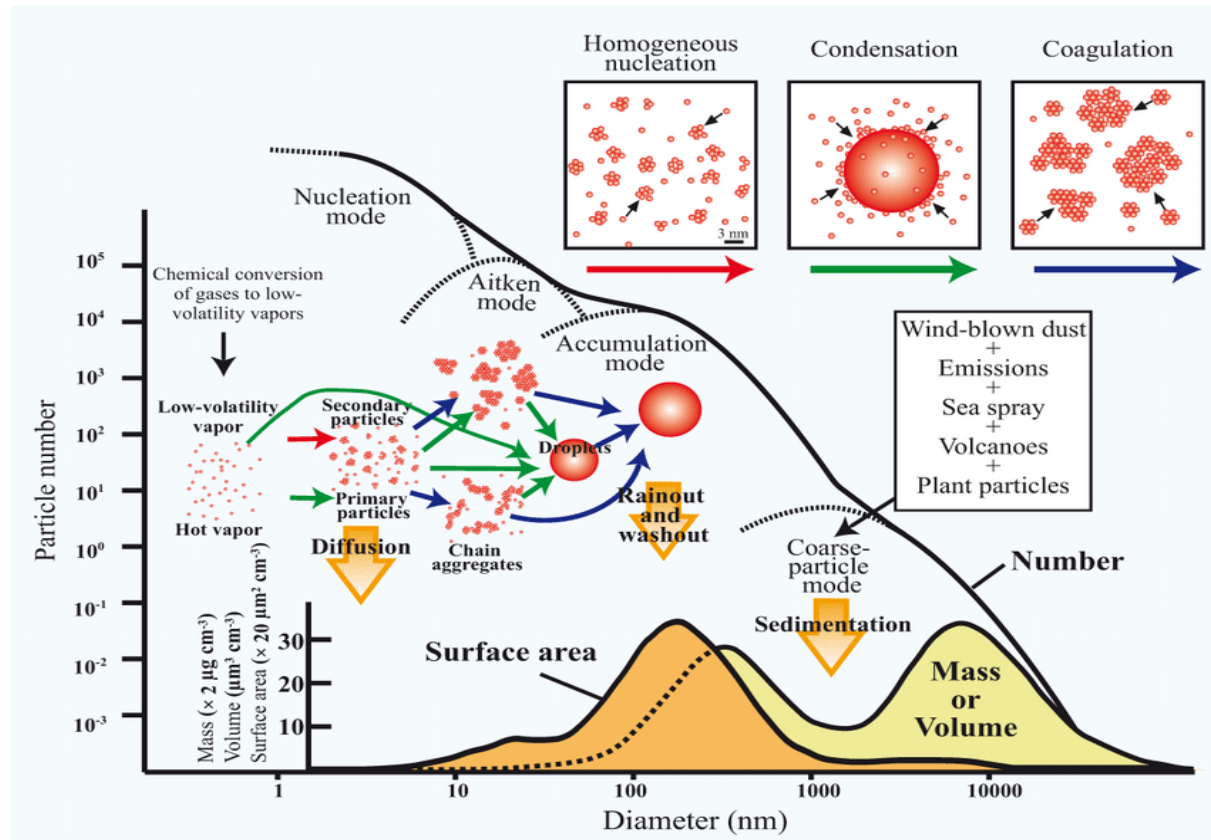


Figure 1-1. Representation of aerosol size distribution and the main formation and removal processes that influence aerosols composition and concentration in the atmosphere (Adachi and Buseck, 2008).

The residence time of aerosols in the troposphere is essentially limited by two processes: dry and wet deposition. Wet deposition is a removal process of particles occurring during precipitation by incorporation of aerosols with right hygroscopic properties inside a cloud droplet in formation and by washing of the air column during rainfalls. Dry deposition or sedimentation is a removal process by the diffusion of small particles to the Earth's surface and gravitational settling of larger particles.

Chapter 1. Atmospheric Aerosols

1.2. Sources of atmospheric aerosols

Particles can be directly released into the atmosphere as primary particles from natural sources (sea spray, volcanic eruptions, forest fires, wind-blown dust etc.) or anthropogenic sources (traffic and industrial emissions, fuel combustion including coal and oil, biomass burning, etc.). They can also be formed in the atmosphere (secondary particles), by gas to particle conversion, condensation growth (acquisition of coating) or In-cloud processing (Calvo et al., 2013; Kulmala and Kerminen, 2008; Pöschl, 2005). The followings, in Table 1-1, are the average aerosol emissions from major sources.

A-Natural Sources	Estimated rate (Tg yr ⁻¹)
<i>Primary</i>	
Mineral dust	1000 – 4000
Sea salt	1400 - 6800
Volcanic dust	Variable ~ 30
Biological particles	50 - 1000
<i>Secondary</i>	
Sulfates from DMS	12.4
Sulfates from volcanic SO ₂	20
Organic aerosol from BVOC	11.2

B- Anthropogenic emissions (Tg.yr⁻¹)	PM₁₀	PM_{2.5}	PM₁	BC	OC+OM
Agriculture	6.6	3.8	2.9	0.3	3.7
Residential combustion	23.1	21.9	20.7	4.2	24.2
Industry + Waste	26.8	16.6	9.2	0.9	3.8
Transports	4.2	3.7	3.3	1.7	3.1
Shipping and Aviation	1.9	1.8	1.6	0.1	0.9
Global anthropogenic	62.5	47.8	37.8	7.3	35.7

Table 1-1. Global emission estimates for major aerosol classes (Fan et al., 2022; IPCC, 2013; Klimont et al., 2017; Seinfeld and Pandis, 2006)

Chapter 1. Atmospheric Aerosols

1.2.1. Anthropogenic sources

1.2.1.1. Traffic

Traffic emissions and particularly road traffic constitute the main source of primary and secondary anthropogenic aerosols in urban areas; that is why their characterisation have been a major area of concern in the scientific community for many years. Traffic emissions can be divided into traffic exhaust emissions and non-exhaust emissions. Depending on the mechanisms involved in their formation, their size and chemical composition vary a lot. The proportion of particulate emissions from non-exhaust sources has increased rapidly in recent years due to the application of more and more severe regulations on exhaust emissions. While traffic exhaust emissions are released from the pipes of vehicles, the main sources of non-exhaust emissions are shown in (Table 1-2) mostly come from brake wear, road surface abrasion, tyre wear and the ejection of particles by resuspension processes (Grigoratos and Martini, 2015).

In addition to elements presented in Table 1-2, non-exhaust emissions also release particles ($PM_{10, 2.5}$, i) containing trace elements such as strontium, copper, molybdenum, barium, cadmium, chromium, manganese and iron together with various organic and inorganic constituents coming from the tyres and rubber debris (Calvo et al., 2013; Charron et al., 2019). Reducing these emissions could help decreasing public health related effects across Europe (Daellenbach et al., 2020).

Chapter 1. Atmospheric Aerosols

			Composition	Emissions
Direct wear emissions	Brake wear	Particles abraded from brake pads and discs that are directly airborne. About half of total brake wear particles are not airborne	Mainly Fe, Cu, Ba et Sb, with Fe sometimes accounting for around 60% varying with the type of plates used	0.01 - 0.5 g.veh ⁻¹ .km ⁻¹
	Tyre wear	The particles eroded from tyres that are directly airborne.	Mainly fine particles (60-80%) of irregular or spherical shapes, principal elements found are C, O, Si, et S (Kwak et al., 2014)	(Amato et al., 2014)
	Road wear (more important in urban settlements)	Particles eroded from road surfaces that are directly airborne.		0.01 - 0.14 g.veh ⁻¹ .km ⁻¹ (Amato et al., 2014)
Road dust suspension or resuspension (38% of road PM ₁₀) (Harrison et al., 2012)	The particles on (paved) road surfaces that are suspended in the air by vehicle traffic. Road dust can consist of brake, tyre and road wear particles that have been deposited on the road, as well as particles that have migrated to the road from other sources.		Mainly S in the fine mode due to asphalted roads and mineral (Si, Ca, K and Al) in the coarse mode (Sjödín et al., 2010)	

Table 1-2. Different types of non-exhaust traffic emissions (adapted from (OECD, 2020))

Chapter 1. Atmospheric Aerosols

On the other hand, traffic exhaust emissions comprise primary pollutants such as nitrogen oxides (main source in urban areas) and SO₂ (ship emissions), a wide range of metals in small concentrations, such as copper, zinc and cadmium, but also platinum, palladium and rhodium from the vehicle catalytic converters and other trace elements such as potassium, bromine or chlorine coming from the motor. In addition, ultrafine particle emissions from exhausts (mostly carbonaceous) are huge considering the emitted particle number, together with secondary pollutants resulting from chemical reactions of nitrogen and sulphur oxides, acting as the chemical precursors of nitrate and sulphate compounds. It is important to highlight the fact that exhaust and non-exhaust traffic-related sources are estimated to contribute roughly in the same proportion to traffic-related PM₁₀ emissions., A study reports a contribution of 50-85% varying according to the season and the location (Ketzal et al., 2007). , with brake wear identified as one of the most important non-exhaust traffic-related source (Charron et al., 2019). This contribution is even more important in Northern European countries due to the use of winter tires and the use of sand and salts on road as antiskid treatment. These emissions are frequently associated with spring dust pollution episodes (Amato et al., 2014; Kukkonen et al., 2005).

1.2.1.2. Industrial activities

There is a wide range of industrial activities that release a huge amount of pollutants in the atmosphere including PM₁₀, PM_{2.5}, nitrogen oxides, sulphur oxides and VOCs. These pollutants are very diverse and their nature depends on the type of industrial process, the technology and the raw material used. Several activities producing ceramics, bricks and cement, foundries and steelworks facilities, mining and quarrying have been identified as the main activities on the basis of their particles emission rates (Querol et al., 2007; Riffault et al., 2015). Depending of the process stage (production, manipulation or transport of the raw material), these activities release large amounts of clusters of primary aerosols which can evolve under different atmospheric conditions, either immediately after emission or during their near-field transport to the close vicinity of industrial zones (Arndt et al., 2021; Marris et al., 2012). More details about composition and size of particles emitted from industrial activities is given in section 1.5 on the scheme of previous studies in the highly industrialized site of the Great Dunkirk Area (GDA).

1.2.1.3. Coal and biomass burning

The combustion of coal leads to the rupture of the chemical bonds resulting to CO₂ formation. Energy is released together with other products from side chemical reactions, which carry toxic airborne

Chapter 1. Atmospheric Aerosols

pollutants and heavy metals into the environment (Koppmann et al., 2005). Coal burning is therefore an important source of particulate matter and gaseous pollutants. It is mainly employed for the production of electricity and heat, even though coal might also be consumed in non-industrial sectors (e.g. residential heating). The pollutants emitted include mercury, lead, sulphur dioxide, nitrogen oxides, PAHs, BC, OC, fly ashes and various other heavy metals which can be very dangerous for human health and environment (Sanderson et al., 2016). While residential coal combustion represents a serious problem in developing countries such as China, the use of coal for energy production has substantially decreased in Europe, over the last decades, favoured by strict regulations adopted by the EU. Thus, the related SO₂ emissions have also decreased.

Biomass burning is globally defined as the burning of living and dead vegetation, including a variety of activities such as agricultural expansion, deforestation, bush control, weed and residue burning, and harvesting practices, mainly caused by humans (over 90%) (Koppmann et al., 2005). It can also occur naturally when forest fires are initiated by lightning. As a consequence, biomass burning is an important source of combustion products to the atmosphere including CO₂, CO, NO_x, CH₄ and non-methane hydrocarbons, soot and organic particulate matter (Seinfeld and Pandis, 2016). Emissions from biomass burning for some pollutants include 40 Tg.yr⁻¹ for CH₄, 700 Tg.yr⁻¹ for CO and 7.1 Tg.yr⁻¹ for NO_x mainly in the tropics where its climatic effects are also significant (Seinfeld and Pandis, 2016). Black carbon emissions are estimated to be 7.1 Tg.yr⁻¹ as shown in Table 1-1.

1.2.2. Natural sources

1.2.2.1. Mineral dust

Mineral dust aerosols refer to a suspension of soil-constituting mineral particles (Nousiainen, 2009), which may only happen if there is no vegetation cover and the soil is dry. The major sources of mineral dust are located in the arid and semi-arid regions of the world such as deserts, dry lake beds and semi-arid surfaces. Mineral dust in the atmosphere is composed essentially of clay and silt. The estimations of global dust emissions range between 1,000 and 4,000 Tg/yr⁻¹ (Seinfeld and Pandis, 2016), with a large uncertainty due to the complexity of dust formation and release into the atmosphere. The Saharan desert is considered as the largest source of dust on earth, whose particles significantly contribute to transboundary pollutant transport over the Mediterranean region for example (Yücekutlu and Yücekutlu, 2014). Indeed, although most of the mineral dust is recognised to be from

Chapter 1. Atmospheric Aerosols

natural origin, there is an increase in the amount of these emissions from anthropogenic sources, resulting from modifications of the soil surface due to land-use changes from forested to agricultural areas and changes in climate and meteorological conditions (Seinfeld and Pandis, 2006).

1.2.2.2. Sea spray

Sea spray aerosols are emitted into the atmosphere during the bubble bursting mechanism occurring at the ocean surface (Tomasi et al., 2017). Sea spray is the most important contributor to the total aerosol mass in the world. Sea spray particles may have different composition features depending on if they are newly emitted or aged. The major constituents include fresh and partly or completely reacted sea salts, resulting from the reaction of NaCl with sulphuric and nitric acid. These reactions lead to the formation of mixed Na, Mg, K, or Ca sulphates and nitrate and the loss of more or less chloride. Sea spray aerosols are very hygroscopic and cover sizes range from typically 100 nanometres (nm) to several tens of micrometres (μm), with a bimodal distribution centred at 1.5 μm and 2.5 μm for fine and coarse modes, respectively (Tomasi et al., 2017). Biological materials and impurities can also be found in sea spray aerosols, making it inappropriate to call them sea salt aerosols for some authors (Boucher, 2015). The oxidation of dimethyl sulphide (DMS) to sulphate aerosols formation is among the main source of marine secondary aerosols.

1.2.2.3. Volcanic eruptions

Volcanic eruptions are responsible for releasing molten rock, or lava, from deep within the Earth, forming new rock on the Earth's surface. But eruptions also impact the atmosphere by emitting huge amount of particle and gaseous species. Ninety-nine percent of the gas molecules emitted during a volcanic eruption are water vapor (H_2O), carbon dioxide (CO_2), and sulphur dioxide (SO_2). The remaining one percent is comprised of small amounts of hydrogen sulphide, carbon monoxide, hydrogen chloride, hydrogen fluoride, and other minor gas species. For particles, the emission rate is variable that's why there are no precise annual mean volcanic dust emissions in the literature. However, some estimations of volcanic dust emissions turn around 30 Tg. yr⁻¹ (Seinfeld and Pandis, 2016). The gases and dust particles thrown into the atmosphere during volcanic eruptions have influences on climate. The eruption of Mount Pinatubo in the Philippines in 1991 released approximately 20 million tons SO_2 up the stratosphere. The impact of these emissions lead to a drop of 0.5°C and 0.6° C respectively for global surface and tropospheric temperatures for 2 years (Parker et al., 1996) . When

Chapter 1. Atmospheric Aerosols

talking about particle emissions from volcanic eruptions, it's also worth to differentiate those directly emitted fragments from magma to the re-suspended particles within urban areas which can significantly impact local air quality (Adachi and Buseck, 2008; Trejos et al., 2021).

1.2.2.4. Biogenic aerosols

Biogenic aerosols are airborne solid or liquid particles emitted from plants, microorganisms and animals and can originate from primary or secondary sources. They are the third most important contributors to natural PM after sea spray and mineral dust. Primary biogenic aerosols consist of pollens, plant debris, microbial particles, insects, humic matters as well as marine colloids and pieces of animal skins. They exhibit different shapes and sizes, resulting from the large variability, typology and diversity of sources from which they are emitted. Biogenic volatile organic compounds emitted by plants act as precursors of SOA into the atmosphere. However, their emission fluxes are highly variable according to the season, location and altitude (Tomasi et al., 2017).

1.3. Impacts of aerosols on climate and human health

1.3.1. Aerosols and climate

Aerosol emissions have changed significantly overtime. Because of the diversity of sources and their increasing ambient amounts, as in the case for increased emissions of greenhouse gases, anthropogenic atmospheric aerosols affect considerably the climate of the Earth (Haywood, 2016). These impacts can be by exerting a significant radiative forcing of climate either via aerosol-radiation (direct effects) or via aerosol-cloud interactions (indirect effects).

The “direct effect” is described as the scattering and absorbing properties of aerosols on Earth’s radiation field (call as “extinction”). Aerosols scatter or absorb sunlight to varying degrees, depending on their physical properties and their composition and since ambient aerosol populations comprise such a broad collection of particles with different properties, the overall effect is anything but simple.

Pure sulphates and nitrates reflect nearly all radiation they encounter, cooling the atmosphere for most of the negative forcing. Black carbon, in contrast, absorbs radiation readily, warming the atmosphere but also darkening the surface (e.g., Bond et al., 2013), giving place to a positive forcing. The impacts

Chapter 1. Atmospheric Aerosols

of mineral dust on radiation depend on the composition of the minerals that comprise the dust grains, and whether they are coated, with black or brown carbon, i.e. soot or organic matter or inorganic salts. The extent to which these aerosols warm or cool down an atmospheric column, through aerosol–radiation interactions, is strongly responsive to atmospheric concentration, altitude, and mixing state (Kodros et al., 2018).

Airborne aerosols can also exert important indirect effects on the terrestrial climate system, by acting as cloud condensation nuclei, leading to changes in their chemical composition, microphysical structure, lifetime, and coverage, therefore influencing their radiative properties and hydrology. This effect, which is known as indirect aerosol effect, tends to cool the global climate (Boucher, 2015).

The absorption of solar radiation by the soot components of particulate matter exerts a semi-direct effect by heating the cloud, resulting in a decrease of its amount. This redistribution of solar energy, as thermal energy, inside cloud layers, will alter the cloud lifetime and strongly influence the heterogeneous chemistry of the atmosphere (Bond et al., 2013; Haywood, 2016; Tomasi et al., 2017).

Although it is widely accepted that the indirect effects can strongly influence the global climate, and potentially mask the warming effect due to anthropogenic CO₂, the magnitudes of indirect aerosol effects are poorly understood. The Intergovernmental Panel on Climate Change (Stocker and IPCC, 2013) classified the indirect effects into two types, denoted as cloud albedo effect and cloud lifetime effect, and considers the indirect effects of aerosols the most uncertain components in forcing of climate change over the industrial period.

1.3.2. Aerosols and health

Human health is strongly influenced by the air quality. Air pollution affects people in all areas of the globe. Health effects of air pollution can be classified into two types, short-term effects and long-term effects. Short term effects result from hours and days exposure caused by episodes of high air pollution, which can lead to an increase in respiratory diseases (exacerbation of asthma, cough, wheezing, shortness of breath etc.), cardiovascular hospitals admissions and mortality. Long-term effects such as stroke, lung cancer, cardiovascular diseases etc., result from months to year's exposure and can lead to a reduction in the human life expectancy (SOGA Report, 2018). According to the State Of Global Air report (SOGA) published by the Health Effects Institute (HEI) and the Institute for Health Metrics and Evaluation (IHME) (SOGA Report, 2018), air pollution is the fifth leading risk factor for worldwide mortality, responsible for more deaths than many better-known risk factors

Chapter 1. Atmospheric Aerosols

such as malnutrition, alcohol use, and physical inactivity. Population with pre-existing lung or heart diseases, as well as elderly people and children, are particularly vulnerable (WHO, 2018). A recent publication investigating mortality attributable to specific PM_{2.5} sources reveals that the fossil fuel (mainly coal) combustion, residential, industry and energy sectors contributed to respectively 1.05, 0.74, 0.45 and 0.35 million premature deaths worldwide mainly from regions with large anthropogenic activities (McDuffie et al., 2021).

Many studies and reviews have investigated the negative impacts of aerosol particles on human health, leading to respiratory diseases and cancer in particular (Ching and Kajino, 2018). The impact of the number concentration, mass concentration, size and composition of the particles on human health have been studied (Atkinson et al., 2015; Pastuszka, 2015; Kim et al., 2015). Particle size has been directly linked to the potential of PM for causing health problems, with smaller particles likely to be deposited in deeper parts of the respiratory system (Ibald-Mulli et al., 2002). The division of the system in three main locations namely, the extrathoracic airway (ET), the tracheobronchial airway (TB), and the alveolar interstitium (AI), where particles can be deposited as function of their size were reported in previous studies (Swuste et al., 1995; Vargas and Terran, 2012) (Figure 1-2).

Particles larger than 5 μm are deposited in the ET, particularly the nasopharynx. They can be absorbed by the digestive tract and most of the time can be removed by blowing or swallowing. Particles whose size is between 2.5 and 5 μm will, however, be able to pass this barrier (ET) and enter the upper airways (TB). PM_{2.5} and particularly PM₁ and PM_{0.1}, is able to penetrate deeply into the cardiovascular system, lung and can enter the AI, hence a reduction in lung function, which can lead to an increase in bronchitis (R. W. Clarke, 1999), asthma and childhood allergies. However, they are usually quickly eliminated by mechanisms such as coughing.

Due to its dominant anthropogenic origin, the impacts of PM₁ and PM_{0.1} are more sensible in urban areas (Landkocz et al., 2017; Y. Li et al., 2016; McDuffie et al., 2021). They play a greater role in human health than PM_{2.5}, because of their ability to penetrate deeper into the alveolar region and their pro-inflammatory potential related to their chemical composition. (Ching and Kajino, 2018) used aerosol mixing state index and particle-resolved simulations to demonstrate the influence of aerosol mixing state on deposition efficiency. It was reported in their study that a modification in the mixing state of particles could make some particles such as soot become more hydrophilic therefore leading to a modification of their size as well as their ability to react in the interstitium liquid. Suggesting that

Chapter 1. Atmospheric Aerosols

models should take into account the mixing state of aerosols to reduce by around 35% their uncertainty in particle deposition pattern inside the respiratory track.

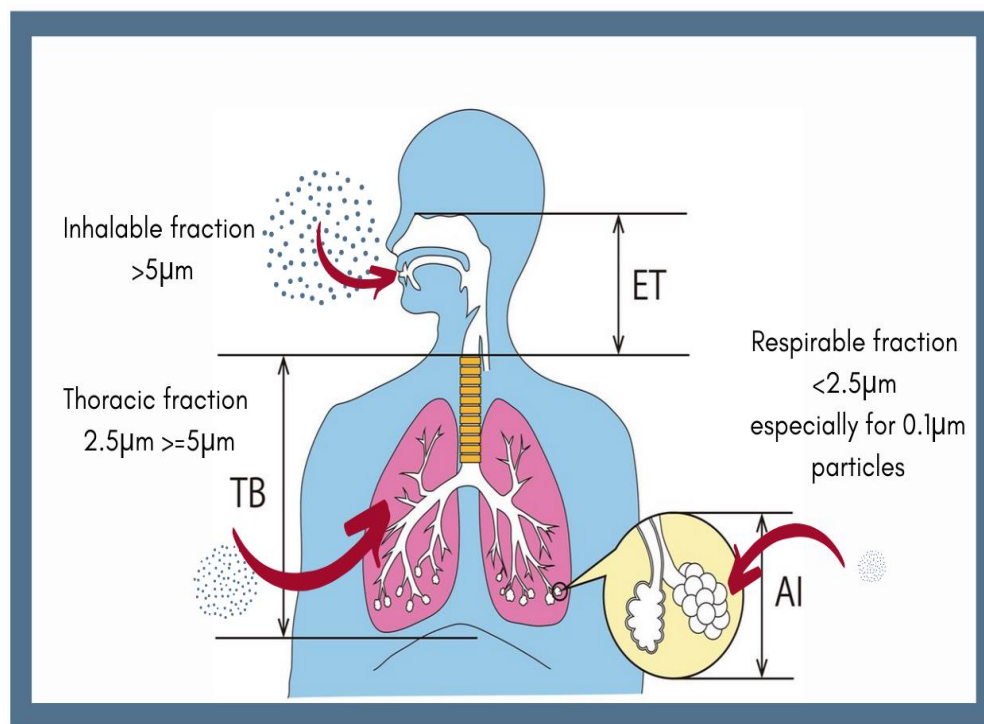


Figure 1-2. Regional deposition of particles in the human respiratory track and names of the different locations: the extrathoracic airway (ET), the tracheobronchial airway (TB), and the alveolar interstitium (AI) (adapted from Snuste et al., 1995)

Quantification of the oxidising ability in human cells of PM namely Oxidative Potential (OP), have been shown to be relevant metric to measure PM toxicity on human health (Daellenbach et al., 2020; Grange et al., 2022; Weber et al., 2021). For example, using OP, a correlation with emergency department visits for multiple cardiorespiratory outcomes including respiratory disease, asthma, and ischemic heart disease was reported and associated with size and PM composition (Abrams et al., 2017; Valavanidis et al., 2008). While mitigation strategies generally focus on reduction in PM concentrations, recent works (Daellenbach et al., 2020; Weber et al., 2021; Grange et al., 2022) showed that it would be more effective, in order to limit the health impact of PM, to control the sources of compounds associated with an high oxidative potential (OP), rather than trying to reduce the overall PM concentration. Thanks to metallic (Cd, Cu, Fe, Mn, Sn, Zn) and organic (levoglucosan, mannosan,

Chapter 1. Atmospheric Aerosols

galactosan,..) tracers of non-exhaust traffic and wood-burning emissions, it was possible to link an increase in the OP of both PM₁₀ and PM_{2.5}, to these emissions (Grange et al., 2022). The role of each of these compounds or metals on the OP however needs to be further investigated (Calas et al., 2017).

Efficient control of air quality and related health effects requires a comprehensive understanding of the sources, atmospheric interactions, and sinks of hazardous pollutants. This highlights the importance of further investigations on the effects of aerosols on human health (Weber et al., 2021).

1.4. Chemical composition of atmospheric aerosols

Atmospheric aerosols exhibit different chemical composition among different size ranges and even among particles within a given size range. Giving a definition of airborne aerosols involves a multidimensional approach which includes aerosol size distribution and chemical composition of the innumerable particles that are, in principle, different from each other. The multitude of sources (natural vs anthropogenic, primary vs secondary), as well as the type and the strength of the sources, together with the physical and chemical atmospheric processes, undergone by the aerosol and its precursors, can affect the chemical composition of aerosols in any given region of the world (Pöschl, 2005).

1.4.1. Organic Aerosols (OA)

OA origins from both natural and anthropogenic sources and contain a tremendous variety of molecular species alkanes, alkenes, alcohols, aromatic compounds, carbonylated compounds, organic acids, amines, organosulphurated compounds,...) (Hallquist et al., 2009). It's possible to distinguish Primary OA (POA) directly emitted from fossil fuel combustion, biomass burning, cooking or even fungal spores, etc. from Secondary OA (SOA) resulting from anthropogenic (AVOC) or biogenic (BVOC) oxidation and gas to particle conversion.(Seinfeld and Pandis, 2006). Almost all studies related to organic aerosols report high complexity in OA composition but also in the formation of SOA (Mithlesh et al., 2021) which is not only due to large amount of AVOC and BVOC precursors but also the complexity residing into each VOC degradation process (Peng et al., 2021). However, considerable advancements have been registered recently in this field based on an exhaustive or nearly exhaustive characterization of certain compounds such as carbohydrates, PAH or fatty acids (Bozzetti et al., 2017; El Haddad et al., 2013; Samaké et al., 2019). Hydrocarbon-like organic aerosol (HOA)

Chapter 1. Atmospheric Aerosols

represents the less oxygenated fraction of OA while the more oxygenated one is defined as oxidized organic aerosol (OOA); this fraction mainly representative of SOA or aged OA.

BVOC is made of isoprenoids, whose denomination depends on the number of Carbone units and is dominated by isoprene, monoterpenes, sesquiterpenes, as well as alkanes, alkenes, carbonyls, alcohols, esters, ethers and acids (Fan et al., 2022). In the global scale, BVOCs were estimated to be 1000 Tg·yr⁻¹ which were roughly eight times higher than those from anthropogenic origins (127 Tg·yr⁻¹) (Fan et al., 2022; Kelly et al., 2018). Consequently, a huge fraction of the global SOA (67–95%) is evaluated to originate from biogenic sources (Kelly et al., 2018) Out of the total BVOCs emissions, isoprene comprises nearly 50% of it; followed by monoterpenes and sesquiterpenes. (BVOCs) (Mithlesh et al., 2021). BVOCs are extremely reactive in the troposphere with their lifetime ranging from minute to hours (Fan et al., 2022). The BVOCs undergo photochemical degradation to form gas phase oxidation products and as a result of various heterogeneous reactions of gaseous precursors (Peng et al., 2021). An example is shown for isoprene in Figure xx extracted from (Fan et al., 2022).

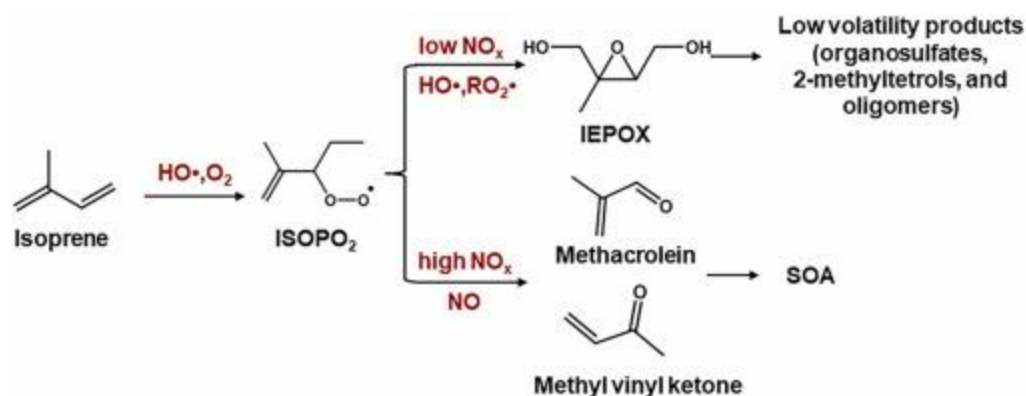


Figure 1-3. *SOA formation from BVOCs reactions under low and high NO_x concentration.*

Isoprene oxidation is initiated by OH radical produces organic peroxy-radical (ISOPO₂) whose by products is influenced by the relative abundance of NO_x concentrations (Peng et al., 2021). Under low NO_x isoprene epoxydiols is produced from the reaction between ISOPO₂ and OH and HO₂ radicals and further transformed into low volatility products. Under high NO_x, ISOPO₂ primarily reacts with NO to form SOA after several intermediate reactions (Peng et al., 2021). Studies have revealed that day time SOA formation is dominated by OH and O₃, however, NO_x initiated SOA production is dominated during night (Fan et al., 2022; Mithlesh et al., 2021; Peng et al., 2021).

Chapter 1. Atmospheric Aerosols

Organic aerosol referred to as organic matter is ubiquitous and an important contributor to $PM_{2.5}$, whereas EC makes up a small fraction of the aerosol in Europe. Concentrations of OM ranges from 15% to more than 50% of $PM_{2.5}$ and (36-64%) PM_1 in Europe (Figure 1-4 and 1-5) and sometimes reaches proportion up to 63% at remote and regional sites (Bressi et al., 2021; Putaud et al., 2004). Similar contribution was found in China (15-45%) (Peng et al., 2021) and globally OM concentrations worldwide are estimated to vary between 20 and 90% of tropospheric particulate matter (Jimenez et al., 2009).

1.4.2. Secondary Inorganic Aerosols (SIA)

1.4.2.1. Ammonium sulphate and nitrate

Secondary inorganic aerosols are an important part of inorganic aerosols that also includes for example mineral dust, volcanic ashes and marine sea-salts. The composition of secondary inorganic aerosols (SIA) is dominated by major ions including nitrate (NO_3^-), sulphate (SO_4^{2-}) and ammonium (NH_4^+). The average composition of $PM_{2.5}$ and PM_1 is presented for 19 and 21 sites in Europe in Figure 1.3. and 1.4. respectively. From Figure 1-3. we can clearly observe that SIA (NO_3^- , SO_4^{2-} and NH_4^+ salts) are dominating, sometimes contributing to more than 50% of the $PM_{2.5}$ mass on average. In the PM_1 fraction, recent reports show that SIA contribute to average 40% to the sum of NR- PM_1 of all the components measured by ACSM. This contribution is more important than those of OM for coastal and industrial sites than regional, remote and urban areas (Bressi et al., 2021).

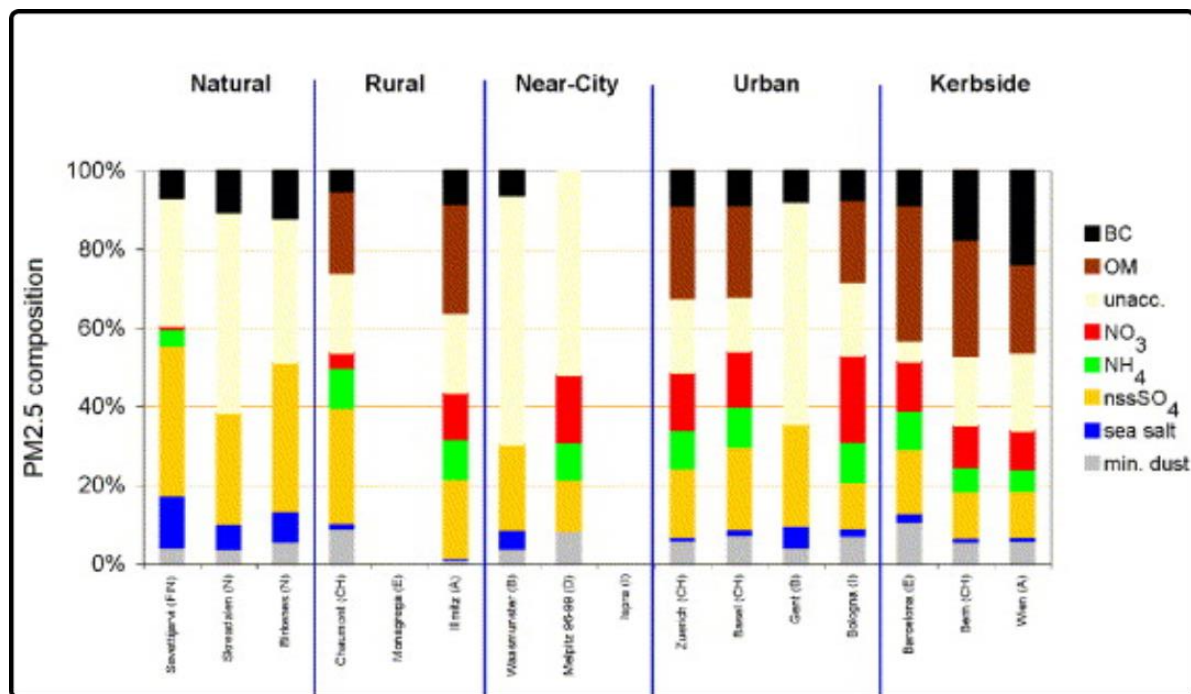


Figure 1-4. $PM_{2.5}$ relative average composition at different European sites (Putaud et al., 2004)

In the atmosphere, the majority of sulphate results from the gas-phase and aqueous-phase oxidation of sulphur dioxide while the fraction associated with sea salt and emitted as primary particles is limited (Putaud et al., 2004). The oxidation of biogenic emissions of reduced sulphur species (H_2S and DMS) can also lead to sulphate formation. Anthropogenic sources of sulphur (energy production, shipping, biomass burning) accounting for about 80% of the global sulphur budget have got the attention in many developed countries including China and India due to their negatives impacts on the environment and climate. (Smith et al., 2011).

Chapter 1. Atmospheric Aerosols

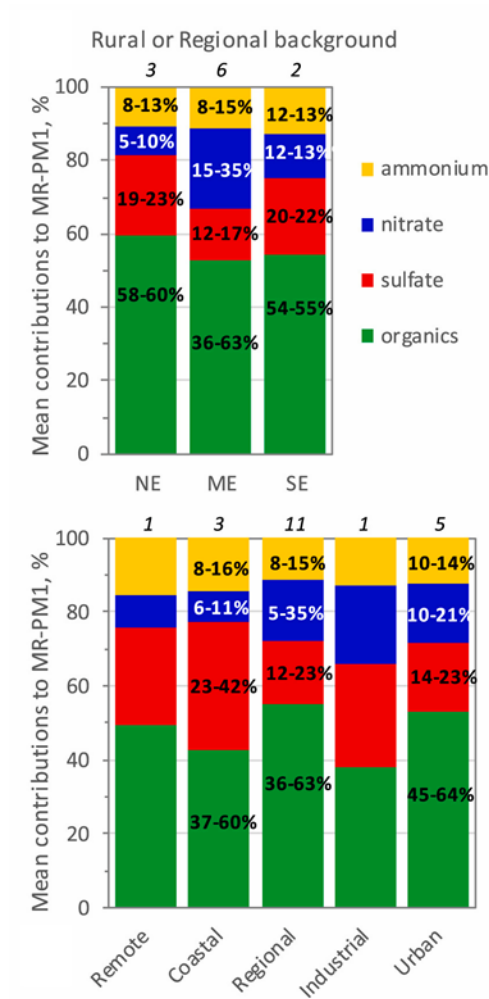


Figure 1-5. Annual average PM₁ relative chemical composition across Europe. In panels (top and bottom), percentages (%) are the ranges of the annual averages and figures in italics are the number of sites for each category.

(Bressi et al., 2021)

The chemical composition of sulphate therefore varies between pure sulphuric acid (H₂SO₄), ammonium hydrogenosulphate (NH₄HSO₄) and ammonium sulphate ((NH₄)₂SO₄). Beyond the sulphate (SO₄²⁻) and ammonium (NH₄⁺) ions, one can also find the nitrate ion (NO₃⁻) so that a SO₄²⁻, NH₄⁺, NO₃⁻ mixture is common. Ammonium is therefore formed by the reaction of ammonia with acidic species (H₂SO₄ and HNO₃). Nitrate is formed by the reaction of NO₂ with the OH radical (daytime) and by the hydrolysis of N₂O₅ in aqueous phase (night-time). Consequently, the global budget of nitrogen aerosols is strongly linked to nitrogen oxides and ammonia budget.

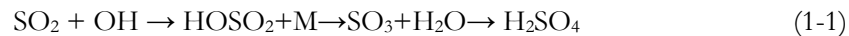
Chapter 1. Atmospheric Aerosols

1.4.2.2. Formation mechanisms of secondary inorganic aerosols

The main source of fine and ultrafine inorganic particles in the atmosphere is gas-to-particle conversion processes, considered to be the dominant source of particles contributing to atmospheric haze. Gas-to-particle conversion is the process by which gaseous molecules become transformed to liquid or solid particles and can occur by three processes: absorption, nucleation, and condensation (Vallero, 2014).

Absorption stands for the transfer of a gas into solution in a liquid phase. Nucleation and condensation are terms associated with aerosol dynamics. Nucleation is the growth of clusters of molecules that become a thermodynamically stable nucleus and depends on the vapor pressure of the condensable species, whereas condensation is the result of collisions between a gaseous molecule and an existing aerosol when supersaturation exists. The formation procedures of secondary inorganic aerosols follow the same steps and take place as follow:

The oxidation of gases precursors is the first phase. It can be either gas or aqueous phase oxidation of gaseous precursors. The gas-phase chemical reaction involves SO_2 , NO_2 (1-1) and OH (1-2), leading to an increase in the gas phase concentration of compounds with low equilibrium vapour pressure such as H_2SO_4 and HNO_3 (Raes et al., 2000) following the equations below:



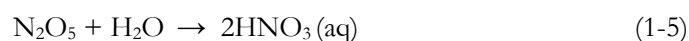
In ambient air, sulfuric acid is formed either by OH-initiated oxidation of SO_2 in the gas phase or by SO_2 (i.e. S(IV)) oxidation to SO_3 (i.e. S(VI)) by ozone (1-3) following SO_2 dissolution (into clouds, fog and aerosol water)(1-4) in the tropospheric aqueous phase (Peng et al., 2021; Raes et al., 2000b)



Sulphuric acid have a high affinity for water leading to its very rapid and efficient removal from the atmosphere by wet processes (Tomasi et al., 2017).

Chapter 1. Atmospheric Aerosols

In contrast, nitric acid (HNO_3) has a much higher saturation vapor pressure. Therefore, the gas-phase concentration of HNO_3 is not high enough to permit nucleation of nitric acid aerosol in typical atmospheric systems (Vallero, 2014). The heterogeneous hydrolysis of N_2O_5 (1-5) might also play an important role in NO_3 production, particularly in spring, where N_2O_5 production rate might be increased by higher O_3 levels (Raes et al., 2000) and can be favoured by the high gas-phase formation rate of NO_3 , the high RH, and the high sulphate content. (Peng et al., 2016).



The second step is the condensation of oxidation products and grown clusters of sulphuric or nitric acid, followed by the neutralization reaction of sulphuric or nitric acid with ammonia as shown in the equation (1-6) below for the case of sulphuric acid.



The formation of ammonium sulphate (1-6) is generally a two-step process starting with the conversion (mostly heterogeneous) of SO_2 to H_2SO_4 and subsequent neutralization with NH_3 .

Ammonium nitrate is a semi-volatile secondary specie resulting from the photo-chemical oxidation of gaseous precursors, mainly ammonia (NH_3) and nitrogen oxides or nitric acid (NO_x/HNO_3), in equilibrium between the gas phase and the particular phase, depending on ambient temperature and humidity (Finlayson-Pitts et al., 2003).

The formation of ammonium nitrate and sulphate is also a function of the concentration levels of these gaseous precursors. The existence of abundant precursor gases (SO_2 , NO_x , NO_y , NH_3 , O_3 , etc.) and catalyst (Fe^{3+}) are important for the formation of secondary inorganic aerosols (Han et al., 2019). Reactive nitrogen compounds (NO_y) have also been identified as precursors for both ozone and fine particulate matter ($\text{PM}_{2.5}$).

O_3 is important for SO_2 oxidation in the atmosphere. A study in northern Taiwan investigated importance of the sea/land breezes on O_3 distribution and transport at a coastal area. The results of the simulations showed that at night or in early morning land breeze can transport the photochemically produced ozone over the sea, resulting in a decrease in inland O_3 concentration. The accumulated O_3 can return to the land with the sea breeze contributing significantly to high-ozone episodes in clean

Chapter 1. Atmospheric Aerosols

coastal areas (Liu et al., 2002). The occurrence of sea breezes can, therefore, lead to an increase of continental O_3 , as well as NO_3^- , SO_4^{2-} and Cl^- concentrations, following the reaction of sea-salts (NaCl) with gaseous NO_2 and SO_2 (Bondy et al., 2017; Colbeck et al., 2002; Xu et al., 2021).

Ammonia is largely derived from agricultural activities. However, important traffic related urban sources have been reported to influence NH_3 concentration (Reche et al., 2012, p. 3; Saraswati et al., 2019). In addition, the use of urea in new-generation catalytic converters could lead to an increase in the influence of automobile traffic on ammonia emissions (Suarez-Bertoa et al., 2014; Yim et al., 2004).

1.4.3. Black Carbon (BC)

Black carbon, BC, is a light absorbing carbonaceous particulate matter generally incorrectly referred to as “soot” (Brewer, 2019). They can be easily identified from SEM and TEM images due to their typical chain-like structure that distinguish them from other particles including sulphate, organic, mineral and metals particles (Adachi and Buseck, 2008). The aggregates are made of spherical particles of diameter generally ranging between 10 to 100 nm (Adachi and Buseck, 2008; Bond et al., 2013; Xu et al., 2020), resulting from incomplete combustion of fossil fuels and biomass, due to the lack of oxygen during combustion processes. Black carbon is considered as the second greatest contributor to global warming after CO_2 (Bond et al., 2013). This can be explained by its strong capacity to absorb solar radiation (Bond et al., 2013; Brewer, 2019). However, its radiative properties can be altered by ageing through physical and chemical processes involving secondary aerosols such as sulphates, nitrates and ammonium (Li et al., 2020; Liu et al., 2020). It is also referred to as the coating of BC (Kodros et al., 2018). This leads to large uncertainties when estimating the warming effects of BC particles on climate (Bond et al., 2013; Liu et al., 2020). In a recent study, three groups of BC particles were identified. Freshly emitted and almost pure with very little amount of organic matter, partially embedded, coated with secondary species and fully embedded where the particle is fully encapsulated (Xu et al., 2020) as shown in the TEM images below.

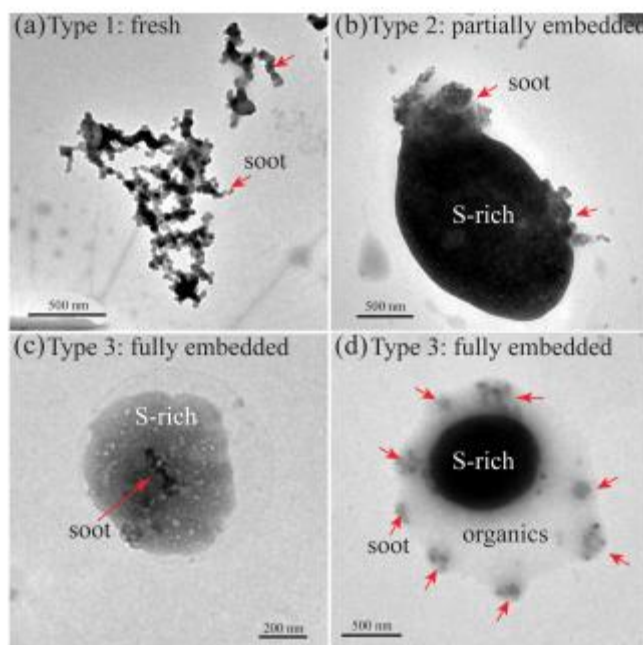


Figure 1-6. TEM images showing morphology of soot-bearing aerosol particles: (a) fresh chain-like soot aggregates with no visible coating; (b) partially embedded soot (c) fully embedded soot (d) a subtype of fully embedded soot: individual soot particles were only embedded in the organic coating on a sulphur-rich particle (Xu et al., 2020).

Moreover, worldwide emissions of BC cause on the order of millions of premature deaths per year (Li et al., 2016; Wang et al., 2021). These effects have been densely discussed in many papers. Premature deaths from lung cancer, cardiovascular problems, lost work and health care costs from chronic and acute cases of asthma and other disorders have been reported (Bauer et al., 2018; Brewer, 2019; Y. Li et al., 2016; Pun and Ho, 2019; Zhou et al., 2020).

1.4.5. Mineral dust

Mineral dust particles can be emitted from both natural (see section 1.2.2.1.) and anthropogenic sources. The anthropogenic sources include road resuspension, industrial activities, construction, cement production etc. On the morphological perspective, TEM and SEM images of mineral particles shows typically crystalline structure and irregular shapes (Adachi et al., 2020; W. Li et al., 2016) (see Figure 1-6). From the chemical perspective, they usually display very complex elemental compositions, rather than pure minerals ((Adachi et al., 2020; Deboudt et al., 2010; Li et al., 2010)). According to (W. Li et al., 2016), they are mainly composed of Si, Al, Ca, and Fe as major elements. This

Chapter 1. Atmospheric Aerosols

composition is directly influenced by their sources and their formation process (Deboudt et al., 2010; Falkovich et al., 2001; Krueger et al., 2004). Example of particle types include clays, quartz (Si-O), and feldspar (K-Al-Si), with minor calcite (CaCO_3), dolomite ($\text{CaMg}(\text{CO}_3)_2$), and other oxides. Aged minerals can be CaSO_4 and $\text{Ca}(\text{NO}_3)_2$. That's why they are generally found in the coarse particle fraction (diameter $> 2 \mu\text{m}$).

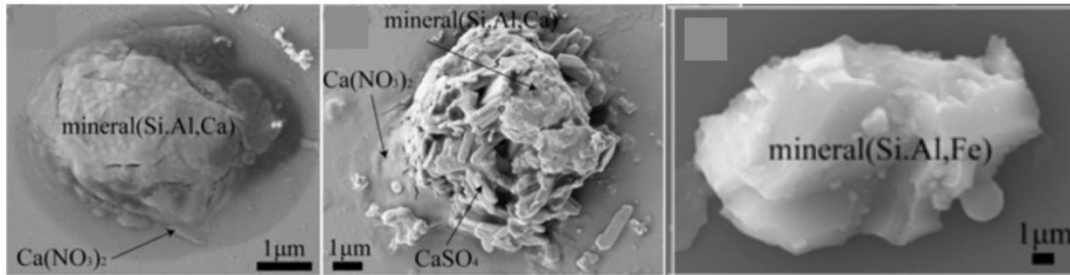


Figure 1-7. Example of SEM images of mineral particles during haze episodes in Jinan City (North China). Mineral particles coated by $\text{Ca}(\text{NO}_3)_2$ (left), mixture of aggregation of many regular CaSO_4 rods and minerals together coated by $\text{Ca}(\text{NO}_3)_2$ (middle) and irregular mineral particle (right). (adapted from (W. Li et al., 2016))

1.4.6. Sea-salt particles

Sea-salt particles (or SSA: Sea Salt Aerosols) are important for a wide variety of processes, including for climate as they contribute to atmospheric cooling because they scatter incoming solar radiation. They are mainly composed of Na, Cl with minor amounts of Mg, Ca, K and S and are considered as the dominant aerosol particle in marine air (W. Li et al., 2016; Xu et al., 2021). They can be found in various shapes and forms including cubic NaCl particles, viscous $\text{MgSO}_4/(\text{NO}_3)_2$ and/or $\text{Na}_2\text{SO}_4/\text{NO}_3$, with some Na_2SO_4 particles having hexagonal shapes (W. Li et al., 2016). As they undergo multiphase reactions in the atmosphere, either continental or marine, sea-salt particles can be found in the atmosphere in three forms: fresh (Figure 1-4.a), generally NaCl and Mg salts; partially aged (Figure 1-4.b) NaCl with a reduced amount of chlorine and increasing amount of N and S and aged sea-salts (Figure 1-4.c), in the form of Na_2SO_4 or NaNO_3 (AzadiAghdam et al., 2019; Bondy et al., 2017; W. Li et al., 2016; Xu et al., 2021). It was also shown that ageing of SSA can happen in the marine atmosphere from the heterogeneous reaction of SSA with continentally transported gaseous species (NO_x , SO_2).

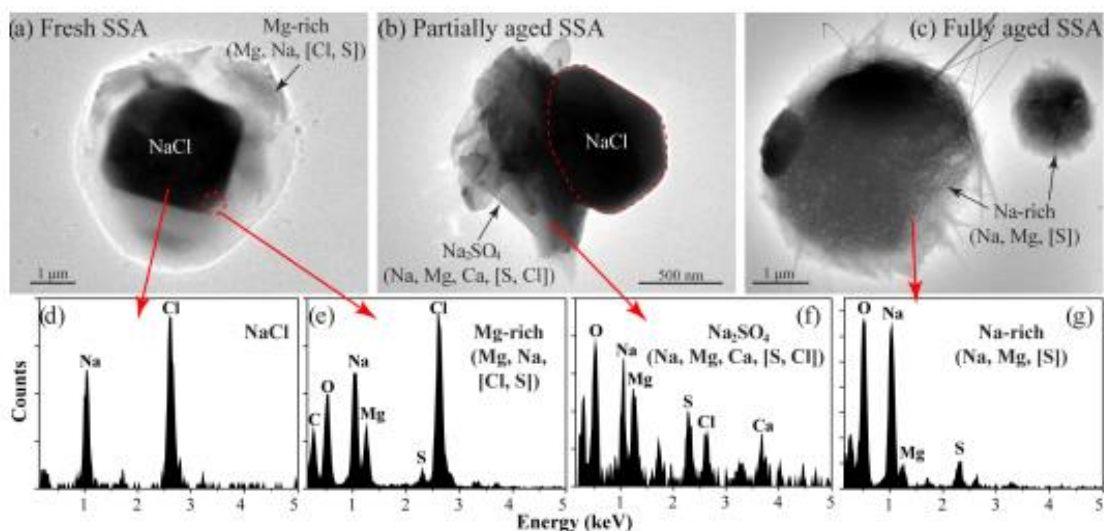


Figure 1-8. TEM images and EDS spectra of the typical fresh, partially aged and fully aged SSA. The main anionic elements are shown in the square brackets (Xu et al., 2021).

1.4.7. Metals

Metal-rich particles are abundant in polluted air influenced by combustion activities, such as waste incineration, biomass burning and biofuel burning. But the main sources are industrial (chemistry, petrochemistry, metallurgy) or related to transport (non-exhaust road emissions ; ship emissions (Beji et al., 2020; Daellenbach et al., 2020)). Metal particles in the fine and ultrafine particle fraction generally contain a wide range of elements including As, Cd, Cr, Cu, Hg, Mn, Ni, Pb, V, Fe, Zn (Mbengue et al., 2014; Riffault et al., 2015; Siciliano et al., 2021). They are generally found mixed with secondary species such as sulfate, nitrate, and organic matter, either at the exit of the chimneys or during their transport over the urban areas. Fe-rich (Figure 1-8.c), Zn-rich (Figure 1-8.a-d), Pb-rich (Figure 1-8.a-b) and Mn-rich particles were reported to be the main components of metal particles found in atmosphere as hematite (Fe_2O_3) and MnO_2 , ZnO , PbO , and PbSO_4 , beside viscous $\text{Zn}(\text{NO}_3)_2$ and ZnSO_4 (W. Li et al., 2016).

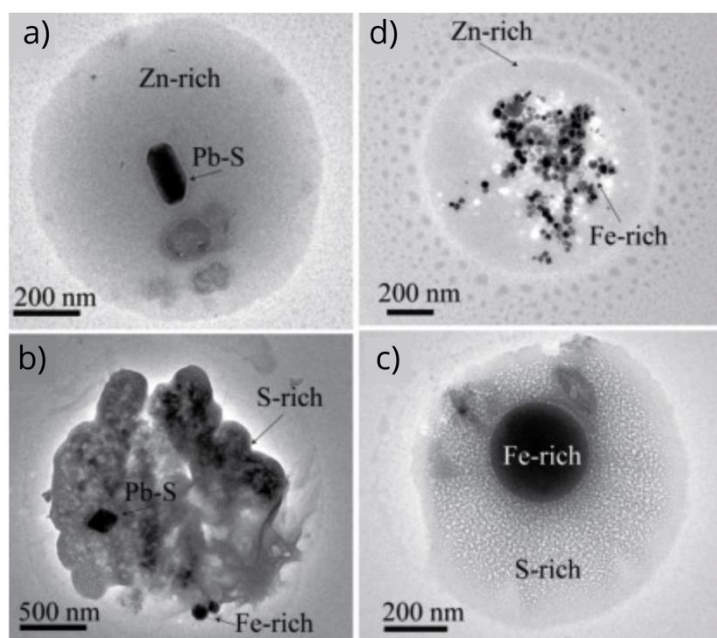


Figure 1-9. Morphology and composition of metal particles in East Asia. (a) one Pb-S bar mixed with Zn-rich coating, with minor S. (b) one regular Pb-S and two Fe-rich (Fe oxides) spheres mixed within S-rich aggregates. (d) one aggregate of many Fe-rich spheres with Zn-rich coating. (c) one Fe-rich sphere mixed within S-rich coating.

(Adapted from (W. Li et al., 2016))

1.5. Previous studies in the Great Dunkirk Area

The composition and sources of PM₁₀ and PM_{2.5} have been widely investigated using both online and offline methods, at different locations over the GDA. Main urban areas are located nearby industrial areas (Figure 2-1), as it is the case in many coastal and industrial areas worldwide (Evyugina et al., 2006; Peng et al., 2021; Siciliano et al., 2021; Squizzato et al., 2013). The presence of a strong industrial component in the GDA has initiated many studies, especially on the steel and metal industry (Hleis et al., 2013; Kfoury et al., 2016; Marris et al., 2012), to estimate the main sources of metal-rich particles present in PM (Alleman et al., 2010; Arndt et al., 2021; Kfoury et al., 2016; Ledoux et al., 2017, 2006). These particles may evolve rapidly, in a few minutes, after emission, both in size and chemical composition, before reaching the surrounding urban areas (Marris et al., 2012). Using models such as Positive Matrix Factorisation (PMF), 8 factors including crustal dust (11%), marine aerosols (12%), ferromanganese industry (6.6%), road transport (15%), resuspension dust (13%), petrochemistry

Chapter 1. Atmospheric Aerosols

(9.2%), steelworks sintering (8.6%) and coke production (12.6%) were identified by (Alleman et al., 2010) to explain the abundance of metal-rich particles in PM_{10} . These authors estimated that the respective contributions of industry, sea salts and road traffic on metals concentration in PM_{10} were 37%, 23% and 15% respectively. By applying the same method to trace elements in finer particles ($PM_{2.5}$), 7 factors nearly similar to those of (Alleman et al., 2010) were identified by (Mbengue et al., 2017). In addition, these last results show that the 40% of metallic particles attributed to industry come mainly from Fe-Mn alloys production and steelworks. These results and those of (Choël et al., 2006), show that, with also 40% of the emissions, the joint contribution of dust resuspension and marine salts is almost equivalent to those of the industry. Moreover, (Mbengue et al., 2014) showed that 60 to 80% of heavy metals over the GDA are found in submicron particles.

The nature of the industrial process and its influence on emissions was also studied. (Kfoury et al., 2016) distinguished between the composition of metal particles from an integrated steelworks plant (ISW, i.e. sintering + blast furnace) and an electric furnace steel plant (ESP). He shows that the Zn/Fe and Zn/Mn ratios allow to differentiate the emissions of the two plants, while Rb/Cr, Pb/Cr or Cu/Cd ratios succeed in attributing a distinct signature to the emissions from the ISW sintering stacks as compared to the ISW fugitive emissions.

During the Nano-Indus campaign, (Setyan et al., 2019) reported the near-field (< 1000 m from the chimneys) chemical and size distribution changes for particles in plumes emitted by a Fe-Mn alloy making plant. Several processes including condensation, coagulation and new particles formation explained these changes, as previously observed by (Marris et al., 2012a)

93% of $PM_{2.5}$ from steelworks activities are nitrates, sulfates, ammonium and total (i.e. elemental + organic) carbon (Kfoury et al., 2016). (Crenn et al., 2017) showed that NR (i.e. Non Refractory)- PM_1 were dominated by organics and nitrates (71%) in winter, while 51% were made of sulphates and nitrates in summer. (Zhang et al., 2021) showed that the contribution of SNA (sulphate, nitrate, ammonium) was estimated to account in average for 65.4% of NR- PM_1 (27.3% for Organic Matter (OM) and 6.7% for BC). This highlight the importance of secondary processes to the formation of aerosols in the vicinity of industrial areas.

The role played by meteorological factors on PM composition and concentrations was also investigated over the GDA. High levels of PM_{10} were observed under anticyclonic conditions (Gengembre, 2018; Rimetz-Planchon et al., 2008a; Roig Rodelas, 2018). Moreover, the coastal location

Chapter 1. Atmospheric Aerosols

of the GDA exposes it to various mechanisms, as low level jets, fogs or sea breeze events. Sea breeze is an important phenomena that impact atmospheric dynamics (Augustin et al., 2020; Talbot et al., 2007), but also pollutant composition and concentrations (Augustin et al., 2020; Bondy et al., 2017; Evtugina et al., 2006; Xu et al., 2021). The sea breeze occurrence is often accompanied by the formation of a temporary and lower altitude layer, the “thermal internal boundary layer” (TIBL). This layer is located below the boundary layer, then lifted by buoyancy, due to the difference in the two air masses temperature (Augustin et al., 2020; Talbot et al., 2007). The occurrence of sea breeze is generally followed by a diminution of local PM levels, as marine clean air penetrates the continent, then the PM mass increases again over the course of the day (Augustin et al., 2020). Increase in halogen species, O₃, and secondary nitrates or sulphates were also reported in these conditions (Bondy et al., 2017; Evtugina et al., 2006; Liu et al., 2002; Xu et al., 2021).

1.6. Mixing state

1.6.1 Definition and importance of the study of the mixing state of aerosol particles

The mixing state of atmospheric aerosols is one of the most challenging issue of aerosol science because of its complexity and the lack of available instruments that can fully describe it. In the discussions regarding the mixing state it is important to make clear the distinction between a particle (individual level), a particle population (aerosol level), whilst addressing their properties. Following that, (Riemer et al., 2019) define the mixing state of an aerosol as the distribution of properties across the particles in the population. This definition includes those of the chemical mixing state, which is the distribution of chemical species over individual particles, within the particle population (Riemer and West, 2013) and the physicochemical mixing state, which adds a layer of complexity to the definition by including physical properties (morphology, size etc.) to afore mentioned chemical properties (Ault and Axson, 2017).

In atmospheric research, discussions of mixing states have focused on chemical mixing state when describing the mixing state of a population. The distinction between a more or less internally or externally mixed population is therefore made to help having a better picture.

Figure 1-9 shows a simple representation of the chemical mixing state within an aerosol population. A **fully externally mixed** assumption represents a population where each particle is composed of a

Chapter 1. Atmospheric Aerosols

single species (Figure 1-9. a). In contrary, if each particle in the population has an equal proportion of each species present in the population, then the population is said to be **fully internally mixed** (Figure 1-9. b). Therefore, the per-particle mass fractions are all equal to the mass fractions of the bulk aerosol (Riemer et al., 2019). However, due to the diversity of sources and mechanisms influencing aerosol compositions, freshly released or aged particles can contain multiple and randomly distributed chemical compounds, complexifying the real chemical mixing state (Riemer and West, 2013), as simply illustrated in Figure 1-9. c).

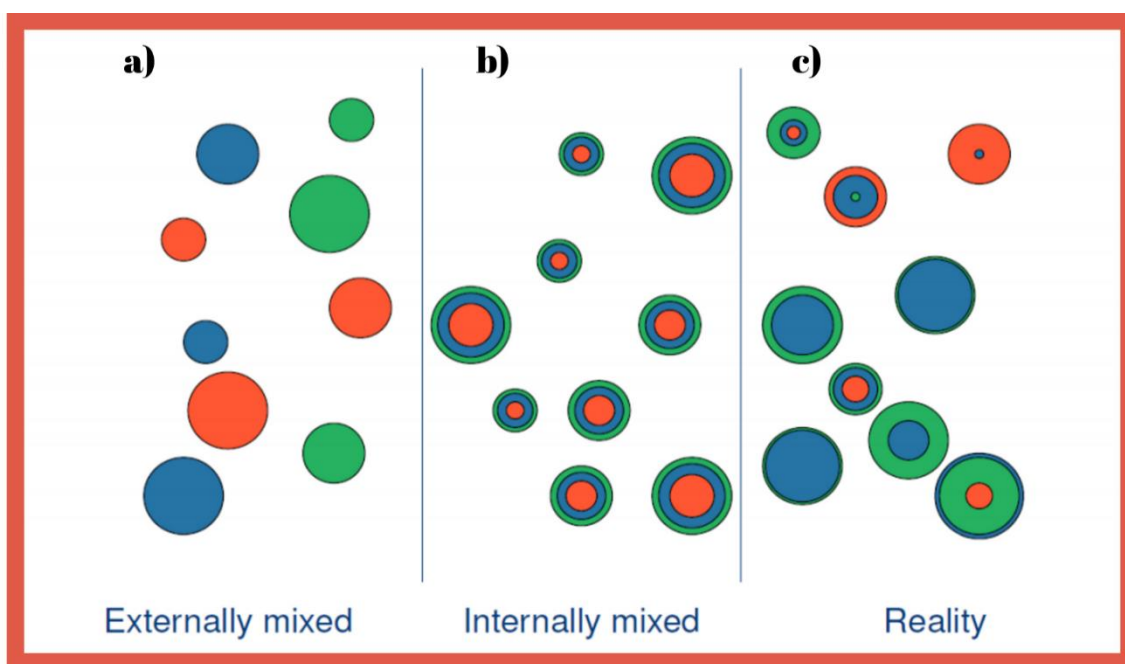


Figure 1-10. Diagram showing a fully externally mixed (a), a fully internally mixed (b) aerosol populations and an intermediate internal mixture (c), close to reality, with three different chemical species, symbolized by the colours blue, green and orange (adapted from Guilband, 2018).

The continuous evolution of particles chemical mixing state in the atmosphere is the result of a number of physico-chemical processes occurring within a particle, between particles or between the particles and the surrounding medium (Pratt et al., 2009; Whiteaker et al., 2002). These processes include the acquisition of coatings and changes in morphology through ageing, the redistribution of species within a single or an aerosol population, induced by different processes such as coagulation, condensation and heterogeneous reactions (W. Li et al., 2016; Liu et al., 2020; Nousiainen, 2009; Xu et al., 2020). These processes together with the introduction of primary aerosols from different sources

Chapter 1. Atmospheric Aerosols

and the formation of secondary aerosols, will lead the mixing state to move toward a more internal or external mixture, throughout the transport of the aerosols (Riemer et al., 2019).

The mixing state of particles significantly affects their physico-chemical properties, in particular their ability to form clouds (Ching et al., 2017; Sullivan et al., 2009), their ability to absorb or reflect incident light (Zhao et al., 2021) or their deposition dynamics within the respiratory tract (Ching and Kajino, 2018).

The acquisition by primary emitted particles (BC, mineral dust.) of coatings of more or less hydrophilic species (functionalised organic matter or inorganic salts as $(\text{NH}_4)_2\text{SO}_4$), will significantly modify their hygroscopicity. As a result, fresh hydrophobic BC particles become aged and hydrophilic and can, therefore, be active to form cloud droplets (Ching et al., 2019; Ching and Kajino, 2018; Stevens and Dastoor, 2019; Sullivan et al., 2009; Xu et al., 2020).

Depending on whether the aerosol is internally or externally mixed, the aerosol mixing state significantly affects concentrations of cloud condensation nuclei (CCN) and ice nuclei (IN), wet removal rates, thermodynamic properties, heterogeneous chemistry, and aerosol optical properties (Ching et al., 2017; Stevens and Dastoor, 2019; Wang et al., 2010). (Ching et al., 2017) estimated that errors in CCN predictions from models varied from -40% to +150% with changes in the mixing state index, highlighting the need to upgrade current models to integrate chemical mixing state information.

The health related effects of particle composition and chemical mixing state have been widely discussed (Ching et al., 2017; Ching and Kajino, 2018; Daellenbach et al., 2020; Kodros et al., 2018; Y. Li et al., 2016; Pastuszka, 2015; Pun and Ho, 2019). The deposition efficiency of particles inside the respiratory track is impacted by the mixing state, due to changes in their hygroscopic properties and then to their size and therefore to their deposition pathways (Ching and Kajino, 2018).

1.6.2. Characterisation of the chemical mixing state

To quantify the chemical mixing state of the aerosol populations, (Riemer and West, 2013b) have developed and proposed a metrics called the **chemical diversity** and **mixing state index**, for more quantitative understanding of the chemical mixing state variations. These metrics describe atmospheric particle mixing states more reasonably and quantitatively (Ault and Axson, 2017). The mixing state index have been used to characterise the chemical mixing state for different environments (Bondy et al., 2018; Fraund et al., 2017; Healy et al., 2014; O'Brien et al., 2015; Ye et al., 2018).

Chapter 1. Atmospheric Aerosols

The mixing state index, χ , is defined as the ratio of mean species diversity (per species) to species diversity (within the total population) (Riemer and West, 2013). Detailed mathematical background and physical meaning of the mixing state index are described below.

Considering a population of N aerosol particles, each consisting of some amounts of A distinct aerosol species. The mass of species \mathbf{a} in particle \mathbf{i} is denoted μ_i^a , for $\mathbf{i} = 1, \dots, N$ and $\mathbf{a} = 1, \dots, A$. From this basic description of the aerosol particles we can construct all other masses, as detailed in Table 1-3.

Quantity	Meaning
μ_i^a	<i>Mass of species a in particle i</i>
$\mu_i = \sum_{a=1}^A \mu_i^a$	<i>Mass of particle i</i>
$\mu^a = \sum_{i=1}^N \mu_i^a$	<i>Mass of the species a in the population</i>
$\mu = \sum_{i=1}^N \mu_i$	<i>Mass of the population</i>

Table 1-3. Aerosol mass definitions and notations. N is the number of particles in the population, and the number of species is A.

The probability of occurrence of the specie \mathbf{a} in the particle \mathbf{i} or in the population is defined as the mass fractions as shown in Table 1-4.

Chapter 1. Atmospheric Aerosols

Quantity	Meaning
$p_i^a = \frac{\mu_i^a}{\mu_i}$	<i>Mass fraction of the species a in the particle i</i>
$p_i = \frac{\mu_i}{\mu}$	<i>Mass fraction of the particle i in the population</i>
$p^a = \frac{\mu^a}{\mu}$	<i>Mass fraction of the species a in the population</i>

Table 1-4. Aerosol mass fraction definitions and notations. N is the number of particles in the population, and the number of species is A.

Using the distribution of aerosol species within the aerosol particles and within the population, we can now define mixing entropies. The entropy defined here is based on the concept of information entropy was introduced by Claude Shannon in 1948 (Shannon, 1948). The Shannon entropy represents the amount of information contained or carried out by a given source.

Given a random variable \mathbf{i} , with possible outcomes, each with probability P_i , the entropy $H(\mathbf{i})$ of \mathbf{i} is as follows:

$$H(\mathbf{i}) = \sum_{i=1}^n P_i \log_b(1/p_i) = \sum_{i=1}^n -P_i \log_2(P_i) \quad (1-7)$$

The more information there is in a signal, the higher Shannon's entropy. It is therefore a measure of the diversity of information. One can therefore consider entropy and diversity as equivalent notions, hence, either could be taken as fundamental. (Riemer and West, 2013) defined the entropy H_i or diversity D_i of a single particle i as measures of how uniformly distributed the constituent species are within the particle or population. They took up the above (1-7) equation in base e ($\ln p_i = \ln 2 \times \log_2 p_i$), by assimilating the mass fraction of the species \mathbf{a} in the particle \mathbf{i} to the probability of appearance of \mathbf{a} in \mathbf{i} . Then comes the followings summed in Table 1-5:

Chapter 1. Atmospheric Aerosols

Quantity	Name	Range	Meaning
$H_i = \sum_{a=1}^A -p_i^a \ln p_i^a$	<i>Mixing entropy of particle i</i>	<i>0 to lnA</i>	<i>Shannon entropy of species distribution within particle i</i>
$H_\alpha = \sum_{i=1}^N p_i H_i$	<i>Average particle mixing entropy</i>	<i>0 to lnA</i>	<i>average Shannon entropy per particle</i>
$H_\gamma = \sum_{a=1}^A -p^a H^a$	<i>Population bulk mixing entropy</i>	<i>0 to lnA</i>	<i>Shannon entropy of species distribution within population</i>
$D_i = e^{H_i}$	<i>Particle diversity of particle i</i>	<i>1 to A</i>	<i>effective number of species in particle i</i>

Table 1-5. Definitions of aerosol mixing entropies and particle diversity.

The diversity D_i of a particle measures the effective number of equally distributed species in the particle. Extending the single-particle diversity D_i to the entire population of particles gives three different measures of population diversity (Table 1-6). Alpha diversity D_α , beta diversity D_β , and gamma diversity D_γ .

Quantity	Name	Range	Meaning
$D_\alpha = e^{H_\alpha}$	<i>Average particle species diversity</i>	<i>1 to A</i>	<i>average effective number of species in each particle</i>
$D_\gamma = e^{H_\gamma}$	<i>Bulk population species diversity</i>	<i>1 to A</i>	<i>effective number of species in the population</i>
$D_\beta = \frac{D_\alpha}{D_\gamma}$	<i>Inter-particle diversity</i>	<i>1 to A</i>	<i>amount of population species diversity due to inter-particle diversity</i>

Table 1-6. Definitions of particle diversities (D_α , D_γ , D_β).

Finally, the mixing state index χ is given by:

Chapter 1. Atmospheric Aerosols

$$\chi = \frac{D_\alpha - 1}{D_\gamma - 1} \quad (1-8)$$

Entropy and diversity values (see Table 1-5) range from the minimum ($H_i = 0, D_i = 1$) when the particle is a single pure species, to the maximum ($H_i = \ln A, D_i = A$) when the particle is composed of equal amounts of all A species. Mixing state index χ of 0 and 100% indicate completely externally-mixed and completely internally-mixed aerosol population, respectively.

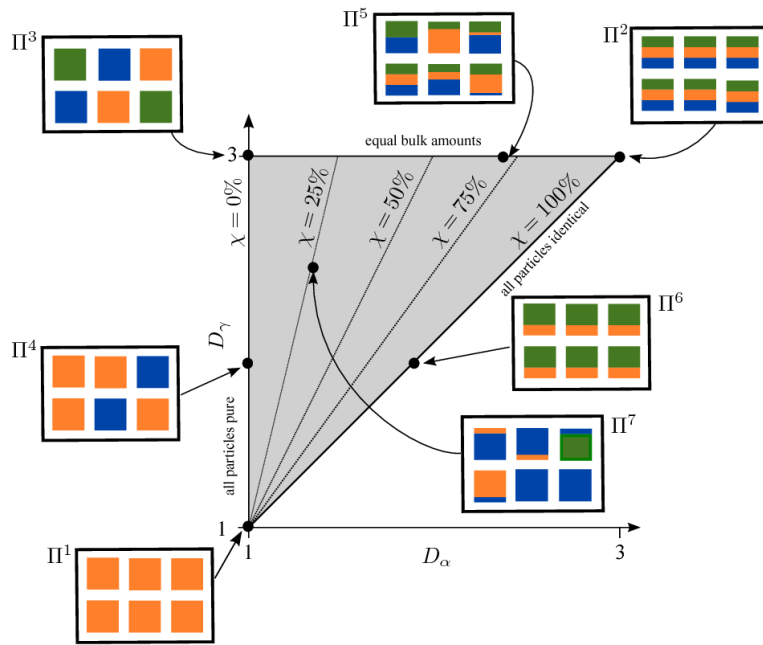


Figure 1-11. Illustration of the relationship between D_α , D_γ and χ for representative aerosol populations (Riemer and West, 2013)

Chapter 1. Atmospheric Aerosols

1.6.3 Studies using the mixing state index, χ

The only way of obtaining particle morphology and direct information about population chemical mixing state is from single-particle measurement techniques (Stevens and Dastoor, 2019). To measure aerosol chemical mixing state experimentally, ambient measurements of individual particles are generally associated to define the properties of the overall population. These single-particle chemical measurements provide diverse type of information (see Figure 1-12), grouped by (Riemer et al., 2019) into three categories: elemental or oxidation state, functional groups, and molecular composition.

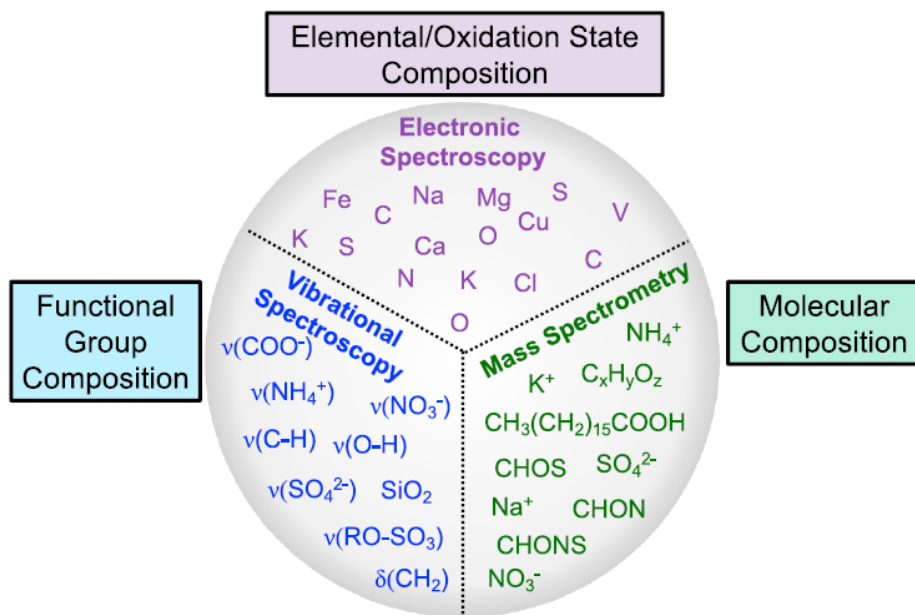


Figure 1-12. Summary of the categories of chemical measurements used for mixing state and the type of information provided (Riemer et al., 2019).

This use of the mixing state index has been applied to several field campaigns. Some of the techniques presented in Figure 1-11 were used to investigate the influence of several factors on chemical diversities (diurnal/nocturnal cycles, air mass origin, particles residence time.). Calculated mixing state indexes are summarized in Table 1-7 (Bondy et al., 2018; Fraund et al., 2017; Healy et al., 2014; O'Brien et al., 2015; Ye et al., 2018).

Chapter 1. Atmospheric Aerosols

Single-particle mass spectrometry was deployed during the MEGAPOLI campaign in Paris (Healy et al., 2014). Their results highlight the dependence of the mixing state upon diurnal/nocturnal cycles and air masses origin. They computed χ values between 0.37 and 0.72. In a similar way, elemental concentrations provided by Computer-Controlled Scanning Electron Microscopy with Energy-Dispersive X-ray spectroscopy (CCSEM-EDX) and Scanning Transmission X-ray Microscopy–Near-Edge X-ray Absorption Fine Structure Spectroscopy (STXM-NEXAFS) were used to compute mixing state parameters during the Carbonaceous Aerosol and Radiative Effects Study (CARES) in the Central Valley of California (O'Brien et al., 2015) and in the Amazon during the “Go Amazon” campaign (Fraund et al., 2017). Unlike to Healy et al., (2014), Fraund et al., (2017) reported no influence of the origin of air masses on χ in the amazon forest.

Data from Table 1-7 also reveal that extreme χ values of 0% or 100% are never reached. This is observed whatever the definition of the chemical species (elemental, molecular, functional), that changes according to the instrument and regardless of the environment studied.

To our knowledge none of the studies in literature specifically investigate the evolution of the χ during periods when PM levels exceed regulated limits.

Chapter 1. Atmospheric Aerosols

Reference	Location	Period	Instruments	Species	Particles size range	Range of χ
(Healy et al., 2014)	Paris, France	26-Jan-2010	ATOFMS	SO ₄ ²⁻ , NO ₃ ⁻ , NH ₄ ⁺ , OA and BC	150–900 nm	37–72%
		11-Feb-2010				
(O'Brien et al., 2015)	Sacramento, CA	27–28 June 2010	STXM/NEXAFS	Organic, inorganic, and BC	0.36–2.5 μ m	62–93%
	Sacramento, CA		27–28 June 2010	CCSEM/EDX	Na, Mg, Al, Si, P, S, Cl, and K,	0.1–2.5 μ m
				Ca, Mn, Fe, and Zn		
(Fraund et al., 2017)	Amazon, Brazil	Selected	STXM/NEXAFS	C, N, O, Na, Mg, P, S, and Cl,	180–320 nm	>80%
		days/times during	SEM/EDX	K, Ca, Mn, Fe, Ni, and Zn		
		September 2014 and Oct-14				
(Bondy et al., 2018)	Centreville, Alabama	5 June - 11 July 2013	CCSEM/EDX	C, N, O, Na, Mg, Al, Si, and P,	56 nm to 1.8 μ m	5%–25
			STXM/NEXAFS			
(Ye et al., 2018)	Pittsburgh, PA	Aug/Sep 2012,	SP-AMS	SO ₄ ²⁻ , NO ₃ ⁻ , NH ₄ ⁺ , OA, and BC	50 nm to 1 μ m	36–70%
		Dec/Jan/Feb				
		2011/2012				

Table 1-7. Field studies that used individual particle data to determine the mixing state index, χ

CHAPTER 2.

MATERIALS AND METHODS

2. Materials and Methods

This chapter covers the details of the instrumentation and methods used for the sampling and analysis of aerosols and gases. The exploitation of individual particles analyses and the computation of the mixing state indexes are presented in details. Chapter 2 is structured as follows:

- Presentation of the study area (section 2.1.)
- Presentation of the MIXTAPE campaign (section 2.2.)
- Methods for physico-chemical characterization of particles (section 2.3.)
- Calculation of the mixing state index from SEM-EDX data (section 2.4.)
- An overview of the collocated instruments (section 2.5.)

2.1. Study area: Air quality in the Hauts de France Region (HDF) and in the Great Dunkirk Agglomeration (GDA)

The “Hauts-de-France” (HDF) region is located in northern France (Figure 2-1. a) with a population of about 6, 000, 000 inhabitants and an area of 31,813 km², it presents a high population density of 188 inhabitants per km². Making it the 2nd most densely populated region of Metropolitan France after the “Île-de-France” region. It is bordered by Belgium to the north-east, by the North Sea to the north and west, by the “Île-de-France” region to the south, by the “Normandie” region to the south-west and by the “Grand-Est” region to the south-east. A total of five departments (Aisne, Nord, Oise, Pas-de-Calais, and Somme) form this region, which until recently was separated in two regions: Nord-Pas-de-Calais (Nord and Pas-de-Calais departments) and Picardie (Aisne, Oise, and Somme).

The region is one of the most industrialised in France with many metallurgical and chemical industries, including steel plants, cement plants, petrochemical installations, automobile factories.

The Great Dunkirk Area (GDA) (Figure 2-1. b) is an important city of the region. Located on the coast, the city is connected by two main highways, with high traffic density (A25: ~ 40 000 vehicles/day; A16: ~ 30 000 vehicles/day) and is the 3rd largest commercial harbour in France (freight transport: 53 million tons in 2019). It is also the first energy platform in the region, with the Gravelines nuclear power plant and the terminal LNG tanker at Loon-Plage.

Chapter 2. Materials and methods

The use of natural gas heating (65% of the heating energy), instead of coal, oil and wood which are less common (10%) for home heating is also characteristic of the GDA.

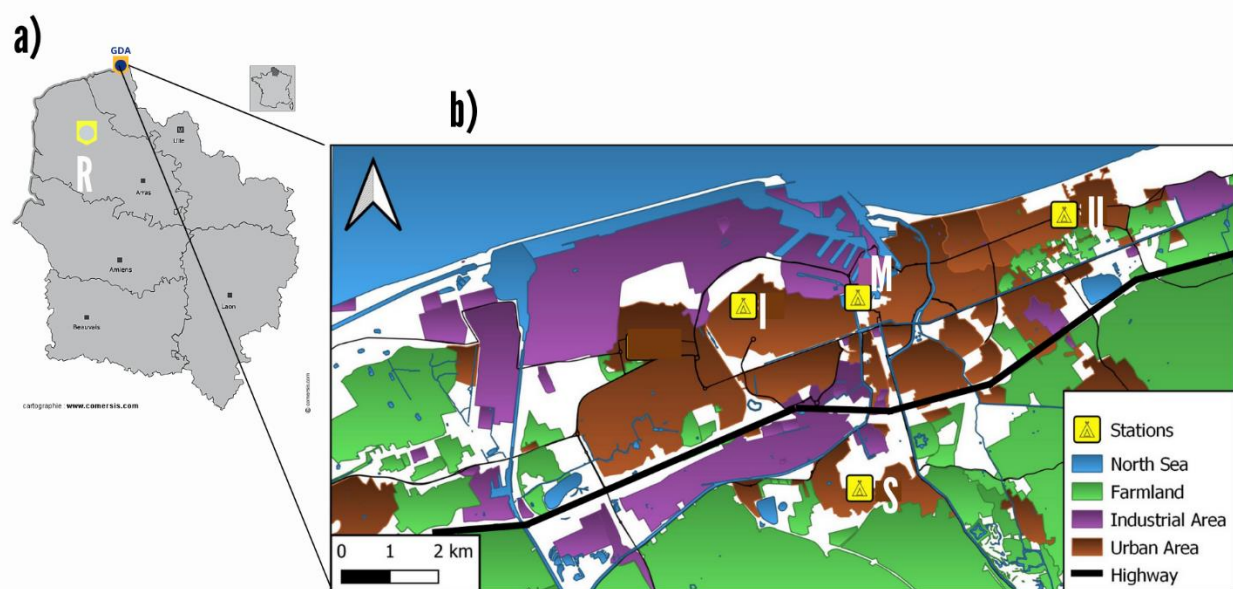


Figure 2-1. Localisation of the Great Dunkirk Area (GDA) (b), in the Hauts-de-France Region (a), located on the North Sea coast of France, close to Belgium and England. Principal land occupation includes industrial areas (purple), urban (brown), the North Sea (blue), farmlands (green) and road network (black). U, I, I2, S and R represent the different air quality monitoring stations, mainly of the air quality monitoring network ATMO-HDF (www.atmo-hdf.fr). M is the MIXTAPE sampling site hosting the meteorological station and presented later.

In the HDF region, the EU annual limit and target values for $PM_{2.5}$ (25 and 20 $\mu g \cdot m^{-3}$, respectively) are often exceeded, especially in winter and spring. The main possible reasons include the location, affected by nearby highly populated and industrial countries, as England (north-west), Belgium and western Germany (east) and the metropolis of Paris in the south and several local activities (road traffic, industrial activities, agriculture, domestic heating, etc.). In Figure 2-2, the contributions of major sectors of activity to the emissions of 6 measured pollutants in 2018 in HDF (ATMO HdF, 2020) are reported.

Chapter 2. Materials and methods

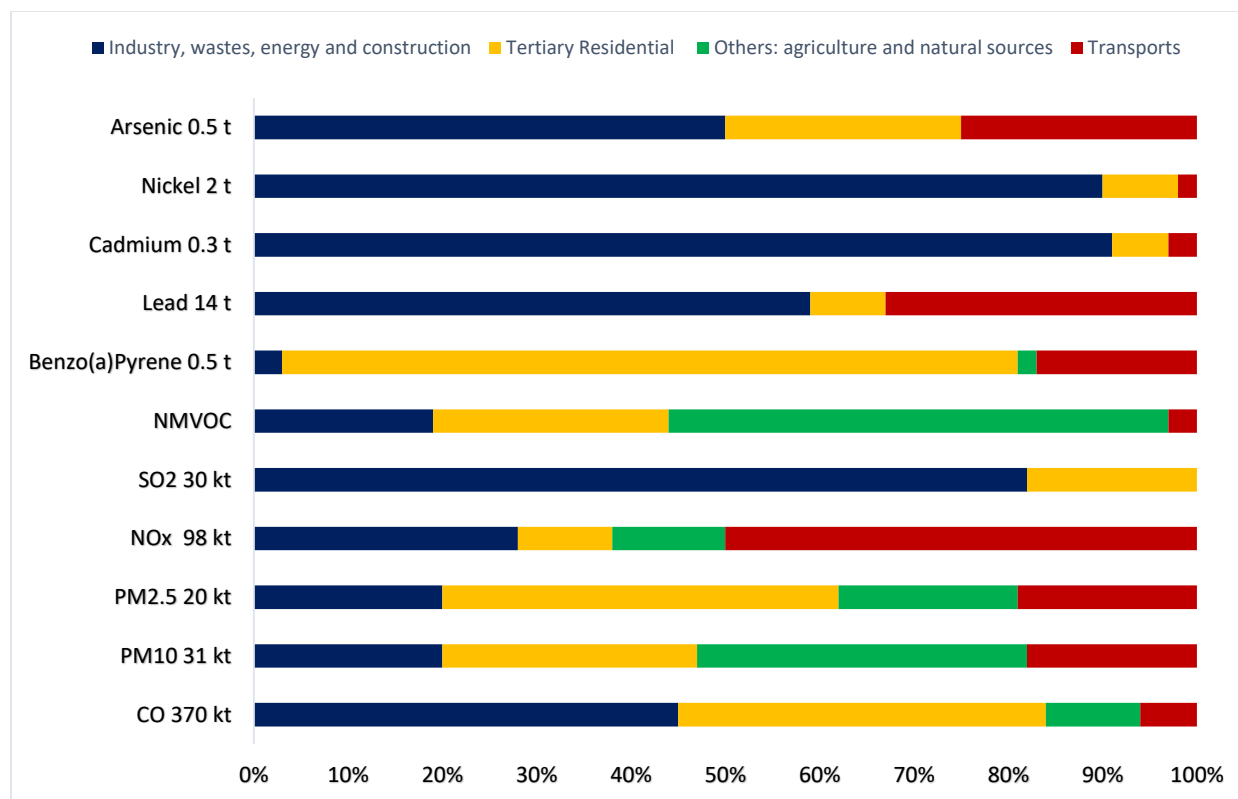


Figure 2-2. Major pollutant emissions according to different sectors of activity in the Hauts de France region in 2018 (adapted from the report “Bilan de la qualité de l’air en 2018”, (ATMO HdF, 2018))

The residential-tertiary sector is the main contributor to the emissions of PM_{2.5} (42%) and benzo(a)pyrene (78%). Road transport is the major contributor to the emissions of NO_x (50%). Agricultural and natural sources are the main emitters (53%) of non-methane volatile organic compounds (NMVOCs) and PM₁₀ particles. Industrial activities are the main emitter of sulphur dioxide (SO₂), heavy metals (Pb, As, Ni and Cd) and carbon monoxide (CO). NO_x emissions (in kilotons) are higher than national average, in particular because of a dense transport network (highways A1, A16, A29, A26).

In the GDA, the industry waste, energy and construction sector contributes to 99% of sulphur dioxide (SO₂) emissions, 89% of the PM_{2.5} particles, 87% of the PM₁₀ and 84% of nitrogen oxides. The GDA is also under the influence of the seashore, which regularly brings marine air masses towards the land.

According to Atmo HDF a pollution episode refers to a period when pollutant concentrations in the air do not respect or may not comply with regulatory levels, according to pre-defined criteria

Chapter 2. Materials and methods

(percentage of area or percentage of population impacted, regulatory level crossed, duration of the episode, ...) (ATMO HdF, 2020). These episodes represent a major public health issue since the industrial revolution. Their occurrence is tried to be minimized with setting regulations worldwide or at the nation levels. The maximum annual number of PM₁₀ pollution episodes (35) from the EU directive is frequently exceeded over the years in the HDF region.

Figure 2-3. presents the number of PM₁₀ pollutions episodes, considered as days when PM₁₀ concentrations exceeded the EU limit of 50 µg.m⁻³, that occurred in the HDF region from 2014 to 2020 (ATMO HdF, 2020). We can see that there is a decrease from 60 days in 2014 to 27 days in 2017 and then an increase from 2017 to 2019, followed by a drop to below 20 days in 2020. This drop in 2020 is certainly linked to the sanitary context and to the containment measures, which limited travel and transportation for several months. From 2017 to 2019 we can also see that there is an increase in consecutive polluted days (yellow), despite a general decrease of 30% in PM₁₀ concentrations from 2008 (27 µg.m⁻³) to 2018 (19 µg.m⁻³) : (ATMO HdF, 2018).

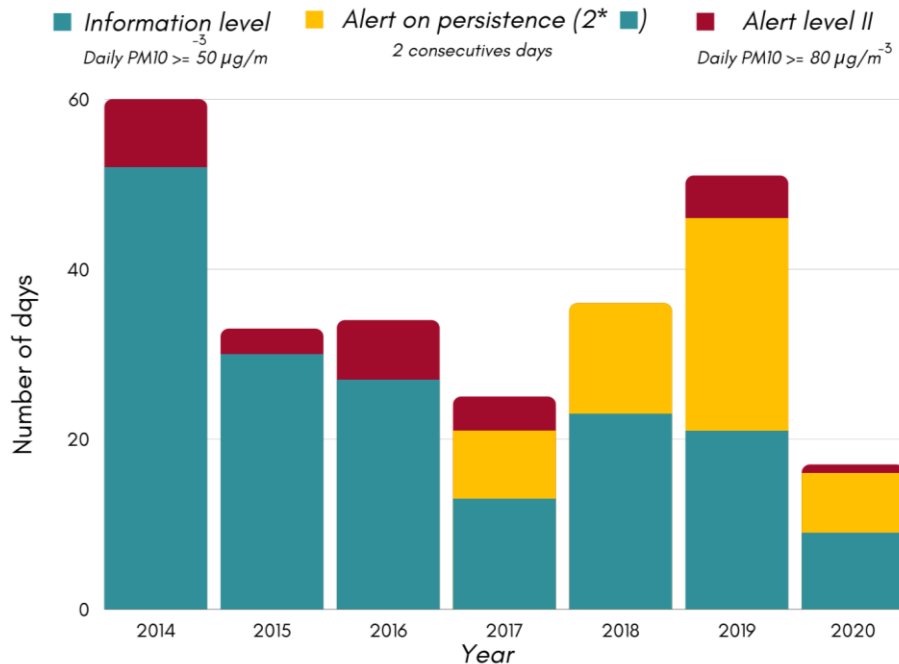


Figure 2-3. Number of days of PM₁₀ levels exceedance of the daily EU limit in Northern France from 2014 to 2020 (ATMO HdF, 2020)

Chapter 2. Materials and methods

2.2. The MIXTAPE campaign

The MIXTAPE campaign lasted 9 months from January to September 2021 and was designed to study the evolution of the mixing state of particles during pollution events roughly defined as periods into which concentrations of PM₁₀ exceed the safe levels according to WHO. Understanding the variation in the chemical heterogeneity of individual particles during pollution days over GDA could help identifying their potential near or distant sources.

2.2.1. Sampling site

Our sampling site, named “M” for MIXTAPE, is located at the University campus (51.02° N; 2.20° E), on the rooftop (around 15 m high) of the IReNE (**I**nnovation et **R**echerche **e**n **E**nvironnement) building (see Figure 2-4). Depending on the wind direction, it is influenced by air masses of industrial, urban or marine origin, as well as by road and ship traffic emissions. Our sampling site is located near the main sampling stations of the air quality monitoring network and allows the discrimination of particles transported across the urban, industrial or marine sectors (Fig. 2-1a). The instruments (aerosols monitoring and gas analysers) are implemented in a shelter (Fig. 2-1c). An air conditioning system is used to maintain the shelter temperature constant at 20°±1C.

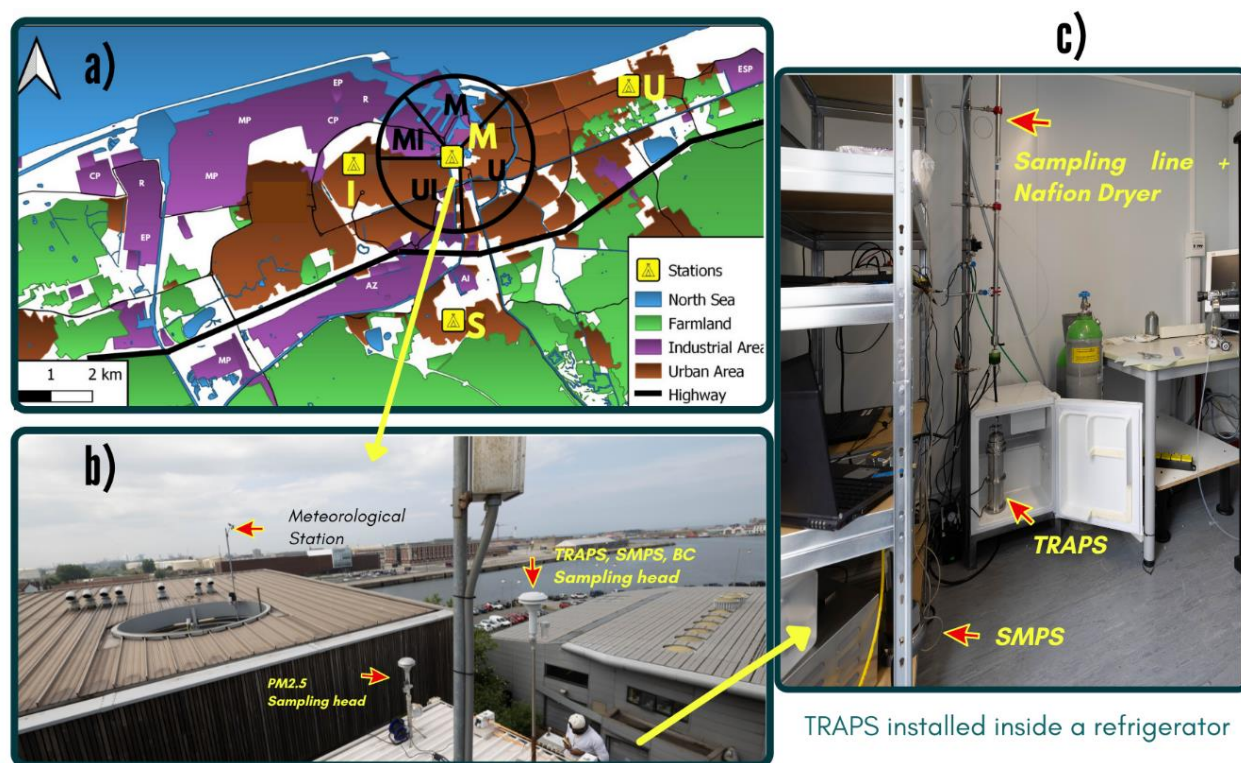


Figure 2-4. Location of the MIXTAPE sampling site on the map of the Great Dunkirk Area (a.), external view of the shelter (b.) into which the instruments for PM sampling and pollutants monitoring are installed (c.). The meteorological station can also be seen on the rooftop of the nearby building in (b.).

2.2.2. Meteorology

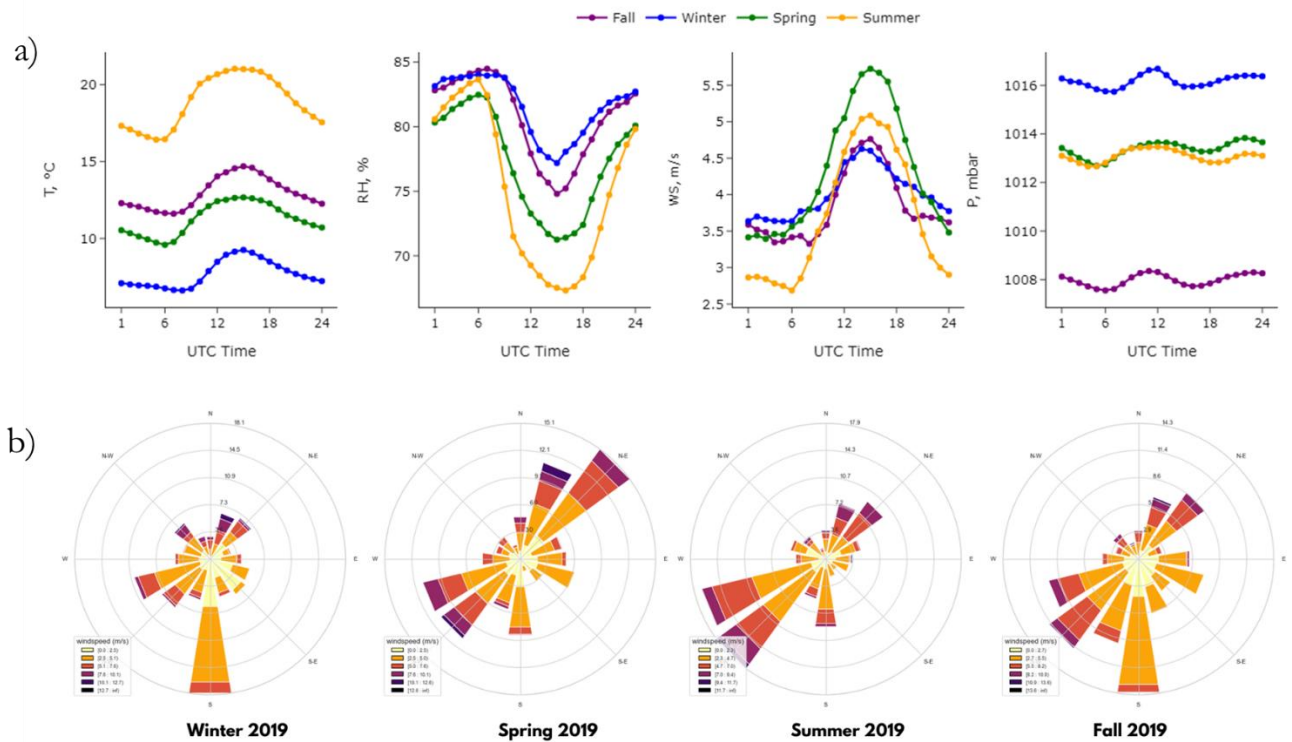
A statistical analysis of the main local meteorological parameters (temperature, relative humidity, wind speed and direction and rainfall), between 2018 and 2020, was performed using data collected at the M station (Figure 2.5). The results are shown in the form of diurnal variations, including a wind rose. In addition to providing information on the seasonal averages of each parameter, the diurnal profiles offer the possibility to observe the daily variation of each parameter and the differences in variation according to the seasons. This information is not accessible by just having averages and standard deviations.

Mean temperatures show limited variations (daily averages: 5.9°C in January and 19.7°C in July), characteristic of a temperate oceanic climate, with nevertheless a broad range of measured values from -3.1°C (in January 2019) to 41.5°C (July 2019). Most of the time the relative humidity is between 70

Chapter 2. Materials and methods

and 85%. Anticyclonic conditions are often observed in winter, whereas low pressure systems prevail in fall.

Wind speeds (WS) and directions show different seasonal features. In Fall, the dominant wind directions were from the south (frequency > 80%) and southwest (20%). In Winter south-westerlies and southerlies were almost equally dominant. In summer the N-NE and S-SW winds occurred more frequently, with higher speeds recorded in the N-NE direction. Due to thermal turbulence currents, the local wind speed is systematically higher at midday, between 11:00 and 17:00 UTC, whatever the season, with of course higher values in spring and summer, when temperatures are higher.



Chapter 2. Materials and methods

on the East and South-East, according to our monitoring site, but a second zone is situated in the SW (Fig. 2-4 a). Table 2-1. Summarizes the main activities and potential particle sources according to wind sectors which can influence our monitoring site.

Wind sector	Wind direction	Potential source/activity	Possible particles
Marine	N-NE	Major: Marine, harbor, Minor: tourism (beach), road traffic, residential heating	Na-rich including Mg and Ca, S-rich, EC/OC, Ca-rich, Si-Al rich
Industrial-marine	W-NW	Major: Steelworks, metallurgy, oil storage, cement industry, chemical and polymer plants, energy production Minor: sea traffic	Metals, EC/OC, S-rich, Na-rich including Mg and Ca
Industrial - urban	S-W	Major: Steelworks, metallurgy, oil storage, cement industry, chemical and polymer plants, energy production Minor: sea traffic, residential heating, road traffic	Metals, EC/OC, S-rich
Urban	S-E	Major: residential heating, road traffic Minor: Agriculture	Secondary species (S, N-rich particles, AOS), K-rich, Metals, EC/OC

Table 2-1. Main potential sources and local activities over the GDA, according to wind sectors, with a focus on possible PM emissions (OC = Organic Carbon, i.e. functionalised; EC = Elemental Carbon, i.e. soot, tar balls,)

Chapter 2. Materials and methods

2.2.3. Forecasting PM pollution episodes

In this study PM sampling were only performed during pollution events. To be able to study particle composition and evolution during these events requires that all the instruments implemented for particle sampling are ready before, during and at the end of the events. The use of air quality and meteorology prediction models is, therefore, essential to this task. A combination of 2 models is used. The first one is a weather information source named “Windy” (<https://www.windy.com/>) developed by Windy. this website offers the possibility to switch between global models such as ECMWF (European Centre for Medium-Range Weather Forecasts, resolution ≈ 9 km, www.ecmwf.com) or GFS (Global Forecast System, resolution ≈ 22 km, <https://www.weather.gov/>) operated by the United States' National Weather Service (NWS) and local models such as NEMS produced by www.meteoblue.com from the Swiss weather geniuses of ~ 4 km resolution only available for Europe. The weather models use observed sources that are available at the time of ingest. Common ingest sources are RADAR, satellite, aircraft reports, weather balloons, ground stations, and ocean buoys. In this study, the ECMWF was used as it offered a wider spatial coverage across Europe allowing to forecast the patterns of air masses. Windy provides 15 days forecast of meteorological parameters (surface pressure, temperature, rain events, cloud coverage, etc.). The second model is “Prevair” (<http://www2.prevail.org/>) provided by INERIS (National institute of industrial environments and risks) in collaboration with Meteo France and CNRS (French National Research Center) and the French central laboratory for monitoring Air quality (LCSQA). It is based on the result of numerical simulations and field observations to predict and map the concentrations of regulated air pollutants. Prevair reports predictions of PM, NO_x and O₃ levels in France over 3 days. In addition, current PM₁₀ and PM_{2.5} concentrations were available online on the website of the regional air quality monitoring network “ATMO Hauts de France” (www.atmo-hdf.fr). PM concentrations reported by ATMO over the GDA are checked every day to compare the model predictions and the evolution of true concentrations.

Chapter 2. Materials and methods

2.2.4. Instrumentation and measurements rationale

The view of the rooftop of the site is shown in Figure 2-6 and the list of all instruments used during the MIXTAPE campaign is presented in Table 2-2. Some instruments are used for continuous measurements, as gas analysers or Beta gauge. Others, as SMPS, BC are only used during pollution events. MIXTAPE was then operated by two ways. First, $PM_{2.5}$ concentrations, as well as meteorological parameters were recorded continuously. The calibration of the Beta-gauge was done twice a year. When processing the data, we checked for outliers and if 75 % of the data over 24 hours are lost due to power failure or other technical problem, values were considered as non-representative and excluded from analysis.



Figure 2-6. View of the shelter in which all the instruments are installed for monitoring. The sampling heads used respectively for the TRAPS, the Beta gauge “MP101” are shown together with the meteorological station. (Credit: Marc Fourmentin).

Chapter 2. Materials and methods

Parameter	Instrument	Temporal Resolution and Period of Measurement	Data availability (%)
Particle Phase			
<i>Particle Number Size Distribution (10-650 nm)</i>	<i>TSI SMPS</i>	<i>3 min. (pollution event)</i>	<i>40% (available during 2/5 of the studied events)</i>
<i>Particle Number Size Distribution (10-1000 nm)</i>	<i>GRIMM SMPS</i>	<i>7 min. (pollution event)</i>	<i>60% (available during 3/5 of the studied events)</i>
<i>Particle Number Size Distribution (20-35 000 nm)</i>	<i>MiniWras Grimm Aerosol Technik; model 1.108</i>	<i>1 min (pollution event)</i>	<i>60% (available during 3/5 of the studied events)</i>
<i>Black Carbon</i>	<i>AE51, Aethlabs</i>	<i>5 min (pollution event)</i>	<i>80% (available during 4/5 of the studied events)</i>
<i>PM_{2.5}</i>	<i>MP101M analyser ENVEA</i>	<i>15 min (continuous)</i>	<i>91%</i>
Atmospheric Dynamics and Meteorology			
<i>Pressure, temperature, relative humidity, solar radiation, rain, wind speed and direction</i>	<i>DAVIS Weather Station</i>	<i>15 min. (continuous)</i>	<i>98%</i>
<i>Wind Lidar</i>	<i>Leosphere</i>	<i>10 min (pollution event)</i>	<i>100%</i>

Table 2-2. List of the instruments deployed during the MIXTAPE Campaign

Chapter 2. Materials and methods

Second, during pollution events, when the models predict the occurrence of an upcoming exceedance of the PM₁₀ or PM_{2.5} levels, instruments necessary for particle measurements were deployed together with the wind Lidar that was necessary to measure vertical and horizontal wind profiles. These instruments are OPC, SMPS, Aethalometer and the TRAPS. In the following section, we will present the TEM-EDX analysis procedure for individual particles collected using the TRAPS.

2.3. Individual particles characterisation during MIXTAPE

2.3.1. Particles sampling using the TRAPS

Cascade impactors operate on the principle of curvilinear motion of particles in the aerosol stream. In a single-stage impactor (Figure 2-7 a), a gas jet containing suspended particles impinges on a flat plate; particles of sufficiently large inertia are deposited on the plate, whereas smaller particles with lower inertia, under the influence of the gas viscosity forces, are carried on with the flowing gas.

Size classification by impaction refers to the particle aerodynamic diameter (d_a), defined as the diameter of a sphere, whose specific mass is 1 g.cm⁻³ and which settles in still air at the same velocity as the impacted particle. d_a is calculated as shown in equation (8):

$$d_a = d_p K \sqrt{\frac{\rho}{\rho_0}} \quad (8)$$

Where d_p is the geometrical diameter of the particle, K is the shape factor (= 1 for a spherical particle), ρ is the specific mass of the particle and ρ_0 is the specific mass of the equivalent particle ($\rho_0 = 1 \text{ g.cm}^{-3}$)

A cascade impactor, consists of a series of single-stage impactors where each subsequent stage collects progressively smaller particles (Figure 2-7. b). Each stage of the impactor will separate ideally aerosol particles into two size ranges (Fig. 2-7. c): 50% of particles larger than the cut-off size will be removed efficiently from the stream and the remaining will have to go through the next successive stages. The decreasing slit nozzle width for the next successive stages, leads to an increase in the impaction velocity of the lower stage compared to the previous one, at constant flowrate.

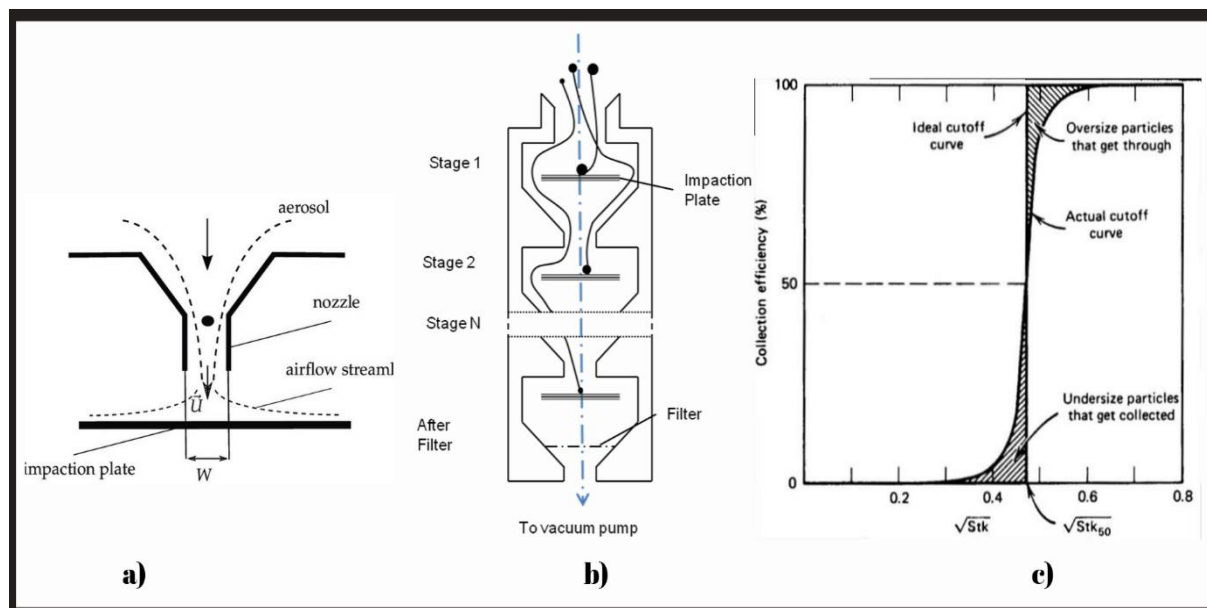


Figure 2-7. Schematic representation of impaction principle (a), a view of a multistage cascade impactor (b) and a collection efficiency curve for stage characterization (c) (Hinds, 2012)

In this study, rapidly tracking the evolution of particle heterogeneity during pollution events is fundamental. There is, thus, the need for a sampler based on cascade impaction technique, able to provide particle samples at high time resolution. That is why the Time-Resolved Atmospheric Particle Sampler (TRAPS) was developed for.

The TRAPS is a non-commercial (homemade) time resolved aerosol sampler designed to give a continuous or time-discrete collection of coarse and fine particles, suitable for a wide range of single particle analysis techniques such as SEM, TEM, Raman etc. It is a two stages cascade impactor with rotating collection plates whose stage collection efficiencies of 1.13 and 0.12 μm were experimentally determined for the coarse and fine stages, respectively (see Chapter 3). The determination of the size segregation characteristics of the TRAPS and its operating conditions was one of the main objective of this thesis. This part of the work is specifically addressed in details in the third chapter of this manuscript.

During the sampling campaign, the air inlet of the TRAPS was connected to a 1.2 m long Nafion Dryer (see Figure 2-8.), which selectively removes water vapour from ambient air, while maintaining

Chapter 2. Materials and methods

dried particles in the air flow. The particle sampling flowrate of the TRAPS is 5 Lpm, therefore requiring a purge flowrate two times the inflow rate. In this campaign, N₂ gas was uninterruptedly injected as purge gas at a flowrate of 10 Lpm during particle sampling. This helped decreasing by almost 80-90% the relative humidity inside the air, allowing for dry particle sampling and measurements.



Figure 2-8. Image showing the instruments used for in-situ characterisation of particles during the MIXTAPE campaign. The TRAPS is set inside a fridge (+4°C). Other instruments installed in the shelter such as the SMPS (TSI Inc.), the Optical Particle Counter (OPC) Mini-Wras (GrimmTM) and the aethalometer AE55 (Mc Gee Scientific) were connected to the same sampling line. (Credit: Marc Fourmentin)

Chapter 2. Materials and methods

Time resolved particle samples were collected on both TEM grids and polycarbonate membranes using the TRAPS (Figure 2-9). TEM copper grids, covered with a Formvar© carbon film, were used. The carbon film is very thin (40 to 60 nm thick) and its contribution to the X-ray emission signal of the analyzed particles is negligible.

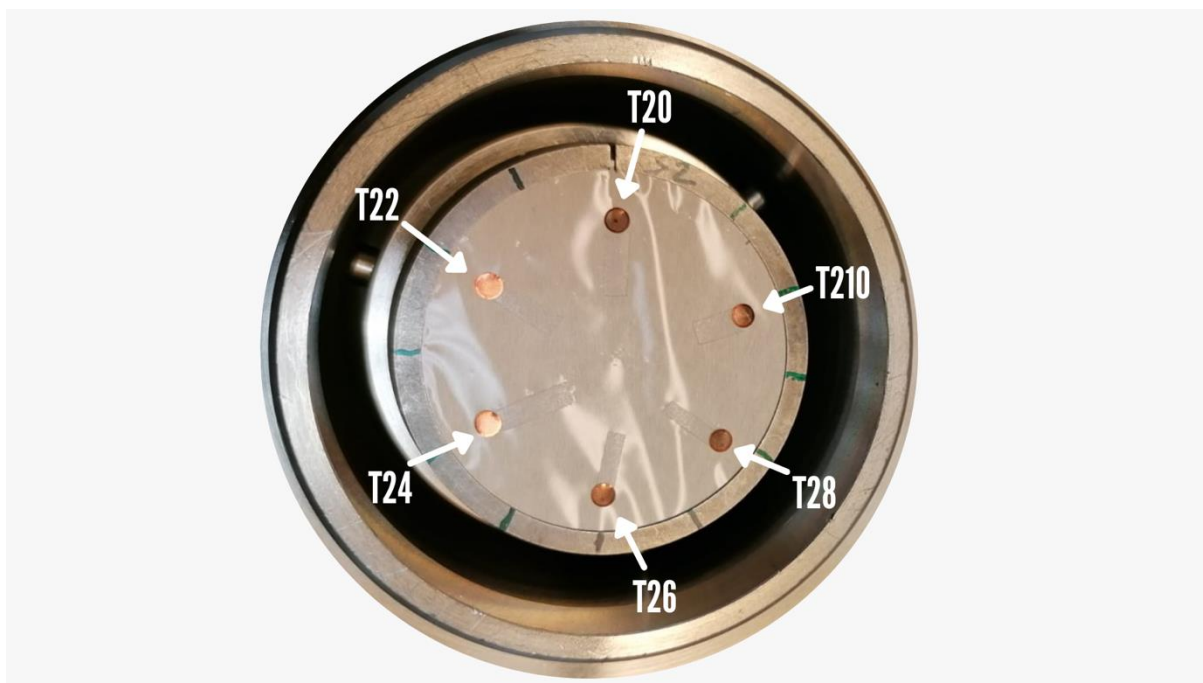


Figure 2-9. View of a TRAPS impaction plate (Stage 2) onto which TEM grids are stacked on the polycarbonate membrane. The rotation of the plate in clockwise favouring collection of samples in a chronological order from T20 the initial sample at position zero to maximum T210 as shown here.

The use of forecasting models, like Windy and Prevaire, does not guarantee that the chosen sampling period will fall exactly at the time of a pollution peak. Therefore, it is necessary to obtain several sets of continuous samples, covering the whole pollution episodes. Furthermore, a few tens of minutes are sufficient to obtain enough individually identifiable particles on the grid, to perform an automated SEM-EDX single particle analysis that makes statistical sense (about a thousand particles analysed). We have therefore chosen, for a given pollution day, to collect the particles by sample of 30 to 120 minutes, according to the $PM_{2.5}$ concentration recorded on that day (Beta gauge).

Chapter 2. Materials and methods

For example, from March 30th to April 1st, 2021, we have collected 24 samples on TEM grids (12 per TRAPS stage), in only 4 sampling periods, as reported in Table 2-2.

Date/Period	TRAPS stage	Grid Position	Sampling duration (min)	Sample Starting time (UTC)
31.03.2021 (Period 1)	Coarse (1-10 μm)	T10	30	8:00
		T12	60	9:00
		T14	120	11:00
	Fine (0.1- 1 μm)	T20	30	8:00
		T22	60	9:00
		T24	120	11:00
31.03.2021 (Period 2)	Coarse (1-10 μm)	T10	30	17.00
		T15	120	22.00
		T19	120	4.00
	Fine (0.1- 1 μm)	T20	30	17.00
		T25	120	22.00
		T29	120	4.00
01.04.2021 (Period 3)	Coarse (1-10 μm)	T10	60	8:10
		T12	60	10:10
		T14	60	12:10
	Fine (0.1- 1 μm)	T20	60	8:10
		T22	60	10:10
		T24	60	12:10
01.04.2021 (Period 4)	Coarse (1-10 μm)	T10	60	17.00
		T15	120	23.00
		T19	60	4.00
	Fine (0.1- 1 μm)	T20	60	17.00
		T25	120	23.00
		T29	60	4.00

Table 2-2. TRAPS sampling plan implemented during the first studied pollution event (PE1). As a maximum of 12 samples (i.e. impaction traces: see Chapter 3) can be collected per impaction plate, T10 represent the grid position of the first sample: i.e T (for Trace), 1 (for the coarse stage S1 or 2 in case of stage 2 see below) and 0 (for the sample 0) (see figure 2-10). The time necessary to rotate from one position to another is 60 seconds.

Chapter 2. Materials and methods

The preparation of a sampling includes:

- 1) installation of the polycarbonate membranes on the impaction plates,
- 2) installation of the grids and their proper positioning perpendicular to the nozzles outlets,
- 3) programming the sequence according to the sampling plan and
- 4) installation of the TRAPS inside fridge before the start of the sampling.

In this study only samples collected on TEM grids were presented and exploited. All samples were stored at -18°C , directly after collection and only those selected for their scientific interest were removed and brought to ambient temperature (in a desiccator) prior to TSEM-EDX analysis.

2.3.2. Individual particle analysis by TSEM-EDX

Microscopic observation and analysis of aerosol particles requires a small amount of samples (i.e. single particles dispersed onto a flat substrate), in order to permit direct observation and measurement of their size, shape and chemical composition. Electron microscopes are used to analyse particles smaller than the limit of resolution of optical microscope and exist in two types Scanning electron microscope (SEM) and Transmission electron microscope (TEM).

2.3.2.1. The TSEM-EDX technique

The working principle of the couple Scanning Electron Microscope (SEM) and Energy Dispersive X-ray spectrometry (EDX) is based on the interactions between light and matter, which leads to emissions of several types of electrons of wavelength much shorter than light. A typical SEM is presented in Figure 2-10. and is made of the following parts:

- An electron source ('Gun')
- Electron lenses
- Sample stages
- Detectors for all signals of interest
- Display output devices (mainly computers)
- And infrastructure requirements including power supply, vacuum system, cooling system and a room free of magnetic or electric field.

Chapter 2. Materials and methods

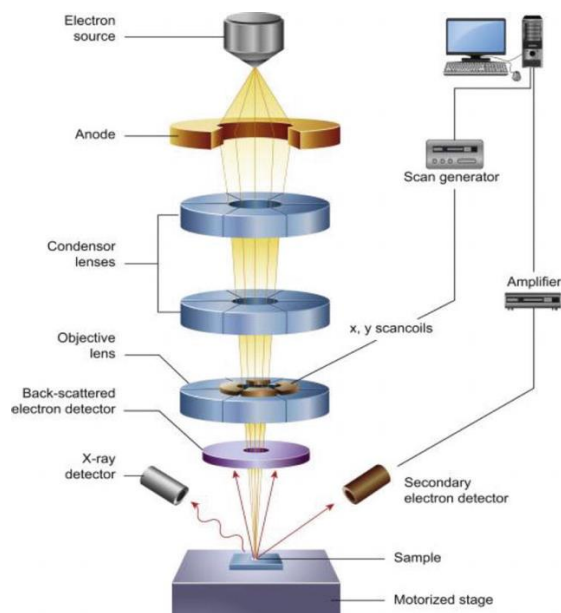


Figure 2-10. Illustration of a scanning electron microscope. Source: Liberal Dictionary
(<https://www.tekportal.net/scanning-electron-microscope/>)

The SEM used in this study (Figure 2-11.) is a FEG-SEM model JEOL JSM-7100F (JEOL Company, Japan). It means that it is equipped with a Schottky Field Effect Gun (FEG). This FEG-SEM is equipped with three EDX Bruker Quantax[®] 800 spectrometers, fitted with 30 mm² silicon windows and a Quorum[®] PP3010 cryogenic system. It can be renamed as FEG-TSEM as specimen observation can also be conducted in transmission mode. It is, thus, possible to obtain images/texture and composition of specimens with a resolution up to 3 nm, at an acceleration voltage of 15 kV, a working distance of 10 mm and under a probe current of 5 nA.



Figure 2-11. Image of the FEG-SEM model JEOL JSM-7100F located inside the IRENE-ULCO research building. (Credit: Marc Fourmentin)

The interaction between the incident electron beam and atoms from the sample leads to the emission of different types of particles and radiation as presented in Figure 2-13:

- secondary electrons which are turn-off from the surface of the sample, following the inelastic interaction between the primary electron beam and the atoms constituting the sample
- backscattered primary electrons which result from the quasi-elastic interaction between the electrons of the incident beam and the nucleus of the atoms of the sample
- transmitted electrons, without interaction with the material crossed
- electrons scattered elastically (without loss of incident energy) and inelastic (with partial loss of energy)
- Auger electrons, linked to the filling of the electronic hole caused by the incident beam, at the level of the internal layers. A higher energy electron then occupies the atomic orbital left

vacant, the energy difference between the two orbitals being transmitted to a peripheral electron which is emitted

- **X rays**, either emitted in competition with the Auger emission (fluorescence phenomenon), or emitted directly after ionization of the atoms. It is this latter phenomenon that is used in X-ray emission spectrometry

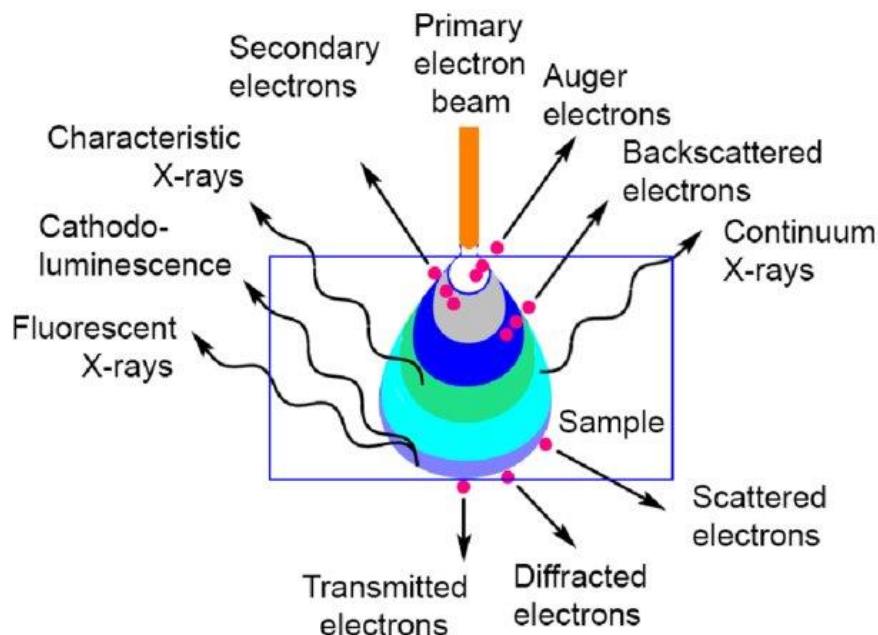


Figure 2-12. Electron matter interactions at different sample depths and derived techniques of analysis (Sharga et al., 2021)

2.3.2.2. Automated TSEM-EDX analysis of individual particles

Using SEM-EDX technique offers the advantage that it is one of the few "non-destructive" micro-analytical techniques, which can provide information on both the morphology and the composition of environmental samples. It is particularly the case for the solid fraction of atmospheric particles. Moreover, it is possible to determine the elemental chemical composition of a large number of particles (more than a thousand), thanks to the automation of this technique. This allow the acquisition of results representative of the whole population of particles, after a robust statistical treatment. It will thus be possible, by identification and quantification of the chemical elements present within the particles, to highlight their sources or their modes of generation.

Chapter 2. Materials and methods

This instrument makes it possible to observe individual particles with a spatial resolution down to 3 nm and to obtain the elemental composition of particles larger than 100 nm. It was operated in high vacuum mode with an acceleration voltage of 15 kV under a probe current ranging between 150–300 pA, with a working distance of 10 mm. Images and elemental composition (elements with an atomic number higher than Boron- $Z \geq 5$) were acquired at magnifications of 2000–4000 and 6000–10000, for the TRAPS coarse and fine stages, respectively. The acquisition time for each particle spectrum was 13 s. An automated particle detection procedure was performed using the ESPRIT[®] software (Bruker[™], Germany).

The combination of "TEM/Gauss/PhiRhoZ" methods was chosen and applied using the Bruker ESPRIT[®] version 2.2 software. With the aim, respectively, to extract the continuous background due to the TEM grids used (TEM), to perform a Gaussian (Gauss) deconvolution of the X-ray emission lines, slightly influenced by the particle size and to achieve a "PhiRhoZ" quantification of the different elements. This combination was selected by (Guilbaud, 2018) as the one offering the most satisfactory conditions for the quantification of the elements present in atmospheric particles.

The operating conditions used during SEM-EDX analyses are summarized in Table 2.3:

Acceleration voltage	15kV		
Working Distance	10 mm		
Probe current (pA)	150-300		
Bruker Software			
Dwell time	8s		
Image capture	13s		
Mapping scan time	50s		
Elemental quantification Method	MET/Gauss/PhiRhoZ		
Sample Stage	Coarse stage (1-10 μm)	Fine stage (0.1-1 μm)	
Magnifications	×2000	×6000	×10000
Image resolution (pixels)	1024×768	1024×768	1024×768
field size (L×l in μm)	60×45	20×15 μm	12×9
Min. size detected (μm)	0.1	0.1	0.1
Pixel size (nm)	58	19	12

Table 2-3. Main parameters applied with Jeol FEG-SEM images and Bruker ESPRIT 2.2 Software to carry out analyses of MIXTAPE samples

Chapter 2. Materials and methods

2.3.2.3. Classification of particles using R and manual screening

The data are first qualified by reviewing the raw and binary images of all analysed fields to ensure that the automatic particle detection has been performed correctly. Spectra corresponding to artifacts (pixels identified as particles when they are not) are then discarded from the data set. The data are then compiled in an Excel file for statistical analysis, based on the particle elemental compositions (atomic percentages). The chemical elements whose content is lower than 0.1%, whatever the particle, are discarded. Then all particles were sorted according to their C content and all those having C above 50% were associated with the first cluster. For the rest of the particles, the atomic percentages are normalized without C and O elements followed by a classification operated using the R[®] statistical software.

From Ascendant Hierarchical Clustering statistical analysis, the particles are classified according to their similarities in composition. This can be defined with the smallest distance between two compositions, and the distance of each average composition compared to the centre of gravity of the whole set, in a N-dimensional mathematical space (N = Number of chemical elements considered). A hierarchical tree is then generated and interpreted from top to bottom. This allow us to choose the number of composition clusters representative of all individual particles, with each cluster characterized by a specific elemental composition.

After classification, each spectrum of the same cluster is reviewed to ensure the environmental consistency of the statistical classification, then the spectra are summed, to obtain a "sum" spectrum for each cluster, in order to improve the signal-to-noise ratio and to be able to quantify with precision the minor elements present in particles.

By this way, a total of **28 029** individual particles for both particles fractions (coarse and fine) were classified, for all studied pollution events. The elemental composition of these particles incorporate 18 elements, including C, O, Al, Ca, Cl, F, Fe, K, Mg, Mn, N, Na, P, Pb, S, Si, Ti and Zn. All the analysed particles were therefore classified into 7 groups (see Table 2-4.), namely: Carbonaceous, Na-rich, S-rich, Ca-rich, Al-Si-rich, Metals and a group named "unclassified" where particles of complex mixtures were incorporated.

Chapter 2. Materials and methods

Particle Type	Elemental composition	Main compounds	Possible source
Carbonaceous	C, O, with minor amounts of N, Si, S	Soot, Organics	Incomplete combustion of biomass or fossil fuel from anthropogenic activities, emissions of volatile and semi-volatile organic compounds, industrial activities, road or ship traffic
S- rich	S, N, K, O, with minor amounts of C, Si, Al, Na, Ca, Fe	Ammonium sulphate, Ammonium nitrate, Potassium sulphate	Secondary aerosols formation, Biomass burning for K-rich,
Na-rich	Na, Cl, N, O, with minor amounts of Mg, S, Ca,	Sodium chloride, Sodium nitrates and sulphates, mixed sodium species	Fresh sea salts, aged marine sea-salts when incorporating N and/or S
Ca-rich	Ca, C, N, S, O, with minor amounts of Na, Si, Al, K, Fe	Calcite, gypsum, mixed Ca salts with aluminosilicates or sea salts	Re-suspended soils, road dust or industrial emissions, marine emissions
Si-Al – rich	Si, Al, , with minor amounts of Ca, Fe, K, Mg	Aluminosilicates, Silica, mixed silicates (with Ca salts or Fe oxides)	Resuspended sand or road dust, industrial ashes, non-exhaust road or ship traffic,
Metals	Fe, Mn, Zn, O, with minor amounts of Ti, Si, Al, Ca, K, S, N	Mainly Iron, Mn and zinc oxydes	Metallurgy, steelworks, coal fire plants, chemical plants and/or oil refineries or storages, resuspended dust, non-exhaust road or ship traffic,
Unclassified particles		Mix of different elements in irrespective proportions	Industry or Traffic (mix Ca-rich/Al,Si-rich, calcite/metallic or mix aluminosilicate/metallic)

Table 2-4. Chemical characteristics and possible sources of different types of individual particles.

Chapter 2. Materials and methods

2.3.3. Identified particle types

Carbonaceous particles

Carbonaceous particles were defined as containing C, O, with minor amounts of N, Si, S. They represent 49% of all analysed particles for both the coarse and fine fractions. They can be divided into 2 categories:

- Soot particles are mainly composed of C (80-100%), a minor amount of O (10-20%) (Figure 2-14. b), and sometimes minor amounts of Si, Ca, Al or secondary species such as S and N. They are generally observed as chain-like aggregates of several tens to hundreds of spherical monomers and stable under the electron beam (Adachi and Buseck, 2008; Kazemimanesh et al., 2019). Soot particles are mainly from the incomplete combustion of biomass and fossil fuel (Bond et al., 2013; Niu et al., 2012). Therefore, an important contribution of these particles from transport and industrial sectors can be expected
- Organic matter (OM) represents particles whose elemental abundance of C ranges between 50-80%, with a significant proportion of O (0-50%) (Figure 2-13.a) (Choël et al., 2010; Singh et al., 2021). They can be found internally mixed with minor amounts of other secondary species especially N and S (Figure 2-13. h.) or form carbonaceous aggregates with elements such as Al, Si, Ca, K or some metals as Fe. Several activities can be identified as sources of organic matter, as industrial activities (steelworks, refineries), transport, energy production or solid waste treatment.

Na-Rich particles

The Na-rich group is the second largest particle group accounting for 30% of all the analysed particles. These particles are expected to be sea-salts, due to the coastal location of the GDA. Na-rich particles were defined as those containing Na, Cl, N, O, with minor amounts of Mg, S, Ca (Figure 2-14 c. and g.). Three main types of Na-rich particles were identified in this study. The first type, mainly representing freshly emitted sea-salts, is composed of particles containing Na, Cl and Mg (Figure 2-14. c). The second one is made of partially aged Na-rich particles, composed of Na, Mg, N or S and reduced amount of Cl. The third type, made of Na, N, O or Na, S, O elements, with small amount of Si, Ca, Fe, K and no Cl, is classified as aged sea-salts (Bondy et al., 2017; Young et al., 2016) ; Figure 2-14.g). Partially aged sea-salts are motes of the time heterogeneous particles with sodium- and chloride-

Chapter 2. Materials and methods

rich cores, surrounded by organic enriched surface layers and containing minor amount of magnesium and calcium (Sultana et al., 2017).

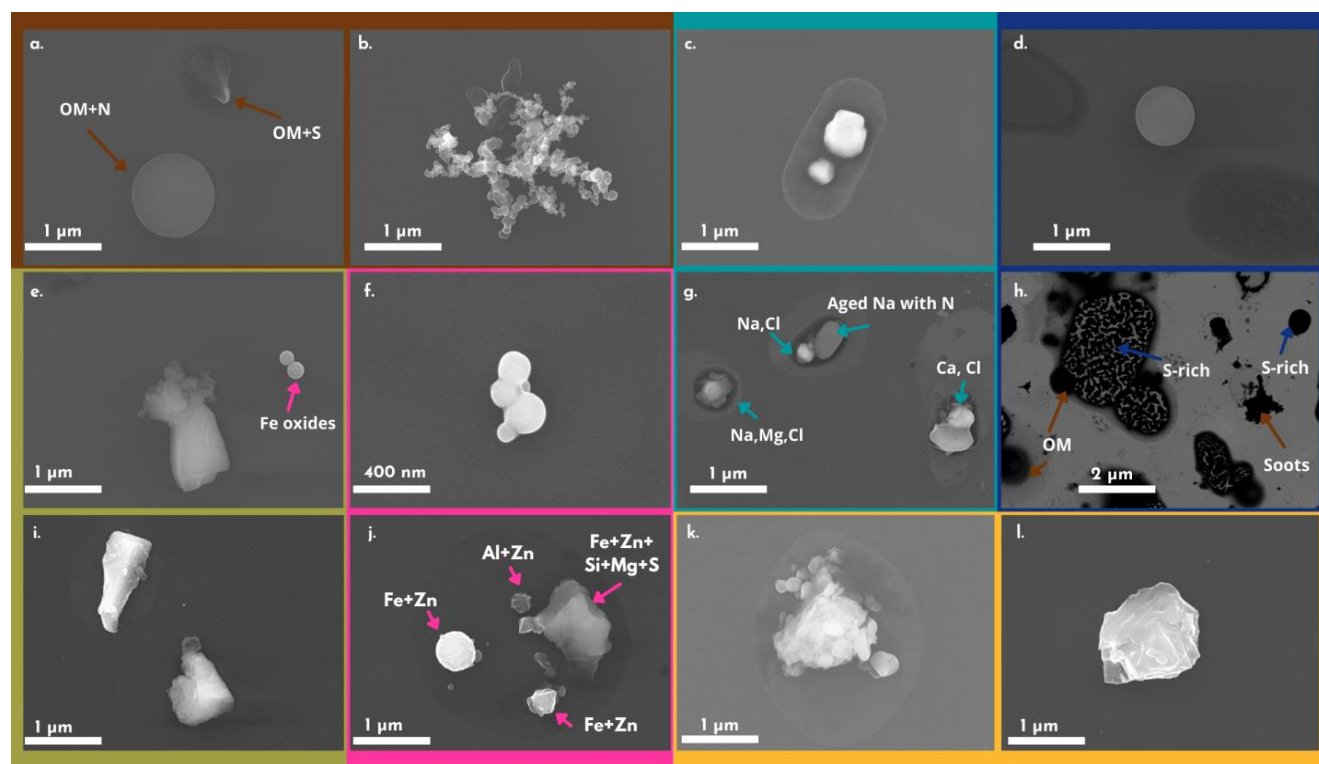


Figure 2-13. SEM images of individual particles collected during the MIXTAPE campaign (a) OM particle coated with N and S, (b) soot particles, (c and g) fresh and aged sea salts particles, (d and h) Ammonium sulphate and internally mixed sulphate particles with OM and soot, (e and i) particles rich in Si, Al, (e, f and j) metal-bearing particles and particularly iron oxides spheres and (k and l) particles mainly composed of Ca.

More than 80% of Na-rich particles were classified as partially or completely aged sea-salts, indicating the degree of processing during transport from the North Sea or the ocean. In coastal regions, Na-rich particles play an important role in tropospheric chemistry, leading to modifications in the trace gas budgets, by acting as a reservoir for oxidized nitrogen and sulphur species. In this study, aged Na-rich particles can be formed by the reaction between fresh sodium chloride and SO_2 and/or NO_x with an industrial origin (Bondy et al., 2017; Xu et al., 2021; Zhang et al., 2021). A recirculation from the continent of aged sea salts, previously formed during the reaction of Na-rich particles with gaseous precursors, is also possible, as evidenced by (Xu et al., 2021) in East Asia. In summary, sea-salts can act, by aging, as a significant source of continental halogen gases (HCl, ClNO_2 , etc.) and as a sink for NO_x/SO_2 oxidation products (AzadiAghdam et al., 2019; Bondy et al., 2017).

Chapter 2. Materials and methods

Metal particles

Metal-rich particles are abundant in polluted air influenced by combustion activities, such as waste incineration, biomass burning and biofuel burning. But the main sources are industrial (chemistry, petrochemistry, metallurgy) or related to transport (non-exhaust road emissions ; ship emissions (Beji et al., 2020; Daellenbach et al., 2020)). Metal particles in the fine and ultrafine particle fraction generally contain a wide range of elements including As, Cd, Cr, Cu, Hg, Mn, Ni, Pb, V, Fe, Zn (Mbengue et al., 2014; Riffault et al., 2015; Siciliano et al., 2021). They are generally found mixed with secondary species such as sulfate, nitrate, and organic matter, either at the exit of the chimneys or during their transport over the urban areas. Fe-rich (Figure 1-8.c), Zn-rich (Figure 1-8.a-d), Pb-rich (Figure 1-8.a-b) and Mn-rich particles were reported to be the main components of metal particles found in atmosphere as hematite (Fe_2O_3) and MnO_2 , ZnO, PbO, and PbSO_4 , beside viscous $\text{Zn}(\text{NO}_3)_2$ and ZnSO_4 (Li et al., 2016).

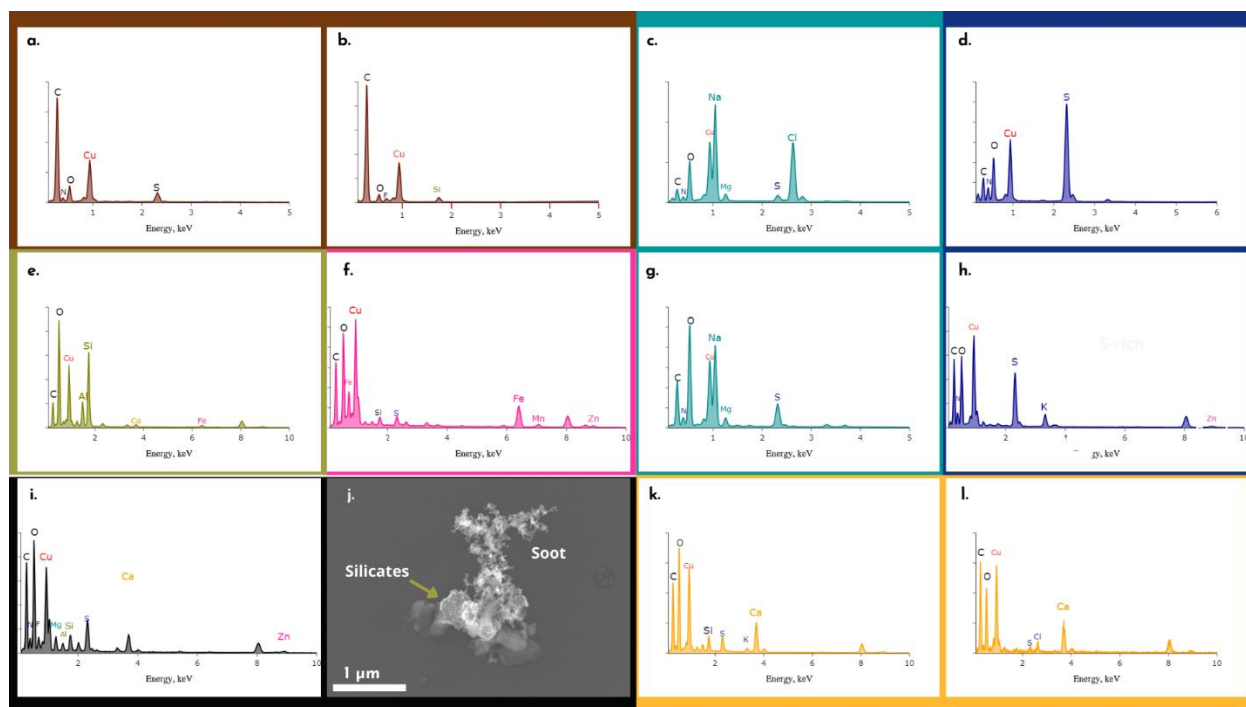


Figure 2-14. mean EDX spectra of the main individual particle types (a and b) Carbonaceous, (c and g) Na-rich, (d and h) S-rich, (e) Si, Al-rich, (f) Metal-rich, (k and l) Ca-rich and (i) Unclassified type. (j) SEM image of the mixed particle composed of soot and silicates. The colours of the spectra are those used to represent each particle in the figures in chapter 5. The Cu-lines are due to the support of the carbon film (Cu-grids).

Chapter 2. Materials and methods

S-rich particles

S-rich particles are defined here as containing S, N, K, O, with minor amounts of C, Si, Al, Na, Ca, Fe and account for 6% of the total analysed particles. S, N and K-rich particles were grouped together and we hypothesise that these S-rich particles (Figure 2-15. d. and h) are mainly in the form of $(\text{NH}_4)_2\text{SO}_4$ and K_2SO_4 . They are generally mixed with OM, aluminosilicates and metal-rich particles containing Si, Al, Fe and Ca. (Figure 2-15.g and h), It's important to mention that they were also found mixed with other particles in the form of sodium or calcium sulphates (Figure 2-15. c,f,k). Due to low proportion of S relative to Na and Ca, they were classified as Na-rich and Ca-rich particles, respectively. Our quantification of species such as NH_4NO_3 is limited by deterioration under the electron beam (Egerton, 2012). $(\text{NH}_4)_2\text{SO}_4$ particles are less volatile and then less sensible to beam damage. They were found in spherical or nearly spherical and irregular shape when coating other particles (Figure 7.d.h.)

Ca-rich particles

Ca-rich particles are mainly composed of Ca, C, N, S, O, with minor amounts of Na, Si, Al, K, Fe (Figure 2-15. k,l). They represent 4 % of the total analysed particles. They are mainly of irregular shape (Figure 2-14. k,l) and stable under the beam irradiation. We assume that they are in the form of Calcite, gypsum and mixed Ca-salts with aluminosilicates or sea-salts. They can result from both anthropogenic and natural sources, mainly from marine emissions. Their occurrence in the atmosphere in the form of gypsum CaSO_4 can be the result of the reaction of marine CaCO_3 with atmospheric sulphur compounds as H_2SO_4 , formed by the oxidation of SO_2 (direct industrial emissions; (Hoornaert et al., 1996). Dust resuspension can also contribute to Ca-rich particles. The industrial sector may also significantly contribute to Ca-rich emissions, especially from metallurgy (CaCO_3 is used as an additive (acid neutralisation agent) in sintering unit dust filters) (Hleis et al., 2013).

Si, Al-rich particles

Si, Al-rich particles were mainly composed of Si, Al, with minor amounts of Ca, Fe, K, Mg (Figure 2-15. e). They represent 3 % of the total analysed particles. They are mainly of irregular shape (Figure 2-14. e and i) and stable under the beam irradiation. The main particles associated with this group are

Chapter 2. Materials and methods

aluminosilicates, Silica, mixed silicates (with Ca salts or Fe oxides) mainly originating from resuspended sand or road dust or industrial ashes.

Unclassified particles

They are defined as particles of complex mixtures of different elements in irrespective proportions that were not associated with any of the types described above and accounted for 1% of all individual particles (Figure 2-15. i,j).

2.4. Computation of the Mixing State Index χ

The determination of χ is based on the method proposed by (Riemer and West, 2013b)(see Chapter 1). The computation of both $(D\alpha)$, $(D\gamma)$ and χ was based on individual particle elemental compositions (atomic percentages) obtained from SEM-EDX analyses, for the 15 major elements: Al, C, Ca, Cl, F, Fe, K, Mg, Mn, N, Na, O, S, Si and Zn.

Before computing $D\alpha$, $D\gamma$ and χ it is necessary to calculate the mass (μ_i) of each individual particle i from its volume v_i and specific mass ρ_i . For this:

- the volume is calculated from the equivalent diameter, deduced from the projected area of the particle (SEM image), considering the particles as spherical.

- the specific mass ρ_i is calculated, for A chemical elements present in the particle (major elements except oxygen being systematically present in the particles and the collection substrate) as follows:

$$\rho_i = \sum_{a=1}^A \text{At. \%} \times \rho_a \quad (2-2)$$

Where “At.%” is the atomic percentage of element a (normalised without oxygen), in the particle i , and ρ_a is the specific mass of the element a in g.cm^{-3} (see Table 2-5).

To determine the specific mass of an element present within the particles, we selected the most abundant solid compound in the atmosphere containing that element. For example, for sulphur, we decided that ammonium sulphate $(\text{NH}_4)_2\text{SO}_4$ is the atmospheric compound that contains almost all of the sulphur within aerosols and then a specific mass of 1.77 g.cm^{-3} was assigned to this element

Chapter 2. Materials and methods

(Table 2-5). For chemical elements associated with several major solid compounds in the atmosphere, the specific mass is obtained by averaging the specific mass of each compound. For example, for sodium, we consider three major solid compounds: sodium nitrate NaNO_3 , sodium chloride NaCl and sodium sulfate Na_2SO_4 . The density assigned to sodium was calculated by averaging the specific mass of these three salts and we obtain 2.36 g.cm^{-3} .

Element	Representative Compound	Specific Mass (g.cm^{-3})	Mean Specific Mass (g.cm^{-3})
Carbon	Soot	1	1
Nitrogen	NH_4NO_3	1.73	1.73
Fluorine	NaF	2.56	2.56
Sodium	NaNO_3	2.26	2.36
	NaCl	2.16	
	Na_2SO_4	2.66	
Magnesium	MgSO_4	2.66	2.81
	MgCO_3	2.96	
Aluminium	Al_2O_3	3.97	3.97
Silicon	SiO_2	2.65	2.65
Sulfur	$(\text{NH}_4)_2\text{SO}_4$	1.77	1.77
Chloride	NaCl	2.16	2.07
Potassium	KCl	1.98	
	K_2O	2.35	
	KCl	1.98	2.28
	KNO_3	2.11	
	K_2SO_4	2.66	
Calcium	CaCO_3	2.71	2.52
	$\text{CaSO}_4 \cdot 2\text{H}_2\text{O}$	2.32	
Manganese	MnO_2	5.03	5.03
Iron	Fe_2O_3	5.24	5.025
	Fe_3O_4	5.17	
Zinc	ZnO	5.61	5.61

Table 2-5. Specific masses of pure compounds used in the calculation of the particle masses

Chapter 2. Materials and methods

The mass μ_i of each particle i is then calculated according to Equation 2-3:

$$\mu_i = \rho_i \times v_i \quad (2-3)$$

ρ_i is here expressed in $\text{pg} \cdot \mu\text{m}^{-3}$ and v_i is the equivalent volume of the particle i in μm^3

The masses μ_i are then summed to calculate the individual particle mass fraction p_i of each particle i in the population of N particles analyzed by SEM-EDX:

$$p_i = \frac{\mu_i}{\mu_{total}} \quad (2-4)$$

With: μ_i mass of particle i in p

μ_{total} : total mass of the population of N particles in pg : $\mu_{total} = \sum_{i=1}^N \mu_i$

The total mass μ_{total} is then used to derive the individual mass fraction p^a of the species a in the population following Equation 2-5.

$$p^a = \frac{\mu^a}{\mu_{total}} \quad (2-5)$$

Where μ^a is the total mass of species a in the population of N particles:

$$\mu^a = \sum_{i=1}^N \mu_i^a \quad (2-6)$$

Considering the important number of particle groups (7) and the number of samples to be analysed (40) we obtain 320 data sets for which we have to compute the mixing state index. In order to reduce the calculation time and the potential errors, the computation has been coded in Python language using the Jupyter Notebook interface (<https://jupyter.org/>). The generated code (available upon request) is then applied to all samples collected during this study.

Chapter 2. Materials and methods

2.5. Other measurements

2.5.1. PM_{2.5} mass concentration

The MP101M analyser (Environment SA) uses the standard Beta gauge method for the measurement of PM_{2.5} mass concentrations. The principle of the technique is based on beta ray attenuation: the particles concentration is determined by measuring the amount of radiation that a sample, collected on a fibre tape, absorbs when exposed to a radioactive source. The absorption is given by an exponential law and is independent of the physical-chemical nature of the particles.

The measurement consists in calculating the absorption ratio between the blank filter, at the start of a measurement cycle and on the charged filter (sample) at the end of the cycle. The mass concentration M_c is calculated by equation 2.7 (Beer-Lambert law):

$$M_c = \frac{10^6 A \cdot \ln(I_0/I)}{\mu \cdot Q \cdot \Delta t} = K \cdot \ln(I_0/I) \quad (2-7)$$

where M_c is in $\mu\text{g}\cdot\text{m}^{-3}$, A is absorption area in cm^2 , I_0 is the incident beta flux, I is the transmitted beta flux, and μ is the mass absorption coefficient in $\text{cm}^2\cdot\text{mg}$. Q is the sampling flow rate in Lpm, Δt is sampling time in minutes, and factor K is a dimensional conversion factor. I_0/I is unitless.

The instrument deployed during this campaign used Radon 222 as the beta source, together with a high performance Geiger-Müller counter as the detector. The sampling port of the instrument is connected to a PM_{2.5} cut-off head (Figure 2-15 B) through a heated sampling tube and operates at a sampling flow rate of $1 \text{ m}\cdot\text{h}^{-1}$. The instrument provides dry PM_{2.5} mass concentrations every 15 minutes.

2.5.2. Aethalometer, SMPS and OPC

These two instruments are located with the MP101M analyser in the campaign shelter and were connected to their own sampling line (Figure 2-16). The latter consists of a PM_{2.5} cut-off head connected to a line made of stainless steel, extended by a Nafion dryer (1.20m long), inside the shelter. The PM_{2.5} head is located approx. 20 meters from ground level and operates at $1 \text{ m}^3\cdot\text{h}^{-1}$ (16.6 Lpm). An additional pump and parallel ports with adapted diameters are used to maintain isokinetic sampling for the two instruments and the TRAPS, when used.

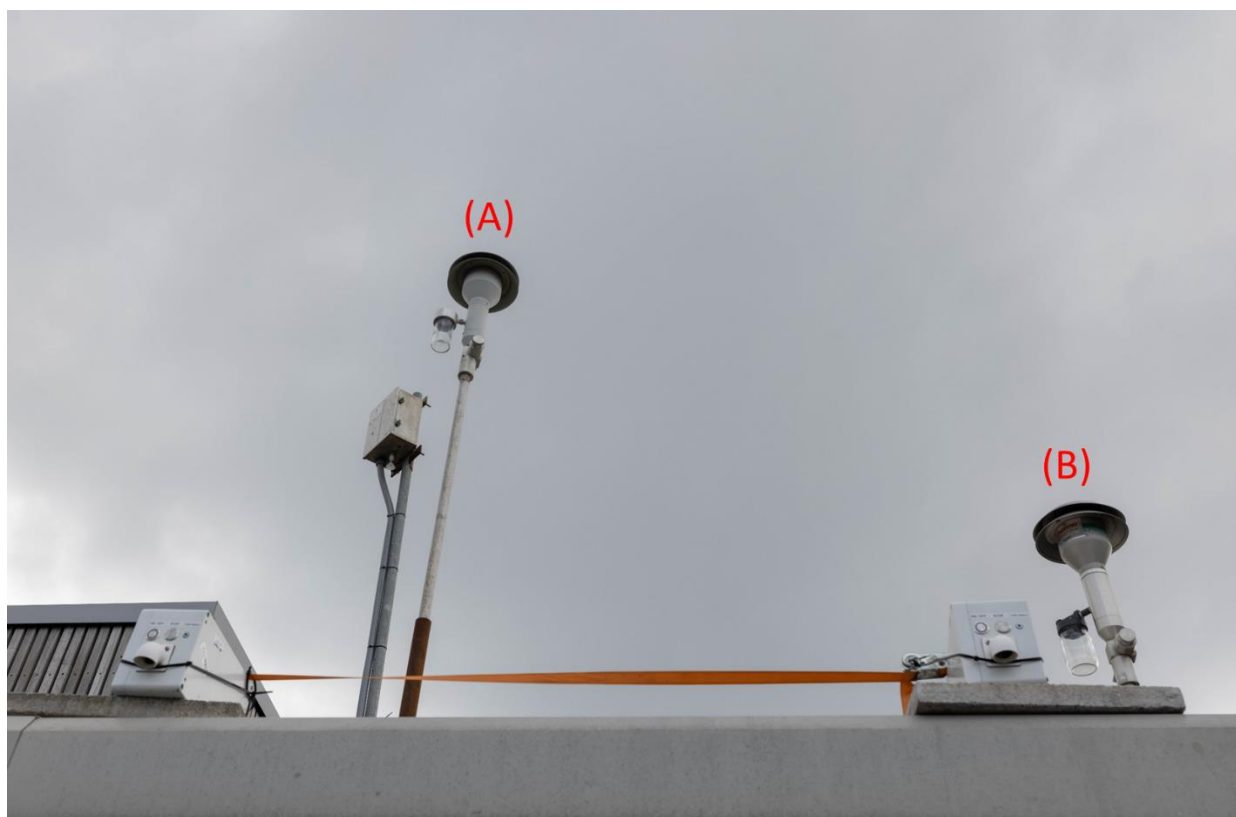


Figure 2-15. External view of the rooftop of the shelter into which the instruments are installed.

*(A) Aethalometer, SMPS, OPC and TRAPS sampling line (left)
(B) : MP101M sampling line (right)*

Aethalometer

The microAeth AE51 (<https://aethlabs.com/>) was used in this study for Black Carbon (BC) measurements. The instrument is based on Aethalometer technology that is widely used to measure light absorbing particles in general and BC measurements in particular. The measurement principle of micro AE51 can be described as follows. An internal pump and mass flow controller draw an air sample onto a filter strip made of Teflon-coated borosilicate glass. A light source emitting at a wavelength of 880 nm illuminates a 3 mm diameter spot on the filter and an optical detector measures the rate of change of attenuation due to the absorbance of transmitted light by particles that are

Chapter 2. Materials and methods

continuously collected on the filter. Black Carbon concentration can thus be derived from Equation 2-8.

$$BC (ng.m^{-3}) = 10^9 \frac{b_{abs}(\lambda)}{\sigma_{air}(\lambda)} \quad (2-8)$$

Where:

$b_{abs}(\lambda)$ is the absorption Coefficient in m^{-1} and $\sigma_{air}(\lambda)$ is the Mass Absorption cross-section (MAC) in $m^2.g^{-1}$. AE51 was deployed only during pollution episodes. It was operated at a sampling flowrate of 150 ml/m^3 providing BC concentrations each 300s. The filter was changed every 2 days in order to avoid sample overload.

SMPS

A SMPS consists in the association of a differential mobility analyser (Figure 2-16) and a condensation particle counter (Figure 2-17) and is used for measurements of the size distribution and concentration of particles in the size range of 2 nm to 1 μm , depending on the model and the manufacturer. The method is based on the ability of a particle to move through an electric field (electrical mobility) in relation to its size. Electrical mobility Z depends on the electric charge and size of a particle, following the Equation 2-9:

$$Z = \frac{V_{TE}}{E} = \frac{qC_c}{3\pi\eta d} \quad (2-9)$$

Where:

Z is the electrical mobility in $m^2/V.s$, V_{TE} is the terminal electrostatic velocity in m/s , E is the electric field strength in V/m , $q = ne$ is the charge of the particle in coulomb, d is the diameter of the particle in and C_c is the Cunningham factor (dimensionless) .

A Differential Mobility Analyser (DMA: Figure 2-16) separates charged aerosol particles according to their mobility in an electric field prior to optical detection by a Condensation Particle Counter (CPC). Atmospheric aerosols are naturally charged, often with multiple elementary charges. These particles

Chapter 2. Materials and methods

are first sampled and mono-charged before being introduced in the DMA electric field, using a stream of beta radiations or X-rays, called “neutralizer”. They are then accelerated by the electric field in the DMA column. By varying the electric field intensity, it is possible to span and measure the integral aerosol size distribution, because only particles having a fixed size (“monodisperse aerosol”) can get out of the analyser and be conducted towards the CPC, for a given electric field.

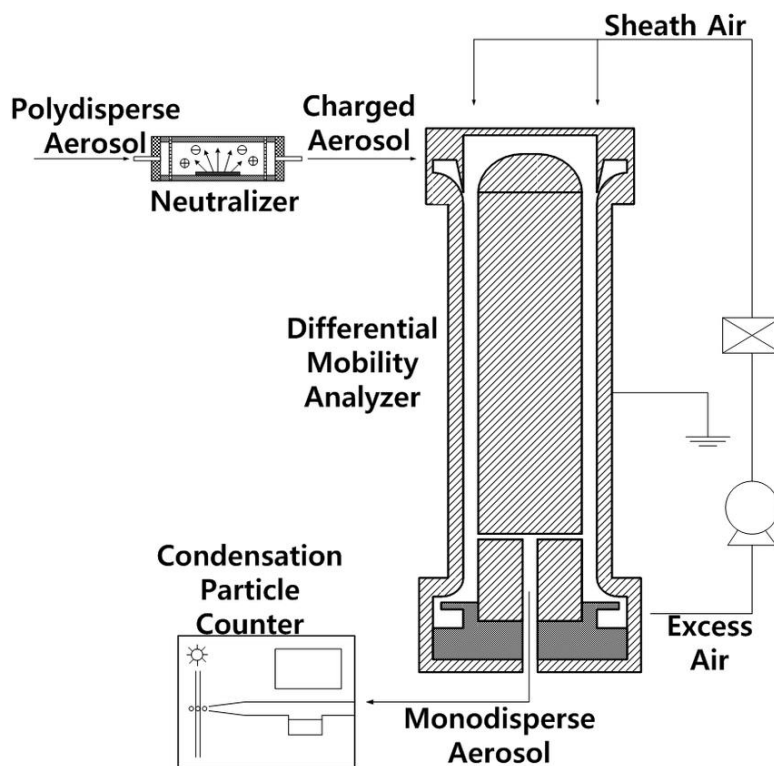


Figure 2-16. Schematic view of a Differential Mobility Analyzer

CPC are widely used to measure the concentration of particles in the range of 2nm to 1 μ m. These instruments work by saturating the carrier gas with vapor and then supersaturating it, in order to cause the condensation of this vapor on the particles. This leads to a growth of the particle to a size of about 10 microns. The CPC counts them by laser scattering, in a very similar way to a standard optical particle counter.

The schematic view of the device used here (Figure 2-17) shows a system where sampled air flows through a warm chamber where it mixes with n-butanol or water (recent CPC models) vapour. A cold condensing chamber, where the alcohol vapor becomes supersaturated and condenses upon the particles allows their detection by optical counting.

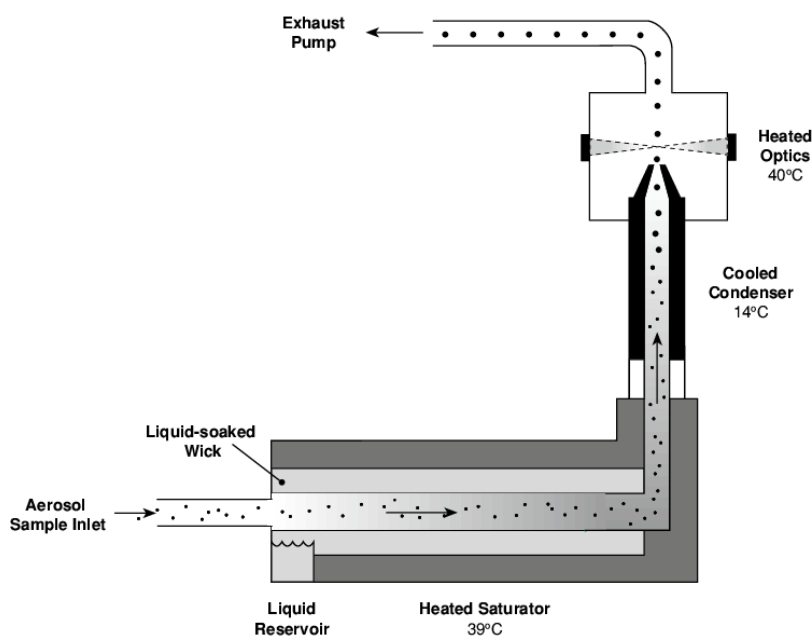


Figure 2-17. Schematic cross-section and operating principle of a Condensation Particle Counter

In this study we used a SMPS Grimm model “SMPS+C” (Grimm Aerosol Technik, Ainring, Germany), featured with a Vienna-type DMA (model 55-900) and a CPC model 5.403. The instrument works at a flow rate of $1.2 \text{ L}\cdot\text{min}^{-1}$ and covers a particle size distribution ranging from 10 to 1000 nm, with a time resolution of 5 min.

A second SMPS (TSI Inc., Shoreview, MN) was used during specific pollution events. It consists in a CPC model 3010, an electrostatic classifier model 3080, and a DMA model 3081, enabling particle counting in the size range 10–760 nm.

For continuous particle size distribution measurements an Optical Particle Counters (OPC) (Mini-Wras were used (measured size range: 20 nm–35 μm in optical diameter).

2.5.3. Meteorology and Atmospheric dynamics

During MIXTAPE local meteorological parameters were measured using a weather station (Davis Instruments, Hayward, CA; model Vantage Pro 2). Wind fields were measured using a scanning wind LIDAR (Windcube WLS 100, Vaisala France, Saclay).

Chapter 2. Materials and methods

This pulsed Doppler Lidar operates at 1543 nm with a repetition rate of 10 kHz and uses a heterodyne technique to measure the Doppler shift of laser radiation backscattered by aerosols. Wind LIDAR provides accurate wind measurement up to 300m, with 20 simultaneous heights measured per second.

In order to see the origin of air masses affecting our study area, the PC Windows-based HYSPLIT model (Stein et al., 2015) was widely used for generating backward trajectories to evaluate potential sources for LRT. The Global Data Assimilation System (GDAS) was used as weather input to the HYSPLIT model. 72-h backward trajectories arriving at 500 m and 1000 m above ground level in the GDA were computed.

CHAPTER 3.
METHODOLOGY OF PHYSICO-
CHEMICAL CHARACTERIZATION
OF ATMOSPHERIC PARTICLES

3. Methodology of physico-chemical characterization of atmospheric particles

The aim of this chapter is to demonstrate the suitability of a Time-Resolved Atmospheric Particles Sampler (TRAPS) for single coarse and fine particle characterization, with high time-resolved sampling, throughout PM_{2.5} pollution episodes. The first part of the chapter focuses on a state of art of available sequential cascade impactors in the literature. In the section 2, a description of the TRAPS and the theoretical considerations during its design is done. The third part presents the methodology and experimental setups used for the determination of its size segregation characteristics. The fourth part presents the results, including cut-off diameters, of ambient and laboratory particle deposition pattern experiments and outcomes, and demonstrating the reliability of the time-resolved sampling. In the last part, we present a case study in which the TRAPS is implemented at a multi-influenced site during a PM_{2.5} pollution event.

This chapter correspond to the article “Development and Characterization of a Time-Sequenced Cascade Impactor: Application to Transient PM_{2.5} Pollution Events in Urbanized and Industrialized Environments”, by Soulemane Halif Ngagine, Karine Deboudt, Pascal Flament, Marie Choël, Pierre Kulinski and Fabien Marteel, published in *Atmosphere*, 2022, 13(2), 244.

3.1. Time-resolved cascade impactors in the literature

Air pollution has been identified as the greatest environmental cause of premature deaths, with seven million deaths per year worldwide due to the direct or indirect effects of exposure to air pollutants (WHO, 2021). Among these pollutants, particulate matter (PM) has the greatest health impact (Kim et al., 2015) particularly PM_{2.5} and PM₁ because of their ability to penetrate the deeper regions of the respiratory tract (Atkinson et al., 2015; Seinfeld and Pandis, 2016; WHO, 2021). Although air quality has significantly been improved in high-income countries, PM_{2.5} exceedances are frequent in large European cities, and a disparity in exposure between highly industrialized/urbanized cities and rural areas is observed (WHO, 2021). This leads us to question the sources of these disparities and, in particular, those responsible for exceeding the regulatory thresholds, especially in urban areas. Most of the source assessment or health impact studies in this respect are based on long-term sampling (typically 24 h), in order to have sufficient quantities of material to be able to perform a chemical characterization as complete as possible, and thus obtain indications on the predominant sources of particulate matter.

Chapter 3. Methodology of Physico-chemical characterization of particles

In doing so, essential information on the dynamics of threshold exceedances is lost, such as those resulting from day/night cycles (Reizer et al., 2021), hence the interest in shorter sampling to assess aerosol composition and sources variabilities (Rai et al., 2021). The difficulty related to the smaller number of particles collected in shorter sampling times (e.g., less than 1 h) can be overcome by using individual particle analysis techniques, such as SEM-EDX (Marris et al., 2012).

Online instrumentation such as Aerosol Mass Spectrometers (AMS) and Aerosol Chemical Speciation Monitors (ACSM) are well suited for air pollutant monitoring, when dealing with long-term measurements at a specific location. However, increasing the spatio-temporal coverage of the monitoring requires more measurement sites and therefore the implementation of less expensive instruments that are quickly and easily operational. When coupled with individual particle analysis techniques, such as SEM-EDX, cascade impactors appear particularly well suited. They can indeed allow short sampling, providing information on the size, morphology and chemical composition of particles (Bzdek et al., 2012; W. Li et al., 2016).

For this, it seems relevant to have a system where the particle collection substrate can be changed very quickly, to carry out successive samplings in a limited, according to the evolution of the meteorological conditions and the dynamics of the boundary layer (Bukowiecki et al., 2008). One of the most suitable solutions is to use a system that automatically switches the particle collection substrate/surface, such as a rotary plate impactor.

To our knowledge, there are two types of commercial cascade impactors able to provide time-resolved and size-segregated aerosol samples: generations of DRUM Impactors (Cahill et al., 1987; Raabe et al., 1988) and Streaker samplers (PIXE InternationalTM) (Annegarn et al., 1988). The Rotative DRUM Impactor (RDI) (Figure 3-1.) is a modified version of a 3-stage DRUM in which rotating wheels were implemented. The sampling flowrate is 16.7 L per minute (Lpm) and the rectangular nozzle of each stage is 10 mm in length and of variable width: 1.52 mm, 0.68 mm and 0.30 mm, corresponding to cut-off diameters of 2.5, 1.0 and 0.1 μm , respectively (Bukowiecki et al., 2009). The RDI wheels (Figure 3-1), replacing the collection plates, have been specifically designed for Synchrotron Radiation-Induced X-Ray Fluorescence (SR-XRF) analysis of uninterrupted aerosol samples, at adjustable sampling durations (generally 1 h), within a sampling period ranging from days to weeks. The films on the wheels are kept consolidated in order to preserve time-resolved information, thus limiting the possibility of sample analyses to only techniques and instruments suitable to analyse the entire film/wheels (Bukowiecki et al., 2008).

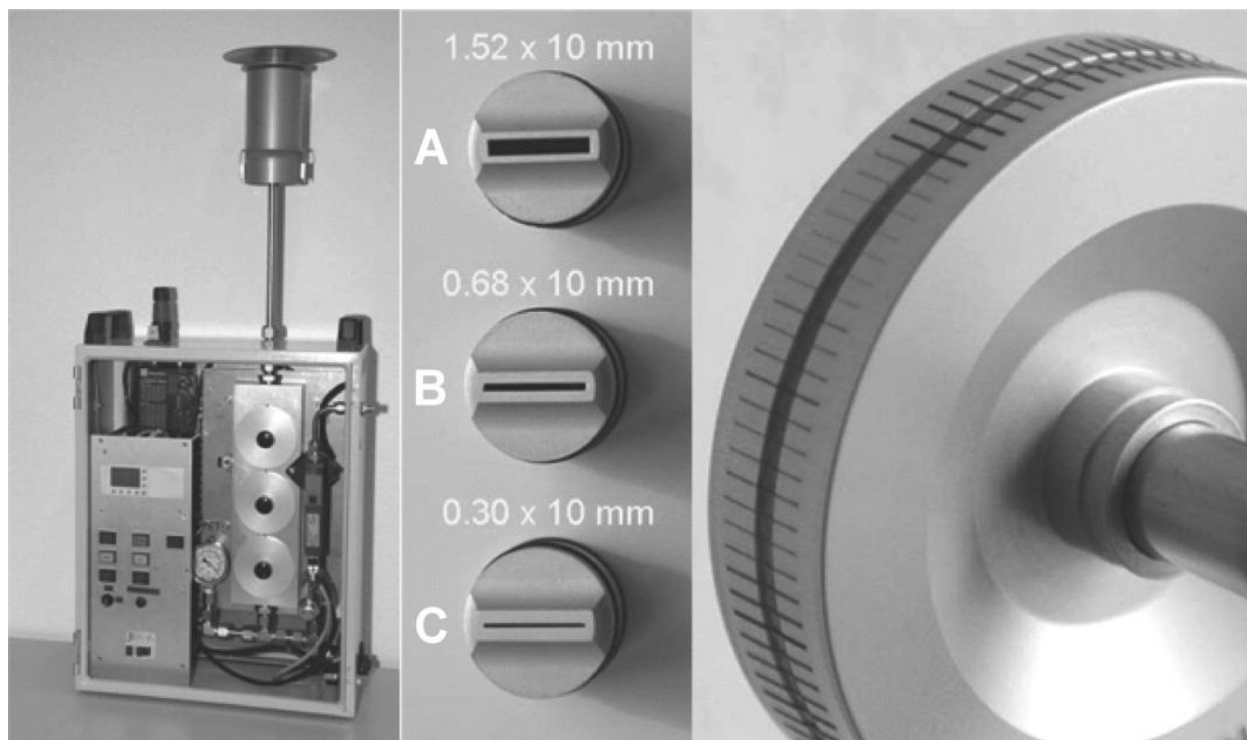


Figure 3-1. Rotating drum impactor (RDI) with PM10 inlet (left picture), nozzles for RDI stages A–C (middle), RDI sampling wheel with a stage C (0.1–1 μm) sample (right picture) (Bukowiecki et al., 2009)

Unlike the RDI, the Streaker sampler (Figure 3-2) uses a collection plate fixed onto a motor instead of a rotating wheel. It is an instrument which allows collection by impaction, on a rotating film substrate, of particles of the coarse fraction (2.5–10 μm), and by filtration of the entirety of the particles whose aerodynamic diameter is below 2.5 μm . The sampling rate is 1 Lpm. The sampling time, adjustable from a few minutes to a few hours, allows the collection of particles on the same substrate over periods of several days or even weeks.

This functionality makes it suitable for long-term continuous observation of particle composition, obtained from a wide range of Ion Beam Analysis (IBA) techniques, such as Particle-induced X-ray emission spectrometry (PIXE) (D'Alessandro et al., 2004; Formenti et al., 1996). The main drawback of the Streaker is that it does not allow a precise aerodynamic separation of the particles from the fine fraction (below 2.5 μm) which are the most abundant in number; this justifies the need for an instrument with this characteristic.

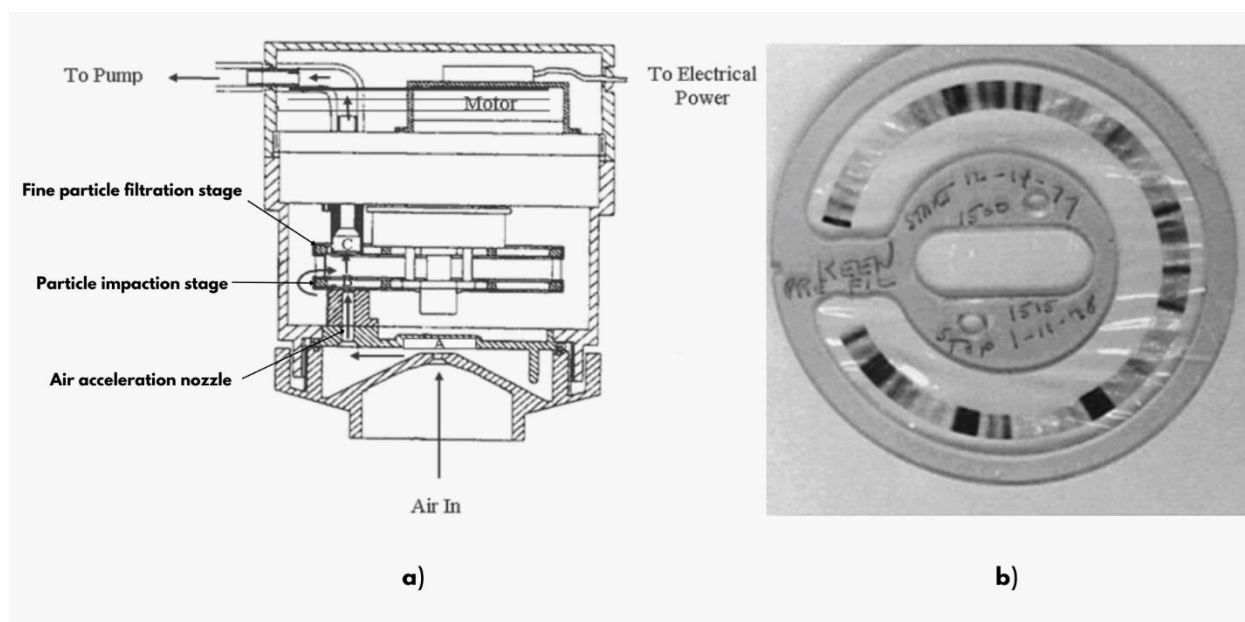


Figure 3-2. Working principle of the Streaker (a) and a view of a typical particles sample on a 82 mm polycarbonate membrane with streaks readily visible (b) (<http://www.pixeintl.com/Streaker.asp>)

The TSI MOUDI II is an aerosol sampling system mainly composed of two parts: the 8-stage cascade impactor and the rotation system (Rotator) inside which the impactor is installed (Marple et al., 1991). A sampling flow rate of 30 Lpm is passed through a nozzle system, whose number per impaction stage increases with the decrease in the nominal cut-off diameter. It goes from three nozzles in stage 1 for a D_{p50} of 10 μm to 2000 nozzles for a D_{p50} of 0.056 μm . Thanks to the combined use of rotating impaction plates and multiple nozzles, a uniform deposition of particles on substrates, with diameters varying between 2.7 and 2.8 cm, is ensured for each impaction stage. Contrary to the RDI and Streaker, the rotation of the MOUDI plate does not allow the collection of individual and time-resolved impaction traces, which is one of the objectives of the TRAPS.

In addition, one of the main drawbacks of the RDI and the Streaker resides in the fact that the user cannot purposely define the sampling substrate or use commercial substrates (TEM grids, polycarbonate membranes, etc.) available on the market. In this context, we developed a cascade impactor, the TRAPS, standing for Time-Resolved Atmospheric Particle Sampler. It is a non-commercial (homemade) instrument, designed for the collection of coarse (1–10 μm) and fine (0.1–1 μm) particles; its aim is qualitative characterization, using a wide range of single-particle analysis techniques, such as SEM-EDX or Micro-Raman Spectroscopy.

Chapter 3. Methodology of Physico-chemical characterization of particles

Samples can be collected on commercial membranes, such as polycarbonate membranes and/or simultaneously on TEM grids. Unlike the Streaker, a more precise size segregation of coarse and fine PM is enabled. Unlike the RDI, the collection of several and discrete impaction traces, on a user-selectable substrate, is possible. In addition, the user can select the sampling time, can adjust the per-sampling duration, and the air flow is cut during the non-sampling periods between two consecutive traces, to avoid any change in the morphology and chemical composition of previously collected particles.

The TRAPS can, therefore, be operated in a semi-continuous sampling mode when necessary. This feature provides the TRAPS with the advantage of limiting the sampling artefacts associated with the chemical evolution of the samples and the loss of semi-volatile species occurring during long sampling times, due to the passage of the air stream over the particles. This highlights the specificity of the TRAPS in monitoring and discriminating aerosols throughout transient atmospheric events. Furthermore, the development of the TRAPS offers the advantage of easy deployment in the field, for complementary use with online instruments for continuous analysis of individual particles' physico-chemical composition for example, AMS, ACSM, optical particle counter (OPC) and scanning mobility particle sizer (SMPS).

3.2. Description and Theoretical Considerations

3.2.1. Description of the TRAPS

The TRAPS is a single jet cascade impactor with two stages on which the collection plate is mounted on a motor for rotation (Figure 3-3. a). Its full size is 10.2 cm by 35 cm, with an approximate weight of 6.75 kg. It is made of stainless steel to minimize contamination due to metal corrosion and electrostatic attraction.

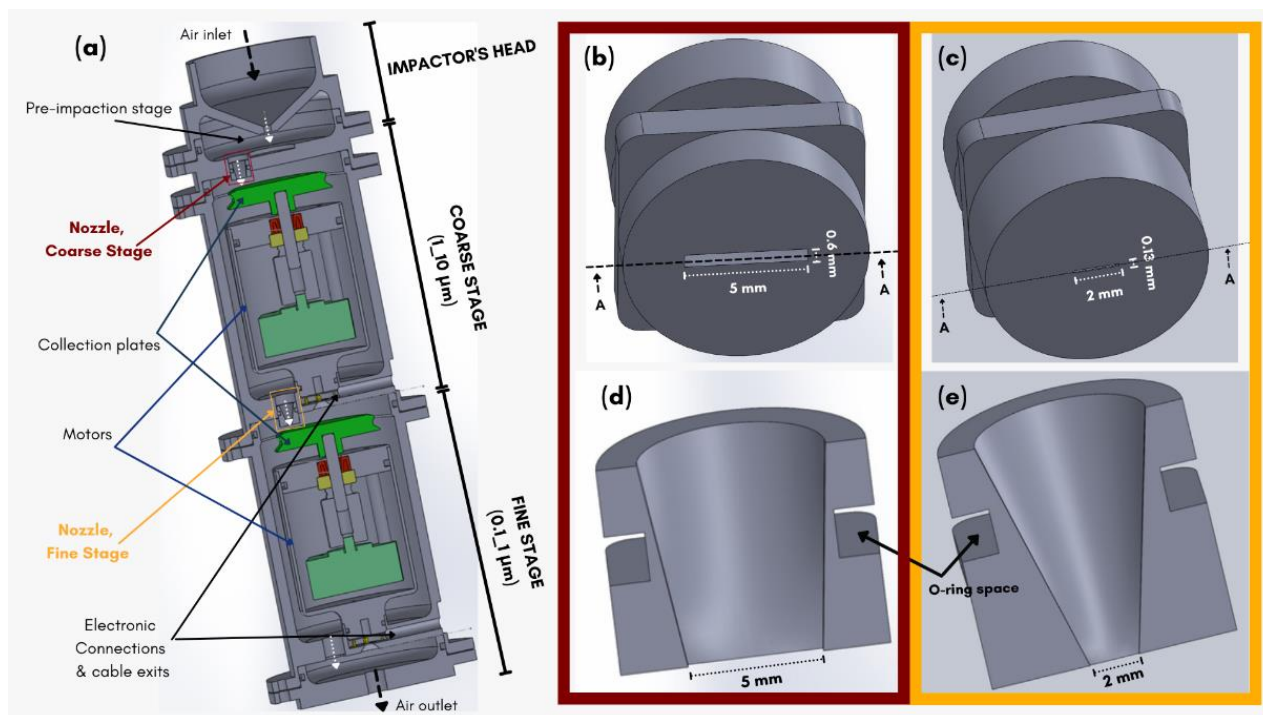


Figure 3-3. Internal view of the TRAPS impactor (a) and scheme of the acceleration nozzles with their dimensions and internal views (A-A cross-sectional drawing), for the coarse (b,d) and fine (c,e) stages.

All of the parts and a fully assembled TRAPS are shown in Figure 3-4-a and -b. The corresponding names, together with technical characteristics, are presented in Table 3-1.

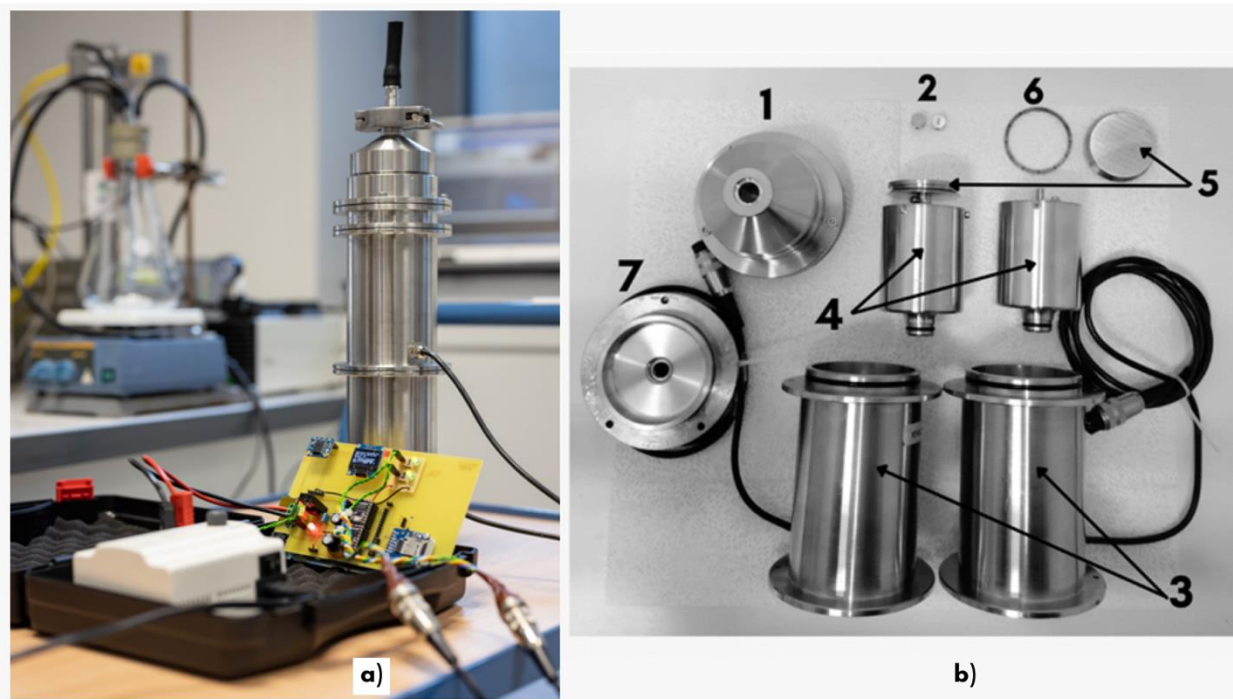


Figure 3-4. Photographs of (a) the fully assembled TRAPS and its command board, (b) TRAPS parts (credit photo: Marc Fourmentin)

Chapter 3. Methodology of Physico-chemical characterization of particles

Name	TRAPS for Time Resolved Atmospheric Particle Sampler
Weight	6.75 kg
Dimensions (d × h)	10.2 × 35 cm
Sample flow	5 L/min
Sampling range	Fine (PM _{0.1-1}) and Coarse mode particles (PM ₁₋₁₀)
Sampling duration	Adjustable (minute, hour, day)
Rotation angle	28.8° (enables the collection of maximum 12 samples/plate)
Sampling substrate	Whatman Nuclepore™ (or equivalent) track-etched polycarbonate membranes (47 mm diameter and 0.015 µm pore size) or TEM grids
Pump type	KNF Laboport N816.18
Parts of the device (see Figure S1.)	<ul style="list-style-type: none"> • Preimpaction head (Air inlet) (1) • 2 rectangular nozzles: PM₁₋₁₀ and PM_{0.1-1} (2) • 2 cylindrical blocks (3) (supporting the motors) (4) • 2 collection plates with their 50 mm diameter clips (5) • Cover (air outlet) (6)

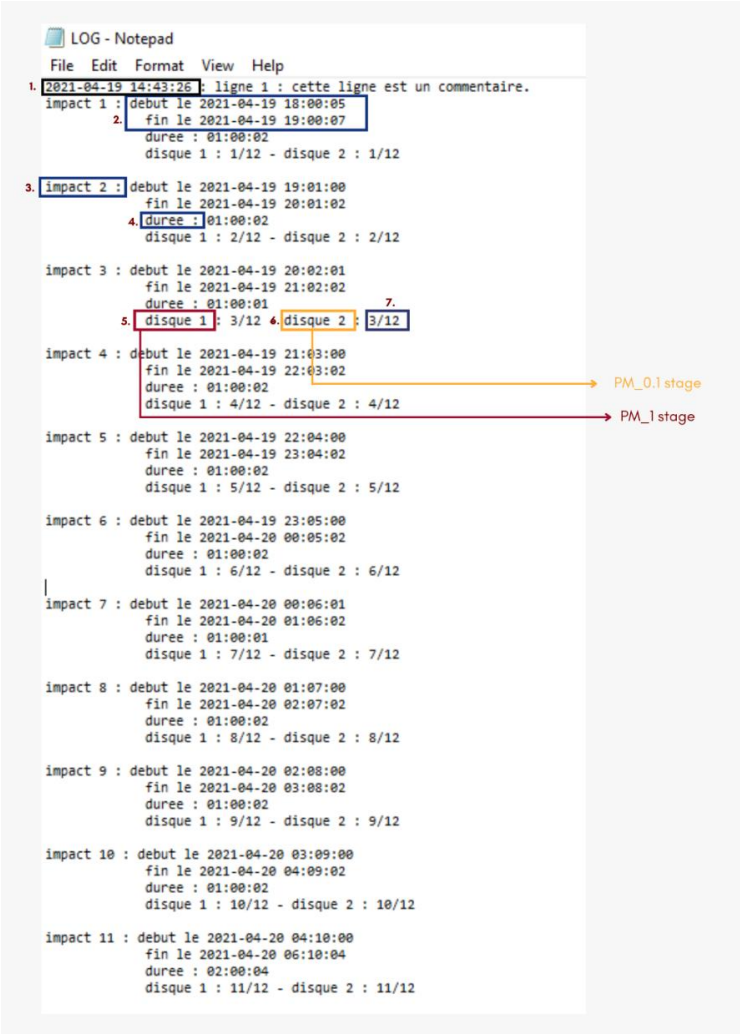
Table 3-1. Technical characteristics of the TRAPS.

The pre-impaction stage, located inside the impactor head, is designed to trap particles of specific mass $1 \text{ g}\cdot\text{cm}^{-3}$, with a 50% collection efficiency for an aerodynamic cut-off diameter of $10 \text{ }\mu\text{m}$ (PM₁₀ head). Each stage is equipped with a single rectangular-shaped acceleration nozzle, with dimensions theoretically adapted to the collection of particles in the size range 0.1 to $1.0 \text{ }\mu\text{m}$ (Figure

Chapter 3. Methodology of Physico-chemical characterization of particles

3-3. b–e) see Section 2.2. Each collection plate can be equipped with a circular commercial membrane (47 mm diam.). A stable sampling flowrate of 5 Lpm is provided by a pump connected at the air outlet (KNF, model Laboport N816.18).

The TRAPS can be used either: (1) in a single impaction mode where all particles are collected on the same trace, with no stage rotation or (2) in a rotating mode, where up to 12 samples can be collected at discrete positions without sample overlap on the same substrate (Figure 2-9). The rotation angle of the TRAPS collection plate is fixed at 28.8° (please refer to the SM for the determination of the rotation angle). The collection of particles can be performed directly on the 47 mm diameter membrane, or on 3 mm TEM grids fixed on it when the study requires transmission microscopy. In this last case, a maximum of 12 TEM grids can be positioned on the impaction plate, according to the stop position of the motor (Figure 2-9).



```
LOG - Notepad
File Edit Format View Help
1. 2021-04-19 14:43:26 : ligne 1 : cette ligne est un commentaire.
impact 1 : debut le 2021-04-19 18:00:05
2. fin le 2021-04-19 19:00:07
duree : 01:00:02
disque 1 : 1/12 - disque 2 : 1/12

3. impact 2 : debut le 2021-04-19 19:01:00
fin le 2021-04-19 20:01:02
4. duree : 01:00:02
disque 1 : 2/12 - disque 2 : 2/12

impact 3 : debut le 2021-04-19 20:02:01
fin le 2021-04-19 21:02:02
duree : 01:00:01
5. disque 1 : 3/12 6. disque 2 : 3/12 7.

impact 4 : debut le 2021-04-19 21:03:00
fin le 2021-04-19 22:03:02
duree : 01:00:02
disque 1 : 4/12 - disque 2 : 4/12
PM_0.1 stage
PM_1 stage

impact 5 : debut le 2021-04-19 22:04:00
fin le 2021-04-19 23:04:02
duree : 01:00:02
disque 1 : 5/12 - disque 2 : 5/12

impact 6 : debut le 2021-04-19 23:05:00
fin le 2021-04-20 00:05:02
duree : 01:00:02
disque 1 : 6/12 - disque 2 : 6/12

|
impact 7 : debut le 2021-04-20 00:06:01
fin le 2021-04-20 01:06:02
duree : 01:00:01
disque 1 : 7/12 - disque 2 : 7/12

impact 8 : debut le 2021-04-20 01:07:00
fin le 2021-04-20 02:07:02
duree : 01:00:02
disque 1 : 8/12 - disque 2 : 8/12

impact 9 : debut le 2021-04-20 02:08:00
fin le 2021-04-20 03:08:02
duree : 01:00:02
disque 1 : 9/12 - disque 2 : 9/12

impact 10 : debut le 2021-04-20 03:09:00
fin le 2021-04-20 04:09:02
duree : 01:00:02
disque 1 : 10/12 - disque 2 : 10/12

impact 11 : debut le 2021-04-20 04:10:00
fin le 2021-04-20 06:10:04
duree : 02:00:04
disque 1 : 11/12 - disque 2 : 11/12
```

Figure 3-5. Output file extracted at the end of each TRAPS sampling series. Main information in the colored frames include: 1. date and time of the introduction of the SD card in the command board; 2. sample's (impact)

Chapter 3. Methodology of Physico-chemical characterization of particles

start and end date and time; 3. sample number; 4. sampling duration; 5. rotation of the PM1 stage; 6. rotation of the fine stage; 7. example of the 3rd out of 12 possible samples.

The positioning of the grids takes into account the stationary position of the nozzle and the clockwise rotation of the impaction plate. After each rotation, a grid is precisely located under the nozzle outlet. An example of TEM grids attached to a polycarbonate membrane is shown in Figure 2-9. The rotation of the collection plates is piloted from a control panel consisting of a microcontroller ATmega2560 chip (Figure 3-4. a), using an Arduino Mega board, that provides enough input and output pins to drive the two TRAPS motors. It can also display important information on an OLED technology screen, using a real time clock module. A micro-SD card is used to communicate with the TRAPS and simultaneously store information such as the start and end time of the sampling or the rotation angle (an example of output file is presented in Figure 3-5).

3.2.2. Theoretical Calculations and TRAPS Design

The flow regime during impaction is defined by the Reynolds number (Re —equation (3-1)) of the fluid (dimensionless), which represents the ratio between the inertial forces (due to the mass of gases present in the air) and the viscosity forces that characterize the resistance to the airflow.

$$Re = \frac{\rho \cdot U \cdot d}{\eta} \quad (3-1)$$

where ρ is the specific mass of air ($1.205 \text{ kg}\cdot\text{m}^{-3}$ at 293 K), U is the air velocity inside the impaction nozzle ($\text{m}\cdot\text{s}^{-1}$), d is the impaction nozzle “equivalent diameter” and η is the dynamic viscosity of air ($1.806 \cdot 10^{-5} \text{ Pa}\cdot\text{s}$ at 293 K). All the values used for Reynolds number calculations are reported in Table 1. In order for the impaction traces to be distinctly separated on the collection surface, we opted for rectangular acceleration nozzles, without any impact on the Reynolds number values.

Chapter 3. Methodology of Physico-chemical characterization of particles

	Coarse Stage	Fine Stage
Nozzle Equivalent Diameter (mm)	1.940	0.564
Cut-off diameter (μm) for $\rho_p=1.80 \text{ g.cm}^{-3}$	1.30	0.15
Air flow rate (L.m^{-1})	5.00	5.00
Air velocity inside the impaction nozzle (m.s^{-1})	28	333
Jet to plate distance ratio (S/W)	2.56	5.32
Nozzle Reynolds number	3450	12,420
Slip correction factor	1.12	2.25
Stokes number (Stk)	0.30	0.31

Table 3-2. Theoretical calculations of the stage parameters of the TRAPS at $T = 293\text{K}$ and $p = 101.3 \text{ kPa}$.

Using Equation (1), Re values of 3540 and 12,420 are obtained, respectively, for the coarse and fine impaction stages. With $Re > 3000$, the flow regime inside the TRAPS has to be considered turbulent. In the case of turbulent flows, Pui et al. [(Pui et al., 1987)] empirically demonstrated that the transport efficiency T of a particle following a curvilinear motion making an angle $\varphi = \pi/2$ rad (90°) with the principal direction of the flow can be calculated following Equation (3-2):

$$T = 10^{-0.963Stk} \quad (3-2)$$

where Stk is the Stokes number, which represents the ratio between the kinetic energy of a particle suspended in a fluid (here the ambient air) and the energy dissipated by friction with the fluid. If the particle kinetic energy is very high ($Stk \gg 1$), it will easily leave the flow lines while approaching the collection surface (inertial regime). On the other hand, if the particle kinetic energy is dissipated by friction ($Stk \ll 1$), the particle will then follow the flow lines regardless of the fluid direction (viscous regime). Stk is calculated by Equation (3-3):

$$Stk = \frac{U \cdot \rho_p \cdot C}{9\eta} \times \frac{D_p^2}{d} \quad (3-3)$$

where ρ_p is the particle density, C is the Cunningham slip factor (which is dimensionless and depends on particle size and pressure (Marple and Willeke, 1976)), D_p is the aerodynamic diameter

Chapter 3. Methodology of Physico-chemical characterization of particles

of the particle (m) and U , η , and d are the same as in Equation (1). All of the values used for Stokes number calculations are reported in Table 3-2.

The central point in the design of the TRAPS is the determination of the diameters of the acceleration nozzles, allowing fixation of the median size (“cut-off” diameter) of the particles collected on a given impaction stage. As the TRAPS is specifically designed to study pollution aerosols, we have chosen median sizes of 1 μm for the coarse stage and 0.1 μm for the fine stage, as the majority of pollution aerosols are submicronic.

In the field of cascade impaction, the median size of the collected particles is defined as the aerodynamic diameter of particles collected with 50% efficiency (D_{p50}), i.e., the equivalent diameter of a sphere of given specific mass, having the same final impaction velocity as the studied particles, with 50% collection efficiency. Calibrated silica particles ($\rho_p = 1.80 \text{ g}\cdot\text{cm}^{-3}$) were used to experimentally determine D_{p50} and compare it with theoretical values reported in Table 3-2. According to impaction dynamic equations detailed above, the AeroCalc[®] software (Baron, 2006) was used to calculate the evolution of the theoretical collection efficiency as a function of particle aerodynamic diameters and to determine the 50% efficiency cut-off diameter for silica particles (Table 3-2).

3.3. Materials and Methods

3.3.1. Experimental Setups for Laboratory Experiments

Experimental determination of the particle collection efficiencies of the coarse and fine stages of the TRAPS was performed with a setup divided into two parts: an aerosol generation part and an aerosol sampling and measurement part.

For the characterization of the fine stage, aerosol particles were generated by nebulizing a water-based solution in which the studied particles were suspended. The setup (Figure 3-6) consisted of a constant output atomizer (model 3076, TSI Inc., Shoreview, MN, USA) used in recirculation mode and at a back pressure of 2 bars (Stabile et al., 2013). A solution was obtained by introducing 50 mg of monodispersed silica spheres (Angström Sphere[™], <https://focenter.com/> or <https://nanocym.com/> (accessed on 20/01/2020)) into 600 mL of ultrapure water ($\rho = 18.2 \text{ M}\Omega\cdot\text{cm}^{-1}$). The particle sizes considered were 0.05, 0.08, 0.1, 0.25, 0.5 and 0.75 μm (relative standard deviations of less than 10%).

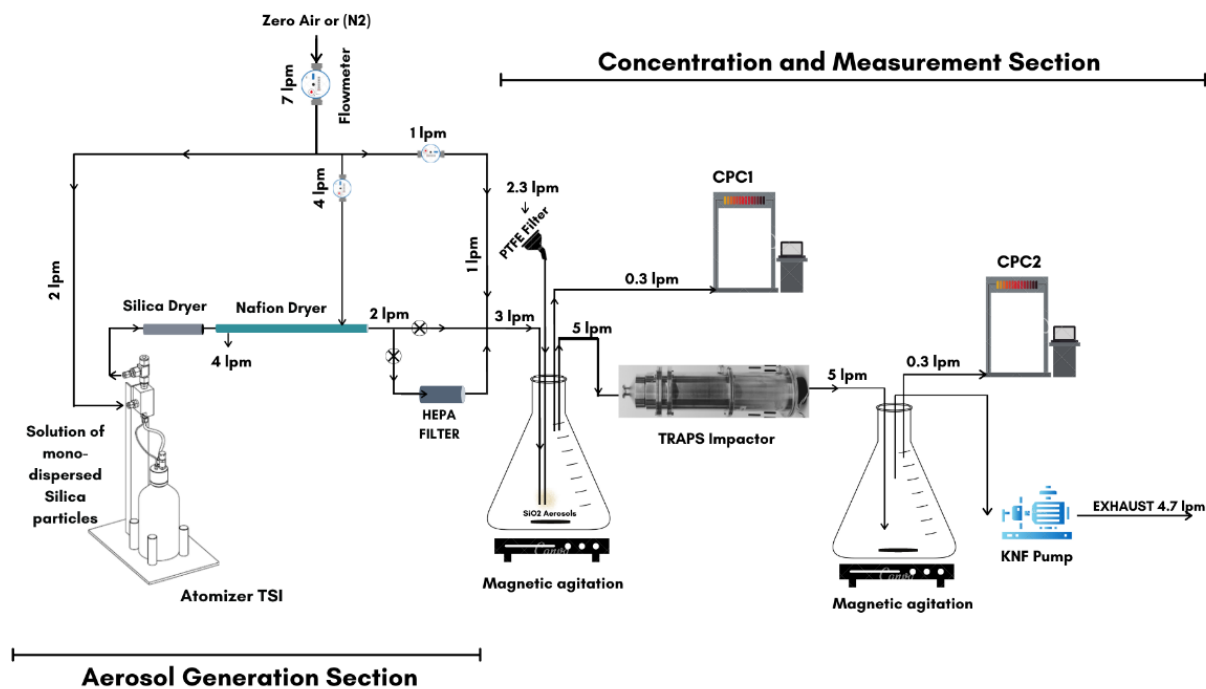


Figure 3-6. Schematic view of the experimental setup for determining the fine stage collection efficiency using nebulized monodisperse silica spheres.

The solution was sonicated for 5 min to minimize particle aggregation. After generation, the obtained wet aerosol was dried using a 30 cm-long tube, containing silica gel, followed by a 120 cm-long membrane dryer (NafionTM, www.permapure.com (accessed on 11/09/2019)). These dryers decreased the relative humidity to less than 20%, which provided silica particles with nearly the size specified by the manufacturer.

The output particle concentration was adjusted to the required value (4000–8000 #.cm⁻³) by using a dilution flow of dry air (or N₂) and, if necessary, by passing a part of the flow through a HEPA filter. The obtained aerosol was introduced in the “concentration and measurement” part of the setup. In this part, a 1 L flask was first connected to a Condensation Particle Counter (CPC1) (model 3775, TSI Inc.) installed upstream, and another 1 L flask was connected to a second particle counter (CPC2) (model Nano 5410, GrimmTM) (Figure 3-6.) downstream of the impactor. To ensure a constant particle concentration throughout the experiment, two magnetic agitators were permanently rotating at a constant speed (600–800 rpm) in both flasks.

Chapter 3. Methodology of Physico-chemical characterization of particles

The constancy of this concentration was checked for 10 min at the beginning of each experiment, upstream of the TRAPS. Flow balance was achieved by introducing 2.3 Lpm of ambient air through the HEPA filter. The total number concentration of particles generated was monitored upstream by the particle counter CPC1 and downstream by the particle counter CPC2, both operating at a low flow mode of 0.3 Lpm. The two CPCs were tested in parallel prior to experiments to allow direct comparison between them (see Annex, Figure A-1.). Finally, the pump ran at 4.7 Lpm to ensure a total constant sampling flowrate inside the TRAPS of 5 Lpm. An image of the experimental set-up is shown in Figure 3-7.

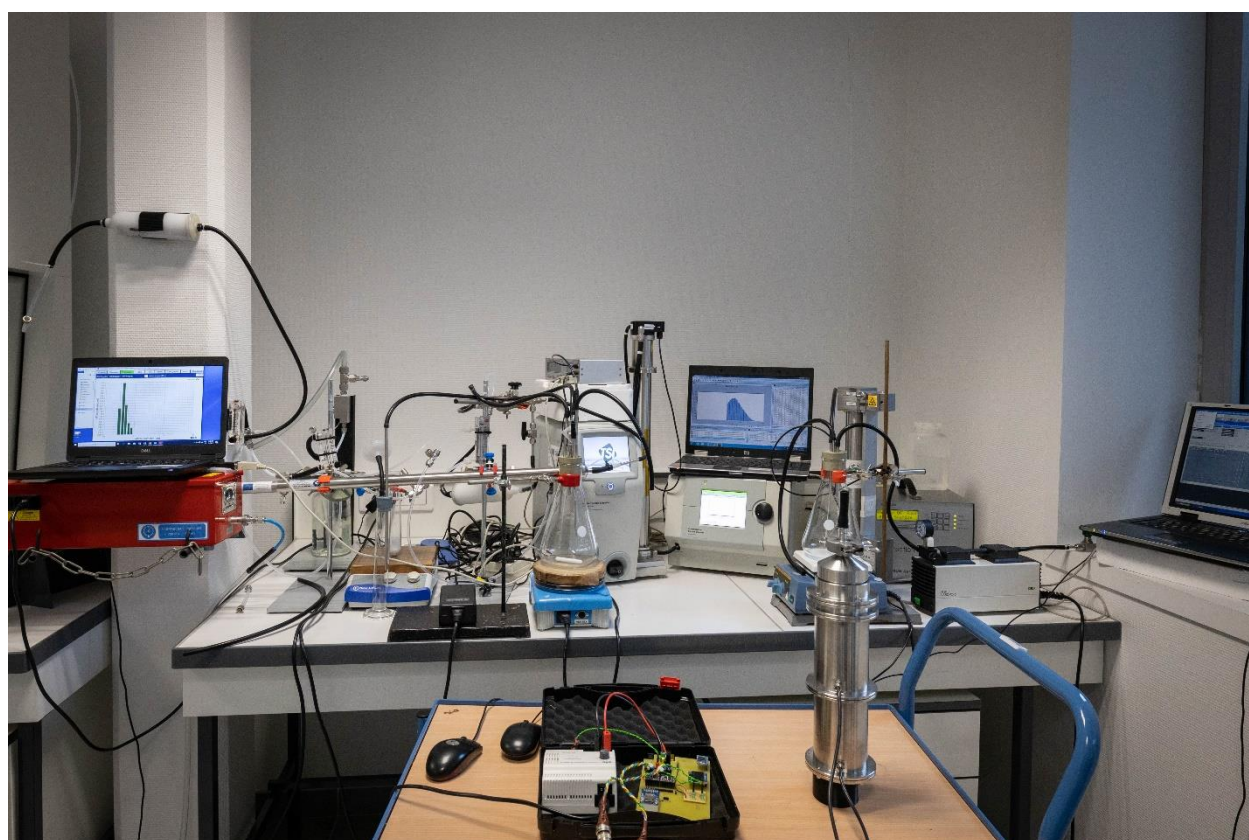


Figure 3-7. Image of the experimental set-up in the laboratory (LPCA-Dunkerque).

For the coarse stage, a dry aerosol was directly generated at a stable and re-producible concentration using a powder generator by vortex shaker (model VS-1000, ADDAIR-IRSN) (Figure 3-8.). For this, monodisperse silica particles of sizes 0.5, 0.75, 1, 1.5, 2 and 4 μm were used (Angström Sphere™, <https://focenter.com/> (accessed on 20/01/2020)). For each size, 0.5 mg of particles was mixed with 3 mg bronze powder and introduced inside the vortex. Bronze powder favored individualized dispersion of the particles. An internal pump provided clean and dry air into the

Chapter 3. Methodology of Physico-chemical characterization of particles

vortex through a pipe. The combination of particle-shaking and arriving airflow contributed to the dispersion of the suspended particles.

For our measurements, an output concentration ranging between 1000 and 10,000 $\#.cm^{-3}$ was obtained with a generation flowrate of 5 Lpm. This output flow was connected to a 1 L flask, itself connected to a HEPA filter to ensure flow balance and atmospheric pressure inside the system (Figure 3-9.). The particle concentrations were monitored upstream of the impactor by an optical particle counter (OPC) (model MiniWras model 1371 GrimmTM) and downstream by the OPS (Optical Particle Sizer) (model 3330 TSI Inc.). Prior to each experiment, the room air was measured by both the OPS and OPC. Both instruments showed similar reading for PM size distributions (see Annex, Figure A-2.).

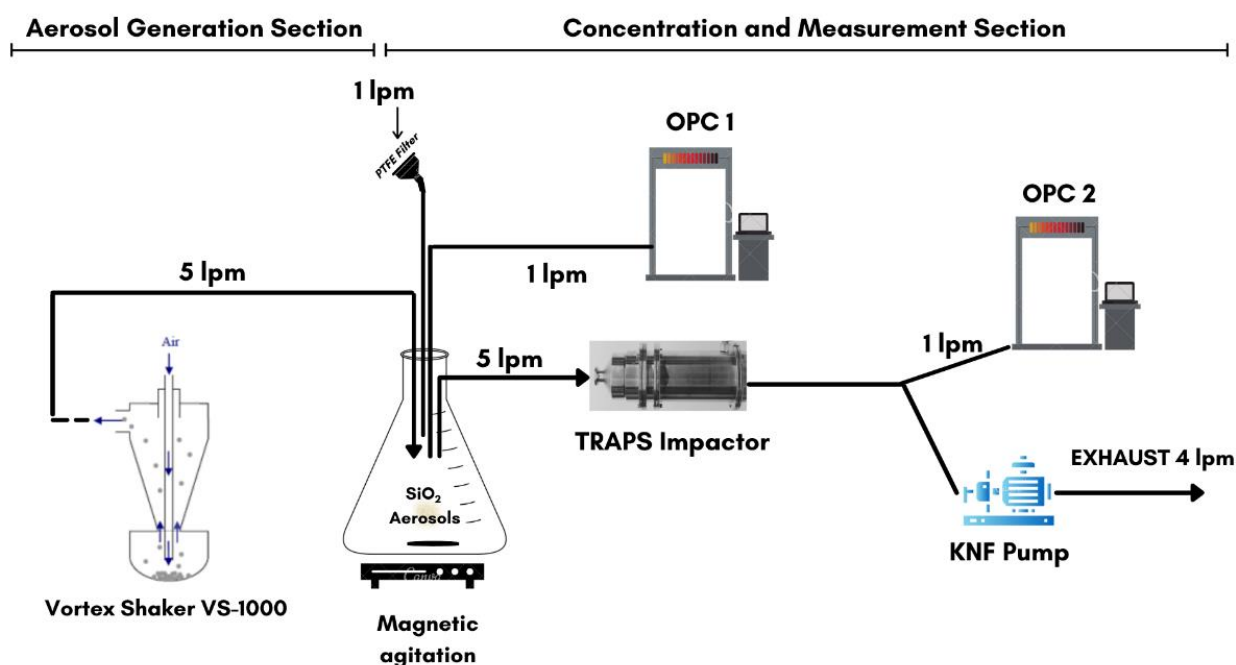


Figure 3-8. Schematic representation of the experimental setup for determining the coarse stage collection efficiency using vortex shaking of powders of monodisperse silica spheres.

For the two experiments (i.e., for the coarse and fine stages), the silicone tubes connecting the different parts of the setups were kept as short as possible, with lengths ranging between 10–40 cm, in order to limit particle losses. The minimum sampling time was 2 min, repeated 5 times for each experiment.

Chapter 3. Methodology of Physico-chemical characterization of particles

3.3.2. Experimental Setup for Atmospheric Applications

For the monitoring of pollution events, atmospheric particles were collected with the TRAPS onto 3 mm diameter Formvar[®] carbon-coated TEM grids (200 Mesh), fixed on polycarbonate membranes, allowing electron microscopy observations in TSEM mode. The TRAPS was connected to a membrane dryer (Nafion[™], www.permapure.com (accessed on 11/09/2019)), equipped with a PM₁₀ sampling head (see refer to the description of the sampling site in Chapter 2). The TRAPS was installed in parallel with other instruments: (1) an MP101 beta gauge (ENVEA[™]) for the measurements of hourly PM_{2.5} mass concentrations. (2) an optical particle counter (MiniWras model 1371 Grimm[™]) for the measurement of the particle size distribution. The date and time were reported in Coordinated Universal Time (UTC).

For the particle analysis using Electron Microscopy, please refer to that section in Chapter 2.

3.4. Results and Discussion

3.4.1. Experimental Determination of the Cut-Off Diameters

Two different calculations were used for the determination of the cut-off diameters of each impaction stage, and to take into account the influence of the coarse stage on the collection efficiency of the fine stage. For each experiment, particles of different sizes were generated separately and the cascade impactor was completely cleaned before and after each test.

Coarse Stage Cut-Off Diameter: The characterization of the coarse stage was performed without the presence of the fine stage, which had no influence on the collection efficiency of the coarse stage. Moreover, the presence of the fine stage during the experiments would make it unfeasible to directly measure the particle concentrations at the outlet of the coarse stage. The experimental setup presented in Figure 3-9 (configurations A and B) was used to determine the collection efficiency C_{eff} of this stage. The procedure applied is similar to that described by Broström et al., (2019).

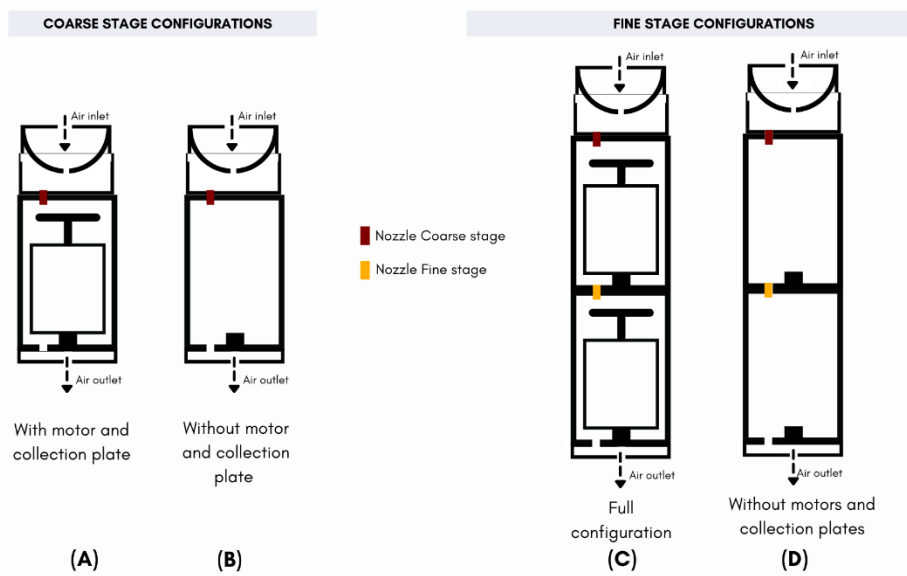


Figure 3-9. Schematic representation of the four configurations used for the experimental determination of the collection efficiency. The nozzles of the coarse and fine stages are represented, respectively, in red and yellow. The motors and plates were removed in configurations (B, D), while the stages were fully assembled (with all their nozzles, motors and collection plates) in configurations (A, C).

Configuration 3-9(B) allows for the quantification of the system losses (SL), i.e., the losses on the walls and tubing as well as possible reading differences of the instruments, while configuration 3-9(A) allows for the quantification of the overall losses (OL), including the particles deposited on the impaction plate. The two particle counters OPC1 and OPC2 were connected upstream and downstream of the impactor. The transmission efficiency of these systems were calculated using the mass concentrations ($C1$ and $C2$, respectively) measured by these OPCs using Equation (3-4):

$$\text{Transmission efficiency } T_{eff} (\%) = \frac{C2}{C1} \times 100 \quad (3-4)$$

The difference in transmission efficiency between configuration 3-9(B) (for SL quantification) and 3-9(A) (for OL quantification) is used to deduce the experimental collection efficiency (C_{eff}) of the stage. Experimental collection efficiencies are plotted in Figure 3-10 as a function of particle size, and compared to the theoretical efficiencies deduced from Section 3.2.

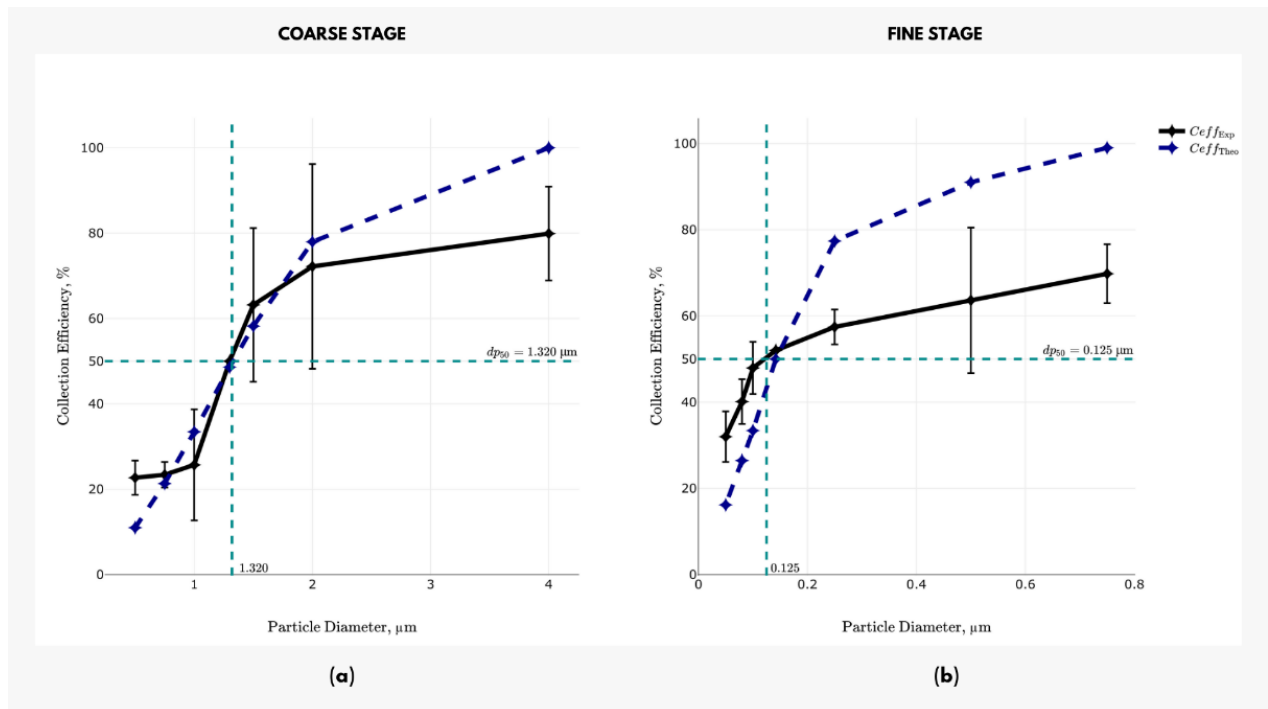


Figure 3-10. Theoretical (blue dotted line) and experimental (black line) collection efficiency curves for the coarse (a) and fine (b) stages (Error bars = 1 S.D with $n = 5$ for the coarse stage and 3 S.D with $n = 5$ for the fine stage).

The experimental cut-off point (D_{p50}) of this stage is obtained at 1.32 μm, which is very close to the theoretical value of 1.30 μm reported in Table 3-2, indicating a reliable design of this stage. The experimental collection efficiency for the largest particles does not reach 100%, which suggests that a non-negligible fraction of particles is affected by particle bounce or re-entrainment at this stage and is not collected (Demokritou et al., 2002).

Fine Stage Cut-Off Diameter: For the determination of the collection efficiency of the fine stage, the experimental set-up must include the coarse stage, which is located upstream, because it directly influences the particle concentration at the inlet of the fine stage. Therefore, configurations 3-9(C) and 3-9(D), using the fully assembled TRAPS with and without motor and collection plates (Figure 3-9), were used for the quantification of the size segregation characteristics of the fine stage.

Considering the CPC1 and CPC2 connected upstream and downstream of the impactor, the System Loss (SL), is calculated using configuration 3-9(D), from the number concentrations $C1$ and $C2$ measured by the CPC1 and CPC2, respectively, using Equation (3-5):

Chapter 3. Methodology of Physico-chemical characterization of particles

$$SL(\%) = \frac{C_1 - C_2}{C_1} \times 100 \quad (3-5)$$

The configuration 3-9(C) (full configuration) is then used to determine the effective collection efficiency, i.e., the fraction of particles impacted on the two collection plates. For this, the concentration of particles overall lost C_{OL} is firstly expressed as the difference between C_2 and C_1 , following Equation (3-6):

$$C_{OL} = C_1 - C_2 \quad (3-6)$$

From this amount, assuming that the SL is similar in configurations C and D, the concentration of particle removed/lost due to the system parts (walls, tubing and coarse stage), C_{SP} is quantified according to Equation (3-7):

$$C_{SP} = C_{OL} \times SL \quad (3-7)$$

It is then possible to calculate the experimental collection efficiency (C_{eff}) for each particle size, which corresponds to the ratio of the collected concentration (C_{OL}) on the collectable concentration (C_1), corrected in both cases by the SL (Equation (3-8)):

$$C_{eff} = \frac{C_{OL} - C_{SP}}{C_1 - C_{SP}} \times 100 \quad (3-8)$$

An experimental cut-off diameter (D_{p50}) of 0.125 μm was graphically determined for this fine stage (Figure 3-10. b). It is lower but almost similar to the theoretical cut-off point D_{p50} of 0.15 μm . As for the coarse stage, this is an indication of the good agreement between design and operational considerations of the TRAPS. As for the coarse stage, the experimental collection efficiency for the largest particles does not reach 100%, which is evidence of significant particle losses inside the cascade impactor. It can be attributed to several factors, including the bounce-off of spherical silica particles. These deviations from the theoretical curve can also be attributed to the diffusional deposition of small particles and the deviation in generated particle size ($\pm 10\%$). Similar limitations were reported for other cascade impactors (Broström et al., 2019; Demokritou et al., 2002; Gomes et al., 1990; Marple and Liu, 1974; Marple and Willeke, 1976; William C. Hinds, 2000). Important error bars observed in the collection efficiency curves can be explained by the variability of the relative humidity in the reactor during the experiments, which causes a change in the particle size and, consequently, their aerodynamic properties.

Chapter 3. Methodology of Physico-chemical characterization of particles

3.4.2. Observation and Analysis of Collected Particles

3.4.2.1. Particles Bouncing Effects

To examine the absence of contamination from one impaction spot to another due to particle bouncing, the surface area of an impaction trace has been studied using calibrated particles impacted on a polycarbonate membrane. The flow regime inside the fine stage nozzle being strongly turbulent ($Re = 12,420$), the risk of particle overlapping between two neighbouring impaction traces is at a maximum for this stage, which justifies its choice for this study. The rotation angle between two traces was fixed to 28.8° , and the sampling duration to 1 and 5 min, respectively (see below). During the experiments, the particle concentration remained consistently close to $300,000 \text{ \#} \cdot \text{cm}^{-3}$. The samples were overloaded (inappropriate for individual particle analysis) so as to easily visualize the spatial distribution of particles over the impaction area.

Two experiments were performed using the experimental set-up described previously (Figure 3-7): one with a solution of silica nanospheres (0.05, 0.08, 0.1, 0.25, 0.5 and $0.75 \mu\text{m}$) and the other with a solution of sodium chloride (NaCl, $M = 400 \text{ mg/L}$). The shape of impaction traces obtained with silica nanospheres (Figure 3-11. b) are much less regular than the rectangular shapes obtained for NaCl particles (Figure 3-11. a). These differences can be explained by the spherical shape of the silica particles that roll easily on the collection substrate after impaction, which is not the case for angular NaCl particles.

The hygroscopicity of NaCl vs. silica particles can also play an important role, as wet particles are more likely to adhere to the collection surface. The lengths of the more loaded traces (5 min sampling) are comparable to the nozzle length (2 mm), whereas their measured widths represent 7–10 times the nozzle width (0.13 mm). This dimension of the impaction area suggests that the working angle of 28.8° , which maintains a distance of around 8 mm between two adjacent impaction areas, is enough to prevent inter-sample contamination.

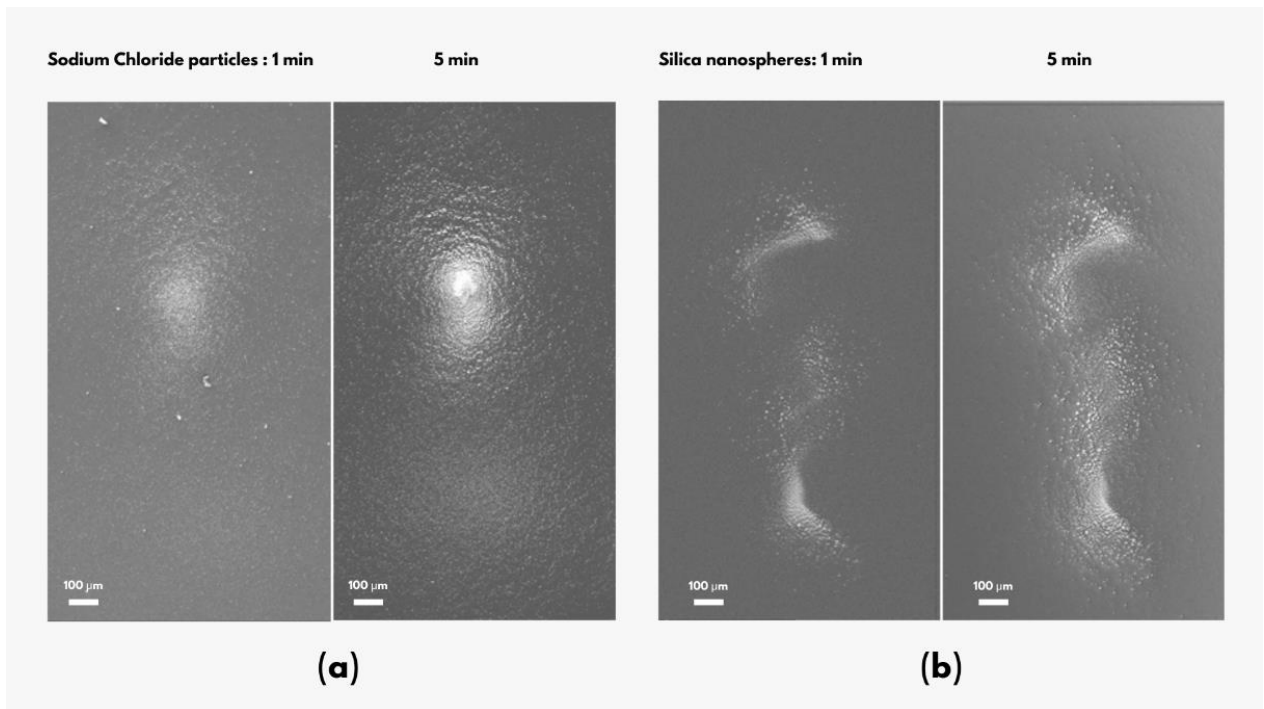


Figure 3-11. TSEM images (magnification: 50 \times , accelerating voltage: 15 kV) of the fine stage samples showing sodium chloride particles (a) and silica nanospheres (b) collected for 1 and 5 min, respectively.

Unlike the experiments conducted for the fine stage, the particle bouncing in the coarse stage was studied by sampling monodisperse silica particles of sizes 0.5, 0.75, 1, 1.5, 2 and 4 μm (Angström Sphere™, <https://focenter.com/> (accessed on 20/01/2020)), using the setup presented in Figure 3-7. The particles were generated and sampled size by size, for 1 min for each size, for a total sampling time of 6 min, and subsequently collected. The concentration of the generated particles varied between 10,000 $\#\cdot\text{cm}^{-3}$ for the finest to 4000 $\#\cdot\text{cm}^{-3}$ for the largest particle sizes. Figure 3-12. shows the spatial distribution of particles collected on a polycarbonate membrane during this experiment. A homogeneous deposit of particles on this trace is observed, which follows the shape of the nozzle. The width of this trace is about 1 mm, i.e., twice that of the nozzle. By comparison, it was 10 times larger for the trace of the fine stage. This demonstrates that particle bouncing is less important at this coarse stage.



Figure 3-12. TSEM images (Magnification: 25 \times , Accelerating voltage: 15 kV) of the coarse stage samples showing silica microspheres collected for 6 min.

3.4.2.2. Particle Deposition Patterns

In order to obtain a complete characterization of the particles associated with air mass, our original methodology is based on the combination of an optical particle counter, time-resolved sampling with the TRAPS and characterization of the collected particles by SEM-EDX. Individual particle analysis is a statistically sound approach—as long as it requires the possibility of analysing a large number of particles ($>10^3$) to have a database that allows robust statistical analyses, and to have a statistically sound result representative of all of the particles present in the studied air mass. Obtaining this representative sample is therefore based on a homogeneous distribution of the particle types/composition on the impaction trace, because only a fraction of this trace is exploited. In order to verify this homogeneity, real particles were collected on TEM grids during a 2 h sampling with the TRAPS, at our monitoring site in Dunkerque, when the $\text{PM}_{2.5}$ mass concentration was $5 \pm 2 \mu\text{g}\cdot\text{m}^{-3}$. The particle size distribution (Figure 3-13) shows a bimodal distribution, with a principal mode centered on $0.2 \mu\text{m}$ and a minor mode at $1 \mu\text{m}$.

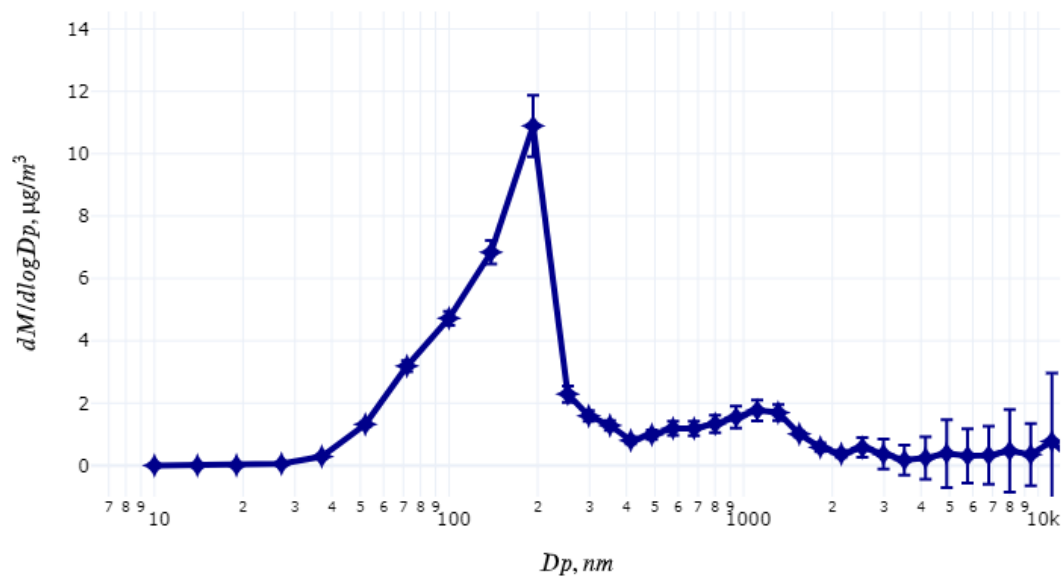


Figure 3-13. Mean particle mass size distribution obtained using an optical particle counter (MiniWRAS model 1371 GrimmTM) on June 13th 2021 from 08:00 to 10:00 UTC.

Consequently, only particles collected on the fine stage were observed for this study (1735 particles analysed). The analysed sections in the TEM grid, highlighted by rectangles of different colours, are located at the extremities (green and purple areas) and at the centre (blue) of the impaction trace (Figure 3-14).

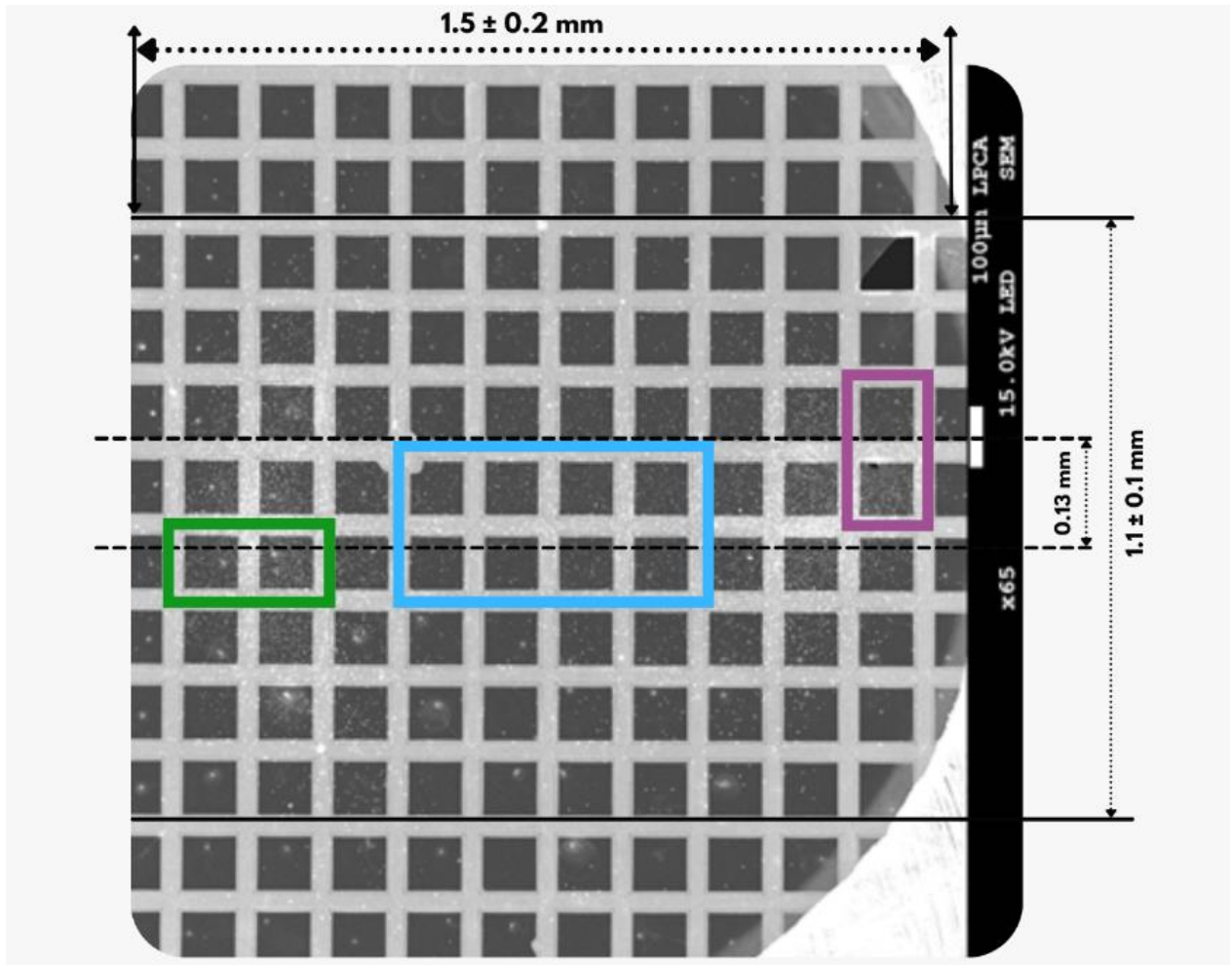


Figure 3-14. Image of the TEM grid (fine stage) used to evaluate the homogeneity of the repartition of impacted particles. The width of the impaction trace is marked by 2 horizontal lines and the nozzle width by 2 dotted lines.

Green, blue and purple rectangles represent the analysed areas.

The distribution of the six particle types over the three rectangles is presented in Figure 3-15. We can observe that particles are more loaded at the extremities than at the center of the trace, which is coherent with observations made in Section 4.1. The homogeneity of this distribution is evaluated by calculating the contribution of each particle type in each of the three observed rectangles. Contributions of the most (Na-rich particles) and a less (Ca-rich particles) abundant particle type, are relatively similar over the whole analysed sections with 88.6% and 3.7%, 77.8% and 3.5%, and 89.5% and 5.3% for the green, blue and purple areas, respectively. This allows us to conclude that, if the number of particles analysed is sufficiently high ($n \approx 1000$ particles) (Choël et al., 2010), the composition of the analysed particles will be representative of all the particles collected on the impaction stage, regardless of the area of the impaction trace observed.

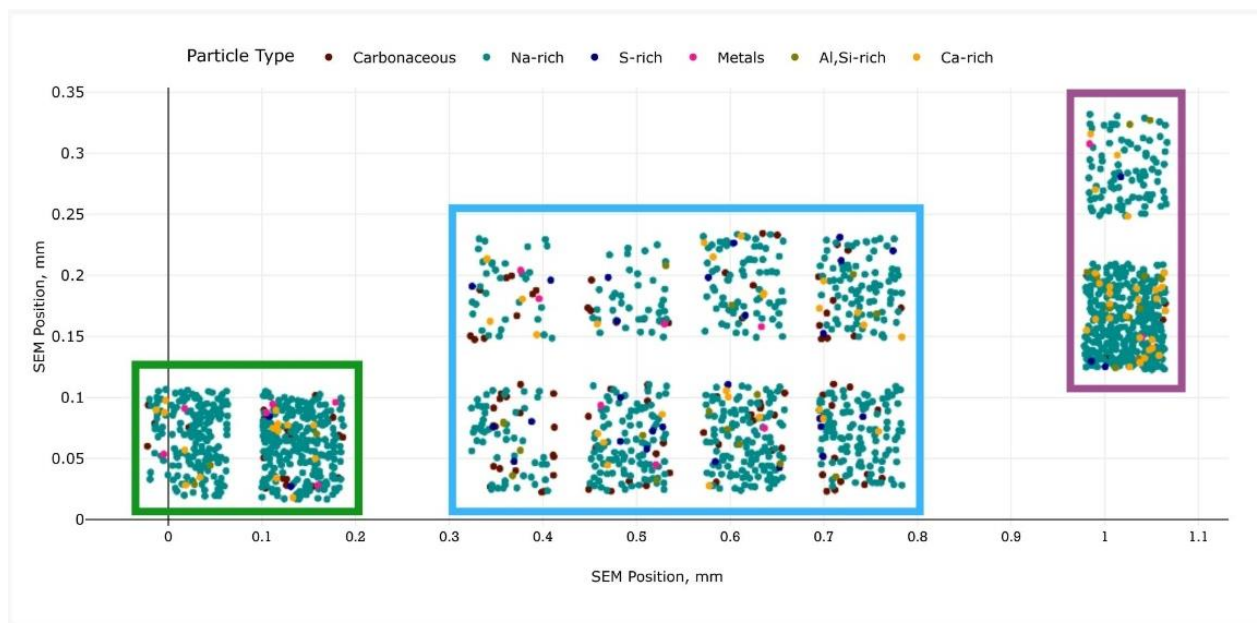


Figure 3-15. Distribution of the 6 particle types over the analysed areas identified in Figure 7. Each point represents a particle and each colour a particle type. A total of 405, 763 and 567 particles are observed in the green, blue and purple areas, respectively.

3.4.3. Application to Fine-Particle Pollution Event Monitoring

The TRAPS was implemented to monitor a transient fine-particle pollution event, from 20 April to 21 April 2021, on the rooftop of the University building located near the coastline, in the vicinity of the Dunkerque ($\approx 200,000$ inhabitants) harbour (“Sampling Site” in Figure 2-1). As highlighted in previous studies, the urban area studied is characterized by the presence of a large industrial complex, which is a source of significant steel and metallurgy emissions (Arndt et al., 2021, 2016; Marris et al., 2012; Mbengue et al., 2017; Setyan et al., 2019). It is also characterized by a dense traffic network, an important agricultural activity and obviously a significant residential area.

The pollution event lasted 33 h, with $PM_{2.5}$ above the WHO daily limit ($15 \mu\text{g}\cdot\text{m}^{-3}$) from 20 April, 9:00 to 21 April, 18:00 (Figure 3-16). During this event, two pollution peaks were observed, with maximal $PM_{2.5}$ concentrations reaching nearly 2.5 times the WHO limit on 20 April, 12:00 and 21 April, 6:00, respectively. Eight samples were automatically collected with the TRAPS during the event (P1–P8) and two of them are of particular interest since they were collected during the pollution peaks: P1 and P5 (Figure 3-17). For these two samples, a total of 2500 particles (N_{Total}) were analyzed by automated TSEM-EDX and classified into six particle types (Figure 3-17.).

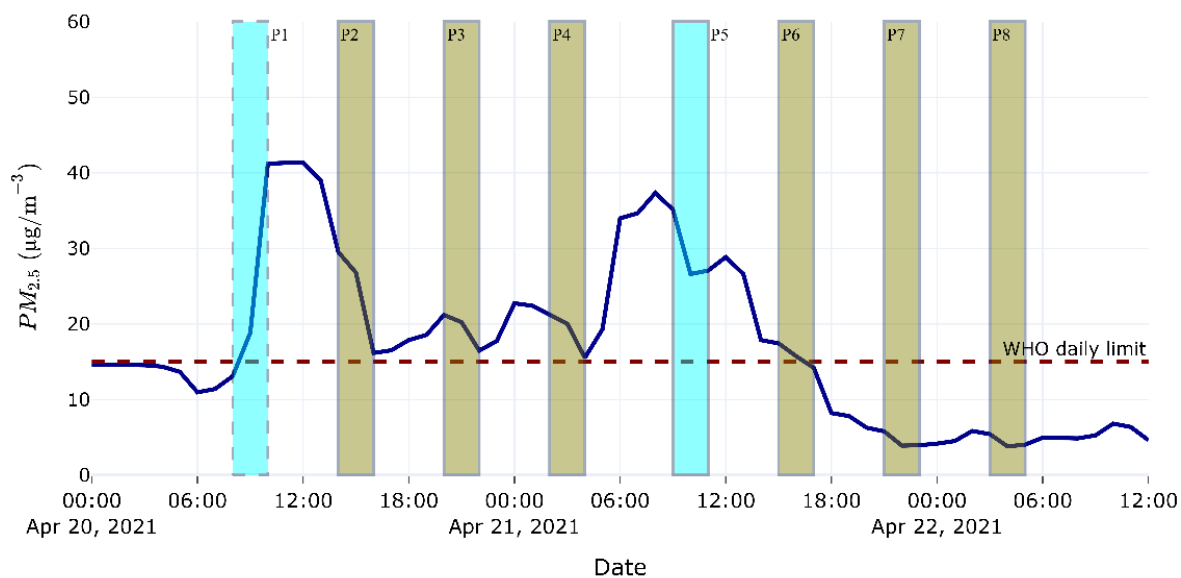


Figure 3-16. Time series evolution of PM_{2.5} mass concentration at our sampling site. Coloured rectangles represent the TRAPS sampling periods, where P1 and P5 (cyan) are the analysed samples whose results are discussed in the paper.

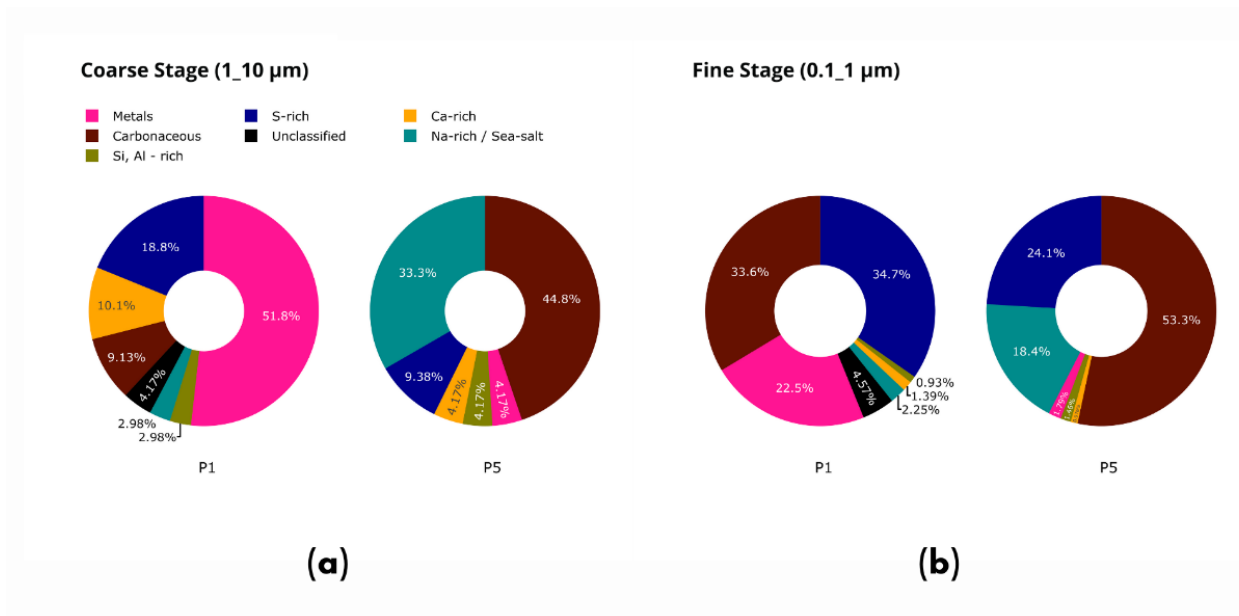


Figure 3-17. Relative contribution of different particle types during P1 and P5, respectively, for the TRAPS fine fraction ((a) coarse stage) and ultrafine fraction ((b) fine stage).

Chapter 3. Methodology of Physico-chemical characterization of particles

During the first pollution peak (P1), the chemical composition was dominated by: metal particles (51.8%), S-rich (18.8%), Ca-rich (10.1%) and carbonaceous particles (9.1%) for the fine fraction (coarse stage); and S-rich (34.7%), carbonaceous (33.6%) and metal-bearing particles (22.5%) in the ultrafine fraction (fine stage). The high predominance of metal-rich particles during this pollution peak was clearly due to emissions from the neighbouring industrial area, located northwest of our sampling site. These particles are typical of steelwork and metallurgical plant emissions, but can also be emitted by coil fire plants, oil refineries or re-suspended road dust from tire abrasion (Beji et al., 2020; Young et al., 2016). These particles of spherical and irregular shapes are composed of Fe and Mn oxides mixed with small amounts of some other elements (Si, Al, K, Ca or Na).

During the second pollution peak (P5), the analysed sample was composed principally of: carbonaceous (44.8%), Na-rich (33.8%) and S-rich (9.3%) particles in the coarse fraction; and carbonaceous (53.3%), S-rich (24.1.3%) and Na-rich (18.4%) particles, in the fine fraction. In contrast to the first pollution peak, this second peak is characterized by the predominance of carbonaceous aerosols (44.8% of analysed particles in the coarse fraction, 53.3% for the fine fraction). Considering that metal-rich particles are virtually absent from the P5 sample (<5% of analysed particles), the dominant carbonaceous particles observed during the second episode most likely do not come from local industrial emissions, but from the regional or long-range transport of particles (see back-trajectories shown in (Figure 3-18)).

Chapter 3. Methodology of Physico-chemical characterization of particles

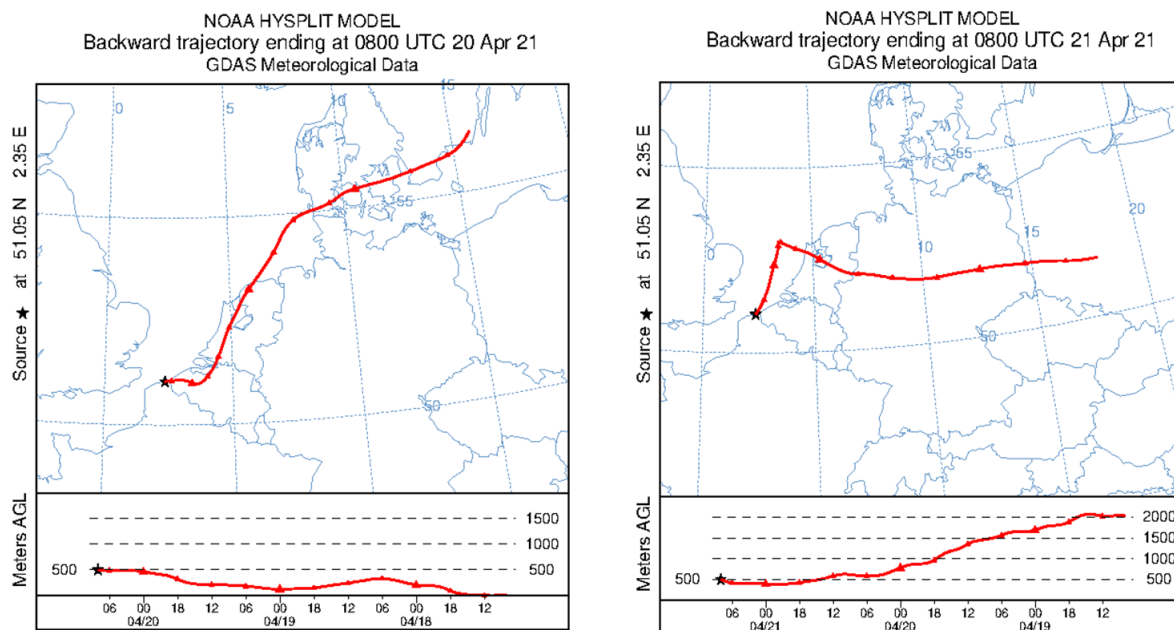


Figure 3-18. 72 hours backtrajectories calculations arriving at 500 m altitude at the sampling site respectively on April 20th and April 21st at 08:00 UTC.

They can be due to the incomplete combustion of fossil fuels (car traffic) or biomass burning. The significant increase in the contribution of sea spray to the $PM_{2.5}$ concentrations, given the fraction of Na-rich particles, also supports the regional origin of particles during P5.

3.5. Conclusion

In summary, this case study demonstrates that the TRAPS, associated with the SEM-EDX technique, is well adapted to describe the evolution of the physico-chemical characteristics of atmospheric particles during pollution events. It can be notably very helpful for the identification of the main sources explaining the transient exceedance of fine particle concentration thresholds, as defined by international organizations such as the WHO.

CHAPTER 4.
ANALYSIS AND EVALUATION
OF TYPICAL
PM10 POLLUTION EPISODES
IN THE GREAT DUNKIRK AREA.

4. Analysis and evaluation of typical PM₁₀ pollution days in the Great Dunkirk Area

In this chapter, PM₁₀ pollution days (PD) that occurred in the Great Dunkirk Area (GDA) between 2018 to 2020 were analyzed, classified and described in term of spatial extent of the pollution plume, associated meteorological conditions and PM concentration level. The main objective is to identify the main characteristics of the different types of PD observed in GDA. In addition, a detailed description of typical PD is realized at the hourly scale to reveal the specific characteristics of each pollution day (similarities and differences) in terms of potential sources and the evolution of the PM concentration. These characteristics can then be related to the composition and mixing state of the particles in chapter 5.

In summary, the following specific objectives are covered:

- Identify and compare PM₁₀ pollution days observed in the Great Dunkirk Area from 2018 to 2020, using international standards.
- Using WHO recommendations, classify them and identify the main parameters characterizing these typical pollution days
- Providing more information on the possible local or distance sources of PM and their possible formation mechanism during these pollution days.

4.1. Data availability

Figure 4-1 shows the geographical localization of the Great Dunkirk Area (GDA) in the Northern-France Region (HDF), as well as the land occupation between industrial (purple), urban (brown), rural (green), coastal (blue) and traffic zones (black). The area is mainly influenced by S and SW winds in winter and fall and NE, SW winds in spring and summer. Three Atmosphere Quality Measurement Stations (AQMS) of the air quality monitoring network (<https://www.atmo-hdf.fr/>) across the GDA are considered in this study (Figure 4-1b): The stations U, S, and I respectively classified as Urban, Sub-urban (located nearby the main highway A16 and close to an agricultural area) and Industrial (urban station in proximity of industrial installations). A 4th AQMS (R) was also selected, inside the forest of Campagne-les-Boulonnais located 67 km far from Dunkirk (Figure 4-1a). This station

classified as Remote site is crucial for measuring regional background levels of pollutants far from pollution sources.

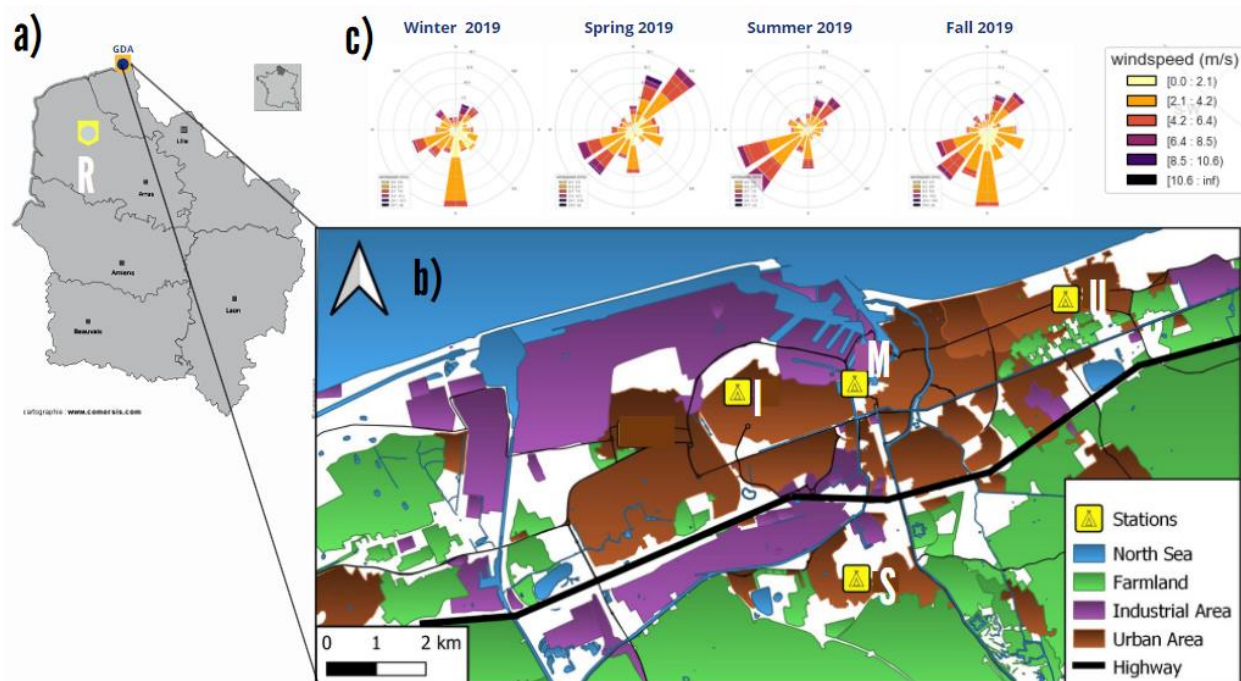


Figure 4-1. Map of the Great Dunkirk Area located in the Northern-France Region. Seasonal variation of wind speed and direction in 2019. The industrial installations (purple), urban settlements (brown), agricultural and forest areas (green), main roads (black) are also represented, together with the different measurement stations of the ATMO HDF air quality monitoring network (AQMS) and the meteorological station M.

According to the AQMS, hourly measurement of PM₁₀, PM_{2.5}, O₃, NO₂ and/or SO₂ in µg/m³ were recorded during the studied period starting from January 2018 to December 2020 (Table 4-1). In complementary, 15 min averaged meteorological parameters including temperature (T), relative humidity (RH), pressure (P), solar radiation (SR), rain (R), wind speed (WS) and wind direction (WD) were recorded at the meteorological station (M) installed at 15 m high, inside Dunkirk harbor on the rooftop of the university research building. These data were resampled to hourly mean for comparison with hourly measurement of the 5 main air pollutants. An algorithm taking into account the zonal and meridional components of the WD was applied when resampling the WD data. Table 4-1 shows the data availability and the mean and maximum values of each parameter measured by each station. More

Chapter 4. Analysis and evaluation of typical PM₁₀ pollution days

than 90% of the data are available for all the parameters, except for PM₁₀ (88%) and SO₂ (87%) of the S station. The data availability is therefore suitable for the analysis carried out in this chapter.

Station	Parameter	Count	Mean	SD	max	% availability
U	PM ₁₀ (µg/m ³)	23895	19.5	13.7	171	92%
	PM _{2.5} (µg/m ³)	23708	11.1	11.5	126.8	91%
I	PM ₁₀ (µg/m ³)	24733	20.2	15.9	239.2	95%
	O ₃ (µg/m ³)	25955	52.8	25.1	197	100%
	SO ₂ (µg/m ³)	25414	2.7	10.1	331.6	98%
	NO ₂ (µg/m ³)	25704	16.8	12.9	108.4	99%
S	PM ₁₀ (µg/m ³)	22739	20.3	14.5	271.9	88%
	O ₃ (µg/m ³)	25058	54.1	26	224.9	96%
	SO ₂ (µg/m ³)	22641	1.7	4.3	198.9	87%
	NO ₂ (µg/m ³)	24732	13.2	11	137.7	95%
R	PM ₁₀ (µg/m ³)	24695	17.1	11.8	245.8	95%
	PM _{2.5} (µg/m ³)	24435	10.5	10.1	128.9	94%
	O ₃ (µg/m ³)	25141	54.1	22.8	222.4	97%
M	T (°C)	25981	12.6	5.6	41.6	100%
	RH (%)	25981	78.7	10.3	95.7	100%
	DewPt. (°C)	25981	8.8	5.1	21.5	100%
	WS (m/S)	25982	4.1	2.3	15.7	100%
	WD	25976				100%
	P (hPa)	25981	1012.5	10.6	1046.5	100%
	Rain (mm/h)	25982	0.02	0.09	2.8	100%
	SR (W/m ²)	25981	125.7	202.8	930	100%

Table 4-1. Data availability in each of the U, S, I, R and M stations for the 3-years studied period (2018-2020).

The count is the number of daily data for this period, SD is for standard deviation.

4.2. Overview of air pollution days in the GDA.

4.2.1. Compliance with air quality standards

In the context of this study, a pollution day (PD) is defined as an exceedance of 24 hourly mean concentration of PM₁₀ and PM_{2.5} based on the limit values of internationally approved standards including European Union (EU) (European Parliament, 2008), US Environmental Protection Agency (EPA) or World Health Organization (WHO) (WHO, 2021). This definition is different from the French regulation definition that takes into account the spatial coverage of the pollution plume and the fraction of the population exposed during the episode (www.atmo-hdf.fr/). These policies do not have the same juridical values. Practically, while WHO “standards” are just guidelines, therefore, not legally binding standards for any country, the EU directive in return is a binding standard for the EU member states.

PM₁₀ and PM_{2.5} data obtained from the four AQMS stations described above (U, I, S and R), between 2018 to 2020, are exploited in this chapter. Table 4-2 presents the number of PD recorded, according to EU, EPA or WHO standards, at the each of the four AQMS.

Standard	PM ₁₀ µg/m ³			PM _{2.5} µg/m ³	
	WHO (24H)	EPA (24H)	EU/FR (24H)	WHO (24H)	EPA (24H)
Reference Value	45	150	50	15	35
Urban (U)	50	0	31	234	41
Industrial (I)	56	0	40	-	
Sub-urban (S)	51	0	29	-	
Remote (R) (67 km away)	24	0	8	-	

Table 4-2. Number of polluted days (PD) at the U, S, I or R stations for WHO, US-EPA and EU standards for the 2018-2020 period.

WHO limit values are lower than those of EPA and EU for the considered pollutants as shown in Table 4-1. The results of the comparison applied to PM₁₀ reveals that while there is no PD observed when applying EPA standard, the number of PD using WHO standard is nearly twice that of the EU

standard for U, I and S stations and 3 times for the R station. The number of PM_{2.5} PD increased by 5.7 times from EPA to WHO standard between 2018 and 2020 at the urban station and is not regulated by EU. Moreover, 234 PD were registered for PM_{2.5}, representing 4.7 times the number of PM₁₀ PD (50) recorded within the same period at the same station (U) relative to WHO standard. Unfortunately, PM_{2.5} data are not available for all studied stations and this has constrained only PM₁₀ to be considered in the following study of PD characterization. As the WHO standard is the most restrictive, a PM₁₀ pollution day will be defined as an exceedance of the WHO daily limit value of 45 µg/m³.

4.2.2. Monthly variability

For the 2018-2020 period, a total of 91 PM₁₀ pollution days (PDs) was accounted, corresponding to days when the daily PM₁₀ level reached the WHO daily limit (45 µg/m³) at least one of the three GDA stations (U, I or S). The monthly and yearly variability of these PDs recorded between 2018 and 2020 are presented in Figure 4-2.

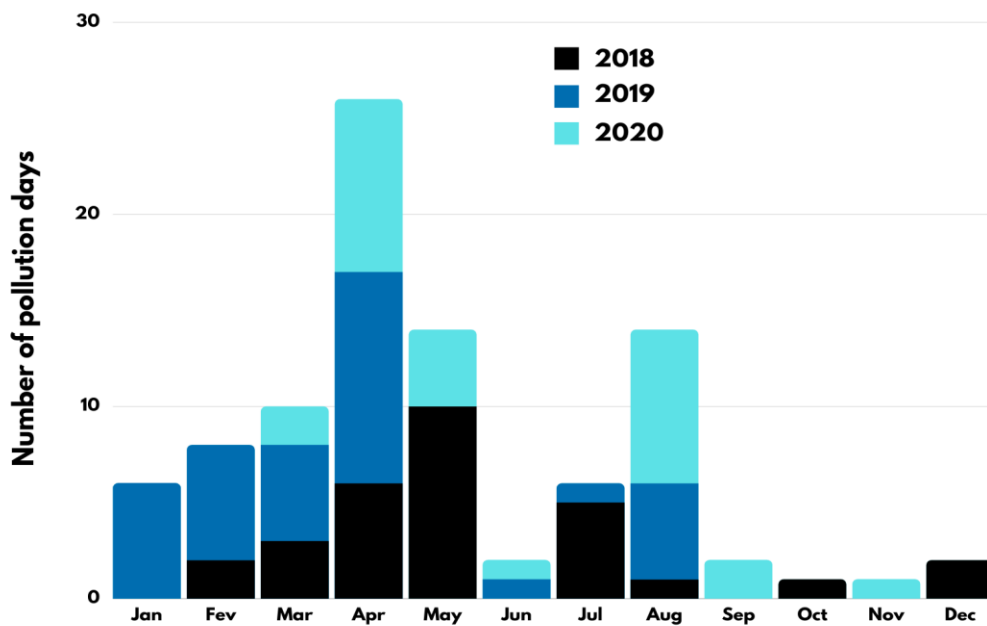


Figure 4-2. Seasonal variability of PM₁₀ polluted days (PD) recorded at at least one of the 3 GDA stations (U, S and I) in 2018 (black), 2019 (dark blue) and 2020 (light blue).

The month of April with a total of 28 PD for 2018-2020 is the most represented month, followed by May (14 PD) and August (14 PD). These results show a clear seasonality in the occurrence of these

Chapter 4. Analysis and evaluation of typical PM₁₀ pollution days

PM₁₀ exceedance days: Most of PM₁₀ PDs (54 %) occur in spring (Mar-Apr-May), 24% in summer (Jun-Jul-Aug), 17% in winter (Dec-Jan-Feb) and 7% in fall (Sep-Oct-Nov).

The lowest occurrence in fall can be explained by maximum frequency of rainfall during this season, as shown in Figure 4-3, associated with low pressure systems favorable to the dispersion of pollutants.

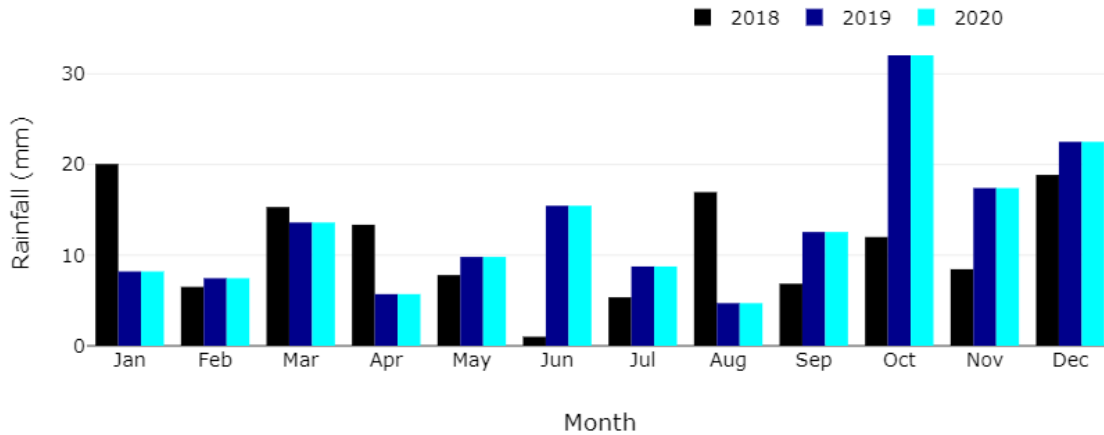


Figure 4-3. Seasonal variation of the total rainfall that was recorded in the GDA from 2018 to 2020.

Indeed, mean rainfall of 42 mm and atmospheric pressure of 1011 ± 9 hPa characteristics of low pressure systems were recorded during fall months between 2018 and 2020. Comparatively, in spring the mean rainfall was 27 mm and 1013 ± 10 hPa. These results are in good agreement with previous studies that showed that the concentration of PM₁₀ and even PM_{2.5} depends on the alternation between low and high pressure systems in northern France in general and in the GDA particularly (Gengembre, 2018; Rimetz-Planchon et al., 2008b).

4.3. Classification of PM₁₀ pollution days in the GDA

In this section, all days for the 2018-2020 periods are classified based on the flowchart presented in Figure 4-4. Here, after distinguishing between clean days (CD) and PD based on daily PM₁₀ concentrations, the detailed characteristics of the different types of PD frequently observed over the GDA are presented. The objective is to identify PD that tend to repeat and describe them.

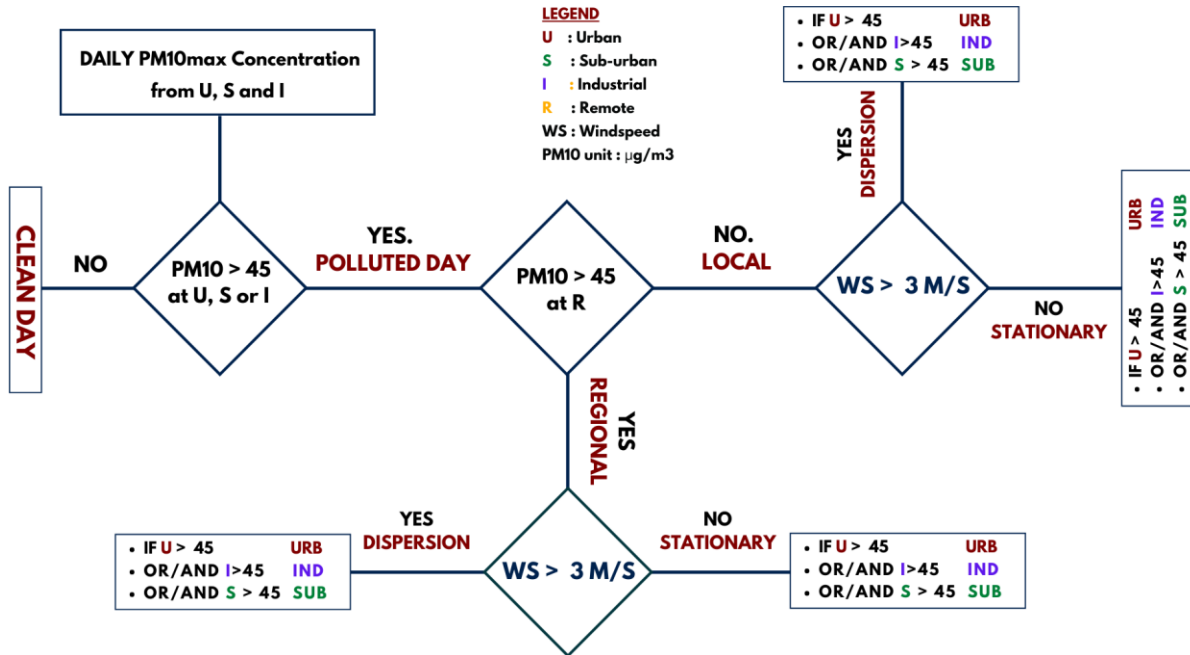


Figure 4-4. Flowchart for the classification of PM₁₀ pollution episodes in the GDA. U, S, I and R refer to the Urban, Sub-urban, Industrial and Remote AQMS. WS refer to the wind speed recorded at the M station.

The classification scheme can be described as follow. First, only days for which the daily mean PM₁₀ concentrations are available for the 4 GDA stations (U, S, I and R) are considered, the other days are classified as “Not Analyzed (NA)”. Then, clean days “CD” are identified as days with daily PM₁₀ concentration lower than the WHO daily limit value ($45 \mu\text{g}/\text{m}^3$) at the three GDA stations (U, S and I), the other days are considered as PD. Among the 1096 days of the 2018-2020 period, 811 (74%) were CD, 76 (6.9%) were PD and 209 (19.1%) were NA.

A PD is then considered as regional (REG) if the PM₁₀ concentration at the remote (R) station is above the standard. If not, the PD is classified as local (LOC). The DPs are then discriminated according to the state of the atmosphere considering the local wind speed (recorded at station M).

Pollution episodes generally happen under anticyclonic conditions characterized by a stagnant atmosphere leading to pollutant accumulation which is mainly frequent in winter (Evtyugina et al., 2006; Hu and Wang, 2021; Peng et al., 2021, 2016; Rimetz-Planchon et al., 2008b; Roig Rodelas et al., 2019). However, PM₁₀ pollution exceedance can also be caused by long range transport (Aggarwal and Kawamura, 2009; Karaca et al., 2009; Kim et al., 2020; Roig Rodelas, 2018). The temporal evolution

of temperature inversion, atmospheric stability and wind speed were found to be among the best meteorological variables that can be used to predict pollution episodes (Kukkonen et al., 2005). In this study, wind speed (WS) being an available data for the entire period (2018-2020), this parameter was considered to distinguish between stationary conditions that can be assimilated to stagnation therefore accumulation of pollutants in opposition of the conditions of dispersion.

A wind speed (WS) value between 1 and 4 m.s⁻¹ is generally associated with conditions of stagnation (Bodor et al., 2020; Hu and Wang, 2021; Ly et al., 2021; Stirnberg et al., 2021; Sun et al., 2016; Yoshino et al., 2021; Yu et al., 2020; Zhang et al., 2021). In this study, a threshold of 3 m/s for the daily mean WS was set to classify PD associated with stationary (STAT) or dispersion (DISP) conditions (see Figure 4-4). On the other hand, if a threshold of 2 m/s had been set, an increase in the proportion of local and regional PD in dispersive conditions of 16% (for LOC-DISP) and 5% (for REG-DISP) would have been registered. However, this is not representative of the real situation because, for PD in which sea breezes occur, WS peaks causing an increase in their daily average value between 2 and 3 m/s are frequently observed, without inducing dispersion conditions as sea breezes generally happen under anticyclonic and stagnant conditions (Talbot et al., 2007). A WS threshold of 3 m/s is therefore fully justified in the coastal area of the GDA to discriminate between stationary (STAT) and dispersion (DISP) conditions.

Finally, the PDs are classified as U, S or/and I depending on whether the daily PM₁₀ levels exceed the WHO daily limit value (45 µg/m³) at the U, S or/and I station.

As an example, the two following cases are considered:

- The daily PM₁₀ concentrations is 12, 48, 24 and 28 µg/m³ at the R, U, S and I station respectively, with a daily WS of 2.3 m/s: This day is classified as LOC-STAT-U
- The daily PM₁₀ concentrations is 12, 48, 24 and 54 µg/m³ at the R, U, S and I station respectively, with a daily WS of 5.8 m/s: This day is classified as LOC-DIS-U-I

The spatial extent of the pollution plume can then be appreciated according to the number of stations classified as PD: 1 (either U, I or S), 2 (U+I, U+S or I+S) or 3 (U+I+S) stations.

4.3.1. Local vs regional polluted days

The results of the classification are presented in Figure 4-5. The contribution of transported pollution from regional, continental or remote sources has a relatively small impact on PM levels during PD, since local PD represent 77.6% of the PD, all meteorological situations considered (STAT or DISP). Therefore, it is mainly local pollution sources that are responsible for the PD in the GDA. Moreover, there are as many PD in the dispersion condition as in the stationary condition. So, it would seem that it is more the sources of pollution than the meteorological conditions that explain these PD.

In addition, while the local episodes are observed all over the year with a more important frequency in winter and spring, the regional episodes are mainly recorded in spring, principally April and May as shown in Figure 4-6. This can be explained by cumulative effects of favorable atmospheric conditions conducive to stagnation, local emissions and also stronger solar radiation compared to winter conducive to more efficient production of atmospheric oxidants such as O₃ and then for secondary aerosol formation (Morawska et al., 2021).

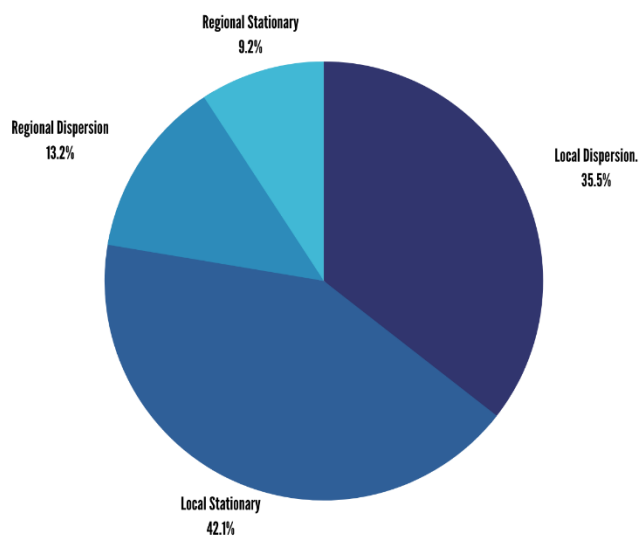


Figure 4-5. Repartition of the 91 PD recorded in 2018-2020, according to the plume extent (local or regional) and atmospheric condition (stationary or dispersion condition).

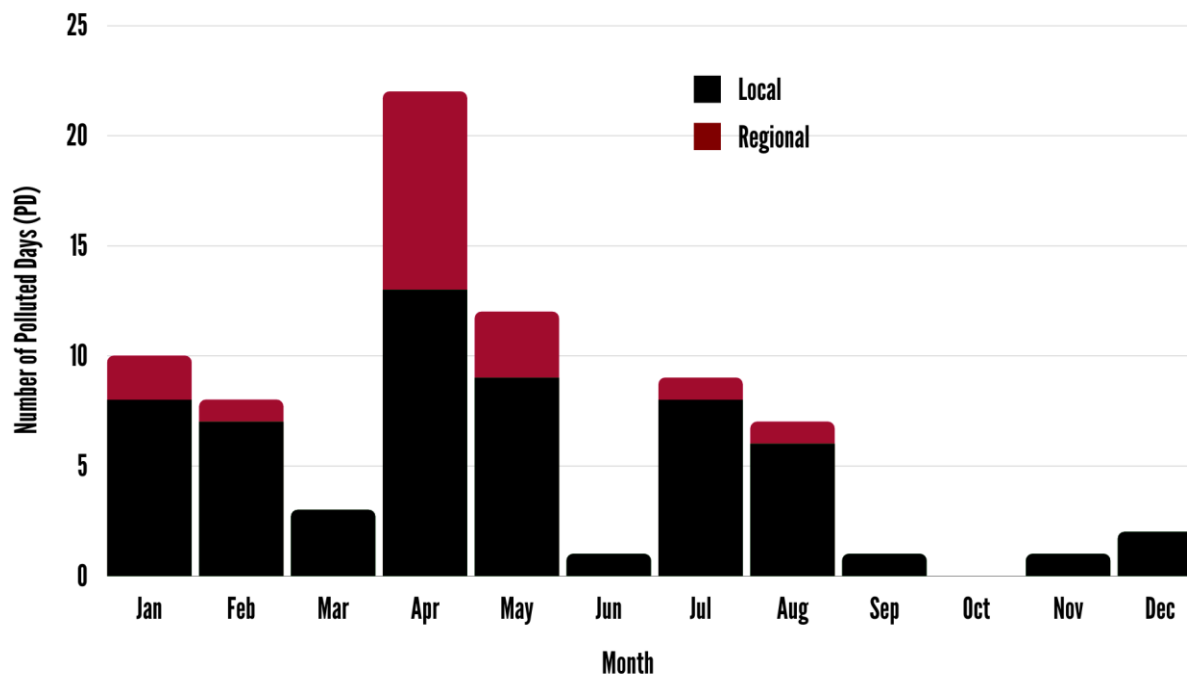


Figure 4-6. Monthly variation of local scale and regional polluted days in the GDA from 2018 to 2020

Considering the strong predominance of DP associated with a local extension of the pollution plume, the following of this study will focus on these DPs.

4.3.2. Local episodes

Among the 59 local pollution days (PD) recorded in 2018-2020 (LOC type), three types can be identified when looking at the contribution of each station (U, I, S), regardless of the stationary or dispersion conditions (Figure 4-7): Those recorded at only 1 station, I, U or S, (LOC-1 Station) which account for 51% of the local PD and those recorded simultaneously at 2 (LOC-2 Stations) or 3 stations (LOC-3 Stations) which account for 29% and 10% of local PD, respectively. The higher the number of stations associated with a PD, the larger the spatial extent of the pollution plume. Consequently, most of the PD with a local extent have a very limited spatial amplitude (LOC-1 Station). Moreover, whatever the spatial extent of the pollution plume (1, 2 or 3 impacted stations), the majority of the PD systematically concern station I. So most of these local PD are caused by industrial sources including plumes from industrial chimneys or shipping emissions.

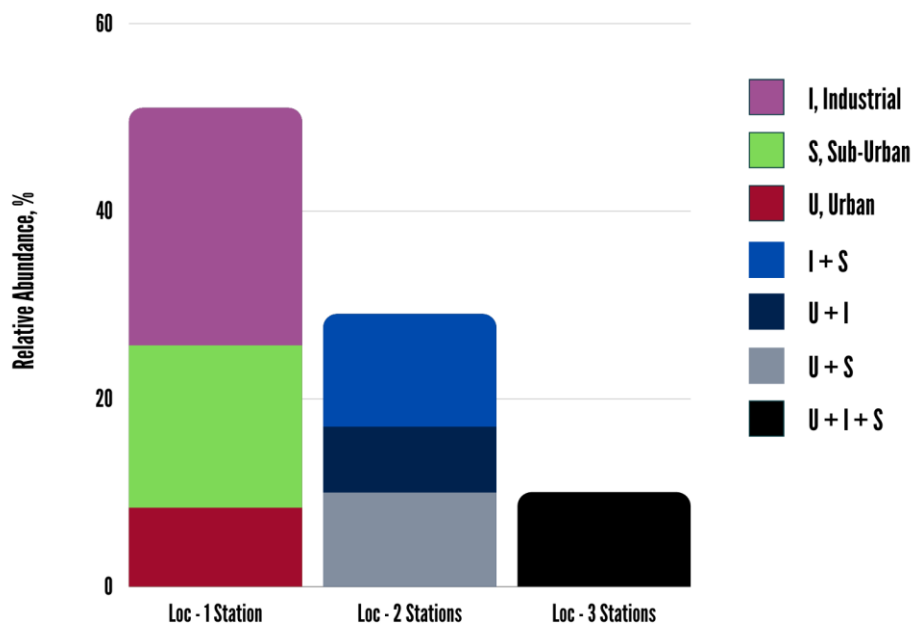


Figure 4-7. Number of stations impacted by the PM₁₀ pollution plume during the local PD recorded from 2018-2020.

In order to discern the influence of industrial sources to PM concentrations, the ratio between daily PM₁₀ measured at I and U and I and S were determined for the mostly represented local pollution days where the I station is concerned. The mean ratios are summarized in Table 4-3. together with mean PM₁₀ at each I, U, S and R station and WS and P.

TYPE		WS	P	PM10 I	PM10 U	PM10 R	PM10 S	I/U	I/S	PM2.5/PM10 U
LOC-DISP-I	Mean	5.3	1018.2	54.9	30.8	23.8	31.2	1.8	1.8	0.5
LOC-DISP-I+U	Mean	3.8	1020.0	70.8	48.9	41.8	36.6	1.4	1.9	0.7
LOC-DISP-I+S	Mean									
LOC-STAT-I	Mean	2.4	1015.0	47.0	37.6	29.7	41.5	1.2	1.1	0.6
LOC-STAT-I+S	Mean	2.0	1012.9	49.8	40.8	28.4	52.5	1.2	0.9	0.4
LOC-STAT-I+U	Mean	2.1	1025.3	48.8	49.7	35.1	41.8	1.0	1.2	0.6
LOC-STAT-3-I+U+S	Mean	2.0	1017.2	60.7	56.3	35.7	56.2	1.1	1.1	0.7

Table 4-3. Average wind speed, pressure and PM₁₀ concentration at the industrial, urban, suburban and remote stations for each class of the most represented local pollution days.

From Table 4-3, high ratios (above 1 and more important for I/S) can be observed. This indicates that regardless of the PD and assuming U and S stations as representative of the background concentrations at their respective locations, supplementary PM₁₀ from industrial sources are systematically recorded. For PDs of very limited spatial amplitude (1 station), there is an important ratio I/U or S is nearly 2 indicating important extra contribution of industrial sources to PM₁₀ during these PDs. This tends to reduce with increasing spatial amplitude of the PDs. If these results show that industrial sources are undoubtedly an essential local PD source, it also suggests that reduced wind speed synonym of stationary conditions caused the nearly uniformly high PM levels across the stations.

4.3.3. Pollution events

A pollution event (PE) is a period during which 2 or more pollution days (PD) are recorded consecutively. The relative abundance of PE recorded in the GDA from 2018 to 2020 is presented in Figure 4-8. The figure reveals that only 25% of the pollution periods are single PD, i.e. 19 PDs, temporally bounded by clean days. Most of these PDs (16) are of type LOC-1 i.e. pollution days of reduced spatial amplitude implying an exposure limited mostly to populations located in the immediate vicinity of the area where exceedance is recorded. In return, 75% of the PDs are comprised in pollution events (PE) i.e. lasted 2 days or more, indicating that in the Great Dunkirk Area (GDA) most of the pollution days are pollution events. Most of the PDs (43) accounted in PEs are of wider spatial coverage therefore a more important fraction of population is exposed. As the fraction of population exposure to PM increases with increasing number of successive pollution days a specific attention should be given to pollution events (PE). In addition, several different types of PDs can occur consecutively during a PE and the transition from one type to another would depend mainly on the meteorological conditions at micro and mesoscale as reported in many studies (Hu and Wang, 2021; Kim et al., 2020; Peng et al., 2021; Sun et al., 2016; Yu et al., 2020).

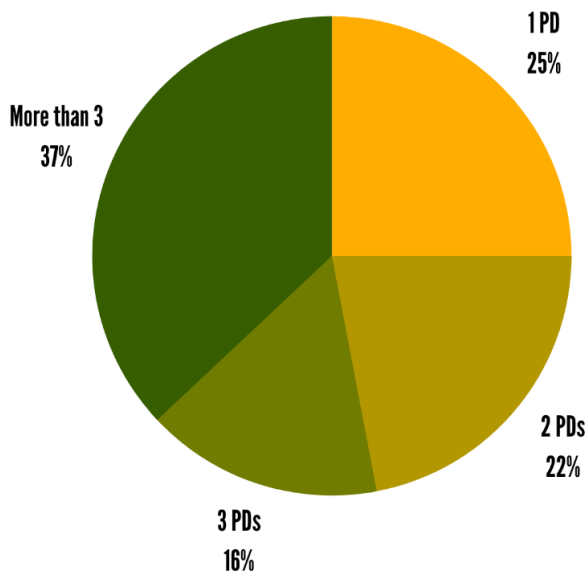


Figure 4-8. Proportion of single pollution days compared to pollution events for 2018-2020.

4.4. Hourly description of few typical PM₁₀ pollution events

In the following sections of this work, a more detailed description of 4 pollution events (PE) including the main types of PDs will be provided, i.e. local pollution plumes (Loc-Stat or Loc-Disp) for which the industrial station is at least impacted (Table 4-4). The PE-A, PE-B and PE-C are composed of 2 PD, while PE-D is composed of 3 PD. While PE-B and PE-C are concerned by an exceedance of the PM₁₀ levels only on the industrial station (I), PE-A is additionally concerned by an exceedance on the urban station (I+U). PE-D is a local plume of larger extent, associated with an exceedance on the 3 GDA stations (U+I+S).

Pollution Event	Pollution Day	Date	WS m/s	P hPa	PM ₁₀ I	PM ₁₀ U	PM ₁₀ R	PM ₁₀ S	PM _{2.5} U	PM _{2.5} /PM ₁₀ U	PM ₁₀ I/U	PM ₁₀ I/S	Type
PE-A	PDA-1	2018-12-27	1.3	1023.9	38.7	48.8	28.9	36.3	40.8	0.8	0.8	1.1	Loc - Stat - U
	PDA-2	2018-12-28	2.0	1027.3	54.9	51.8	29.9	42.3	41.1	0.8	1.1	1.3	Loc - Stat - U+I
PE-B	PDB-1	2019-01-05	5.0	1034.3	50.6	22.9	23.0	20.6	11.3	0.5	2.2	2.5	Loc - Disp - I
	PDB-2	2019-01-06	4.1	1032.9	50.7	24.5	22.1	22.7	11.6	0.5	2.1	2.2	Loc - Disp - I
PE-C	PDC-1	2019-01-08	8.9	1022.1	71.1	25.4	13.7	28.9	6.5	0.3	2.8	2.5	Loc - Disp - I
	PDC-2	2019-01-09	9.7	1022.4	56.8	26.3	14.1	19.1	6.3	0.2	2.2	3.0	Loc - Disp - I
PE-D	PDD-1	2019-03-29	2.4	1026.8	45.9	48.5	37.9	40.9	38.3	0.8	0.9	1.1	Loc - Stat - U+I
	PDD-2	2019-03-30	1.4	1018.8	83.0	92.2	46.0	74.8	75.1	0.8	0.9	1.1	Reg - Stat - U+I+S
	PDD-3	2019-03-31	5.9	1020.5	58.4	51.6	49.5	49.6	33.0	0.6	1.1	1.2	Reg - Disp - U+I+S

Table 4-4. Summary of the daily mean values of PM₁₀ (U, S, I and R), PM_{2.5} (U), wind speed (WS), and atmospheric pressure (P) associated to the different types of PD comprising the studied PE.

The PM_{2.5} levels are unfortunately not available at the industrial site, but the study of the PM_{2.5}/PM₁₀ ratio at the urban site (U) shows that it is strongly dependent on the PM₁₀ levels (Figure X).

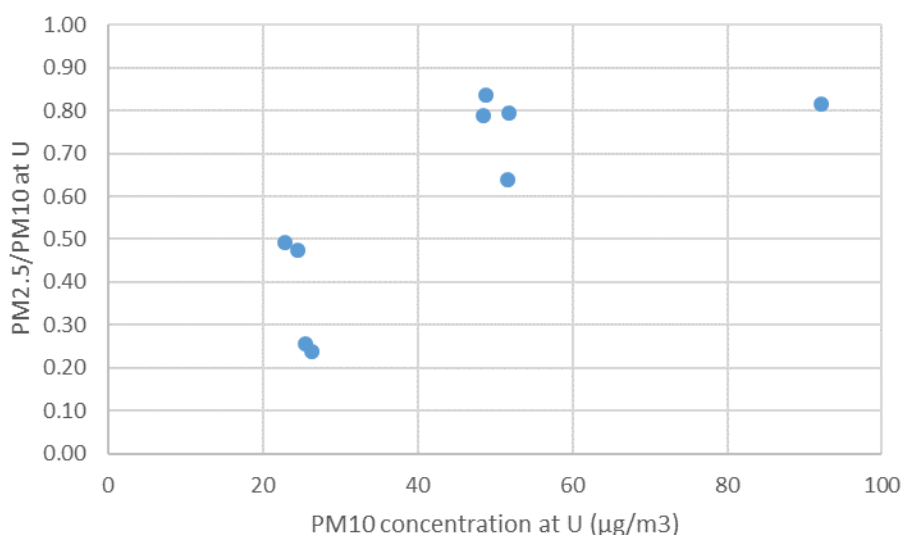


Figure 4-9. Evolution of the PM_{2.5}/PM₁₀ ratio according to PM₁₀ concentrations (in µg/m³) at the urban site (U).

Thus, the high concentrations in PM₁₀ at the urban site are associated with a relatively high contribution of the fine mode, which is consistent with industrial and urban emissions in the GDA generally associated with fine particle emissions (Alleman et al., 2010; Hleis et al., 2013; Kfoury et al., 2016; Ledoux et al., 2006; Marris et al., 2012; Mbengue et al., 2017).

4.4.1. PM evolution and meteorology

The time series evolution of PM₁₀, PM_{2.5}, SO₂, O₃, NO₂ and meteorological parameters including T°, RH, WS, WD and SR during PE-A, PE-B and PE-C and PE-D are presented respectively in Figure 4-10, 4-11 and 4-12. Except for PE-B (Figure 4-11.) where a sawtooth evolution alternating growth and decrease of PM₁₀ concentrations can be observed, the evolution of PM₁₀ during PE-A (Figure 4-10.), PE-C (Figure 4-11.) and PE-D (Figure 4-12.) is nearly similar. Indeed, a progressive increase in PM₁₀ concentrations is observed until the pollution peak is reached for all the events. However, while the evolution of urban PM_{2.5} follows that of all local PM₁₀ during PE-A and PE-D, it is not the case during PE-B and C (see Figure 4-11.) which is expected since these PE do not impact the urban station (U) but only the industrial station (I). During PE-A and PE-D, the PM₁₀ pollution peaks of 95.1 and

150.1 µg/m³ representing 2 and 3 times the WHO limit is reached during the night (22:00 and 21:00 respectively). During PE-B and PE-C both daytime peaks and early morning (3:00 and 5:00) peaks are observed. This is an indication that different mechanisms contribute to the occurrence of these peaks and globally to aerosol formation and evolution during these pollution events.

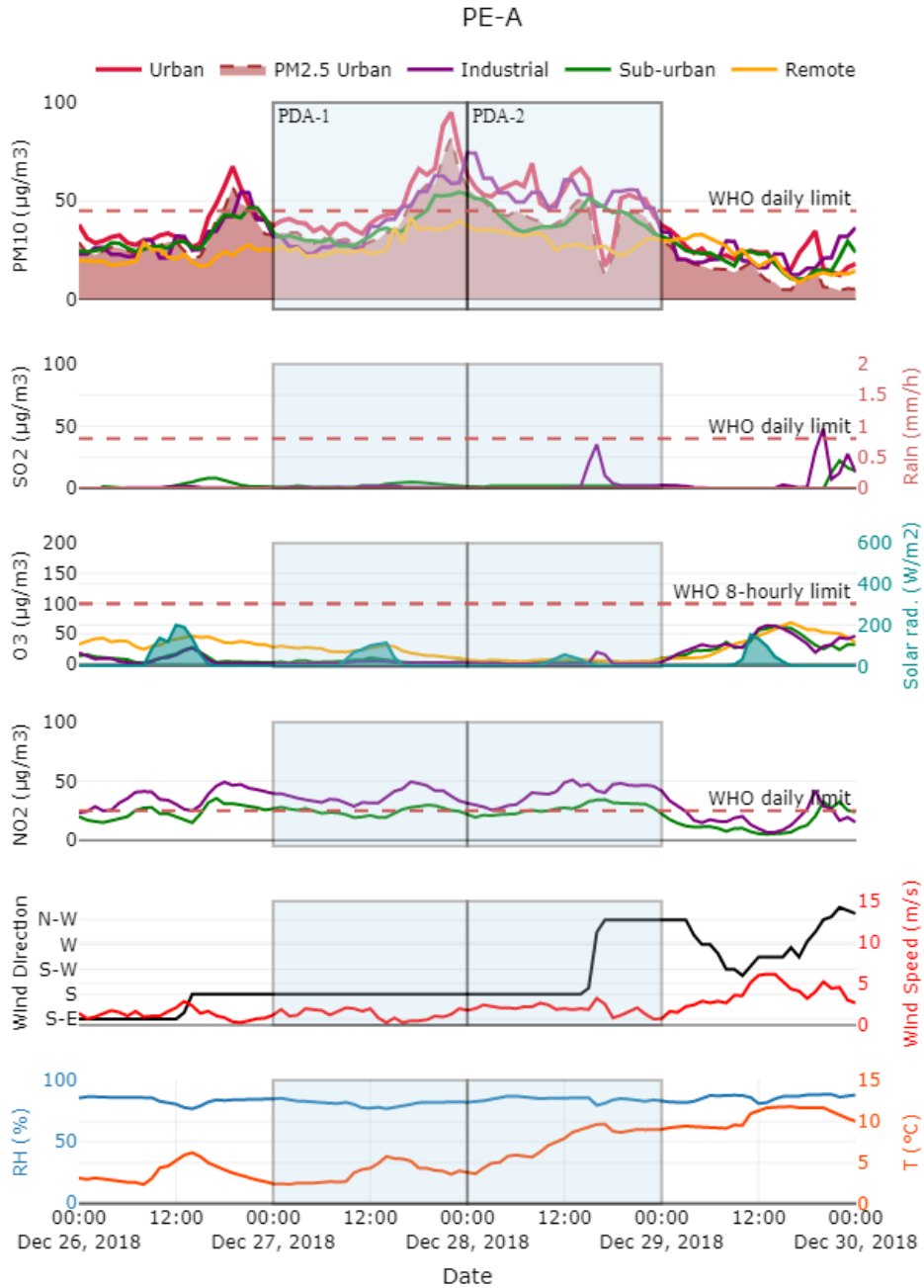


Figure 4-10. Evolution of PM, precursor gases and meteorological parameters during PEA

Considering meteorological parameters, anticyclonic conditions (see P values in Table 4-4.) prevailed during all the studied PE. The evolution PM₁₀ during PE-A cannot be isolated from the evolution of PM₁₀ on Dec 26th. Indeed, changing wind direction from SE to S, an increase in RH and decrease in T initiated the event by a progressive increase in PM₁₀ concentrations at U, S and I from 6:00 until the first exceedance is recorded on Dec 26th at 17:00 (Figure 4-9). The WD remained unchanged at nearly constant speed during nearly 48 hours of the event. With median RH and solar radiation respectively of 83% and 0 w/m². This is an indication of the presence of an important and stable cloud cover preventing incoming sunlight to reach the ground. Considering the mean wind speed below 2 m/s, the meteorological conditions prevailing during this event are characteristic of atmospheric stagnation leading to pollutant accumulation frequently observed in winter. Under these conditions, nighttime thermal inversions are frequently observed and might explain the nighttime PM₁₀ peak recorded on Dec. 27th. With the PM₁₀ concentrations at the remote station remaining below the WHO daily limit (mean = 28.8 µg/m³), these observations well support the classification of these PDs as local in stationary conditions (Loc-Stat).

During PE-D, two PD were marked by the occurrence of sea breezes: On March 29th and 30th, starting at around 13:00-14:00 (Figure 4-11). A sea breeze is a mesoscale atmospheric phenomenon that occurs on the coast, generally by spring and summer weather under anticyclonic conditions. Indeed, the heating of the continental low atmospheric layers during the day leads to their elevation by convection and increases the temperature gradient between the sea and the coast. This creates an area of low atmospheric pressure over the continent and leads to a movement of a generally colder air mass from the sea to the continent, replacing the warmer continental air mass that has risen. This circulation, which lasts a few hours and can sometimes extend into the night after sunset, is called a sea breeze. The opposite phenomenon, called land breeze, usually occurs during the night. In the GDA, the occurrence of the sea breeze is generally marked by a sudden shift of the wind direction towards the north followed by a sharp decrease in temperature and increase in relative humidity (Augustin et al., 2020; Talbot et al., 2007). During PE-D, a high pressure system (1023±7 hPa) synonym of anticyclonic conditions was prevailing, the sudden shift in WD from E to NE on march 29th and S to N on March 30th, accompanied by decreasing T and increasing RH and WS when SR reaches daily maximum indicate the presence of sea breeze dynamics during these 2 days.

Chapter 4. Analysis and evaluation of typical PM₁₀ pollution days

The meteorological conditions during PE-D3 and during PE-B and C were nearly similar. During PE-B and PE-C, high wind speed sometimes reaching 10 m/s were observed and their variation was not influenced by highly fluctuating wind direction which, however, significantly influenced the evolution of PM₁₀ concentrations during this event. As shown in Figure 4-11, the highly variability of PM₁₀ as well as SO₂, NO₂ and to a lesser extend O₃ are influenced by the wind direction. The event ended during PE-C2 when stable northerly wind of high speed prevailed in the GDA.

In conclusion, the evolution of PM concentrations is inherently influenced by meteorological conditions and particularly changing wind direction and speed before the starting, during and after the pollution peaks during pollution events in the GDA.

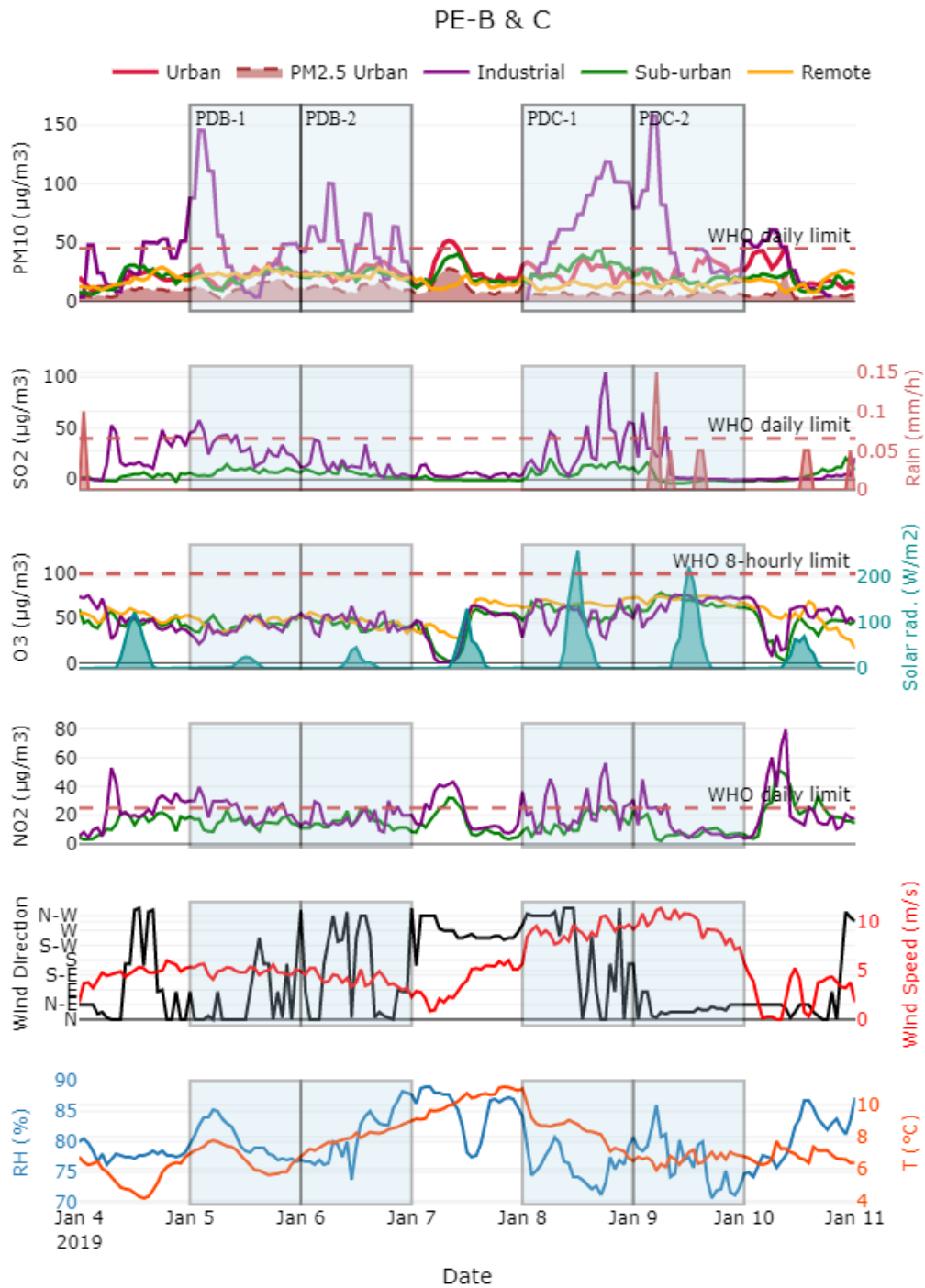


Figure 4-11. Evolution of PM, precursor gases and meteorological parameters during PE-B and PE-C

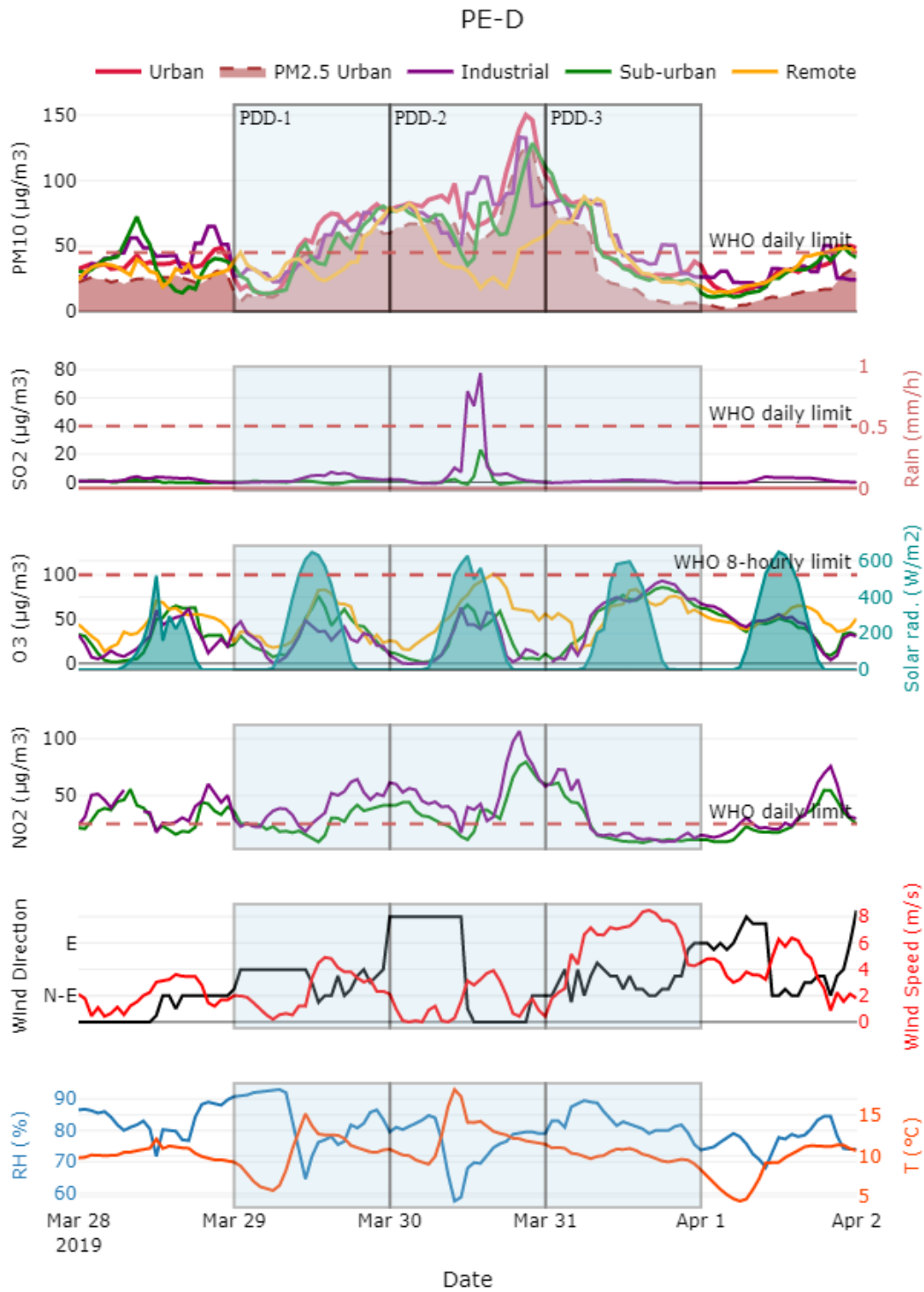


Figure 4-12. Evolution of PM₁₀, precursor gases and meteorological parameters during PE-D

4.4.2. Sources of PM during PE-A

For memory, PE-A is composed of two PD classified respectively as Loc-Stat-U and Loc-Stat-U+I. High levels of urban PM_{2.5} concentrations reaching 3 times the WHO limit of 15µg/m³ were recorded during PE-A and plotted in Figure 4-10. The results of the correlation performed on pollutant and meteorological data of PE-A show that PM₁₀ at U, I and S stations are highly related to PM_{2.5} at U with respective Pearson coefficients of 0.97, 0.80, 0.85 as shown in Table 4-5. It was shown earlier that nearly 80% of the PM during PE-A was in the fine mode. In northwestern Europe, the main sources of PM_{2.5} in 2019 were respectively residential and tertiary (43%), industry and energy (29%), traffic (road or not) (18%), waste (5%) and agriculture (3%) (EEA, 2021). The time series evolution of PM_{2.5} was similar with the evolution of PM₁₀ at the same station U, reaching their respective maxima at the same time: Dec 26th at 15:00, Dec 27th at 22:00 and Dec 28th at 14:00. In winter, the contribution of carbonaceous species from biomass burning due to residential heating is particularly important in Dunkirk (Crenn et al., 2018) and might significantly contribute to the peak observed at the end of the day during PDA-1 on Dec 27th. However, the daytime peaks are observed in the periods not corresponding to the diurnal peaks (08:00 and 18-20:00) associated with residential heating. These peaks can be related to prolonged daytime heating as a lot of people are on Christmas holidays. In the GDA, 89% of PM_{2.5} are emitted by the waste, industry and energy sector (according to the air quality report of (ATMO HdF, 2018), suggesting that high PM_{2.5} levels and peaks could also be associated to industrial emissions from industries located southward (see figure 4-13 a) this also supported by the very localized PM_{2.5} pollution area in the pollution polar plot (Figure 4-13).

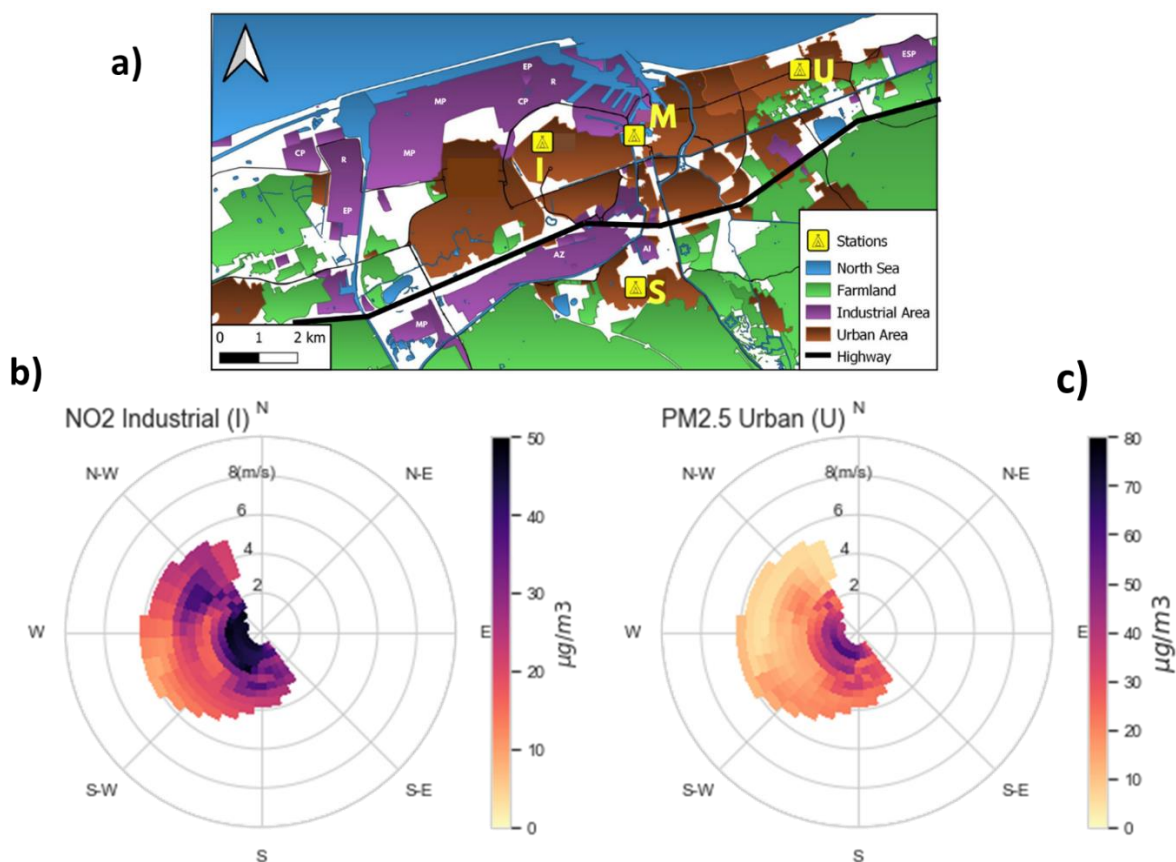


Figure 4-13. Location of the main land occupation map in the GDA together with pollution roses of urban PM_{2.5} (a) and industrial NO₂ (b) concentrations during PEA (both PDA-1 and PDA-2). Urban (brown) and industrial (purple) areas can be identified in the south-western direction using the urban station (U) as a reference.

Beside direct emissions of fine particles from industries, traffic or residential areas, secondary aerosols formation could also explain high PM_{2.5} in this event. Indeed, during PE-A, PM₁₀ at U ($r=0.64$), S ($r=0.64$) and I ($r=0.59$) were highly related to NO₂ from the industrial station. The evolution of NO₂ measured at the sub-urban and industrial stations are presented in Figure 4-9. During PE-A high NO₂ values above the daily WHO limits ($25 \mu\text{g}/\text{m}^3$) are permanently observed. The daily profile of NO₂ shows 2 maxima at 08:00 and 20:00. NO₂ and NO_x in general are principally emitted by traffic and industries in Dunkirk and are precursors of nitrate particles. Nitrates are formed under high RH, low temperature and stagnant conditions. In these conditions, gaseous nitric acid (HNO₃), resulting from NO₂ oxidation by OH radicals, can be solubilized into water droplets to form NO₃⁻ particles.

Chapter 4. Analysis and evaluation of typical PM₁₀ pollution days

In conclusion, beside primary emissions from industries, transport and residential heating, secondary aerosols formation account among the possible sources of PM₁₀ during this PE-A. In addition, temperature inversion, that happens under stagnant conditions and leading to a trap of the pollutants near the surface at night, could better explain the exceedance of the WHO limits during PE-A (Kukkonen et al., 2005; Sun et al., 2016).

	PM10 U	PM10 S	PM10 I	PM10 R	PM2.5 U	PM2.5 R	O3 S	O3 R	NO2 S	NO2 I	SO2 I	T°C	RH %	WS m/s	WD
PM10 U	1.00														
PM10 S	0.81	1.00													
PM10 I	0.80	0.89	1.00												
PM10 R	0.67	0.68	0.66	1.00											
PM2.5 U	0.97	0.85	0.80	0.71	1.00										
PM2.5 R	0.70	0.70	0.64	0.95	0.76	1.00									
O3 S	-0.64	-0.71	-0.61	-0.59	-0.72	-0.68	1.00								
O3 R	-0.58	-0.69	-0.68	-0.81	-0.60	-0.78	0.70	1.00							
NO2 S	0.49	0.61	0.57	0.21	0.51	0.28	- 0.73	- 0.38	1.00						
NO2 I	0.64	0.64	0.59	0.37	0.66	0.44	- 0.79	- 0.47	0.83	1.00					
SO2 I	-0.23	-0.09	-0.08	-0.31	-0.30	-0.37	0.15	0.16	0.27	0.01	1.00				
T°C	-0.41	-0.39	-0.21	-0.30	-0.53	-0.47	0.67	0.16	-0.34	-0.40	0.41	1.00			
RH %	-0.20	-0.32	-0.15	-0.28	-0.26	-0.26	0.26	0.16	-0.12	-0.22	0.15	0.31	1.00		
WS m/s	-0.52	-0.53	-0.41	-0.44	-0.61	-0.57	0.82	0.44	-0.54	-0.72	0.33	0.71	0.32	1.00	
WD	-0.35	-0.21	-0.10	-0.17	-0.42	-0.31	0.38	- 0.05	-0.04	-0.20	0.46	0.80	0.20	0.43	1.00

Table 4-5. Determination of the correlation factors between PM₁₀, PM_{2.5}, O₃, NO₂, SO₂, T°, RH, WS and WD at the Urban, Industrial, Sub-urban or Remote stations during PEA in the GDA.

4.4.3. Sources of PM during PE-B and PE-C

In Figure 4-11, it is noticeable that the variation in NO₂ and SO₂ concentration follows that of PM₁₀ concentrations at the I station. In northern France and particularly Dunkirk, NO_x are mainly emitted by road transport (around 40 to 50%) due to the dense transport network of the region connected with three main highways A16, A26 and A29. The industry, waste, energy and construction sectors contribute to almost 30% of NO_x emissions with the highest fraction attributed to energy production. The GDA is the first energy platform in northern France; NO_x can be emitted from the combustion processes happening in the refinery plants and waste incineration or from shipping emissions (EEA, 2021; Ledoux et al., 2018). SO₂ in return is a tracer of industrial activities and 80% of its emissions are associated with the industrial sector. The Pearson correlation factor between NO₂, SO₂ and PM₁₀ at the I station is weak for the NO₂ ($r=0.29$) and significant for SO₂ ($r=0.5$). In the meantime, relatively high and constant O₃ levels, above the seasonal mean, of $48.7 \pm 17.3 \mu\text{g}/\text{m}^3$ and $50.1 \pm 17.3 \mu\text{g}/\text{m}^3$, at I and S are recorded.

As O₃ production depends on insolation which was significantly low during these events, only long range transport could explain the levels of O₃ recorded. By saying it we assume that beside local industrial source of PM₁₀ a contribution from LRT is also to take into account especially when air masses come from the north as shown in the backward trajectories in Figure 4-14. During these events, air masses arriving in the GDA at 500 m altitude, principally came from the UK. As an example, the air mass that arrived on January 5th at 02:00 during the first peak carried pollutants from the densely populated cities of Birmingham from inner England before passing by the industrial city of Hull, then Norwich before arriving to Dunkirk. There was no correlation ($r=-0.04$) between urban PM_{2.5} and industrial PM₁₀ as it was observed during PE-A and the urban PM_{2.5}/PM₁₀ ratios were low (0.5 in PE-B and 0.3, 0.2 in PE-C) indicating the primary origin of PM₁₀ during these pollution days.

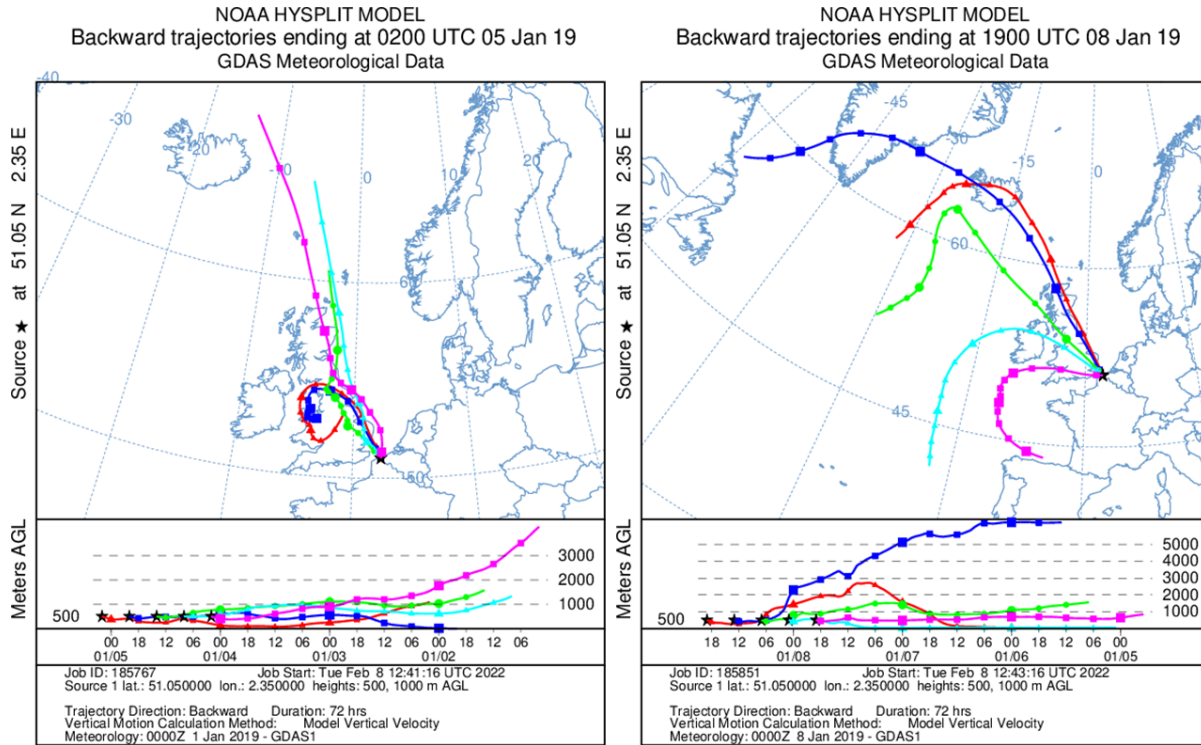


Figure 4-14. 3 days backward trajectories simulation showing air masses crossing the UK before arriving at 500 m altitude in the GDA during 2 pollution peaks recorded during PE-B and PE-C using the web-based version of HYSPLIT (<https://www.ready.noaa.gov/>).

4.4.4. Sources of PM during PE-D

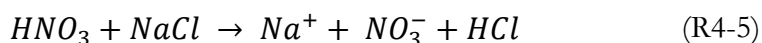
On march 31st, prevailing high WS increasing during the day can be correlated with decreasing PM₁₀ at the local stations (U, S and I) and increasing PM₁₀ at the R station located southwestward from the GDA. This indicates that beside strong background PM₁₀ concentrations, strong NE winds have probably carried some pollution from the GDA to the remote station on the last episode day, which is coherent with our classification (Regional episode in dispersion condition).

The results of the correlation analysis were performed on pollutant and meteorological data during PE-D are shown in Table 4-6. Concentration time series of PM_{2.5} in Figure 4-12 shows similar evolution between PM_{2.5} and PM for all the stations U, I and S except R. The Pearson correlation factor between urban PM_{2.5} and PM₁₀ at U (0.99), S (0.89) and I (0.84) is high indicating important contribution of fine PM during this event. This is valid for the first and second PD of PE-D where

the urban PM_{2.5}/PM₁₀ ratio was 0.8. On the third PD the ratio is 0.6 indicating the presence of a greater contribution of coarse and probably primary PM.

In Figure 4-15, the diurnal variation of PM₁₀ (a.), O₃ (b.), NO₂ (c.) and SO₂ (d.) is presented for spring 2019 (left) and the 3 days of PE-D (right). In spring O₃ and NO₂ have similar behaviors whatever the station. Morning and afternoon NO₂ peaks are likely related to traffic rush hours and midday in O₃ peak increasing with decreasing NO₂ indicating possible photochemical production of O₃. At the urban station U, PM₁₀ and PM_{2.5} concentrations are approximately constant all over the day (with a PM₁₀/PM_{2.5} mass concentration ratio \approx 2) and SO₂ increases during the day probably due to higher frequency of northerly winds passing through the industrial sector located upwind of I and S stations. During PE-D PM₁₀ and PM_{2.5} concentrations are of course higher. The levels are comparable and nearly constant at all stations from 01:00 and 11:00. From 12:00 to 24:00 an increase in PM levels is observed for all the stations, but more pronounced at the U and I stations.

The peak is localized between 21:00 and 24:00 indicating that nighttime processes might explain high levels of PM during this event. During this event the Pearson correlation factor (r) between PM_{2.5} and NO₂ at sites I and S is respectively 0.66 and 0.73. In comparison, this factor is low with SO₂ (0.16) indicating limited contribution of SO₂ and significant contribution of NO₂ to PM_{2.5} formation from secondary processes during PE-D. This is possible during the day; we assume the formation of gaseous HNO₃ as a result of NO₂ oxidation by OH radicals. Nitric acid can then be transformed into particulate nitrates as a result of the heterogeneous reaction with sea salts following the reaction R4-1:



This does not mean that there are not nighttime processes contributing to nitrate formation. However, we attribute nighttime maximum PM_{2.5} concentrations to the decrease of the boundary layer height followed by a reduction in the mixing volume and leading to an increase of the accumulated PM_{2.5} concentrations.

Chapter 4. Analysis and evaluation of typical PM₁₀ pollution days

	PM10 U	PM10 S	PM10 I	PM10 R	PM2.5 U	O3 S	O3 R	NO2 S	NO2 I	SO2 I	T°C	RH %	WS m/s	WD
PM10 U	1.00													
PM10 S	0.90	1.00												
PM10 I	0.84	0.82	1.00											
PM10 R	0.50	0.64	0.50	1.00										
PM2.5 U	0.99	0.89	0.84	0.49	1.00									
O3 S	-0.33	-0.51	-0.24	-0.41	-0.39	1.00								
O3 R	0.10	-0.07	0.16	-0.46	0.06	0.66	1.00							
NO2 S	0.65	0.76	0.59	0.42	0.66	0.74	0.23	1.00						
NO2 I	0.71	0.68	0.61	0.39	0.73	0.67	0.18	0.91	1.00					
SO2 I	0.14	0.08	0.32	-0.16	0.16	0.16	0.38	-0.05	0.03	1.00				
T°C	0.57	0.47	0.46	0.15	0.55	0.07	0.45	0.22	0.27	0.39	1.00			
RH %	-0.18	-0.03	-0.01	0.30	-0.13	0.36	0.51	0.21	0.16	-0.37	0.52	1.00		
WS m/s	-0.30	-0.32	-0.14	-0.10	-0.37	0.80	0.49	-0.52	-0.55	0.01	0.09	0.06	1.00	
WD	-0.05	-0.09	-0.21	0.22	-0.08	0.05	0.32	-0.27	-0.20	-0.23	0.25	0.20	0.11	1.00

Table 4-6. Determination of the correlation factors between PM₁₀, PM_{2.5}, O₃, NO₂, SO₂, T°, RH, WS and WD at the Urban, Industrial, Sub-urban or Remote stations during PED in the GDA.

Chapter 4. Analysis and evaluation of typical PM₁₀ pollution days

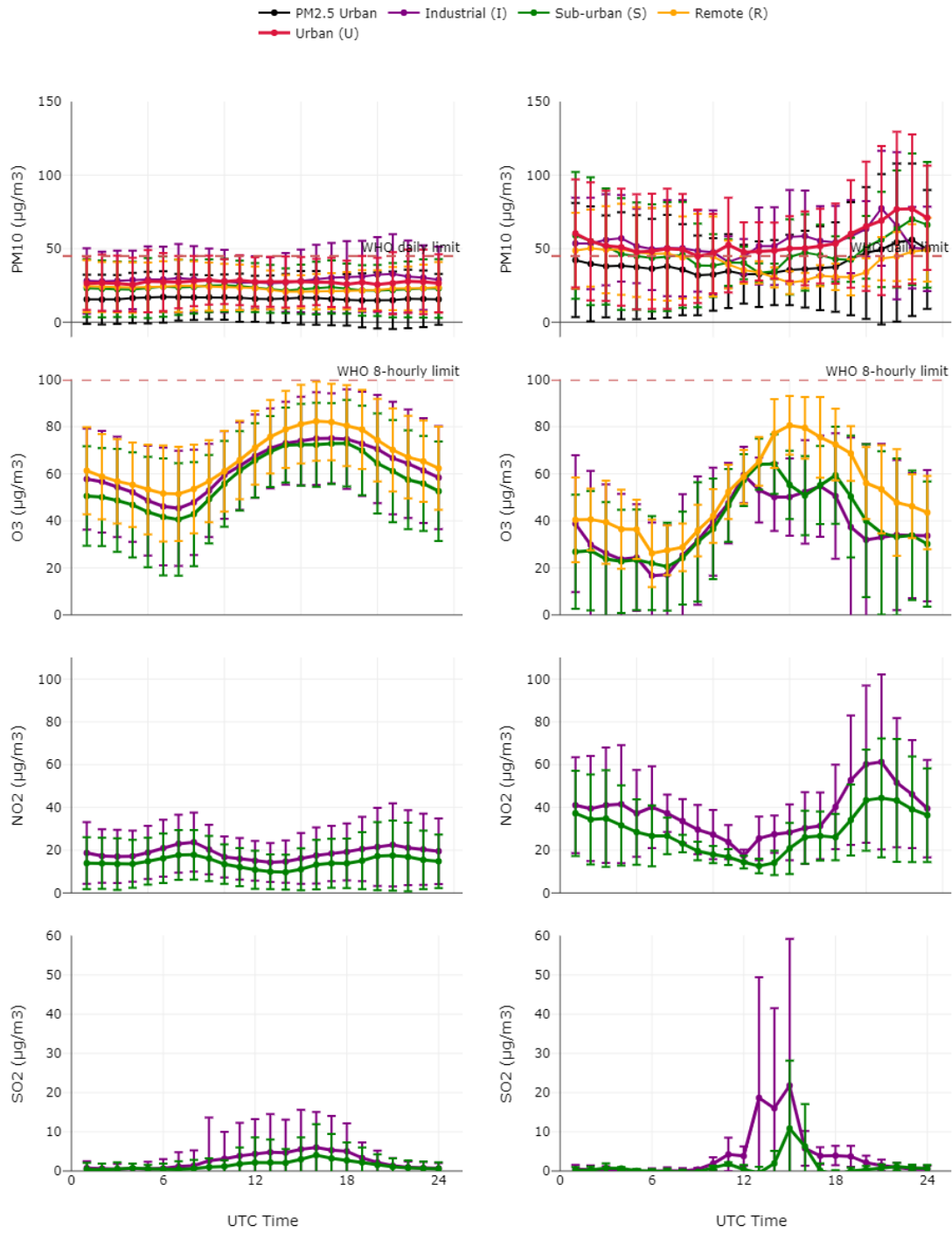


Figure 4-15. Daily cycle of PM₁₀, O₃, NO₂ and SO₂ concentrations during PED for remote (orange), sub-urban (green), industrial (purple) and urban (brown).

4.5. Conclusion

In conclusion, pollution days in the Great Dunkirk Area (GDA) are dominated in number by local episodes. Their spatial and temporal variability is clearly noticeable. January to May is the period with the highest number of pollution days mainly due to favorable meteorological conditions at local and synoptic scale enabling the trapping of emitted local or transported pollutants, their accumulation resulting in the exceedance of regulatory limits. Local episodes of reduced amplitude observed at one station are the highest in number and generally last one day, however those of wider coverage can be observed during longer periods varying from 2 to event 7 days increasing the fraction of the population exposed. These consecutive pollution days were defined in the context of this study as pollution events and were finely studied at hourly resolution in order to identify the potential sources that can explain PM exceedance of the WHO levels. The object of following Chapter 5 is to perform a physico chemical characterization of individual particles collected during similar pollution events during the MIXTAPE Campaign.

CHAPTER 5.
PHYSICO-CHEMICAL
CHARACTERIZATION OF COARSE AND
FINE INDIVIDUAL PARTICLES
DURING POLLUTION EVENTS IN THE
GREAT DUNKIRK AREA.

5. Physico-chemical characterization of coarse and fine individual particles during pollution events in the Great Dunkirk Area.

In order to study the physico-chemical characteristics of fine and ultrafine particles and their evolution during pollution events, a sampling campaign named MIXTAPE for MIXing sTate of Atmospheric Particles during Pollution Events) has been performed in the Great Dunkirk Area (GDA) from January to October 2021. In this Chapter, we will discuss the results of the MIXTAPE campaign and focus on the physico-chemical composition, the chemical diversity and the mixing state of individual particles collected using highly time resolved particle sampling with the TRAPS. This fifth chapter is divided into 3 main sections:

- Overview of the MIXTAPE campaign (section 5.1)
- Assessment of the influence of different environmental factors on the evolution of individual particle composition and mixing state index (section 5.2)
- And a case study of the evolution of individual particle composition and mixing state index correlated with the evolution of PM, meteorology and dynamics during a typical pollution event. (section 5.3 and 5.4.)

5.1. MIXTAPE campaign overview

A set of instruments used for *in situ* monitoring and characterization of aerosols, meteorology as well as atmospheric dynamics have been deployed progressively at the MIXTAPE site (M) during the campaign. The site is located inside the Dunkirk harbor (see Figure 5-1) on the rooftop of the university building and was described in Chapter 2.

The campaign lasted from January to October 2021. In 2021, monthly mean temperatures were lower than those of years 2018 and 2019 especially in spring-summer months and were comparable to those of the year 2020 (see Figure 5-2. a). From January to September 2021 (period of the campaign), meteorological conditions were mild during winter, spring and summer with temperatures varying between 8.03 °C in January to maximum 15.8°C in July. The maximum temperature of 26.3°C was recorded in July 2021 which is nearly half of that recorded in 2019 (41.5°C) suggesting an overall mild summer.

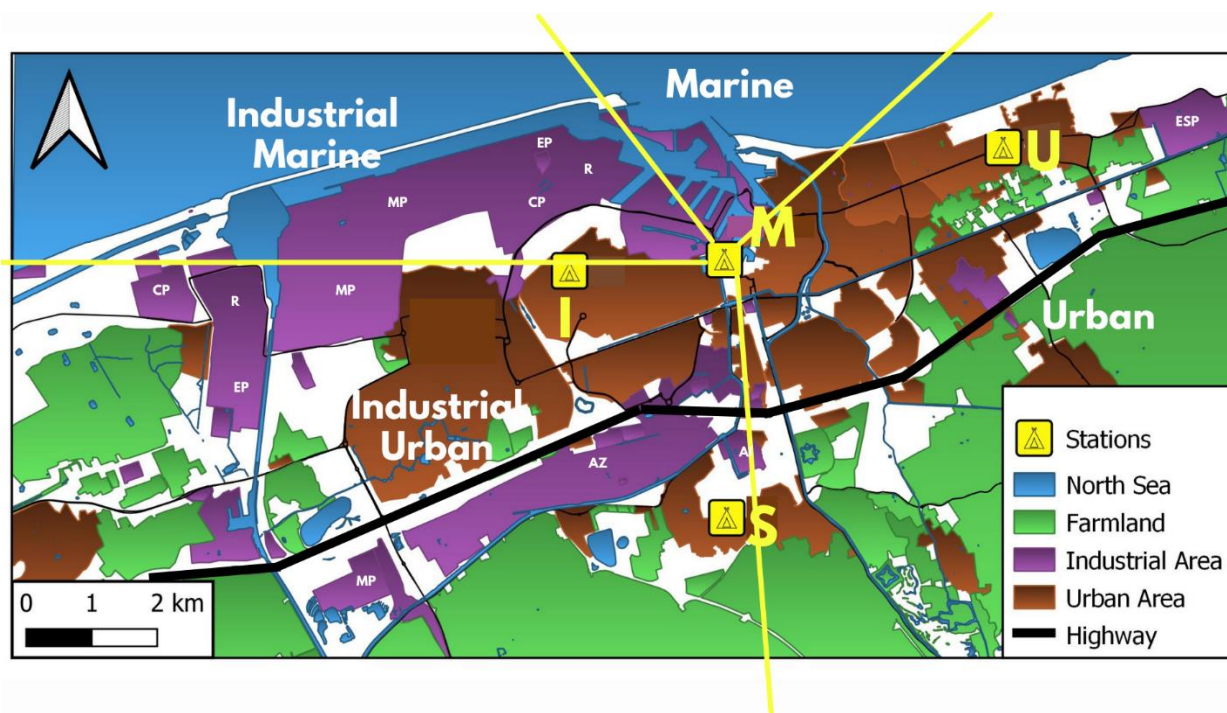
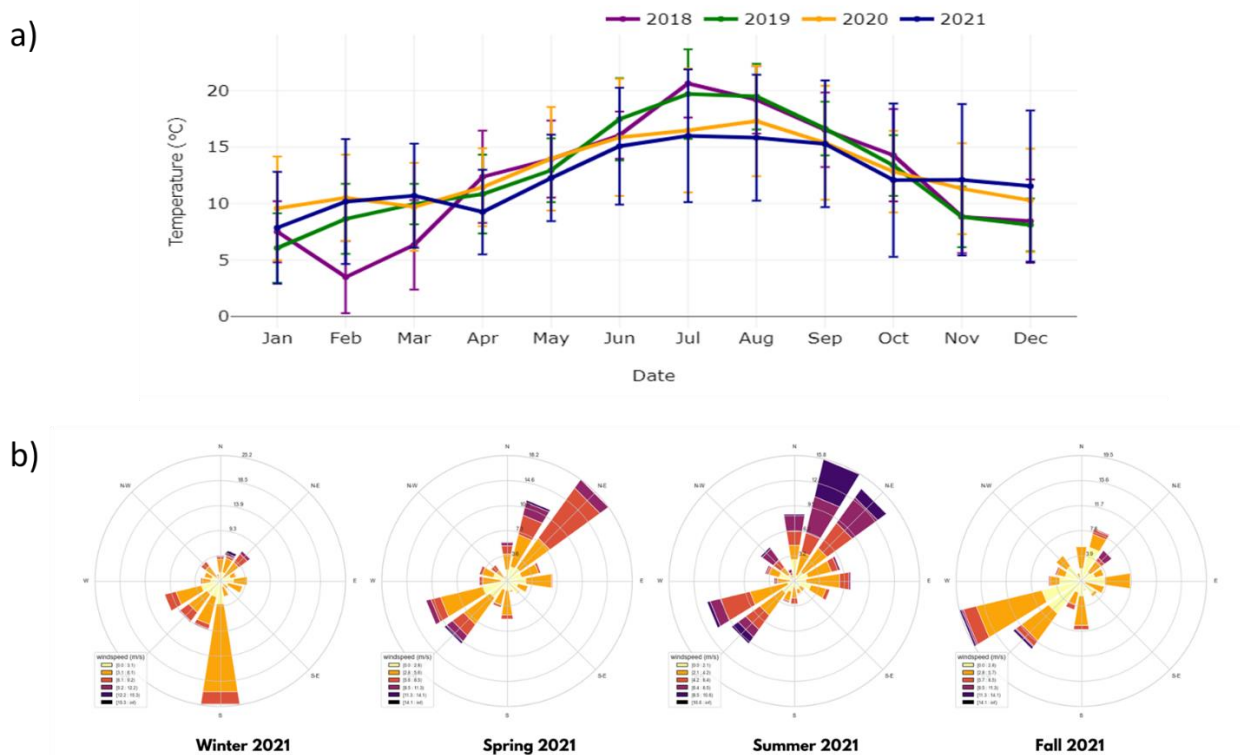


Figure 5-1. Map showing the Mixtape sampling site (M) and air quality monitoring stations (U, I and S) of the Atmo-HdF (www.atmo-bdf.fr) network. Industrial (purple) and urban (brown) areas, farmlands (green), northern sea (blue) as well as the road network (black lines) characteristics of the GDA are also presented. 4 main wind sectors influencing the M site are also represented: the marine, industrial-marine, industrial urban and urban sectors. MP: Metallurgy plant, EP: energy plant, R: Oil Refinery, CP: Chemical plant, AZ: Astra Zeneca, ESP: Electrical steel plant are among the main industrial installations across the study area.

Wind distribution was similar than that of year 2019 (presented in Chapter 2), the main directions being South-southwest (S-SW) in winter and fall and NE-SW in spring and summer. The mean wind speeds were comparable from one month to the next during the campaign (around 4 m/s) however the frequency of highest speeds (above 5 m/s) were recorded in summer, mainly from the NE direction associated with marine air masses (Figure 5-2. b). This could explain the moderate temperatures recorded in summer.

Chapter 5. Physico-chemical characterization of individual particles



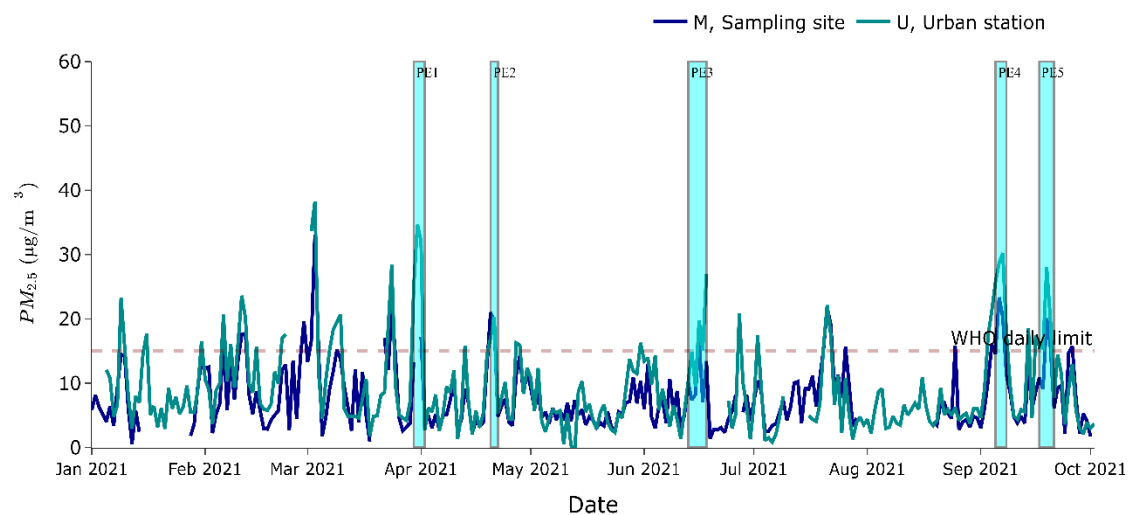


Figure 5-3. Temporal variation of daily $PM_{2.5}$ concentrations at the M and U stations from January to September 2021. Cyan rectangles highlight the studied pollution events where particle samples were collected.

These periods presented in Table 5-1, corresponded to: PE1 with 2 PDs from March 31st (PD1-1) to April 1st (PD1-2) respectively classified as Loc-Stat-3 and Reg-Disp-3. PE2, were only the first day on April 20th was classified as Reg-Stat-1 i.e. regional episode in stationary conditions where only one local station shows exceedance of PM_{10} levels (I station here). PE3 with 2 PDs (PD3-1 and PD3-2) recorded on June 16th and 17th at the I station, in both stationary and dispersion conditions, and classified as Loc-Stat-1 and Loc-Disp-1. These 3 events are assigned to the most common PD categories occurring in the Great Dunkirk Area (GDA) based on the typology presented in chapter 4. PE4 and PE5 were $PM_{2.5}$ pollution days. For these 2 events, although the PM_{10} limit at none of the local stations were exceeded, the $PM_{2.5}$ levels recorded at the urban station U were above the WHO limits. These $PM_{2.5}$ levels were similar to those observed during the first PE (PE1) for which the urban site U was concerned by the exceedance of the PM_{10} level.

Chapter 5. Physico-chemical characterization of individual particles

		Date	WS (m/s)	P (hPa)	PM10 I	PM10 U	PM10 R	PM10 S	PM2.5 U	PM2.5 R	PM2.5 M	BC M	TYPE
PE1	PD1-2	2021-03-31	1.2	1018	69	48	40	63	35	28	-	-	Loc-Stat-I+U+S
	PD1-3	2021-04-01	4.3	1014	62	51	55	60	32	35	-	-	Reg-Disp-I+U+S
PE2	PD2-1	2021-04-20	1.9	1015	69	24	45	36	17	36	21	0.9	Reg-Stat-I
	PD2-2	2021-04-21	5.7	1018	38	34	47	36	20	36	20	0.4	PM2.5
PE3	PD3-1	2021-06-14	2.3	1018	57	24	22	28	15	12	7	0.6	Loc-Stat- I
	PD3-2	2021-06-16	2.7	1010	45	31	24	28	20	16	17	0.7	Loc-Stat- I
	PD3-3	2021-06-17	3.1	1008	51	18	15	37	15	12	7	0.5	Loc-Disp-I
PE4	CD	2021-09-06	2.8	1020	33	36	27	38	29	22	23	0.9	PM2.5
	CD	2021-09-07	2.3	1019	-	39	31	38	30	21	20	1.0	PM2.5
PE5	CD	2021-09-18	1.7	1012	18	17	12	18	15	9	9	0.6	-
	CD	2021-09-19	2.1	1011	41	27	23	29	28	22	20	0.7	PM2.5

Table 5-1. Classification of the pollution days (PD) investigated during MIXTAPE. Daily mean PM₁₀, PM_{2.5} and BC concentrations are given in µg/m³

During this campaign, a total of 29 samples arranged in a chronological order, from the first S1 collected during PE1 to the last sample S29 (Table 5-2) collected during PE5, are exploited in the following sections. These samples were collected during classified PM₁₀ PDs, during PM_{2.5} PDs for polluted samples “PS” and during periods where any of the threshold values were exceeded for both PM₁₀ and PM_{2.5}. Those last samples were classified as clean samples “CS”. The SEM-EDX data of all samples were available for the fine particle fraction, but not for the coarse fraction.

Chapter 5. Physico-chemical characterization of individual particles

PE		Sample	Date	Starting time
PE1	PD1-1	S1	3/31.	08.00
		S2	3/31.	17.00
		S3	3/31.	22.00
	PD1-2	S4	4/1.	04.00
		S5	4/1.	08.00
		S6	4/1.	12.00
		S7	4/1.	17.00
PE2	PD2-1	S8	4/20.	08.00
	PD2-2	S9	4/21.	09.00
PE3	CD	S10	6/13.	01.00
	PD3-1	S11	6/14.	04.00
		S12	6/14.	24.00
	CD	S13	6/15.	12.00
	CD	S14	6/15.	11.00
	CD	S15	6/15.	18.00
	PD3-2	S16	6/16.	01.00
		S17	6/16.	11.00
		S18	6/16.	16.00
		S19	6/16.	21.00
	PD3-3	S20	6/17.	02.00
PE4	CD	S21	9/6.	11.00
		S22	9/6.	16.00
	CD	S23	9/7.	08.00
		S24	9/7.	14.00
PE5	CD	S25	9/18.	18.00
	CD	S26	9/19.	24.00
		S27	9/19.	05.00
		S28	9/19.	16.00
		S29	9/19.	21.00

Table 5-2. Sample ID and collection starting time

Chapter 5. Physico-chemical characterization of individual particles

5.2. Overview of individual particle composition and mixing state during MIXTAPE

A total of 22714 and 5315 individual particles were analyzed respectively from the fine (0.1-1 μ m) and coarse (1-10 μ m) fractions and classified according to their dominant elements into 7 types: Carbonaceous, S-rich, Na-rich, Ca-rich, Si, Al-rich, Metals and unclassified (see details on this classification in Chapter 2, section 2.3.2.5). It is important not to consider these types as pure, because each group bears the name of the predominant element, but the presence of other elements, although in minority proportions, is not excluded.

In order to quantify and describe the chemical evolution of particles during this pollution events, a mixing state index χ was calculated based on the concept of mixing entropy (Riemer and West, 2013) from automated TSEM-EDX data of individual particles. This mixing state index indicates the distribution of elemental species across particle population of an aerosol, as exposed in Chapter 2. For memory, χ varies between 0 when each particle in the population bears single element (external mixing) to 1 when each element present in the population is present in the same proportion at the particle level (full internal mixing). Calculated from the affine ratio between the average particle diversity ($D\alpha$) representing the number of effective elements present in particles and the bulk diversity $D\gamma$ representing the number of effective elements in the population. In this study, the values of $D\alpha$ and $D\gamma$ vary between 1 and 13 which is the total number of elements considered during the determination of the mixing state index, χ .

5.2.1. Evaluation of the accuracy of TSEM-EDX data

In order to correctly interpret this parameter, it is imperative to firstly evaluate the associated errors. The relative error can influence the interpretation of the results on many aspects as it concerns the relative abundance of individual particles, the calculation of $D\alpha$, $D\gamma$ diversities and χ . In a recent publication, (Gasparik et al., 2020) evaluated the error introduced in quantifying aerosol mixing states due to a limited particle sample size, by using models and observation data from a field campaign. By varying the sample size from 10 to 10 000 individual particles, they demonstrated that small sample sizes led to an overestimation of the average particle diversity $D\alpha$ while the bulk diversity $D\gamma$ was underestimated. This leads to an overestimation of χ . Although a mathematical function was not proposed to quantify directly the error associated with χ , these results suggest that it decreases as the number of analyzed particles N increases with a rate of $1/\sqrt{N}$, which is in the same line with counting

Chapter 5. Physico-chemical characterization of individual particles

error associated with SEM-EDX analysis. In our study, the relative error associated to $D\alpha$, $D\gamma$ and χ for fine particle fraction (Figure 5-4) varies between 2% to 11%. 75% of the samples are associated with a relative error below 5% and 97% below 10%. If we consider 10% as the maximal acceptable error, we can conclude that the interpretation of the results of this study for all the sample's $D\alpha$, $D\gamma$ diversities and χ are reliable. However, the $D\alpha$, $D\gamma$ diversities and χ of individual particles (Carbonaceous, S-rich, Na-rich, Ca-rich, Si, Al-rich and Metals) might have been over and or underestimated especially for samples of N lower than 1000 and for individual particle fraction lower than 10% (Choël et al., 2010).

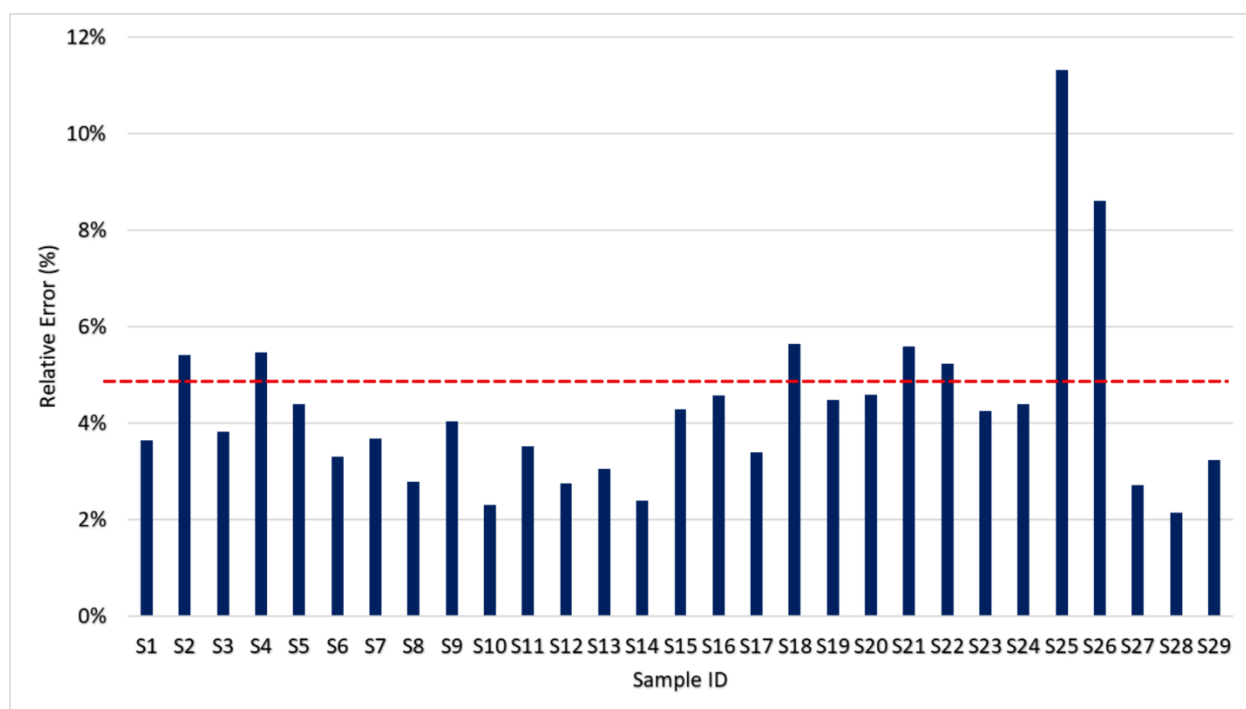


Figure 5-4. Relative error associated to $D\alpha$, $D\gamma$ and χ for the different samples (S1 to S29) of fine particle fraction.

In conclusion, only 7 samples have a relative error associated to $D\alpha$, $D\gamma$ and χ above 5% due to the sample size. Others limitations on the TSEM-EDX data could also be considered in this study:

- Analytical and counting errors on C and O during TSEM-EDX analysis associated with the presence of these two elements in the formvar carbon film of TEM grids used as substrate for particle sampling, that can lead to overestimation of these elements.

Chapter 5. Physico-chemical characterization of individual particles

- The EDX quantification method (PhiRhoZ) from the Bruker software used in this study is subject to overestimation of nitrogen due to a limited correction of the X-ray absorption of this element by the ultra-thin window of the detector. Considering the high number of analyzed particles for this study, a time-consuming quantification using the Monte Carlo method and leading to a more reliable quantification was not considered.
- Sampling and analytical artefacts due to the loss of volatile and semi-volatile compounds such as ammonium nitrates and some organics (Worobiec et al., 2003). Since the EDX analyses were performed at room temperature, only the most refractory compounds were detected.

5.2.2. Individual particle composition and mixing state during MIXTAPE

An overview of particles composition as well as their diversities ($D\alpha$ and $D\gamma$) and mixing state index (χ) for all samples collected during the Mixtape campaign are respectively presented in Figure 5-5 for the coarse and Figure 5-6 for the fine fraction. These results reveal that individual particle composition is dominated by carbonaceous and Na-rich particles, representing nearly 40 and 30% of all particles in both fractions, followed by S-rich (between 9 and 17%) and metal-bearing particles (around 5%). A high variability of particle composition and mixing state index is observed and cannot be related to the relative error.

Chapter 5. Physico-chemical characterization of individual particles

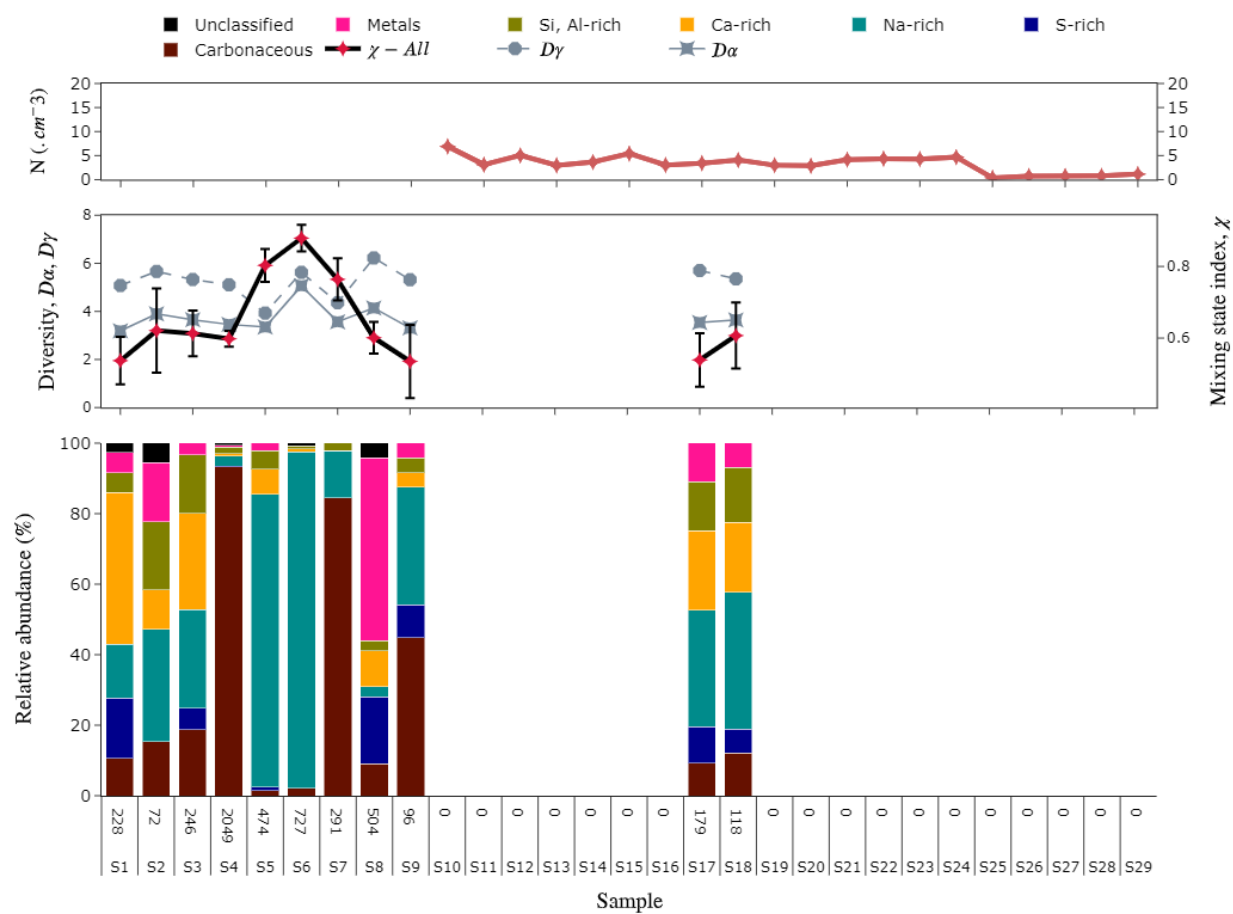


Figure 5-5. Atmospheric concentration (in cm^{-3} , 1-10 μm range) (top), D_α , D_γ and χ (middle), and relative abundance of individual particles (bottom) for all the samples collected on the coarse stage (1-10 μm) during this MIXTAPE campaign. Error bars plotted together with χ values. The number of analyzed particles is indicated above the sample number.

Chapter 5. Physico-chemical characterization of individual particles

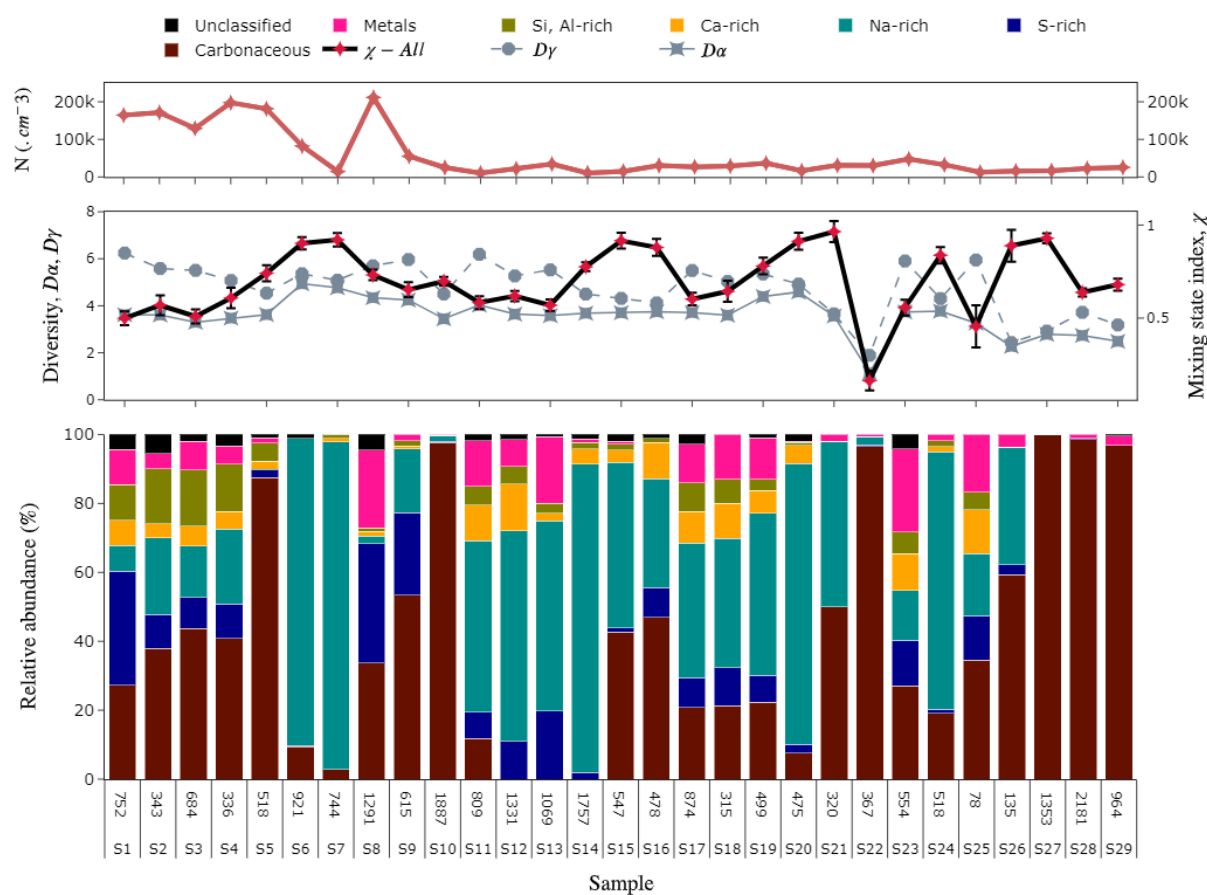


Figure 5-6. Atmospheric concentration (in cm^{-3} , 0.1-0.7 μm range) (top), D_α , D_γ and χ (middle) and relative abundance of individual particles (bottom) collected on the fine stage (0.1-1 μm) for all the samples collected during the MIXTAPE campaign. Error bars plotted together with χ values. The number of analyzed particles is indicated above the sample number (S_x).

These results also highlight that individual particles apparently identical in composition can hide important diversities in their mixing state. As an example, the fine fraction of samples S5, S10, S22 are all dominated by carbonaceous particles (Figure 5-6), but they are associated with very diversified mixing state, with χ values ranging from 0.16 to 0.74 indicating more or less heterogeneous particles and populations of particles. In the same way, S6 and S12 are both dominated by sea-salt particles, but their mixing states are completely different.

Chapter 5. Physico-chemical characterization of individual particles

Thus, with automated individual particle analysis, and thanks to the mixing state index, we can show that cases that may seem simple can be more complex without resorting to the more time-consuming methods of fine particle observation such as TEM.

Furthermore, the high variability of mixing state index for particles with apparently a rather similar chemical composition allows to conclude that the exploitation of the mixing state is meaningful only if it is related to the environmental conditions observed during the sampling. There is thus, a need to investigate the factors influencing it.

5.3. Impact of environmental factors on the composition and mixing state of fine particles

In this section we will investigate the influence of several environmental factors on individual particle composition and the mixing state index. First of all, the pollution level will be considered by a comparison of individual particles collected during clean and polluted days. Then, the influence of local dominant winds that affected the GDA during the events will be assessed. Finally, the influence of the type of pollution day as defined in Chapter 4 (local or regional, with stationary or dispersion conditions) on particle characteristics will be studied. As coarse particles are not available for all samples, only particles collected in the fine fraction will be discussed in this section 5.3. Although they represent a low fraction of particle mass (PM_{10} and $PM_{2.5}$), this fine fraction dominates the number concentration of aerosols and has an incontestable impact on human health.

5.3.1. Influence of pollution level

The 29 samples collected on the fine impactor stage during the five PE of the MIXTAPE campaign are considered here (22 714 analyzed particles by TSEM-EDX). All the samples collected when hourly average PM_{10} and/or $PM_{2.5}$ concentrations at any local station (M, S, I and U) were below respectively 45 and $15 \mu\text{g}\cdot\text{m}^{-3}$ were considered as Clean Samples (CS). The remaining samples were then classified as PM_{10} or $PM_{2.5}$ Polluted Samples (PS) when respectively PM_{10} or $PM_{2.5}$ exceeded the WHO limits during the collection time. Samples exceeding only the $PM_{2.5}$ limits are classified as $PM_{2.5}$ PS. Thus, PM_{10} PS is characterized by a coarser particulate pollution than $PM_{2.5}$ PS. The relative number percentage ($N(\text{typei})/N(\text{total})\cdot 100$) of particle types for each sample category (CS, PM_{10} PS and $PM_{2.5}$ PS) are provided in Table 5-3. and presented in Figure 5-7. It can be noted that the atmospheric concentration of particles (PC) in the range 0.1- $1\mu\text{m}$ is not very different between CS, $PM_{2.5}$ PS and

Chapter 5. Physico-chemical characterization of individual particles

half of PM₁₀ PS (from S9 to S20), but the composition of these particles is clearly different. For CS, the fine particles were composed in majority of Carbonaceous (45%) and Na-rich (42%) particles. For PM₁₀ PS, the proportion of Na-rich (39%) and Carbonaceous (28%) is slightly lower than for CS, to the profit of S-rich (13%), metals (8%) and Si-rich (5% each). The increase of the relative contribution of S-rich particles is an indication of the presence of secondary particles during PM₁₀ polluted samples. For PM_{2.5} polluted samples, the particles were composed essentially of carbonaceous particles (82 %).

Sample category	NS	NP	PC	Carb.	S-rich	Na-rich	Ca-rich	Si, Al-rich	Met.	Uncl.	χ	D α	D γ
CS	5	5871	32312	45%	3%	42%	5%	2%	3%	1%	0.77±0.17	4.3±0.6	5.2±0.2
PM ₁₀ PS	9	6898	125044	28%	13%	39%	5%	5%	8%	2%	0.63±0.10	3.8±0.4	5.5±0.5
PM _{2.5} PS	8	6392	27763	82%	1%	12%	1%	1%	3%	0%	0.71±0.26	2.8±0.9	3.5±1.2

Table 5-3. Relative number percentage of individual particles for clean samples (CS), PM₁₀ and PM_{2.5} polluted samples (PS). NS is the number of samples, NP the number of analyzed particles and PC the mean Particle Concentration (in #.cm³) for the fine (0.1-1 μ m) size fraction.

In Figure 5-7, the evolution of D α , D γ and χ for all the sample categories is also presented. The D α , D γ and χ showcased similar variation whatever of the sample type (CS, PS). The mean (D α , D γ and χ) are (4.3, 5.2, 0.77), (3.8, 5.5, 0.63) and (2.8, 3.5 and 0.71) respectively for CS, PM₁₀ PS and PM_{2.5} PS. The high variability in particle mixing state within different categories can be related to the alternation between more homogeneous population composed of mainly Na-rich and Carbonaceous (S6, S7) and highly diverse heterogeneous populations (S3, S4). There is no significant difference between χ values during clean and polluted periods for this fine fraction, so the mixing state variability would be explained by factors other than the exceedance or not of PM₁₀ and/or PM_{2.5} concentrations.

Chapter 5. Physico-chemical characterization of individual particles

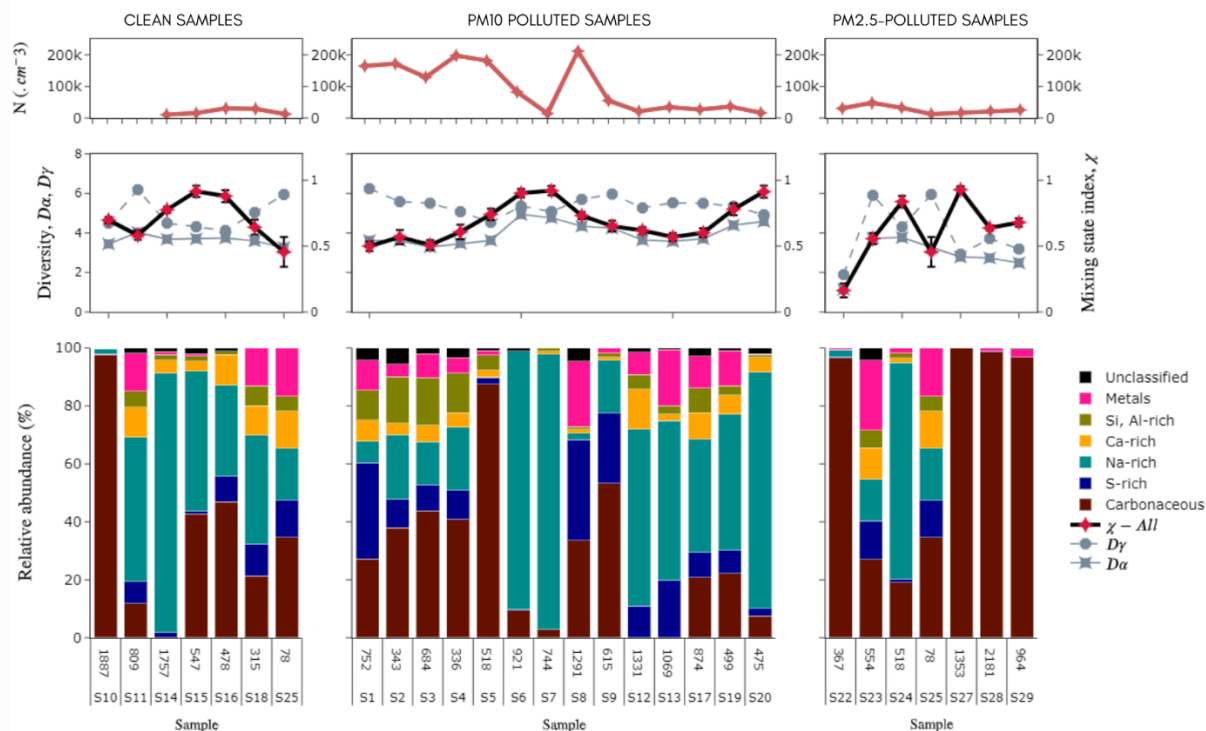


Figure 5-7. Atmospheric concentration (in cm^{-3} , 0.1- 0.7 μm range) (top), $D\alpha$, $D\gamma$ and χ (middle) and relative abundance of individual particles (bottom) collected on the fine stage (0.1-1 μm) during clean days (left) and polluted days (right) for samples S1 to S29.

5.3.2. Influence of the local wind sector

In this section, the influence of local wind direction on particle composition and mixing state was investigated. As particle composition in the GDA is known to be significantly influenced by meteorology, knowing the origin of the wind during periods of PM exceedance could help to identify the potential local or regional sources of particles. For this study, the seven samples collected during clean days were removed, the 22 other samples are classified according to the prevailing local wind sector: urban, marine, mixed industrial-marine or mixed industrial urban (Figure 5-1). A total of 16844 individual particles were compared and the results are provided in Figure 5-8.

Chapter 5. Physico-chemical characterization of individual particles

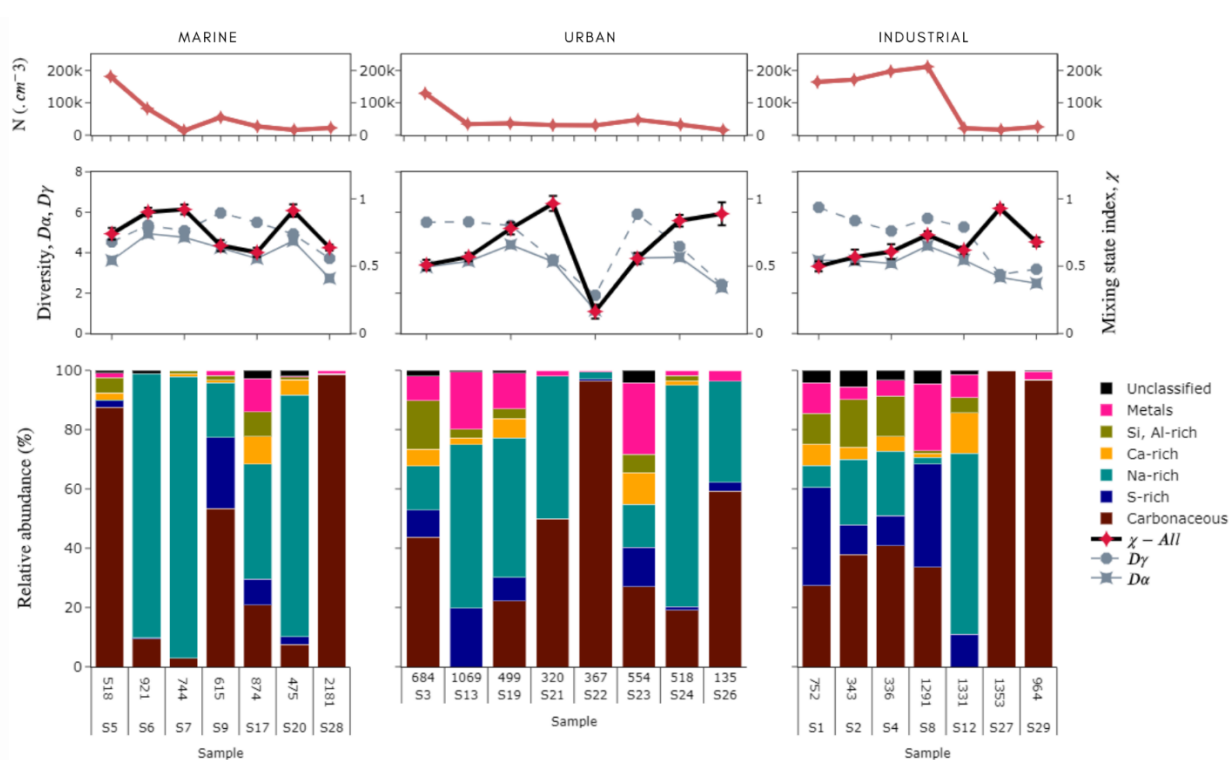


Figure 5-8. Atmospheric concentration (in cm^{-3} , 0.1-0.7 μm range) (top), $D\alpha$, $D\gamma$ and χ (middle) and relative abundance of individual particles (bottom) collected on the fine stage (0.1-1 μm) under blowing winds from sectors Marine, Urban, Industrial (Industrial-urban and Industrial-Marine) sectors.

Whatever the wind sector considered, all particle types are observed. Moreover, for a same wind sector, the relative proportion of particle types presents a very strong variability which suggests that the local wind direction does not permit to discriminate the fine particle sources.

Concerning particle mixing state (Figure 5-8, top), χ values oscillate between 0.6 and 0.92 except in the urban sector where a minimal χ value of 0.2 was obtained for one sample. Mean $D\alpha$, $D\gamma$ and χ are 4.1 ± 0.6 , 5.1 ± 0.7 and 0.77 ± 0.14 for the marine sector, 3.2 ± 1.0 , 4.3 ± 1.5 and 0.7 ± 0.1 for the urban sector and 3.4 ± 0.6 , 4.9 ± 1.3 and 0.6 ± 0.14 for the mixed industrial/marine and industrial/urban sectors. Therefore, there is no significant difference between the mixing state of the different wind sectors.

The conclusion of this classification is that the samples of the same wind sector present a very great heterogeneity in composition and mixing state, which tends to show that this classification is not relevant and that other parameters than the wind direction must be considered.

Chapter 5. Physico-chemical characterization of individual particles

5.3.3. Influence of the pollution type

The 29 samples collected during the five studied pollution events in 2021 were classified base on daily PM₁₀ data recorded at U, S, I and R stations as in Chapter 4. 2 non classified (NC) samples (in case of missing PM₁₀ data for one station) as well as 7 samples collected during clean days were excluded from this analysis. PM_{2.5} pollution samples were also added as a complementary group with PM_{2.5} concentrations recorded on the M station. The relative number percentage of individual particle types and their mixing state (D α , D γ and X values) are presented in Figure 5-9 and Table 5-4. It should be kept in mind that the analyzed particles were collected at station M which is located between stations I and U (Figure 5-1), while the classification of the sample is based on the PM₁₀ levels recorded at the four Air Quality Monitoring Station (U, S, I and R stations). One of the goals here is firstly to reveal if the composition of fine particles at station M is related to the PM₁₀ exceedances observed at the other 3 sites (I, U and S) in GDA.

Type	NP	NS	Carbonaceous	S-rich	Na-rich	Ca-rich	Si, Al - rich	Metals	Unclassified
Loc-Disp-1-I	1806	2	12%	8%	61%	10%	3%	5%	1%
Loc-Disp-2-I+U	1618	2	13%	5%	65%	6%	5%	6%	1%
Loc-Stat-1-I	1568	2	26%	12%	42%	3%	2%	13%	1%
Loc-Stat-2-I+U	1291	1	34%	35%	2%	1%	1%	23%	5%
Loc-Stat-3-U+I+S	1779	3	36%	19%	13%	6%	14%	8%	4%
Reg-Disp-1-U	615	1	53%	24%	18%	1%	1%	2%	0%
Reg-Disp-2-U+I	921	1	9%	0%	89%				1%
Reg-Loc-3-U+I+S	854	2	69%	5%	9%	3%	9%	3%	2%
PM2.5	5320	6	93%	0%	5%	0%	0%	1%	0%

Table 5-4. Relative number percentage of individual particles calculated for each PD type based on hourly PM₁₀ concentrations (NP = number of analyzed particles, NS = number of analyzed samples)

Chapter 5. Physico-chemical characterization of individual particles

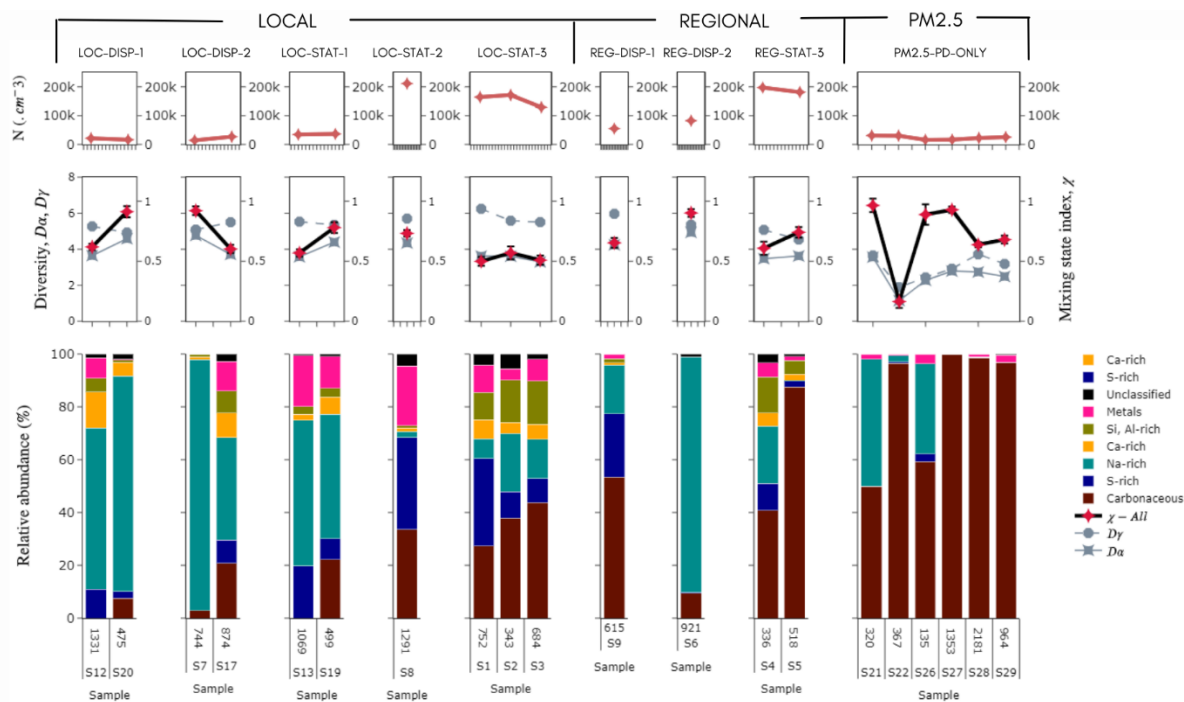


Figure 5-9. Atmospheric concentration (in cm^{-3} , 0.1-0.7 μm range) (top), D_α , D_y and χ (middle) and relative abundance of individual particles (bottom) collected on the fine stage (0.1-1 μm) for each type of polluted day. Results of the samples collected when only PM_{2.5} levels exceedance were observed are also presented.

By focusing on the four samples collected when polluted air mass has a very local extent (only one station in PM₁₀ exceedance), although it is the industrial station I which is always the only station in exceedance (S12, S20, S13 and S19), the particle chemical composition associated to these samples is highly variable. As an example, no metals-rich particle is observed in sample S20 while this particle type, good tracer of industrial emissions in the GDA, is clearly present for the 3 other samples.

In the same way, the three samples collected when the local polluted air mass is slightly more extensive (S7, S17 and S8 with I+U stations in PM₁₀ exceedance) have very different chemical composition. As an example, S7 is essentially composed of Na-rich particles while S8 does not contain them.

It is difficult to comment D_α , D_y and χ values for each episode, however, the differentiation based on stationary and conditions of dispersion allow us to say that:

- In stationary conditions, the Loc-Stat-2 and Loc-Stat-3 episodes show relatively low mixing state index (close to 0.5) which indicates a significant contribution of externally mixed particles so

Chapter 5. Physico-chemical characterization of individual particles

probably freshly emitted particles. Under the same stationary conditions for the Loc-stat-1 and reg-stat-3 episodes, high χ (close to 1) are observed. This shows that during these episodes the particles are older and strongly heterogeneous. In conclusion neither the number of stations nor the wind strength conditions might explain variation in the mixing state index.

- Under dispersion conditions, the Loc-Disp-1, Loc-Disp-2, Reg-Disp-1 and Reg-Disp-2 episodes present χ varying between 0.58 and 0.91 with an average around 0.74. This allows us to say that under these conditions we have mixed populations of rather fresh and aged particles. It's possible to say that the condition of dispersion does not influence the mixing state index. However, the limited number of samples does not favor clear-cut conclusions.
- There are no significant differences in the individual composition and mixing state of the particles for the local and regional episodes.
- The Lowest $D\alpha$ and $D\gamma$ (around mean 2 effective species) are observed during $PM_{2.5}$ episodes where the composition of the particles is dominated by carbonaceous (80%) particles which are mainly composed of C and O. These particles would thus be composed of soot (C) and organic matter (C and O). For these episodes, despite χ varying between 0.16 and 0.97, it's not possible to conclude on whether they were freshly emitted or aged particles. More attention in these particles is necessary.

5.4. Temporal variability of particulate pollution at the hourly scale

Classification of samples by local wind sector or by sample type (local/regional steady state/dispersion) did not provide conclusive findings on particle composition and mixing state. In fact, it seems that a fine analysis of the pollution episode on an hourly scale is necessary to understand the origin of the air masses impacting the M station and to apprehend the physicochemical processes impacting the composition and the mixing state of the particles. Thus, it is proposed in this section to study in depth the pollution event PE-1 which is typical of the pollutant events encountered in the Great Dunkirk Area (GDA).

The pollution event PE-1 is made of 2 pollution days (PD) respectively classified as "Loc-Stat-3" PD i.e. a local plume concerning 3 stations in stationary conditions and "Reg-Disp-3" i.e. a regional scale plume in conditions of dispersion as shown in Table 5-1. Local episodes account for nearly 77% of all episodes observed in the GDA. This event is therefore highly interesting as it accounted both a local and a regional pollution day consecutively from March 31st to April 1st, 2021.

Chapter 5. Physico-chemical characterization of individual particles

As we can see in table 5-1, $PM_{2.5}$ data of the MIXTAPE sampling site (station M) are missing due to instrument malfunction. In this case, we referred to the $PM_{2.5}$ of the urban station located around 10 km away from the M station. The hourly $PM_{2.5}$ measured at these two stations (M and U) during a similar pollution day (Loc-Stat-3) observed in August 2020 are relatively correlated (Figure 5-10, $R^2 = 0.64$), as the variability can be explained by changes in wind direction during the day.

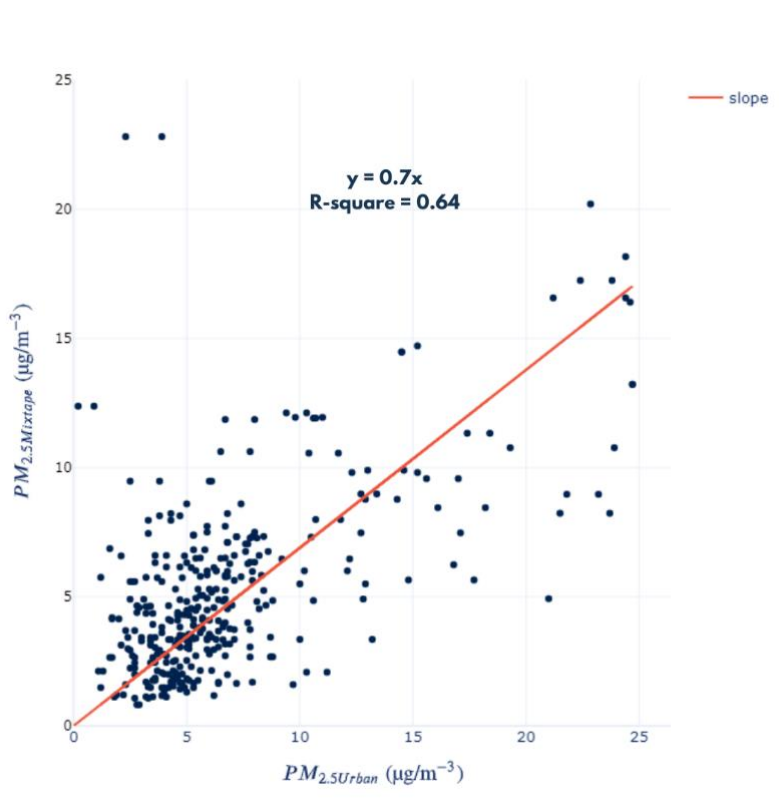


Figure 5-10. Linear regression between hourly Mixtape $PM_{2.5}$ and urban $PM_{2.5}$ data

7 particles samples from S1 to S7 were collected at various characteristic periods throughout PE1 as shown in Figure 5-11. S1 was sampled during the first PM peak under stagnant conditions. S2 in return was sampled at 16:00 during the sea breeze which can be identified by sudden change in wind direction from South to north followed by an increase in RH and decrease in temperature. The third sample S3 was collected at 22:00, at the transition period when winds shifted from northern to eastern direction and from low speed (below 2 m/s) to higher wind speed that might indicate potential LRT. The pollution peak was recorded at 04:00 when $PM_{2.5}$ concentrations value of $70 \mu g \cdot m^{-3}$, nearly 5 times the WHO limit, was reached. This corresponded to the period when sample S4 was collected. S5 was collected during a lower peak under easterlies of high speed. Samples S6 and S7 however, were

Chapter 5. Physico-chemical characterization of individual particles

collected when $PM_{2.5}$ were returned to safe levels during a clean period. The individual fine and coarse particle composition and the mixing state index of these particles are discussed hereafter.

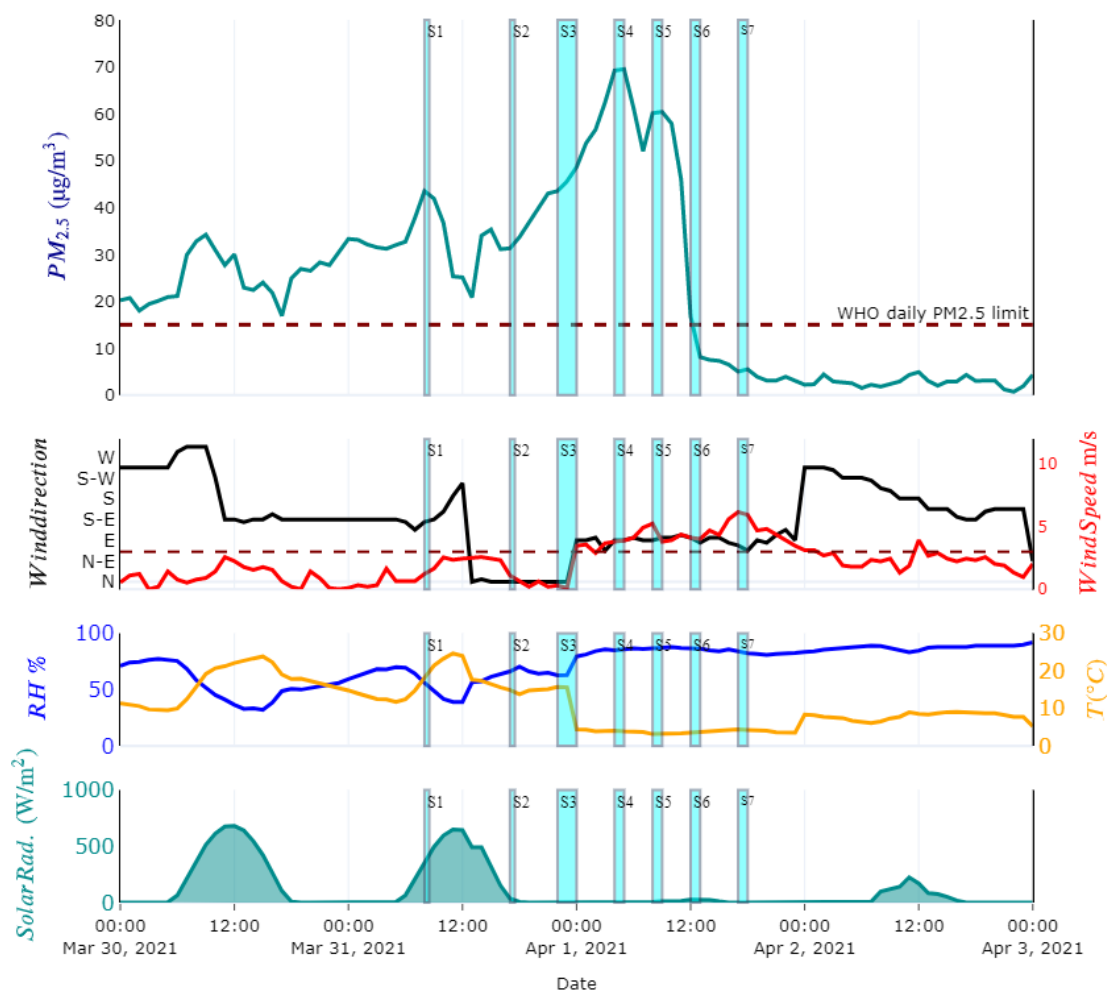


Figure 5-11. Time series evolution of $PM_{2.5}$ at the U station (darkcyan) and meteorological parameters: WS (red), WD (black), T (orange), RH (blue), SR (filled dark cyan). Colored rectangles in cyan represent TRAPS sampling periods.

In summary, the accumulation of pollutants in the atmosphere and the continuous increase of $PM_{2.5}$ concentrations during the first part of the PE, until April 1st at 4:00 am, can be explained by stationary atmospheric conditions. The stagnant air masses were then enriched by local pollution emissions. The sudden drop in concentration is due to a drastic the evolution of atmospheric dynamics towards a pollutant dispersion regime, as illustrated in Figure 5-12. Indeed, we observe an increase in the

Chapter 5. Physico-chemical characterization of individual particles

horizontal wind speed for this time (April 1st, 4:00 am), as well as in the vertical wind dispersion. This results in a strong increase of the atmospheric turbulence and a dispersion of local emissions in a regional air mass. The PM_{2.5} levels then return to concentrations well below the WHO daily PM_{2.5} limit (Figure 5-11).

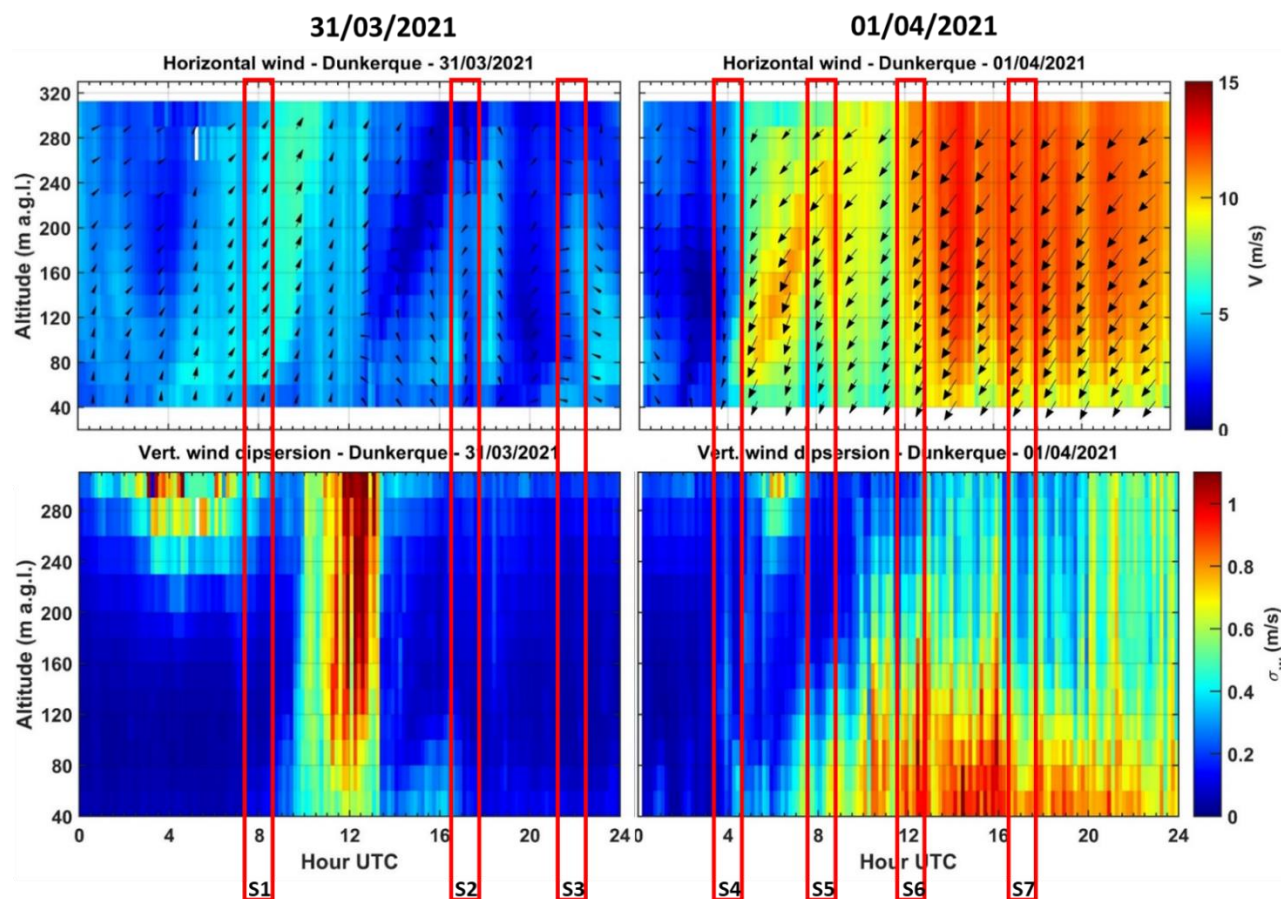


Figure 5-12. Time-height cross-sections of horizontal wind speeds and wind direction (top) and vertical wind dispersion (bottom) measured by the Doppler Lidar on March 31th and April 1st. Rectangles in red represent particle sampling periods

Therefore, an evolution of the particle composition and mixing state during these days is expected.

5.4.1. Evolution of individual particle composition and mixing state

The relative number percentage ($N(\text{type})/N(\text{total}) \times 100$) of individual particles according to each event type is provided in Table 5-5.

Chapter 5. Physico-chemical characterization of individual particles

TRAPS' Stage	Day	PD	N	Carbonaceous	S-rich	Na-rich	Ca-rich	Si, Al-rich	Metals	Unclassified
Stage 1	March 31st	Loc-Stat-3	546	15%	10%	23%	32%	12%	6%	2%
	April 1st	Reg-Disp-3	3250	60%	0%	35%	2%	2%	1%	1%
Stage 2	March 31st	Loc-Stat-3	1779	36%	19%	13%	6%	14%	8%	4%
	April 1st	Reg-Disp-3	1775	38%	3%	50%	2%	4%	1%	1%

Table 5-5. Relative number percentage of individual particles collected using the TRAPS coarse (Stage 1) and fine (Stage 2) stages per pollution day type during PE1.

On average, during “Loc-Stat-3” PD (S1, S2 and S3), the refractory particles were composed of Ca-rich (32%), Na-rich (23%), carbonaceous (15%), Si-Al-rich (12%), S-rich (10%), Metals (6%) and unclassified (2%) for the coarse particle fraction (Stage 1) and carbonaceous (36%), S-rich (16%), Si-Al-rich (14%), Na-rich (13%), Metals (8%), Ca-rich (6%) and others (4%) for the fine particle fraction (Stage 2). Thus, the contribution of minerals (Ca-rich and Si-Al-rich) is very important as observed in Figures 5-13 and 5-14. The Ca-rich particles varied from high contribution during S1 under south easterlies to low contribution (S2) under northerlies and rose again during S3 under N-NE winds. This suggest that different anthropogenic and natural sources of Ca-rich including residential installations, re-suspended soil dust, road dust and marine emissions are probably the sources of Ca-rich particles during S1, S2 and S3.

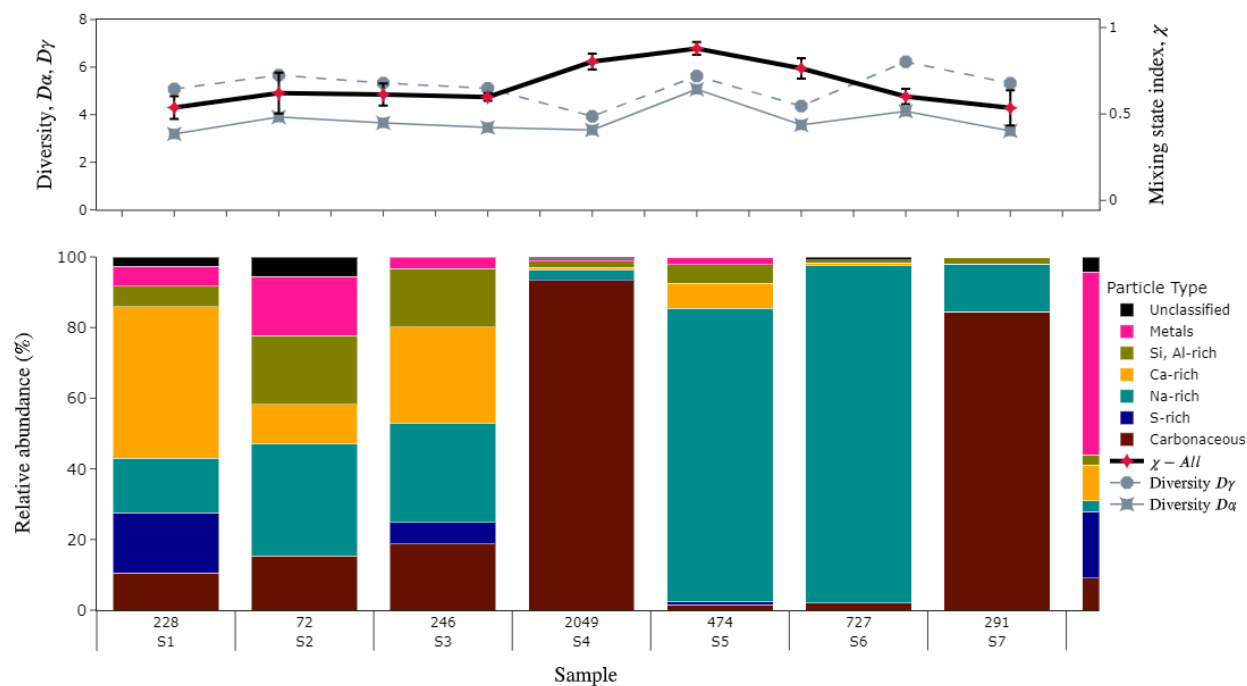


Figure 5-13. Evolution of D_α , D_γ and χ (top) and relative abundance of coarse (1-10 μm) individual particles for all the samples collected during PE1 from S1 to S7. Error bars plotted together with χ values.

During “Reg-Disp-3” PD (S4, S5 and S6), in the coarse fraction (stage 1), particle composition was dominated by carbonaceous (60%), Na-rich (35%), Ca and Si-Al-rich (4%), Metals (1%) and others (1%). The fine particle fraction was mainly composed of Na-rich (50%), carbonaceous (36%), Si-Al-rich (4%), S-rich (3%), Ca-rich (2%), Metals (1%) and others (1%).

There individual particle composition during PE1 is highly variable from S1 to S7 for both fractions. The chemical composition of individual particles is diverse for the first 3 samples (S1 to S3) and more homogeneous for samples S4 to S6 with a predominance of carbonaceous or Na-rich particles in variable proportions from the coarse to the fine fraction. This high variability can be explained by the change of wind direction which was more variable during “Loc-Stat-3” PD (SE and N winds of low speed) and dominated by Easterlies of high speed during “Reg-Disp-3” PD.

Chapter 5. Physico-chemical characterization of individual particles

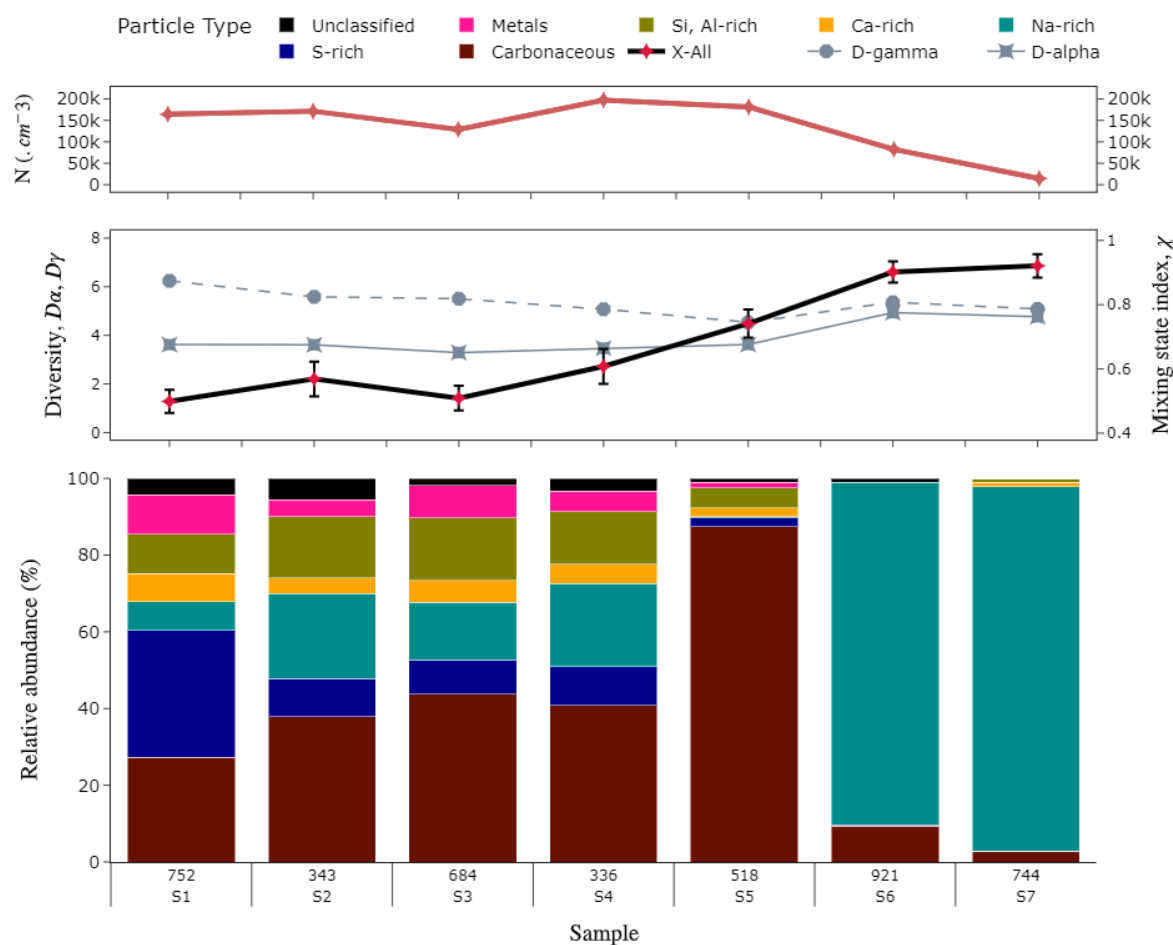


Figure 5-14. Atmospheric concentration (in cm^{-3} , 0.1- 0.7 μm range) (top), D_α , D_γ and χ (middle) and relative abundance of individual particles (bottom) collected on the fine stage (0.1-1 μm) for all the samples collected during PE1 from S1 to S7. Error bars plotted together with χ values. The evolution of particle number concentration (100-750 nm) is also plotted on the top.

In the “Reg-Disp-3” PD type, the particles collected during the high $PM_{2.5}$ concentrations (S4 and S5) are dominated by carbonaceous and Na-rich particles. There is a clearly decrease in the relative amount of minerals and metals while the proportion of carbonaceous and Na-rich is increasing as we move from S1 to S6 (Figure 5-13 and 5-14). Carbonaceous particles can be emitted from various activities mainly from combustion processes whereas Na-rich are mainly carried to the continent from the sea (AzadiAghdam et al., 2019). Prevailing marine sector winds of high wind speed at the collection time indicate a non-local but rather regional or LRT source of the carbonaceous particles.

Chapter 5. Physico-chemical characterization of individual particles

The evolution of the particle mixing state described by $D\alpha$, $D\gamma$ and χ is presented in Figure 5-13 for the coarse (Stage 1, top) and Figure 5-14 for the fine (Stage 2, middle) particle fraction. χ varies between a minimum value of 0.5 during S1 and maximum value of 0.92 during S7 depicting an increasing trend as we move from S1 to S7. This shows that particles tend to be more heterogeneous (internally mixed) over the course of PE1.

On March 31st (samples S1 to S3), an average χ value of 0.6 and 0.56 were respectively obtained for the coarse and fine fractions. $D\alpha$ and $D\gamma$ values varied similarly for the three samples in both fractions resulting in highly diverse particles and heterogeneous populations (rather externally mixed). On April 1st, an increasing $D\alpha$ and slightly decreasing $D\gamma$ is observed during the time. ($D\alpha$) becomes nearly equivalent to ($D\gamma$). Consequently, χ increased to a nearly full internal mixing synonym of a more homogeneous population. It shows that the contribution of different emission sources with different particle types positively influences $D\gamma$. Indeed, on March 31st, S-SW winds from the industrial and urban sector prevails at the early hours until 11:00/13:00 when the pattern abruptly changed from SW to Northerly winds carrying marine particles (see Figure 5-11 and 5-12.). This change in wind direction is accompanied by a simultaneously increase in T and vertical wind dispersion (VWD). The replacement of buoyant SW air mass by those coming from the north is accompanied by an increase in RH and simultaneous decrease in T. This is an indication of the occurrence of a sea breeze dynamic characteristic of coastal areas that lasted until midnight under stagnant conditions.

In the second day, a reduced influence of local emissions marked by prevailing N-E winds (see Figure 5-12) associated with decreasing number individual particles led to a more homogeneous population of Carbonaceous and Na-rich particles. This is also supported by 72 hours' backward trajectories of air masses arriving to our sampling site at 500 and 1000 m altitude on April 1st at 12:00 (Figure 5-15). It reveals that the air mass arriving at 500 and 1000 m altitude during sample S4 and S5 of April 1st left the continent on March 30th, then successively crossed the English Channel and the Northern Sea before arriving to our site from NE.

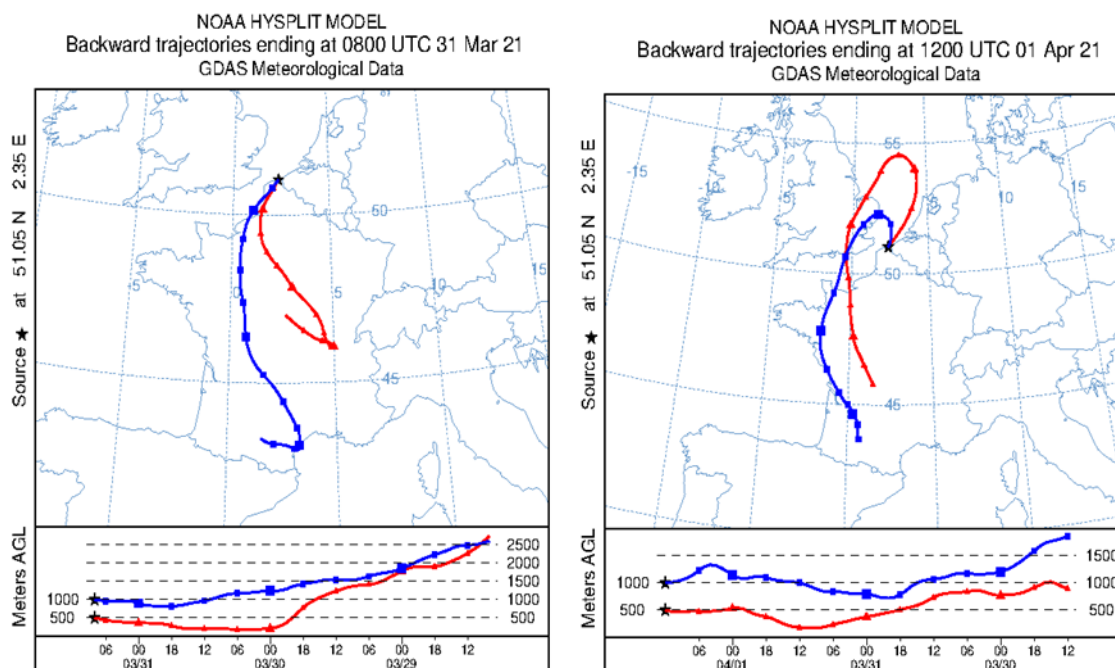


Figure 5-15. Three-day back trajectories of continental air (left) arriving in Dunkirk from the W-SW direction in March 21st, 2021 and both continental and marine air arriving in Dunkirk from NE direction in April 1st, 2021 at 12:00. In the second day both continental pollutants from the great Paris region and the English Channel and marine pollutants can be transported to Dunkirk.

With increasing residential time in the atmosphere, particles can undergo physico-chemical transformations through coagulation, condensation and heterogeneous reactions. This leads to an increase in $D\alpha$, thus, an increase in χ . In conclusion, particles become on average more heterogeneous i.e. more aged, therefore, leading to a more internally mixed population.

5.4.2. Evolution of particles mixing state according to their particle type

The previous paragraph focused on a global evolution of the composition and mixing state of the particles during the PE-1. However, two samples may appear similar in composition (for example, S3 and S4 in Figure 5-14), whereas if we focus on one type of particle (Na-rich for example), differences may appear. Indeed, the composition and mixing state of the Na-rich particles can vary between these two samples (S3 and S4), although Na remains the dominant element. It is therefore interesting to

Chapter 5. Physico-chemical characterization of individual particles

take a deeper look at the physico-chemical evolution of the main types of particles during a pollution event. Nevertheless, it must be kept in mind that a minimum number of particles is necessary for the accuracy calculated on the mixing state index to be reliable (see section 5.2.1). For that, the following discussion will focus on the fine fraction of major particle types observed during this PE-1, i.e. carbonaceous and Na-rich particles.

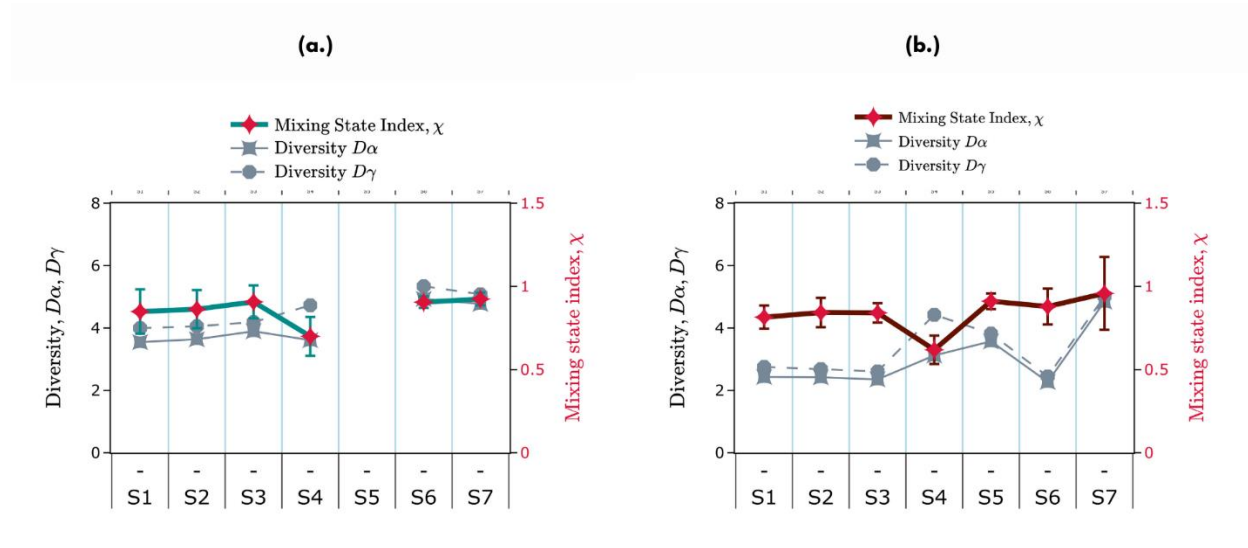


Figure 5-16. Evolution of D_α , D_γ and χ of (a) carbonaceous particles and (b) Na-rich particles for each sample from S1 to S7.

With χ above 0.8, the fine Na-rich particles are internally mixed for all samples (Figure 5-16 a). The samples S1 to S3 were collected under stagnant atmosphere and are characterized by similar mixing state. The elemental bulk diversity D_γ then increases from S3 to S4, as for carbonaceous particles, which results in a decrease of the mixing state index χ . The sample S4 was collected during the maximal $PM_{2.5}$ concentrations at 04:00 on April 1st (Figure 5-11). At this time, the vertical turbulence was below 0.3 m/s and the vertical wind dispersion (Figure 5-12 bottom) suggested stagnant atmosphere as for sample S3. However, an increase of wind speed and a shift of wind direction from North to North-East can explain this change in the particle mixing state, although the particle chemical composition does not significantly change from S3 to S4 (Figure 5-14). Under these change in atmospheric dynamics, a mix of transported and more aged sea-salts with local sea-salts and also carbonaceous particles available on the site is possible (Bondy et al., 2017). As a result, an increase in their D_γ is

Chapter 5. Physico-chemical characterization of individual particles

observed. Later, the $D\gamma$ decreases from S6 to S7 from an average of 4 elements to an average of 3 effective elements. Under the influence of local sea-salt emissions, Na-rich particles are more diverse because other elements such as Mg, Ca, and Al can be found in small proportions. On the other hand, at S6 the average elemental composition shows a domination of Na, O and N elements, which is an indication that the Na-rich particles are completely aged at S6 compared to S1.

Carbonaceous particles showed high χ (above 0.8) for all samples during PE1 except for S4 when a decrease in χ was observed (Figure 5-16 b.). $D\alpha$ and $D\gamma$ varied from nearly 2.5 effective elements during the first day (S1, S2 and S3) to nearly ≈ 5 elements with a high variability during the second day (S4 to S6). This variability can be explained by the mixing of local emissions with regional air masses during this time characterized by the starting of turbulent atmospheric conditions. It results in the mixing of homogeneous freshly emitted particles with aged carbonaceous particles associated with longer residential time. This change in the chemical composition of carbonaceous particle is chemically possible for example for soot particles as they can experience aging process by acquiring coating of either organic or inorganic species (Adachi and Buseck, 2008; Liu et al., 2020; Peng et al., 2016).

5.5. Conclusion

29 individual particle samples were collected during the MIXTAPE campaign and analyzed by TSEM-EDX. The results of the analyses allowed the identification of 7 main individual particles types whose names are attributed on the basis of the major elements constituting them. Thus, carbonaceous particles, Na-rich, S-rich, Ca-rich, Si, Al-rich, metals and unclassified types were identified for both the fine (0.1-1 μm) and the coarse fraction (1-10 μm) of TRAPS sampler. The unavailability of a large part of the samples of the coarse fraction has resulted to focus the interpretation of the majority of the results only on the fine fraction, whose health impact is not to be demonstrated.

In order to quantify the particle chemical diversity, the mixing state index (χ) has been calculated for each sample. The influence of environmental factors such as pollution level, local wind origin and pollution type on this mixing state index has then been tested on the fine fraction samples. Comparisons between the different pollution day categories within these factors showed that neither the pollution level, nor the type of pollution, nor the origin of the local wind explain the observed variations of the mixing state index. Therefore, we were interested in the evolution of the individual composition of the particles and of the mixing state throughout a typical pollution event in the Great Dunkirk Area. An increasing mixing state index of the particles is observed during the pollution event,

Chapter 5. Physico-chemical characterization of individual particles

which tends towards an internal mixing state with the increase of the residence time of the particles. Local coverage is associated with externally mixing while regional coverage leads to a more internal mixing of atmospheric particles. The residence time can also be correlated to the duration of the event during which the meteorological conditions and atmospheric dynamics which favors the physico-chemical evolution of the particles particularly in the case of a regional pollution day. Consequently, there is an increase of the average particle diversity i.e. of the heterogeneity of the particles. This can be explained by mechanisms such as condensation, coagulation etc. during transport which are characteristic of pollution episodes. The study of the mixing state variability of carbonaceous and Na-rich particles characteristic of our site reveal that an increase in diversity within the population does not necessarily imply an increase of the diversity of each particle type. This allows us to highlight the influence of the singular evolution of each type of particles on the evolution of the overall mixing state of the population.

During the MIXTAPE campaign, high values of the mixing state index are recorded ($0.45 < \chi < 0.98$) in the fine fraction and ($0.54 < \chi < 0.88$) in the coarse fraction. The average mixing state in the GDA during the pollution days is 0.70 in the fine fraction and 0.65 in the coarse fraction. Similar results were reported in the literature for different field campaigns. Overall, this study shows that with high mixing state index (above 0.5), the pollution particles are in general very heterogeneous in GDA.

The levels of pollutants frequently used in regulations to reduce population exposure to PM have low or no influence on the mixing state of PM. Approaching the issue from a health perspective, recent studies showed that there would be a significant benefit if pollution reduction measures targeted specific sources of particularly harmful particles, such as carbonaceous and metals. With this methodology, it is possible to track the physico-chemical changes observed within potentially harmful particles at high temporal resolution. A study combining the use of the mixing state index and the oxidative potential of PM could be of major use for improving pollution mitigation strategies.

General Conclusion

Despite a significant decrease in the levels of air pollutants (except for ozone) during the last 10 years in Europe in general and in France in particular, exceedances of the WHO thresholds for atmospheric particles are frequently observed, thus exposing the health of nearly 97% of the urban population of the EU as indicated by the European Environment Agency in its 2021 report (EEA, 2021). Indeed, populations living in urban and industrial sites are exposed to pollutants from a multitude of sources. On the other hand, the exceedance of thresholds for these pollutants is the result of a combination of emissions and meteorological factors. When these sites are located near the coast, the specific meteorological conditions make it complex to analyze the physico-chemical and dynamics mechanisms that lead to exceedance of the daily PM thresholds.

In this context, the main objective of this thesis was to propose a methodology to study the physico-chemical characteristics of atmospheric particles during pollution events on the industrial and urban Great Dunkirk Area (GDA), notably their chemical composition and mixing state. The experiments were to allow observations and sampling of the particles with a high temporal resolution but also at a lower cost.

In the first part of this thesis, a state of knowledge on atmospheric aerosols was summarized. Knowledge on sources, global and individual chemical composition, formation processes, health and climate effects, as well as the chemical mixing state of aerosols were provided. The complexity of aerosols and the need for a better understanding of atmospheric processes were highlighted. In the last part of this chapter, we have underlined the incompatibility between the instruments available on the market for sampling particles at high temporal resolution and the achievement of the objectives of this thesis. This justifies the need to develop a device able to provide timely and cost-effective samples for analysis by scanning electron microscopy.

In Chapter 2, the methodology for the physico-chemical characterization of particles and the determination of their chemical mixing state have been extensively discussed. The 9 months' field campaign (MIXTAPE), designated to achieve the objectives of this thesis, was presented. After presenting the study site in GDA and a state of the art on previous aerosol studies conducted there, the set of instruments deployed for both sampling and measurement of particles and gases, as well as monitoring of meteorological conditions, was presented. A particular emphasis was put on the use of the scanning electron microscopy technique, coupled with X-ray emission spectrometry (SEM-EDX)

General Conclusion

for the analysis of atmospheric particles. The elemental chemical composition data provided by the SEM-EDX can be processed with robust statistical methods, in order to identify the main groups of particles that constitute each of our samples. Once these particles are classified, their intra-particle diversity, their global diversity and their chemical mixing state index can be calculated. In order to reduce the computation time and the potential errors, the calculation methodology has been coded in “Python” language using the Jupyter Notebook interface. The generated code is applied, in Chapter 5, to all samples collected during this study.

To obtain a detailed characterization of particles when concentrations exceed the regulatory thresholds, a new rotary cascade impactor named the Time-Resolved Atmospheric Particle Sampler (TRAPS) was designed in our laboratory and tested for coarse and fine particle sampling. The determination of the cut-off diameters and deposition dynamics of the sampled particles using TRAPS are discussed in Chapter 3. After describing the impactor, a presentation of the theoretical calculations of the cut-off diameters was made, resulting in a collection efficiency of 50% for particles with diameter of 1.3 μm and 0.15 μm , for the coarse and fine stage, respectively. These calculations were confirmed by laboratory experiments, with experimental cut-off diameters of 1.32 and 0.13 μm found for the coarse and fine stages, respectively. The homogeneous distribution of collected particles over an impaction trace was also verified, allowing us, in the same time: 1) to estimate the magnitude of the bouncing effects and trace overlap within TRAPS for each impaction stage; 2) to observe the influence of the particle shape on the aspect of the impaction trace; 3) to determine the particles spatial distribution, over the impaction trace, which is a crucial factor for saving time during SEM observations, by thoughtfully selecting the analysed areas and finally 4) to estimate the sampling time required to obtain individualized particles. The last two objectives were achieved by organizing two short sampling campaigns of ambient aerosols.

In Chapter 4, a classification of pollution days over the GDA was carried out using a 3 years’ data base on gaseous pollutants (SO_2 , NO_2 , O_3) and PM_{10} and $\text{PM}_{2.5}$, as well as wind speeds. This classification is based on 3 local stations (urban, industrial and peri-urban) and a remote station, from the air quality monitoring network ATMO-Hauts de France. The pollution days were identified according to the atmospheric dynamics (dispersion or stationary conditions) and the extent of the pollution plume (regional, local or very localized). The local episodes, with a limited extent (only one station in PM_{10} exceedance) are the most frequent and were observed all over the year. Five typical

General Conclusion

episodes were then finely studied in order to describe atmospheric phenomena explaining the PM₁₀ exceedances.

The previous classification is then applied to the MIXTAPE campaign in Chapter 5. 29 samples were collected during the campaign and analyzed by TSEM-EDX for both the fine fraction (0.1-1 µm) and the coarse fraction (1-10 µm) of TRAPS. 7 individual particle-types including Carbonaceous, Na-rich, S-rich, Ca-rich, Si, Al-rich, Metals and Unclassified particles were identified, after analyzing 28 029 single particles. Based on the calculated error which is <5% for 77% of the analyzed samples and <10% for 97% of the samples, we showed that our results on the particles chemical composition and mixing state are reliable. High variability in composition and chemical mixing state were observed, considering the total particle population and at the single particle level. The influence of several factors on the mixing state index was tested. Results show that neither local winds and PM₁₀ mass concentrations, nor the geographical coverage of the pollution event (local vs. regional) significantly influence the mixing state index. Conversely, an evolution of this index and of the chemical composition of single particles were observed when, during the same pollution event, a local extension of the pollution plume evolves rapidly (a few hours) to a plume of regional amplitude, signifying a transported pollution. In conclusion, the dynamics of the pollution plumes significantly influence the single particle chemical composition and the mixing state index. This results in a parallel augmentation of the mixing state index with the atmospheric residence time of the particles

To our knowledge, this study is the first to provide information on single particles chemical mixing states at an industrial and coastal site, for such a long period (9 months). Although being a meteorological parameter easy to measure, the local wind direction cannot be related to the evolution of the mixing state index and thus does not allow to conclude, within a multi-influenced and thus complex environment, about the influence of local sources on the nature of particles driving air quality.

Conversely, rapid changes in the pollution plume coverage significantly influences the chemical composition and diversity of the particles. This would tend to prove that single particles chemical composition and the resulting mixing state are principally influenced by their local vs. transported origin, i.e. their residence time.

The perspectives of this work principally covers two aspects: the improvements of the TRAPS instrument and the potential link between the mixing state of atmospheric particles and their oxidative potential.

General Conclusion

About the TRAPS, a few ways of improvement are already in consideration. First, to limit the risk of incorrect positioning of TEM grids on the impaction plate, an engraving according to the rotation angle is currently investigated. The use of an upstream dryer could also extend the sampling time up to several hours, for chemical analyses needing larger numbers of particles. Experiments will be performed to optimize sampling times with and without a dryer for this purpose. Finally, in this work, only the refractory part of particulate matter was studied, for both the fine and coarse fractions. The implementation of the TRAPS could be of great interest in the future for the study of secondary aerosols and their mixing state. These aerosols have the characteristic to be often semi-volatile and unstable under the SEM electron beam. For this, the TRAPS would be installed in a refrigerated chamber to allow a better sampling of semi-volatile particles and their subsequent analysis by Cryo-SEM-EDX.

The other next step of this work could be to relate the chemical diversity of the particles to an indicator of their health impact, as their oxidative potential (OP). With the help of complementary instruments (OPC/SMPS for real time size distribution measurements), by performing parallel sampling with the TRAPS for SEM-EDX characterization and a high volume sampler for OP determination, the main sources contributing to OP, as non-exhaust traffic emissions as an example, could be identified both in term of composition but also in term of chemical diversity. The results of this work could then be used to improve pollution mitigation strategies.

References

References

- Abrams, J.Y., Weber, R.J., Klein, M., Samat, S.E., Chang, H.H., Strickland, M.J., Verma, V., Fang, T., Bates, J.T., Mulholland, J.A., Russell, A.G., Tolbert, P.E., 2017. Associations between Ambient Fine Particulate Oxidative Potential and Cardiorespiratory Emergency Department Visits. *Environ. Health Perspect.* 125, 107008. <https://doi.org/10.1289/EHP1545>
- Adachi, K., Buseck, P.R., 2008. Internally mixed soot, sulfates, and organic matter in aerosol particles from Mexico City. *Atmos Chem Phys* 13.
- Adachi, K., Oshima, N., Gong, Z., de Sá, S., Bateman, A.P., Martin, S.T., de Brito, J.F., Artaxo, P., Cirino, G.G., Sedlacek III, A.J., Buseck, P.R., 2020. Mixing states of Amazon basin aerosol particles transported over long distances using transmission electron microscopy. *Atmospheric Chem. Phys.* 20, 11923–11939. <https://doi.org/10.5194/acp-20-11923-2020>
- Adamson, I.Y.R., Prieditis, H., Vincent, R., 1999. Pulmonary Toxicity of an Atmospheric Particulate Sample Is Due to the Soluble Fraction. *Toxicol. Appl. Pharmacol.* 157, 43–50. <https://doi.org/10.1006/taap.1999.8658>
- Aggarwal, S.G., Kawamura, K., 2009. Carbonaceous and inorganic composition in long-range transported aerosols over northern Japan: Implication for aging of water-soluble organic fraction. *Atmos. Environ.* 43, 2532–2540. <https://doi.org/10.1016/j.atmosenv.2009.02.032>
- Alleman, L.Y., Lamaison, L., Perdrix, E., Robache, A., Galloo, J.-C., 2010. PM10 metal concentrations and source identification using positive matrix factorization and wind sectoring in a French industrial zone. *Atmospheric Res.* 96, 612–625. <https://doi.org/10.1016/j.atmosres.2010.02.008>
- Amato, F., Cassee, F.R., Denier van der Gon, H.A.C., Gehrig, R., Gustafsson, M., Hafner, W., Harrison, R.M., Jozwicka, M., Kelly, F.J., Moreno, T., Prevot, A.S.H., Schaap, M., Sunyer, J., Querol, X., 2014. Urban air quality: The challenge of traffic non-exhaust emissions. *J. Hazard. Mater.* 275, 31–36. <https://doi.org/10.1016/j.jhazmat.2014.04.053>
- Annegarn, H.J., Cahill, T.A., Sellschop, J.P.F., Zucchiatti, A., 1988. Time sequence particulate sampling and nuclear analysis. *Phys. Scr.* 37, 282–290. <https://doi.org/10.1088/0031-8949/37/2/016>
- Arndt, J., Deboudt, K., Anderson, A., Blondel, A., Eliet, S., Flament, P., Fourmentin, M., Healy, R.M., Savary, V., Setyan, A., Wenger, J.C., 2016. Scanning electron microscopy-energy dispersive X-ray spectrometry (SEM-EDX) and aerosol time-of-flight mass spectrometry (ATOFMS) single

References

- particle analysis of metallurgy plant emissions. *Environ. Pollut.* 210, 9–17. <https://doi.org/10.1016/j.envpol.2015.11.019>
- Arndt, J., Healy, R.M., Setyan, A., Flament, P., Deboudt, K., Riffault, V., Alleman, L.Y., Mbengue, S., Wenger, J.C., 2021. Characterization and source apportionment of single particles from metalworking activities. *Environ. Pollut.* 270, 116078. <https://doi.org/10.1016/j.envpol.2020.116078>
- Atkinson, R.W., Mills, I.C., Walton, H.A., Anderson, H.R., 2015. Fine particle components and health—a systematic review and meta-analysis of epidemiological time series studies of daily mortality and hospital admissions. *J. Expo. Sci. Environ. Epidemiol.* 25, 208–214. <https://doi.org/10.1038/jes.2014.63>
- ATMO HdF, 2020. Atmo Hauts-de-France - Publications et ressources [WWW Document]. URL <https://www.atmo-hdf.fr/publications.html> (accessed 9.11.20).
- ATMO HdF, 2018. Bilan de la qualité de l'air 2018 [WWW Document]. URL https://www.atmo-hdf.fr/joomlatools-files/docman-files/Bilan_annuel/Bilan_QA_2018.pdf (accessed 10.30.19).
- Augustin, P., Billet, S., Crumeyrolle, S., Deboudt, K., Dieudonné, E., Flament, P., Fourmentin, M., Guilbaud, S., Hanoune, B., Landkocz, Y., Méausoone, C., Roy, S., Schmitt, F.G., Sentchev, A., Sokolov, A., 2020. Impact of Sea Breeze Dynamics on Atmospheric Pollutants and Their Toxicity in Industrial and Urban Coastal Environments. *Remote Sens.* 12, 648. <https://doi.org/10.3390/rs12040648>
- Ault, A.P., Axson, J.L., 2017. Atmospheric Aerosol Chemistry: Spectroscopic and Microscopic Advances. *Anal. Chem.* 89, 430–452. <https://doi.org/10.1021/acs.analchem.6b04670>
- AzadiAghdam, M., Braun, R.A., Edwards, E.-L., Bañaga, P.A., Cruz, M.T., Betito, G., Cambaliza, M.O., Dadashazar, H., Lorenzo, G.R., Ma, L., MacDonald, A.B., Nguyen, P., Simpas, J.B., Stahl, C., Sorooshian, A., 2019. On the nature of sea salt aerosol at a coastal megacity: Insights from Manila, Philippines in Southeast Asia. *Atmos. Environ.* 216, 116922. <https://doi.org/10.1016/j.atmosenv.2019.116922>
- Baldauf, R.W., Lane, D.D., Marote, G.A., 2001. Ambient Air Quality Monitoring Network Design for Assessing Human Health Impacts from Exposures to Airborne Contaminants. *Environ. Monit. Assess.* 66, 63–76. <https://doi.org/10.1023/A:1026428214799>
- Baron, P.A., 2006. Description of an aerosol calculator, in: Proceedings of the Seventh International Aerosol Conference, Presented at the Seventh International Aerosol Conference, Biswas P,

References

- Chen DR, Hering S, eds. Mount Laurel, NJ: American Association for Aerosol Research, St. Paul, Minnesota, USA, p. 555.
- Bauer, K., Bosker, T., Dirks, K.N., Behrens, P., 2018. The impact of seating location on black carbon exposure in public transit buses: Implications for vulnerable groups. *Transp. Res. Part Transp. Environ.* 62, 577–583. <https://doi.org/10.1016/j.trd.2018.04.009>
- Beji, A., Deboudt, K., Khardi, S., Muresan, B., Flament, P., Fourmentin, M., Lumière, L., 2020. Non-exhaust particle emissions under various driving conditions: Implications for sustainable mobility. *Transp. Res. Part Transp. Environ.* 81, 102290. <https://doi.org/10.1016/j.trd.2020.102290>
- Bodor, Z., Bodor, K., Keresztesi, Á., Szép, R., 2020. Major air pollutants seasonal variation analysis and long-range transport of PM10 in an urban environment with specific climate condition in Transylvania (Romania). *Environ. Sci. Pollut. Res.* 27, 38181–38199. <https://doi.org/10.1007/s11356-020-09838-2>
- Bond, T.C., Doherty, S.J., Fahey, D.W., Forster, P.M., Berntsen, T., DeAngelo, B.J., Flanner, M.G., Ghan, S., Kärcher, B., Koch, D., Kinne, S., Kondo, Y., Quinn, P.K., Sarofim, M.C., Schultz, M.G., Schulz, M., Venkataraman, C., Zhang, H., Zhang, S., Bellouin, N., Guttikunda, S.K., Hopke, P.K., Jacobson, M.Z., Kaiser, J.W., Klimont, Z., Lohmann, U., Schwarz, J.P., Shindell, D., Storelvmo, T., Warren, S.G., Zender, C.S., 2013. Bounding the role of black carbon in the climate system: A scientific assessment. *J. Geophys. Res. Atmospheres* 118, 5380–5552. <https://doi.org/10.1002/jgrd.50171>
- Bondy, A.L., Bonanno, D., Moffet, R.C., Wang, B., Laskin, A., Ault, A.P., 2018. The diverse chemical mixing state of aerosol particles in the southeastern United States. *Atmospheric Chem. Phys.* 18, 12595–12612. <https://doi.org/10.5194/acp-18-12595-2018>
- Bondy, A.L., Wang, B., Laskin, A., Craig, R.L., Nhliziyo, M.V., Bertman, S.B., Pratt, K.A., Shepson, P.B., Ault, A.P., 2017. Inland Sea Spray Aerosol Transport and Incomplete Chloride Depletion: Varying Degrees of Reactive Processing Observed during SOAS. *Environ. Sci. Technol.* 51, 9533–9542. <https://doi.org/10.1021/acs.est.7b02085>
- Boucher, O., 2015. *Atmospheric Aerosols*. Springer Netherlands, Dordrecht. https://doi.org/10.1007/978-94-017-9649-1_2
- Bozzetti, C., El Haddad, I., Salameh, D., Daellenbach, K.R., Fermo, P., Gonzalez, R., Minguillón, M.C., Iinuma, Y., Poulain, L., Elser, M., Müller, E., Slowik, J.G., Jaffrezzo, J.-L., Baltensperger, U., Marchand, N., Prévôt, A.S.H., 2017. Organic aerosol source apportionment by offline-

References

- AMS over a full year in Marseille. *Atmospheric Chem. Phys.* 17, 8247–8268. <https://doi.org/10.5194/acp-17-8247-2017>
- Bressi, M., Cavalli, F., Putaud, J.P., Fröhlich, R., Petit, J.-E., Aas, W., Äijälä, M., Alastuey, A., Allan, J.D., Aurela, M., Berico, M., Bougiatioti, A., Bukowiecki, N., Canonaco, F., Crenn, V., Dusanter, S., Ehn, M., Elsassler, M., Flentje, H., Graf, P., Green, D.C., Heikkinen, L., Hermann, H., Holzinger, R., Hueglin, C., Keernik, H., Kiendler-Scharr, A., Kubelová, L., Lunder, C., Maasikmets, M., Makeš, O., Malaguti, A., Mihalopoulos, N., Nicolas, J.B., O'Dowd, C., Ovadnevaite, J., Petralia, E., Poulain, L., Priestman, M., Riffault, V., Ripoll, A., Schlag, P., Schwarz, J., Sciare, J., Slowik, J., Sosedova, Y., Stavroulas, I., Teinemaa, E., Via, M., Vodička, P., Williams, P.I., Wiedensohler, A., Young, D.E., Zhang, S., Favez, O., Minguillón, M.C., Prevot, A.S.H., 2021. A European aerosol phenomenology - 7: High-time resolution chemical characteristics of submicron particulate matter across Europe. *Atmospheric Environ.* X 10, 100108. <https://doi.org/10.1016/j.aeaoa.2021.100108>
- Brewer, T.L., 2019. Black carbon emissions and regulatory policies in transportation. *Energy Policy* 129, 1047–1055. <https://doi.org/10.1016/j.enpol.2019.02.073>
- Brostrøm, A., Kling, K.I., Koponen, I.K., Hougaard, K.S., Kandler, K., Mølhav, K., 2019. Improving the foundation for particulate matter risk assessment by individual nanoparticle statistics from electron microscopy analysis. *Sci. Rep.* 9, 8093.
- Bukowiecki, N., Lienemann, P., Zwicky, C.N., Furger, M., Richard, A., Falkenberg, G., Rickers, K., Grolimund, D., Borca, C., Hill, M., Gehrig, R., Baltensperger, U., 2008. X-ray fluorescence spectrometry for high throughput analysis of atmospheric aerosol samples: The benefits of synchrotron X-rays. *Spectrochim. Acta Part B At. Spectrosc.* 63, 929–938. <https://doi.org/10.1016/j.sab.2008.05.006>
- Bukowiecki, N., Richard, A., Furger, M., Weingartner, E., Aguirre, M., Huthwelker, T., Lienemann, P., Gehrig, R., Baltensperger, U., 2009. Deposition Uniformity and Particle Size Distribution of Ambient Aerosol Collected with a Rotating Drum Impactor. *Aerosol Sci. Technol.* 43, 891–901. <https://doi.org/10.1080/02786820903002431>
- Bzdek, B.R., Pennington, M.R., Johnston, M.V., 2012. Single particle chemical analysis of ambient ultrafine aerosol: A review. *J. Aerosol Sci.* 52, 109–120. <https://doi.org/10.1016/j.jaerosci.2012.05.001>
- Cahill, T.A., Goodart, C., Nelson, J.W., Eldred, R.A., Nasstrom, J.S., Feeney, P.J., 1987. Design and Evaluation of the DRUM Impactor, in: *Proceedings of International Symposium on*

References

- Particulate and Multi-Phase Processes. Hemisphere Publishing Corporation, Washington, D.C.
- Calas, A., Uzu, G., Martins, J.M.F., Voisin, D., Spadini, L., Lacroix, T., Jaffrezo, J.-L., 2017. The importance of simulated lung fluid (SLF) extractions for a more relevant evaluation of the oxidative potential of particulate matter. *Sci. Rep.* 7, 11617. <https://doi.org/10.1038/s41598-017-11979-3>
- Calvo, A.I., Alves, C., Castro, A., Pont, V., Vicente, A.M., Fraile, R., 2013. Research on aerosol sources and chemical composition: Past, current and emerging issues. *Atmospheric Res.* 120–121, 1–28. <https://doi.org/10.1016/j.atmosres.2012.09.021>
- Charron, A., Polo-Rehn, L., Besombes, J.-L., Golly, B., Buisson, C., Chanut, H., Marchand, N., Guillaud, G., Jaffrezo, J.-L., 2019. Identification and quantification of particulate tracers of exhaust and non-exhaust vehicle emissions. *Atmospheric Chem. Phys.* 19, 5187–5207. <https://doi.org/10.5194/acp-19-5187-2019>
- Ching, J., Adachi, K., Zaizen, Y., Igarashi, Y., Kajino, M., 2019. Aerosol mixing state revealed by transmission electron microscopy pertaining to cloud formation and human airway deposition. *Npj Clim. Atmospheric Sci.* 2, 1–7. <https://doi.org/10.1038/s41612-019-0081-9>
- Ching, J., Fast, J., West, M., Riemer, N., 2017. Metrics to quantify the importance of mixing state for CCN activity. *Atmospheric Chem. Phys.* 17, 7445–7458. <https://doi.org/10.5194/acp-17-7445-2017>
- Ching, J., Kajino, M., 2018. Aerosol mixing state matters for particles deposition in human respiratory system. *Sci. Rep.* 8, 1–11. <https://doi.org/10.1038/s41598-018-27156-z>
- Choël, M., Deboudt, K., Flament, P., 2010. Development of Time-Resolved Description of Aerosol Properties at the Particle Scale During an Episode of Industrial Pollution Plume. *Water, Air, Soil Pollut.* 209, 93–107. <https://doi.org/10.1007/s11270-009-0183-9>
- Choël, M., Deboudt, K., Flament, P., Lecornet, G., Perdrix, E., Sobanska, S., 2006. Fast evolution of tropospheric Pb- and Zn-rich particles in the vicinity of a lead smelter. *Atmos. Environ.* 40, 4439–4449. <https://doi.org/10.1016/j.atmosenv.2006.04.027>
- Colbeck, I., Chung, M.-C., Eleftheriadis, K., 2002. Formation and Transport of Atmospheric Aerosol over Athens, Greece. *Water Air Soil Pollut. Focus* 2, 223–235. <https://doi.org/10.1023/A:1021335401558>
- Crenn, V., Chakraborty, A., Fronval, I., Petitprez, D., Riffault, V., 2018. Fine particles sampled at an urban background site and an industrialized coastal site in Northern France—Part 2:

References

- Comparison of offline and online analyses for carbonaceous aerosols. *Aerosol Sci. Technol.* 52, 287–299. <https://doi.org/10.1080/02786826.2017.1403008>
- Crenn, V., Fronval, I., Petitprez, D., Riffault, V., 2017. Fine particles sampled at an urban background site and an industrialized coastal site in Northern France — Part 1: Seasonal variations and chemical characterization. *Sci. Total Environ.* 578, 203–218. <https://doi.org/10.1016/j.scitotenv.2015.11.165>
- Daellenbach, K.R., Uzu, G., Jiang, J., Cassagnes, L.-E., Leni, Z., Vlachou, A., Stefenelli, G., Canonaco, F., Weber, S., Segers, A., Kuenen, J.J.P., Schaap, M., Favez, O., Albinet, A., Aksoyoglu, S., Dommen, J., Baltensperger, U., Geiser, M., El Haddad, I., Jaffrezo, J.-L., Prévôt, A.S.H., 2020a. Sources of particulate-matter air pollution and its oxidative potential in Europe. *Nature* 587, 414–419. <https://doi.org/10.1038/s41586-020-2902-8>
- D'Alessandro, A., Nava, S., Van Ham, R., Adriaens, A., Lucarelli, F., Marcazzan, G., Prati, P., Valli, G., Vecchi, R., Zucchiatti, A., 2004. PIXE and ToF-SIMS analysis of streaker samplers filters. *Nucl. Instrum. Methods Phys. Res. Sect. B Beam Interact. Mater. At.* 222, 261–269. <https://doi.org/10.1016/j.nimb.2004.02.014>
- Deboudt, K., Flament, P., Choël, M., Gloter, A., Sobanska, S., Colliex, C., 2010. Mixing state of aerosols and direct observation of carbonaceous and marine coatings on African dust by individual particle analysis. *J. Geophys. Res. Atmospheres* 115. <https://doi.org/10.1029/2010JD013921>
- Demokritou, P., Gupta, T., Ferguson, S., Koutrakis, P., 2002. Development and Laboratory Performance Evaluation of a Personal Cascade Impactor. *J. Air Waste Manag. Assoc.* 52, 1230–1237. <https://doi.org/10.1080/10473289.2002.10470855>
- EEA, E., 2021. Air quality in Europe 2021 — European Environment Agency [WWW Document]. URL <https://www.eea.europa.eu/publications/air-quality-in-europe-2021/air-quality-in-europe-2021> (accessed 1.31.22).
- Egerton, R.F., 2012. Mechanisms of radiation damage in beam-sensitive specimens, for TEM accelerating voltages between 10 and 300 kV. *Microsc. Res. Tech.* 75, 1550–1556. <https://doi.org/10.1002/jemt.22099>
- El Haddad, I., D'Anna, B., Temime-Roussel, B., Nicolas, M., Boreave, A., Favez, O., Voisin, D., Sciare, J., George, C., Jaffrezo, J.-L., Wortham, H., Marchand, N., 2013. Towards a better understanding of the origins, chemical composition and aging of oxygenated organic aerosols:

References

- case study of a Mediterranean industrialized environment, Marseille. *Atmospheric Chem. Phys.* 13, 7875–7894. <https://doi.org/10.5194/acp-13-7875-2013>
- European Parliament, 2008. Directive 2008/50/EC of the European Parliament and of the council of 21 May 2008 on ambient air quality and cleaner air for Europe [WWW Document]. URL <https://eur-lex.europa.eu/legal-content/en/ALL/?uri=CELEX%3A32008L0050> (accessed 3.21.21).
- Evtyugina, M.G., Nunes, T., Pio, C., Costa, C.S., 2006. Photochemical pollution under sea breeze conditions, during summer, at the Portuguese West Coast. *Atmos. Environ.* 40, 6277–6293. <https://doi.org/10.1016/j.atmosenv.2006.05.046>
- Falkovich, A.H., Ganor, E., Levin, Z., Formenti, P., Rudich, Y., 2001. Chemical and mineralogical analysis of individual mineral dust particles. *J. Geophys. Res. Atmospheres* 106, 18029–18036. <https://doi.org/10.1029/2000JD900430>
- Fan, W., Chen, T., Zhu, Z., Zhang, H., Qiu, Y., Yin, D., 2022. A review of secondary organic aerosols formation focusing on organosulfates and organic nitrates. *J. Hazard. Mater.* 430, 128406. <https://doi.org/10.1016/j.jhazmat.2022.128406>
- Favez, O., Weber, S., Petit, J.-E., Alleman, L.Y., Albinet, A., Riffault, V., Chazeau, B., Amodeo, T., Salameh, D., Zhang, Y., Srivastava, D., Samaké, A., Aujay-Plouzeau, R., Papin, A., Bonnaire, N., Boullanger, C., Chatain, M., Chevrier, F., Detournay, A., Dominik-Sègue, M., Falhun, R., Garbin, C., Ghersi, V., Grignon, G., Levigoureux, G., Pontet, S., Rangognio, J., Zhang, S., Besombes, J.-L., Conil, S., Uzu, G., Savarino, J., Marchand, N., Gros, V., Marchand, C., Jaffrezo, J.-L., Leoz-Garziandia, E., 2021. Overview of the French Operational Network for In Situ Observation of PM Chemical Composition and Sources in Urban Environments (CARA Program). *Atmosphere* 12, 207. <https://doi.org/10.3390/atmos12020207>
- Finlayson-Pitts, B.J., Wingen, L.M., Sumner, A.L., Syomin, D., Ramazan, K.A., 2003. The heterogeneous hydrolysis of NO₂ in laboratory systems and in outdoor and indoor atmospheres: An integrated mechanism. *Phys. Chem. Chem. Phys.* 5, 223–242. <https://doi.org/10.1039/B208564J>
- Formenti, P., Prati, P., Zucchiatti, A., Lucarelli, F., Mandò, P.A., 1996. Aerosol study in the town of Genova with a PIXE analysis. *Nucl. Instrum. Methods Phys. Res. Sect. B Beam Interact. Mater. At., Accelerators in Applied Research and Technology* 113, 359–362. [https://doi.org/10.1016/0168-583X\(95\)01409-8](https://doi.org/10.1016/0168-583X(95)01409-8)

References

- Fraund, M., Pham, D.Q., Bonanno, D., Harder, T.H., Wang, B., Brito, J., De Sá, S.S., Carbone, S., China, S., Artaxo, P., Martin, S.T., Pöhlker, C., Andreae, M.O., Laskin, A., Gilles, M.K., Moffet, R.C., 2017. Elemental Mixing State of Aerosol Particles Collected in Central Amazonia during GoAmazon2014/15. *Atmosphere* 8, 173. <https://doi.org/10.3390/atmos8090173>
- Gasparik, J.T., Ye, Q., Curtis, J.H., Presto, A.A., Donahue, N.M., Sullivan, R.C., West, M., Riemer, N., 2020. Quantifying errors in the aerosol mixing-state index based on limited particle sample size. *Aerosol Sci. Technol.* 54, 1527–1541. <https://doi.org/10.1080/02786826.2020.1804523>
- Gengembre, C., 2018. Variabilité multi-échelles de la météorologie et des aérosols en situation littorale sous influence industrielle (thesis). Littoral.
- Gomes, L., Bergametti, G., Dulac, F., Ezat, U., 1990. Assessing the actual size distribution of atmospheric aerosols collected with a cascade impactor. *J. Aerosol Sci.* 21, 47–59. [https://doi.org/10.1016/0021-8502\(90\)90022-P](https://doi.org/10.1016/0021-8502(90)90022-P)
- Grange, S.K., Uzu, G., Weber, S., Jaffrezo, J.-L., Hueglin, C., 2022. Linking Switzerland's PM₁₀ and PM_{2.5} oxidative potential (OP) with emission sources. *Atmospheric Chem. Phys. Discuss.* 1–31. <https://doi.org/10.5194/acp-2021-979>
- Grigoratos, T., Martini, G., 2015. Brake wear particle emissions: a review. *Environ. Sci. Pollut. Res.* 22, 2491–2504. <https://doi.org/10.1007/s11356-014-3696-8>
- Guilbaud, S., 2018. Etude du vieillissement des aérosols inorganiques industriels en milieu urbain (thesis). Littoral.
- Hallquist, M., Wenger, J.C., Baltensperger, U., Rudich, Y., Simpson, D., Claeys, M., Dommen, J., Donahue, N.M., George, C., Goldstein, A.H., Hamilton, J.F., Herrmann, H., Hoffmann, T., Iinuma, Y., Jang, M., Jenkin, M.E., Jimenez, J.L., Kiendler-Scharr, A., Maenhaut, W., McFiggans, G., Mentel, T.F., Monod, A., Prévôt, A.S.H., Seinfeld, J.H., Surratt, J.D., Szmigielski, R., Wildt, J., 2009. The formation, properties and impact of secondary organic aerosol: current and emerging issues. *Atmospheric Chem. Phys.* 9, 5155–5236. <https://doi.org/10.5194/acp-9-5155-2009>
- Han, B., Wang, Y., Zhang, R., Yang, W., Ma, Z., Geng, W., Bai, Z., 2019. Comparative statistical models for estimating potential roles of relative humidity and temperature on the concentrations of secondary inorganic aerosol: Statistical insights on air pollution episodes at Beijing during January 2013. *Atmos. Environ.* 212, 11–21. <https://doi.org/10.1016/j.atmosenv.2019.05.025>

References

- Harrison, R.M., Jones, A.M., Gietl, J., Yin, J., Green, D.C., 2012. Estimation of the Contributions of Brake Dust, Tire Wear, and Resuspension to Nonexhaust Traffic Particles Derived from Atmospheric Measurements. *Environ. Sci. Technol.* 46, 6523–6529. <https://doi.org/10.1021/es300894r>
- Haywood, J., 2016. Chapter 27 - Atmospheric Aerosols and Their Role in Climate Change, in: Letcher, T.M. (Ed.), *Climate Change (Second Edition)*. Elsevier, Boston, pp. 449–463. <https://doi.org/10.1016/B978-0-444-63524-2.00027-0>
- Healy, R.M., Riemer, N., Wenger, J.C., Murphy, M., West, M., Poulain, L., Wiedensohler, A., O'Connor, I.P., McGillicuddy, E., Sodeau, J.R., Evans, G.J., 2014. Single particle diversity and mixing state measurements. *Atmospheric Chem. Phys.* 14, 6289–6299. <https://doi.org/10.5194/acp-14-6289-2014>
- Hidy, G.M., 1984. *Aerosols, an industrial and environmental science*. Academic Press.
- Hleis, D., Fernández-Olmo, I., Ledoux, F., Kfoury, A., Courcot, L., Desmonts, T., Courcot, D., 2013. Chemical profile identification of fugitive and confined particle emissions from an integrated iron and steelmaking plant. *J. Hazard. Mater.* 250–251, 246–255. <https://doi.org/10.1016/j.jhazmat.2013.01.080>
- Hoornaert, S., Van Malderen, H., Van Grieken, R., 1996. Gypsum and Other Calcium-Rich Aerosol Particles above the North Sea. *Environ. Sci. Technol.* 30, 1515–1520. <https://doi.org/10.1021/es9504350>
- Hu, Y., Wang, S., 2021. Formation mechanism of a severe air pollution event: A case study in the Sichuan Basin, Southwest China. *Atmos. Environ.* 246, 118135. <https://doi.org/10.1016/j.atmosenv.2020.118135>
- Ibald-Mulli, A., Wichmann, H.-E., Kreyling, W., Peters, A., 2002. Epidemiological Evidence on Health Effects of Ultrafine Particles. *J. Aerosol Med.* 15, 189–201. <https://doi.org/10.1089/089426802320282310>
- IPCC, 2013. *AR5 Climate Change 2013: The Physical Science Basis — IPCC*. URL <https://www.ipcc.ch/report/ar5/wg1/> (accessed 4.6.22).
- Jimenez, J.L., Canagaratna, M.R., Donahue, N.M., Prevot, A.S.H., Zhang, Q., Kroll, J.H., DeCarlo, P.F., Allan, J.D., Coe, H., Ng, N.L., Aiken, A.C., Docherty, K.S., Ulbrich, I.M., Grieshop, A.P., Robinson, A.L., Duplissy, J., Smith, J.D., Wilson, K.R., Lanz, V.A., Hueglin, C., Sun, Y.L., Tian, J., Laaksonen, A., Raatikainen, T., Rautiainen, J., Vaattovaara, P., Ehn, M., Kulmala, M., Tomlinson, J.M., Collins, D.R., Cubison, M.J., E., Dunlea, J., Huffman, J.A., Onasch, T.B.,

References

- Alfarra, M.R., Williams, P.I., Bower, K., Kondo, Y., Schneider, J., Drewnick, F., Borrmann, S., Weimer, S., Demerjian, K., Salcedo, D., Cottrell, L., Griffin, R., Takami, A., Miyoshi, T., Hatakeyama, S., Shimojo, A., Sun, J.Y., Zhang, Y.M., Dzepina, K., Kimmel, J.R., Sueper, D., Jayne, J.T., Herndon, S.C., Trimborn, A.M., Williams, L.R., Wood, E.C., Middlebrook, A.M., Kolb, C.E., Baltensperger, U., Worsnop, D.R., 2009. Evolution of Organic Aerosols in the Atmosphere. *Science* 326, 1525–1529. <https://doi.org/10.1126/science.1180353>
- Karaca, F., Anil, I., Alagha, O., 2009. Long-range potential source contributions of episodic aerosol events to PM₁₀ profile of a megacity. *Atmos. Environ.* 43, 5713–5722. <https://doi.org/10.1016/j.atmosenv.2009.08.005>
- Kazemimanesh, M., Dastanpour, R., Baldelli, A., Moallemi, A., Thomson, K.A., Jefferson, M.A., Johnson, M.R., Rogak, S.N., Olfert, J.S., 2019. Size, effective density, morphology, and nanostructure of soot particles generated from buoyant turbulent diffusion flames. *J. Aerosol Sci.* 132, 22–31. <https://doi.org/10.1016/j.jaerosci.2019.03.005>
- Kelly, J.M., Doherty, R.M., O'Connor, F.M., Mann, G.W., 2018. The impact of biogenic, anthropogenic, and biomass burning volatile organic compound emissions on regional and seasonal variations in secondary organic aerosol. *Atmospheric Chem. Phys.* 18, 7393–7422. <https://doi.org/10.5194/acp-18-7393-2018>
- Ketzel, M., Omstedt, G., Johansson, C., Düring, I., Pohjola, M., Oetl, D., Gidhagen, L., Wählin, P., Lohmeyer, A., Haakana, M., Berkowicz, R., 2007. Estimation and validation of PM_{2.5}/PM₁₀ exhaust and non-exhaust emission factors for practical street pollution modelling. *Atmos. Environ.* 41, 9370–9385. <https://doi.org/10.1016/j.atmosenv.2007.09.005>
- Kfoury, A., Ledoux, F., Roche, C., Delmaire, G., Roussel, G., Courcot, D., 2016. PM_{2.5} source apportionment in a French urban coastal site under steelworks emission influences using constrained non-negative matrix factorization receptor model. *J. Environ. Sci., Changing Complexity of Air Pollution* 40, 114–128. <https://doi.org/10.1016/j.jes.2015.10.025>
- Kim, H., Zhang, Q., Sun, Y., 2020. Measurement report: Characterization of severe spring haze episodes and influences of long-range transport in the Seoul metropolitan area in March 2019. *Atmospheric Chem. Phys.* 20, 11527–11550. <https://doi.org/10.5194/acp-20-11527-2020>
- Kim, K.-H., Kabir, E., Kabir, S., 2015. A review on the human health impact of airborne particulate matter. *Environ. Int.* 74, 136–143. <https://doi.org/10.1016/j.envint.2014.10.005>

References

- Klimont, Z., Kupiainen, K., Heyes, C., Purohit, P., Cofala, J., Rafaj, P., Borken-Kleefeld, J., Schöpp, W., 2017. Global anthropogenic emissions of particulate matter including black carbon. *Atmospheric Chem. Phys.* 17, 8681–8723. <https://doi.org/10.5194/acp-17-8681-2017>
- Kodros, J.K., Hanna, S.J., Bertram, A.K., Leaitch, W.R., Schulz, H., Herber, A.B., Zanutta, M., Burkart, J., Willis, M.D., Abbatt, J.P.D., Pierce, J.R., 2018. Size-resolved mixing state of black carbon in the Canadian high Arctic and implications for simulated direct radiative effect. *Atmospheric Chem. Phys.* 18, 11345–11361. <https://doi.org/10.5194/acp-18-11345-2018>
- Koppmann, R., von Czapiewski, K., Reid, J.S., 2005. A review of biomass burning emissions, part I: gaseous emissions of carbon monoxide, methane, volatile organic compounds, and nitrogen containing compounds. *Atmospheric Chem. Phys. Discuss.* 5, 10455–10516. <https://doi.org/10.5194/acpd-5-10455-2005>
- Krueger, B.J., Grassian, V.H., Cowin, J.P., Laskin, A., 2004. Heterogeneous chemistry of individual mineral dust particles from different dust source regions: the importance of particle mineralogy. *Atmos. Environ.* 38, 6253–6261. <https://doi.org/10.1016/j.atmosenv.2004.07.010>
- Kukkonen, J., Pohjola, M., S Sokhi, R., Luhana, L., Kitwiroon, N., Fragkou, L., Rantamäki, M., Berge, E., Ødegaard, V., Håvard Slørdal, L., Denby, B., Finardi, S., 2005. Analysis and evaluation of selected local-scale PM10 air pollution episodes in four European cities: Helsinki, London, Milan and Oslo. *Atmos. Environ., Fourth International Conference on Urban Air Quality: Measurement, Modelling and Management*, 25-28 March 2003 39, 2759–2773. <https://doi.org/10.1016/j.atmosenv.2004.09.090>
- Kulmala, M., Kerminen, V.-M., 2008. On the formation and growth of atmospheric nanoparticles. *Atmospheric Res., 17th International Conference on Nucleation and Atmospheric Aerosols* 90, 132–150. <https://doi.org/10.1016/j.atmosres.2008.01.005>
- Kwak, J., Lee, Sunyoun, Lee, Seokhwan, 2014. On-road and laboratory investigations on non-exhaust ultrafine particles from the interaction between the tire and road pavement under braking conditions. *Atmos. Environ.* 97, 195–205. <https://doi.org/10.1016/j.atmosenv.2014.08.014>
- Landkocz, Y., Ledoux, F., André, V., Cazier, F., Genevray, P., Dewaele, D., Martin, P.J., Lepers, C., Verdin, A., Courcot, L., Boushina, S., Sichel, F., Gualtieri, M., Shirali, P., Courcot, D., Billet, S., 2017. Fine and ultrafine atmospheric particulate matter at a multi-influenced urban site: Physicochemical characterization, mutagenicity and cytotoxicity. *Environ. Pollut.* 221, 130–140. <https://doi.org/10.1016/j.envpol.2016.11.054>

References

- Ledoux, F., Courcot, L., Courcot, D., Aboukais, A., Puskaric, E., 2006. A summer and winter apportionment of particulate matter at urban and rural areas in northern France. *Atmospheric Res.*, 16th International Conference on Nucleation and Atmospheric Aerosols 82, 633–642. <https://doi.org/10.1016/j.atmosres.2006.02.019>
- Ledoux, F., Kfoury, A., Delmaire, G., Roussel, G., El Zein, A., Courcot, D., 2017. Contributions of local and regional anthropogenic sources of metals in PM_{2.5} at an urban site in northern France. *Chemosphere* 181, 713–724. <https://doi.org/10.1016/j.chemosphere.2017.04.128>
- Ledoux, F., Roche, C., Cazier, F., Beaugard, C., Courcot, D., 2018. Influence of ship emissions on NO_x, SO₂, O₃ and PM concentrations in a North-Sea harbor in France. *J. Environ. Sci.* 71, 56–66. <https://doi.org/10.1016/j.jes.2018.03.030>
- Li, W., Shao, L., Wang, Z., Shen, R., Yang, S., Tang, U., 2010. Size, composition, and mixing state of individual aerosol particles in a South China coastal city. *J. Environ. Sci.* 22, 561–569. [https://doi.org/10.1016/S1001-0742\(09\)60146-7](https://doi.org/10.1016/S1001-0742(09)60146-7)
- Li, W., Shao, L., Zhang, D., Ro, C.-U., Hu, M., Bi, X., Geng, H., Matsuki, A., Niu, H., Chen, J., 2016. A review of single aerosol particle studies in the atmosphere of East Asia: morphology, mixing state, source, and heterogeneous reactions. *J. Clean. Prod., Preventing Smog Crises* 112, 1330–1349. <https://doi.org/10.1016/j.jclepro.2015.04.050>
- Li, X., Yang, Y., Liu, S., Zhao, Q., Wang, G., Wang, Y., 2020. Light absorption properties of brown carbon (BrC) in autumn and winter in Beijing: Composition, formation and contribution of nitrated aromatic compounds. *Atmos. Environ.* 223, 117289. <https://doi.org/10.1016/j.atmosenv.2020.117289>
- Li, Y., Henze, D.K., Jack, D., Henderson, B.H., Kinney, P.L., 2016. Assessing public health burden associated with exposure to ambient black carbon in the United States. *Sci. Total Environ.* 539, 515–525. <https://doi.org/10.1016/j.scitotenv.2015.08.129>
- Liu, D., He, C., Schwarz, J.P., Wang, X., 2020. Lifecycle of light-absorbing carbonaceous aerosols in the atmosphere. *Npj Clim. Atmospheric Sci.* 3, 1–18. <https://doi.org/10.1038/s41612-020-00145-8>
- Liu, K.-Y., Wang, Z., Hsiao, L.-F., 2002. A modeling of the sea breeze and its impacts on ozone distribution in northern Taiwan. *Environ. Model. Softw., Australia-Taiwan Joint Symposium on Environmental Modelling* 17, 21–27. [https://doi.org/10.1016/S1364-8152\(01\)00049-4](https://doi.org/10.1016/S1364-8152(01)00049-4)
- Ly, B.-T., Matsumi, Y., Vu, T.V., Sekiguchi, K., Nguyen, T.-T., Pham, C.-T., Nghiem, T.-D., Ngo, I.-H., Kurotsuchi, Y., Nguyen, T.-H., Nakayama, T., 2021. The effects of meteorological

References

- conditions and long-range transport on PM_{2.5} levels in Hanoi revealed from multi-site measurement using compact sensors and machine learning approach. *J. Aerosol Sci.* 152, 105716. <https://doi.org/10.1016/j.jaerosci.2020.105716>
- Marple, V.A., Liu, B.Y.H., 1974. Characteristics of laminar jet impactors. *Environ. Sci. Technol.* 8, 648–654. <https://doi.org/10.1021/es60092a003>
- Marple, V.A., Rubow, K.L., Behm, S.M., 1991. A Microorifice Uniform Deposit Impactor (MOUDI): Description, Calibration, and Use. *Aerosol Sci. Technol.* 14, 434–446. <https://doi.org/10.1080/02786829108959504>
- Marple, V.A., Willeke, K., 1976. Impactor design. *Atmospheric Environ.* 1967 10, 891–896. [https://doi.org/10.1016/0004-6981\(76\)90144-X](https://doi.org/10.1016/0004-6981(76)90144-X)
- Marris, H., Deboudt, K., Augustin, P., Flament, P., Blond, F., Fiani, E., Fourmentin, M., Delbarre, H., 2012a. Fast changes in chemical composition and size distribution of fine particles during the near-field transport of industrial plumes. *Sci. Total Environ.* 427–428, 126–138. <https://doi.org/10.1016/j.scitotenv.2012.03.068>
- Mbengue, S., Alleman, L.Y., Flament, P., 2017. Metal-bearing fine particle sources in a coastal industrialized environment. *Atmospheric Res.* 183, 202–211. <https://doi.org/10.1016/j.atmosres.2016.08.014>
- Mbengue, S., Alleman, L.Y., Flament, P., 2014. Size-distributed metallic elements in submicronic and ultrafine atmospheric particles from urban and industrial areas in northern France. *Atmospheric Res.* 135–136, 35–47. <https://doi.org/10.1016/j.atmosres.2013.08.010>
- McDuffie, E.E., Martin, R.V., Spadaro, J.V., Burnett, R., Smith, S.J., O'Rourke, P., Hammer, M.S., van Donkelaar, A., Bindle, L., Shah, V., Jaeglé, L., Luo, G., Yu, F., Adeniran, J.A., Lin, J., Brauer, M., 2021. Source sector and fuel contributions to ambient PM_{2.5} and attributable mortality across multiple spatial scales. *Nat. Commun.* 12, 3594. <https://doi.org/10.1038/s41467-021-23853-y>
- Mészáros, E., 1999. Fundamentals of atmospheric aerosol chemistry. Akadémiai Kiadó, Budapest.
- Mithlesh, mahilang, Manas, K.D., Shamsh, P., 2021. Biogenic secondary organic aerosols: A review on formation mechanism, analytical challenges and environmental impacts. *Chemosphere* 262, 127771. <https://doi.org/10.1016/j.chemosphere.2020.127771>
- Morawska, L., Zhu, T., Liu, N., Amouei Torkmahalleh, M., de Fatima Andrade, M., Barratt, B., Broomandi, P., Buonanno, G., Carlos Belalcazar Ceron, L., Chen, J., Cheng, Y., Evans, G., Gavidia, M., Guo, H., Hanigan, I., Hu, M., Jeong, C.H., Kelly, F., Gallardo, L., Kumar, P.,

References

- Lyu, X., Mullins, B.J., Nordström, C., Pereira, G., Querol, X., Yezid Rojas Roa, N., Russell, A., Thompson, H., Wang, H., Wang, L., Wang, T., Wierzbicka, A., Xue, T., Ye, C., 2021. The state of science on severe air pollution episodes: Quantitative and qualitative analysis. *Environ. Int.* 156, 106732. <https://doi.org/10.1016/j.envint.2021.106732>
- Niu, H., Shao, L., Zhang, D., 2012. Soot particles at an elevated site in eastern China during the passage of a strong cyclone. *Sci. Total Environ.* 430, 217–222. <https://doi.org/10.1016/j.scitotenv.2012.04.050>
- Nousiainen, T., 2009. Optical modeling of mineral dust particles: A review. *J. Quant. Spectrosc. Radiat. Transf.*, XI Conference on Electromagnetic and Light Scattering by Non-Spherical Particles: 2008 110, 1261–1279. <https://doi.org/10.1016/j.jqsrt.2009.03.002>
- O'Brien, R.E., Wang, B., Laskin, A., Riemer, N., West, M., Zhang, Q., Sun, Y., Yu, X.-Y., Alpert, P., Knopf, D.A., Gilles, M.K., Moffet, R.C., 2015. Chemical imaging of ambient aerosol particles: Observational constraints on mixing state parameterization. *J. Geophys. Res. Atmospheres* 120, 9591–9605. <https://doi.org/10.1002/2015JD023480>
- OECD, 2020. Non-exhaust Particulate Emissions from Road Transport: An Ignored Environmental Policy Challenge. OECD. <https://doi.org/10.1787/4a4dc6ca-en>
- Parker, D.E., Wilson, H., Jones, P.D., Christy, J.R., Folland, C.K., 1996. The Impact of Mount Pinatubo on World-Wide Temperatures. *Int. J. Climatol.* 16, 487–497. [https://doi.org/10.1002/\(SICI\)1097-0088\(199605\)16:5<487::AID-JOC39>3.0.CO;2-J](https://doi.org/10.1002/(SICI)1097-0088(199605)16:5<487::AID-JOC39>3.0.CO;2-J)
- Pastuszka, J.S., 2015. Adverse Health Effects of the Exposure to the Spherical Aerosol [WWW Document]. *Synerg. Infl. Gaseous Part. Biol. Pollut. Hum. Health.* <https://doi.org/10.1201/b19592-8>
- Peng, J., Hu, M., Gong, Z., Tian, X., Wang, M., Zheng, J., Guo, Q., Cao, W., Lv, W., Hu, W., Wu, Z., Guo, S., 2016. Evolution of secondary inorganic and organic aerosols during transport: A case study at a regional receptor site. *Environ. Pollut.* 218, 794–803. <https://doi.org/10.1016/j.envpol.2016.08.003>
- Peng, J., Hu, M., Shang, D., Wu, Z., Du, Z., Tan, T., Wang, Y., Zhang, F., Zhang, R., 2021. Explosive Secondary Aerosol Formation during Severe Haze in the North China Plain. *Environ. Sci. Technol.* 55, 2189–2207. <https://doi.org/10.1021/acs.est.0c07204>
- Pöschl, U., 2005. Atmospheric Aerosols: Composition, Transformation, Climate and Health Effects. *Angew. Chem. Int. Ed.* 44, 7520–7540. <https://doi.org/10.1002/anie.200501122>

References

- Pratt, K.A., Hatch, L.E., Prather, K.A., 2009. Seasonal Volatility Dependence of Ambient Particle Phase Amines. *Environ. Sci. Technol.* 43, 5276–5281. <https://doi.org/10.1021/es803189n>
- Pui, D.Y.H., Romay-Novas, F., Liu, B.Y.H., 1987. Experimental Study of Particle Deposition in Bends of Circular Cross Section. *Aerosol Sci. Technol.* 7, 301–315. <https://doi.org/10.1080/02786828708959166>
- Pun, V.C., Ho, K., 2019. Blood pressure and pulmonary health effects of ozone and black carbon exposure in young adult runners. *Sci. Total Environ.* 657, 1–6. <https://doi.org/10.1016/j.scitotenv.2018.11.465>
- Putaud, J.-P., Raes, F., Van Dingenen, R., Brüggemann, E., Facchini, M.-C., Decesari, S., Fuzzi, S., Gehrig, R., Hüglin, C., Laj, P., Lorbeer, G., Maenhaut, W., Mihalopoulos, N., Müller, K., Querol, X., Rodriguez, S., Schneider, J., Spindler, G., Brink, H. ten, Tørseth, K., Wiedensohler, A., 2004. A European aerosol phenomenology—2: chemical characteristics of particulate matter at kerbside, urban, rural and background sites in Europe. *Atmos. Environ.* 38, 2579–2595. <https://doi.org/10.1016/j.atmosenv.2004.01.041>
- Querol, X., Viana, M., Alastuey, A., Amato, F., Moreno, T., Castillo, S., Pey, J., de la Rosa, J., Sánchez de la Campa, A., Artíñano, B., Salvador, P., García Dos Santos, S., Fernández-Patier, R., Moreno-Grau, S., Negral, L., Minguillón, M.C., Monfort, E., Gil, J.I., Inza, A., Ortega, L.A., Santamaría, J.M., Zabalza, J., 2007. Source origin of trace elements in PM from regional background, urban and industrial sites of Spain. *Atmos. Environ.* 41, 7219–7231. <https://doi.org/10.1016/j.atmosenv.2007.05.022>
- R. W. Clarke, J.J.G., P.J. Catalano, P. Koutrakis, G.G. Krishna Murthy, C. Sioutas, J. Paulauskis, B. Coull, S. Ferguson, 1999. Urban Air Particulate Inhalation Alters Pulmonary Function and Induces Pulmonary Inflammation in a Rodent Model of Chronic Bronchitis. *Inhal. Toxicol.* 11, 637–656. <https://doi.org/10.1080/089583799196781>
- Raabe, O.G., Braaten, D.A., Axelbaum, R.L., Teague, S.V., Cahill, T.A., 1988. Calibration studies of the drum impactor. *J. Aerosol Sci.* 19, 183–195. [https://doi.org/10.1016/0021-8502\(88\)90222-4](https://doi.org/10.1016/0021-8502(88)90222-4)
- Raes, F., Dingenen, R.V., Vignati, E., Wilson, J., Putaud, J.-P., Seinfeld, J.H., Adams, P., 2000a. Formation and cycling of aerosols in the global troposphere. *Atmos. Environ.* 34, 4215–4240. [https://doi.org/10.1016/S1352-2310\(00\)00239-9](https://doi.org/10.1016/S1352-2310(00)00239-9)
- Rai, P., Slowik, J.G., Furger, M., El Haddad, I., Visser, S., Tong, Y., Singh, A., Wehrle, G., Kumar, V., Tobler, A.K., Bhattu, D., Wang, L., Ganguly, D., Rastogi, N., Huang, R.-J., Necki, J., Cao, J.,

References

- Tripathi, S.N., Baltensperger, U., Prévôt, A.S.H., 2021. Highly time-resolved measurements of element concentrations in PM₁₀ and PM_{2.5}: comparison of Delhi, Beijing, London, and Krakow. *Atmospheric Chem. Phys.* 21, 717–730. <https://doi.org/10.5194/acp-21-717-2021>
- Reche, C., Viana, M., Pandolfi, M., Alastuey, A., Moreno, T., Amato, F., Ripoll, A., Querol, X., 2012. Urban NH₃ levels and sources in a Mediterranean environment. *Atmos. Environ.* 57, 153–164. <https://doi.org/10.1016/j.atmosenv.2012.04.021>
- Reizer, M., Calzolari, G., Maciejewska, K., Orza, J.A.G., Carraresi, L., Lucarelli, F., Juda-Rezler, K., 2021. Measurement report: Receptor modeling for source identification of urban fine and coarse particulate matter using hourly elemental composition. *Atmospheric Chem. Phys.* 21, 14471–14492. <https://doi.org/10.5194/acp-21-14471-2021>
- Riemer, N., Ault, A.P., West, M., Craig, R.L., Curtis, J.H., 2019a. Aerosol Mixing State: Measurements, Modeling, and Impacts. *Rev. Geophys.* 57, 187–249. <https://doi.org/10.1029/2018RG000615>
- Riemer, N., West, M., 2013. Quantifying aerosol mixing state with entropy and diversity measures. *Atmospheric Chem. Phys.* 13, 11423–11439. <https://doi.org/10.5194/acp-13-11423-2013>
- Riffault, V., Arndt, J., Marris, H., Mbengue, S., Setyan, A., Alleman, L.Y., Deboudt, K., Flament, P., Augustin, P., Delbarre, H., Wenger, J., 2015a. Fine and Ultrafine Particles in the Vicinity of Industrial Activities: A Review. *Crit. Rev. Environ. Sci. Technol.* 45, 2305–2356. <https://doi.org/10.1080/10643389.2015.1025636>
- Rimetz-Planchon, J., Perdrix, E., Sobanska, S., Brémard, C., 2008a. PM₁₀ air quality variations in an urbanized and industrialized harbor. *Atmos. Environ.* 42, 7274–7283. <https://doi.org/10.1016/j.atmosenv.2008.07.005>
- Roig Rodelas, R., 2018. Chemical characterization, sources and origins of secondary inorganic aerosols measured at a suburban site in Northern France. Université de Lille.
- Roig Rodelas, R., Perdrix, E., Herbin, B., Riffault, V., 2019. Characterization and variability of inorganic aerosols and their gaseous precursors at a suburban site in northern France over one year (2015–2016). *Atmos. Environ.* 200, 142–157. <https://doi.org/10.1016/j.atmosenv.2018.11.041>
- Samaké, A., Jaffrezo, J.-L., Favez, O., Weber, S., Jacob, V., Albinet, A., Riffault, V., Perdrix, E., Waked, A., Golly, B., Salameh, D., Chevrier, F., Oliveira, D.M., Bonnaire, N., Besombes, J.-L., Martins, J.M.F., Conil, S., Guillaud, G., Mesbah, B., Rocq, B., Robic, P.-Y., Hulin, A., Le Meur, S.,

References

- Descheemaeker, M., Chretien, E., Marchand, N., Uzu, G., 2019. Polyols and glucose particulate species as tracers of primary biogenic organic aerosols at 28 French sites. *Atmospheric Chem. Phys.* 19, 3357–3374. <https://doi.org/10.5194/acp-19-3357-2019>
- Sanderson, P., Su, S.S., Chang, I.T.H., Delgado Saborit, J.M., Kepaptsoglou, D.M., Weber, R.J.M., Harrison, R.M., 2016. Characterisation of iron-rich atmospheric submicrometre particles in the roadside environment. *Atmos. Environ.* 140, 167–175. <https://doi.org/10.1016/j.atmosenv.2016.05.040>
- Saraswati, Sharma, S.K., Saxena, M., Mandal, T.K., 2019. Characteristics of gaseous and particulate ammonia and their role in the formation of secondary inorganic particulate matter at Delhi, India. *Atmospheric Res.* 218, 34–49. <https://doi.org/10.1016/j.atmosres.2018.11.010>
- Seinfeld, J.H., Pandis, S.N., 2016. *Atmospheric Chemistry and Physics: From Air Pollution to Climate Change*, Second Edition. ed. John Wiley & Sons, inc.
- Seinfeld, J.H., Pandis, S.N., 2006. *Atmospheric Chemistry and Physics: From Air Pollution to Climate Change*, 2nd ed. ed. John Wiley & Sons, inc., Hoboken, New Jersey.
- Setyan, A., Flament, P., Locoge, N., Deboudt, K., Riffault, V., Alleman, L.Y., Schoemaeker, C., Arndt, J., Augustin, P., Healy, R.M., Wenger, J.C., Cazier, F., Delbarre, H., Dewaele, D., Dewalle, P., Fourmentin, M., Genevray, P., Gengembre, C., Leonardis, T., Marris, H., Mbengue, S., 2019. Investigation on the near-field evolution of industrial plumes from metalworking activities. *Sci. Total Environ.* 668, 443–456. <https://doi.org/10.1016/j.scitotenv.2019.02.399>
- Shannon, C., 1948. *A Mathematical Theory of Communication*. Wikipedia.
- Sharga, B., Pylypiv, D., Feketa, V., 2021. *MEDICAL BIOLOGY PRACTICALS. CYTOLOGY. Practical 2. Electron microscopy.* pp. 18–34.
- Siciliano, T., Giua, R., Siciliano, M., Di Giulio, S., Genga, A., 2021. The morphology and chemical composition of the urban PM10 near a steel plant in Apulia determined by scanning electron microscopy. *Source Apportionment. Atmospheric Res.* 251, 105416. <https://doi.org/10.1016/j.atmosres.2020.105416>
- Singh, N., Banerjee, T., Deboudt, K., Chakraborty, A., Khan, M.F., Latif, M.T., 2021. Sources, Composition, and Mixing State of Submicron Particulates over the Central Indo-Gangetic Plain. *ACS Earth Space Chem.* 5, 2052–2065. <https://doi.org/10.1021/acsearthspacechem.1c00130>

References

- Sjödin, Å., Ferm, M., Björk, A., Rahmberg, M., Gudmundsson, A., Swietlicki, E., Johansson, C., Gustafsson, M., Blomqvist, G., 2010. Wear particles from road traffic - a field, laboratory and modelling study. Final report. IVL Svenska Miljöinstitutet.
- Smith, S.J., van Aardenne, J., Klimont, Z., Andres, R.J., Volke, A., Delgado Arias, S., 2011. Anthropogenic sulfur dioxide emissions: 1850–2005. *Atmospheric Chem. Phys.* 11, 1101–1116. <https://doi.org/10.5194/acp-11-1101-2011>
- SOGA Report, 2018. State of Global Air [WWW Document]. URL <https://www.stateofglobalair.org/sites/default/files/soga-2018-report.pdf> (accessed 10.8.19).
- Squizzato, S., Masiol, M., Brunelli, A., Pistollato, S., Tarabotti, E., Rampazzo, G., Pavoni, B., 2013. Factors determining the formation of secondary inorganic aerosol: a case study in the Po Valley (Italy). *Atmospheric Chem. Phys.* 13, 1927–1939. <https://doi.org/10.5194/acp-13-1927-2013>
- Stabile, L., Trassier, C.V., Dell'Agli, G., Buonanno, G., 2013. Ultrafine Particle Generation through Atomization Technique: The Influence of the Solution. *Aerosol Air Qual. Res.* 13, 1667–1677. <https://doi.org/10.4209/aaqr.2013.03.0085>
- Stein, A.F., Draxler, R.R., Rolph, G.D., Stunder, B.J.B., Cohen, M.D., Ngan, F., 2015. NOAA's HYSPLIT Atmospheric Transport and Dispersion Modeling System. *Bull. Am. Meteorol. Soc.* 96, 2059–2077. <https://doi.org/10.1175/BAMS-D-14-00110.1>
- Stevens, R., Dastoor, A., 2019a. A Review of the Representation of Aerosol Mixing State in Atmospheric Models. *Atmosphere* 10, 168. <https://doi.org/10.3390/atmos10040168>
- Stirnberg, R., Cermak, J., Kotthaus, S., Haefelin, M., Andersen, H., Fuchs, J., Kim, M., Petit, J.-E., Favez, O., 2021. Meteorology-driven variability of air pollution (PM₁) revealed with explainable machine learning. *Atmospheric Chem. Phys.* 21, 3919–3948. <https://doi.org/10.5194/acp-21-3919-2021>
- Stocker, T.F., IPCC (Eds.), 2013. Climate change 2013: the physical science basis ; summary for policymakers, a report of Working Group I of the IPCC, technical summary, a report accepted by Working Group I of the IPCC but not approved in detail and frequently asked questions ; part of the Working Group I contribution to the fifth assessment report of the Intergovernmental Panel on Climate Change. Intergovernmental Panel on Climate Change, New York.

References

- Suarez-Bertoa, R., Zardini, A.A., Astorga, C., 2014. Ammonia exhaust emissions from spark ignition vehicles over the New European Driving Cycle. *Atmos. Environ.* 97, 43–53. <https://doi.org/10.1016/j.atmosenv.2014.07.050>
- Sullivan, R.C., Moore, M.J.K., Petters, M.D., Kreidenweis, S.M., Roberts, G.C., Prather, K.A., 2009. Effect of chemical mixing state on the hygroscopicity and cloud nucleation properties of calcium mineral dust particles. *Atmospheric Chem. Phys.* 9, 3303–3316. <https://doi.org/10.5194/acp-9-3303-2009>
- Sultana, C.M., Collins, D.B., Prather, K.A., 2017. Effect of Structural Heterogeneity in Chemical Composition on Online Single-Particle Mass Spectrometry Analysis of Sea Spray Aerosol Particles. *Environ. Sci. Technol.* 51, 3660–3668. <https://doi.org/10.1021/acs.est.6b06399>
- Sun, Y., Chen, C., Zhang, Y., Xu, W., Zhou, L., Cheng, X., Zheng, H., Ji, D., Li, J., Tang, X., Fu, P., Wang, Z., 2016. Rapid formation and evolution of an extreme haze episode in Northern China during winter 2015. *Sci. Rep.* 6, 27151. <https://doi.org/10.1038/srep27151>
- Swuste, P., Corn, M., Goelzer, B., 1995. Hazard prevention and control in the work environment: A report of a WHO meeting. *Saf. Sci.* 21, 75–78. [https://doi.org/10.1016/0925-7535\(95\)00007-0](https://doi.org/10.1016/0925-7535(95)00007-0)
- Talbot, C., Augustin, P., Leroy, C., Willart, V., Delbarre, H., Khomenko, G., 2007. Impact of a sea breeze on the boundary-layer dynamics and the atmospheric stratification in a coastal area of the North Sea. *Bound.-Layer Meteorol.* 125, 133–154. <https://doi.org/10.1007/s10546-007-9185-6>
- Tomasi, C., Fuzzi, S., Kokhanovsky, A., 2017. *Atmospheric Aerosols: Life Cycles and Effects on Air Quality and Climate*, 1st ed. John Wiley & Sons.
- Trejos, E.M., Silva, L.F.O., Hower, J.C., Flores, E.M.M., González, C.M., Pachón, J.E., Aristizábal, B.H., 2021. Volcanic emissions and atmospheric pollution: A study of nanoparticles. *Geosci. Front.* 12, 746–755. <https://doi.org/10.1016/j.gsf.2020.08.013>
- Valavanidis, A., Fiotakis, K., Vlachogianni, T., 2008. Airborne Particulate Matter and Human Health: Toxicological Assessment and Importance of Size and Composition of Particles for Oxidative Damage and Carcinogenic Mechanisms. *J. Environ. Sci. Health Part C* 26, 339–362. <https://doi.org/10.1080/10590500802494538>
- Vallero, D.A., 2014. *Fundamentals of Air Pollution*. Academic Press.
- Vargas, M.P.S., Terran, L.M., 2012. (14) (PDF) Air pollution: Impact and prevention [WWW Document]. ResearchGate. URL

References

- https://www.researchgate.net/publication/228060023_Air_pollution_Impact_and_prevention (accessed 11.2.19).
- Via, M., Minguillón, M.C., Reche, C., Querol, X., Alastuey, A., 2021. Increase in secondary organic aerosol in an urban environment. *Atmospheric Chem. Phys.* 21, 8323–8339. <https://doi.org/10.5194/acp-21-8323-2021>
- Wang, J., Cubison, M.J., Aiken, A.C., Jimenez, J.L., Collins, D.R., 2010. The importance of aerosol mixing state and size-resolved composition on CCN concentration and the variation of the importance with atmospheric aging of aerosols. *Atmospheric Chem. Phys.* 10, 7267–7283. <https://doi.org/10.5194/acp-10-7267-2010>
- Wang, W., Shao, L., Mazzoleni, C., Li, Y., Kotthaus, S., Grimmond, S., Bhandari, J., Xing, J., Feng, X., Zhang, M., Shi, Z., 2021. Measurement report: Comparison of wintertime individual particles at ground level and above the mixed layer in urban Beijing. *Atmospheric Chem. Phys.* 21, 5301–5314. <https://doi.org/10.5194/acp-21-5301-2021>
- Wang, Y., Li, X., Shi, Z., Huang, L., Li, J., Zhang, H., Ying, Q., Wang, M., Ding, D., Zhang, X., Hu, J., 2021. Premature Mortality Associated with Exposure to Outdoor Black Carbon and Its Source Contributions in China. *Resour. Conserv. Recycl.* 170, 105620. <https://doi.org/10.1016/j.resconrec.2021.105620>
- Weber, S., Uzu, G., Favez, O., Borlaza, L.J.S., Calas, A., Salameh, D., Chevrier, F., Allard, J., Besombes, J.-L., Albinet, A., Pontet, S., Mesbah, B., Gille, G., Zhang, S., Pallares, C., Leoz-Garziandia, E., Jaffrezo, J.-L., 2021. Source apportionment of atmospheric PM₁₀ oxidative potential: synthesis of 15 year-round urban datasets in France. *Atmospheric Chem. Phys.* 21, 11353–11378. <https://doi.org/10.5194/acp-21-11353-2021>
- Whiteaker, J.R., Suess, D.T., Prather, K.A., 2002. Effects of Meteorological Conditions on Aerosol Composition and Mixing State in Bakersfield, CA. *Environ. Sci. Technol.* 36, 2345–2353. <https://doi.org/10.1021/es011381z>
- WHO, 2021. WHO global air quality guidelines: particulate matter (PM_{2.5} and PM₁₀), ozone, nitrogen dioxide, sulfur dioxide and carbon monoxide. WHO, Geneva.
- WHO, 2018. world-air-quality-report-2018-en.pdf.
- William C. Hinds, M.L., 2000. *Aerosol Technology Properties, Behavior, and Measurement of Airborne Particles*: William C. Hinds. Wiley, New York (1999). ISBN 0-471-19410-7. 464 pages+Index.

References

- Worobiec, A., Hoog, J. de, Osan, J., Szaloki, I., Ro, C.-U., Grieken, R. van, 2003. Thermal stability of beam sensitive atmospheric aerosol particles in electron probe microanalysis at liquid nitrogen temperature. *Spectrochim. Acta Part B At. Spectrosc.* 58. [https://doi.org/10.1016/S0584-8547\(03\)00013-2](https://doi.org/10.1016/S0584-8547(03)00013-2)
- Xu, L., Fukushima, S., Sobanska, S., Murata, K., Naganuma, A., Liu, L., Wang, Y., Niu, H., Shi, Z., Kojima, T., Zhang, D., Li, W., 2020. Tracing the evolution of morphology and mixing state of soot particles along with the movement of an Asian dust storm. *Atmospheric Chem. Phys.* 20, 14321–14332. <https://doi.org/10.5194/acp-20-14321-2020>
- Xu, L., Liu, X., Gao, H., Yao, X., Zhang, D., Bi, L., Liu, L., Zhang, J., Zhang, Y., Wang, Y., Yuan, Q., Li, W., 2021. Long-range transport of anthropogenic air pollutants into the marine air: insight into fine particle transport and chloride depletion on sea salts. *Atmospheric Chem. Phys.* 21, 17715–17726. <https://doi.org/10.5194/acp-21-17715-2021>
- Ye, Q., Gu, P., Li, H.Z., Robinson, E.S., Lipsky, E., Kaltsonoudis, C., Lee, A.K.Y., Apte, J.S., Robinson, A.L., Sullivan, R.C., Presto, A.A., Donahue, N.M., 2018. Spatial Variability of Sources and Mixing State of Atmospheric Particles in a Metropolitan Area. *Environ. Sci. Technol.* 52, 6807–6815. <https://doi.org/10.1021/acs.est.8b01011>
- Yim, S.D., Kim, S.J., Baik, J.H., Nam, I.-S., Mok, Y.S., Lee, J.-H., Cho, B.K., Oh, S.H., 2004. Decomposition of urea into NH₃ for the SCR process. *Ind. Eng. Chem. Res.* 43, 4856–4863.
- Yoshino, A., Takami, A., Hara, K., Nishita-Hara, C., Hayashi, M., Kaneyasu, N., 2021. Contribution of Local and Transboundary Air Pollution to the Urban Air Quality of Fukuoka, Japan. *Atmosphere* 12, 431. <https://doi.org/10.3390/atmos12040431>
- Young, G., Jones, H.M., Darbyshire, E., Baustian, K.J., McQuaid, J.B., Bower, K.N., Connolly, P.J., Gallagher, M.W., Choulaton, T.W., 2016. Size-segregated compositional analysis of aerosol particles collected in the European Arctic during the ACCACIA campaign. *Atmospheric Chem. Phys.* 16, 4063–4079. <https://doi.org/10.5194/acp-16-4063-2016>
- Yu, C., Zhao, T., Bai, Y., Zhang, L., Kong, S., Yu, X., He, J., Cui, C., Yang, J., You, Y., Ma, G., Wu, M., Chang, J., 2020. Heavy air pollution with a unique “non-stagnant” atmospheric boundary layer in the Yangtze River middle basin aggravated by regional transport of PM_{2.5} over China. *Atmospheric Chem. Phys.* 20, 7217–7230. <https://doi.org/10.5194/acp-20-7217-2020>
- Yücekutlu, A., Yücekutlu, Y., 2014. INVESTIGATION OF THE DYNAMIC TRANSPORT OF SAHARAN DESERT DUST–IV, International Congress on Landscape Ecology.

References

- Proceeding., in: International Congress on Landscape Ecology Understanding Mediterranean Landscapes: Human vs. Nature.
- Zhang, S., 2016. Analyse dynamique, en champ proche et à résolution temporelle fine, de l'aérosol submicronique en situation urbaine sous influence industrielle (thesis). Littoral.
- Zhang, S., Tison, E., Dusanter, S., Beaugard, C., Gengembre, C., Augustin, P., Fourmentin, M., Delbarre, H., Riffault, V., 2021. Near real-time PM1 chemical composition measurements at a French urban background and coastal site under industrial influence over more than a year: Temporal variability and assessment of sulfur-containing emissions. *Atmos. Environ.* 244, 117960. <https://doi.org/10.1016/j.atmosenv.2020.117960>
- Zhou, H., Lin, J., Shen, Y., Deng, F., Gao, Y., Liu, Y., Dong, H., Zhang, Y., Sun, Q., Fang, J., Tang, S., Wang, Y., Du, Y., Cui, L., Ruan, S., Kong, F., Liu, Z., Li, T., 2020. Personal black carbon exposure and its determinants among elderly adults in urban China. *Environ. Int.* 138, 105607. <https://doi.org/10.1016/j.envint.2020.105607>

Annex

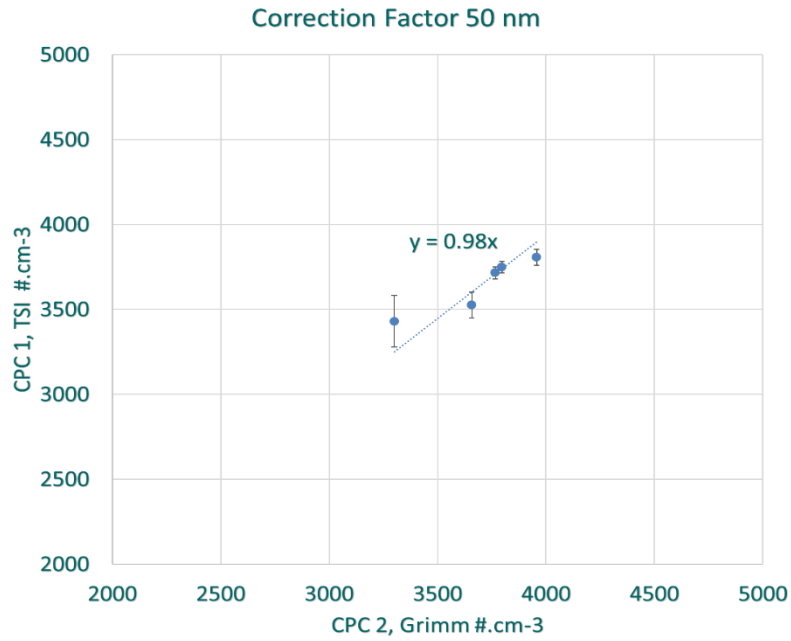


Figure A-1. Determination of the correction factor between CPC1 and CPC2. A Linear regression was drawn from the different levels of particle number concentrations measured with collocated CPC1 and CPC2.

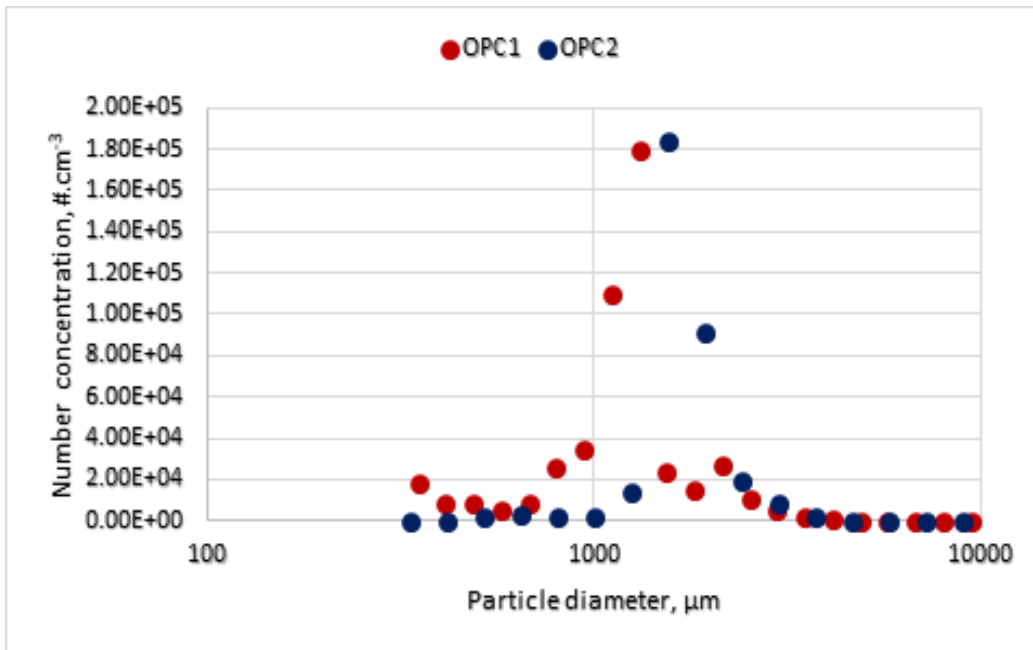


Figure A-2. Comparison between OPC MiniWRAS Grimm and OPS TSI for particle size distribution. The observed shift is related to the differences in the measurement channels of the two instruments.

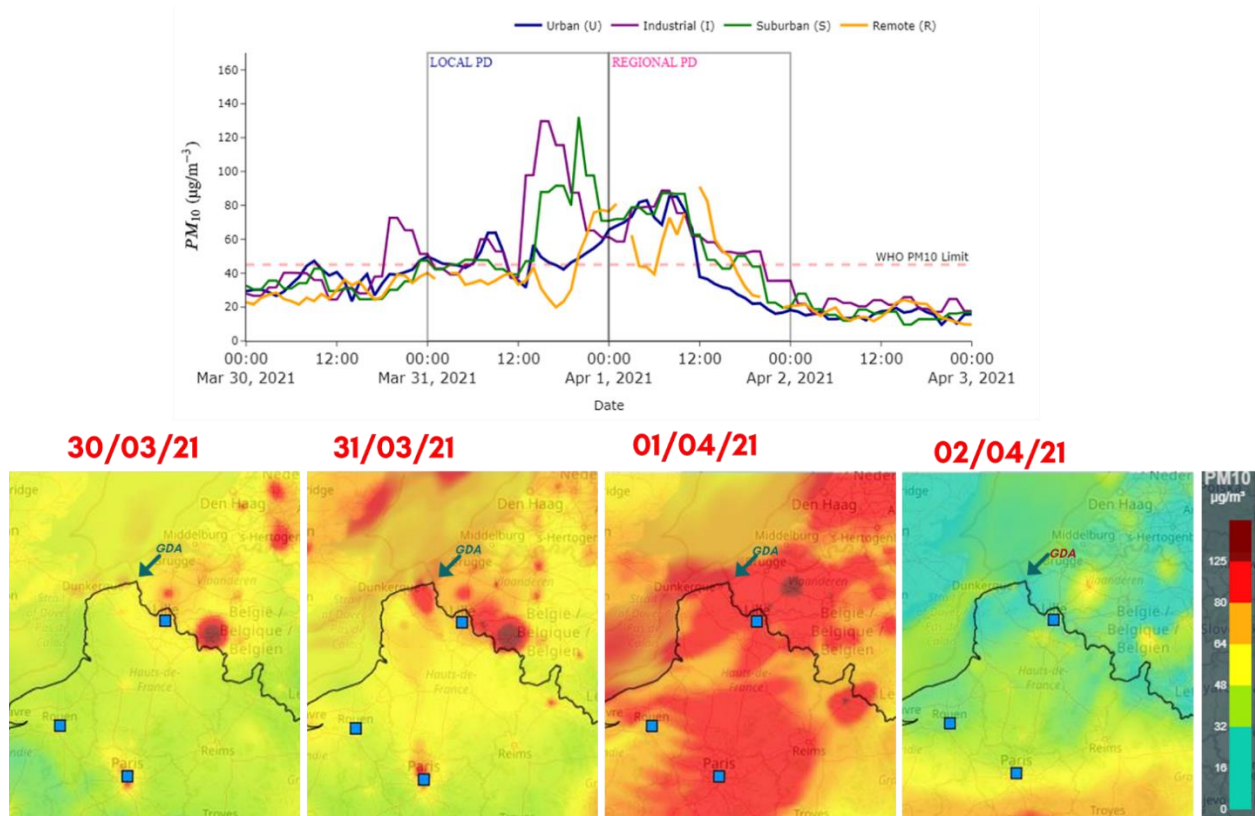


Figure A-3. Time series evolution of PM₁₀ concentration (top) from the industrial (I), urban (U), suburban (S) and remote (R) stations from March 30th to April 2nd 2021 period of PE1. The daily mean PM₁₀ concentrations maps (bottom) obtained from <http://www2.prevoir.org/> are presented for the same period. We can clearly distinguish between the local pollution day on 31/03/2021 and the regional one on 01/04/2021.

Communications

Articles

Ngagine, S.H.; Deboudt, K.; Flament, P.; Choël, M.; Kulinski, P.; Marteel, F. Development and Characterization of a Time-Sequenced Cascade Impactor: Application to Transient PM2.5 Pollution Events in Urbanized and Industrialized Environments. *Atmosphere* 2022, 13, 244. <https://doi.org/10.3390/atmos13020244>

Amouei Torkmahalleh, M., Akhmetvaliyeva, Z., Omran, A.D., Darvish Omran, F., Kazemitabar, M., Naseri, M., Naseri, M., Sharifi, H., Malekipirbazari, M., Kwasi Adotey, E., Gorjinezhad, S., Egtesadi, N., Sabanov, S., Alastuey, A., de Fátima Andrade, M., Buonanno, G., Carbone, S., Cárdenas-Fuentes, D.E., Cassee, F.R., Dai, Q., Henríquez, A., Hopke, P.K., Keronen, P., Khwaja, H.A., Kim, J., Kulmala, M., Kumar, P., Kushta, J., Kuula, J., Massagué, J., Mitchell, T., Mooibroek, D., Morawska, L., Niemi, J.V., **Ngagine, S.H.**, Norman, M., Oyama, B., Oyola, P., Öztürk, F., Petäjä, T., Querol, X., Rashidi, Y., Reyes, F., Ross-Jones, M., Salthammer, T., Savvides, C., Stabile, L., Sjöberg, K., Söderlund, K., Sunder Raman, R., Timonen, H., Umezawa, M., Viana, M., Xie, S. (2021). Global Air Quality and COVID-19 Pandemic: Do We Breathe Cleaner Air? *Aerosol Air Qual. Res.* 21, 200567. <https://doi.org/10.4209/aaqr.200567>

Broomandi P, Amouei Torkmahalleh M, Akturk M, **Ngagine SH**, Gorjinezhad S, Ozturk F, Kocak M, Kim J. A new exposure route to trace elements in indoor particulate matter. *Indoor Air.* 2020 May;30(3):492-499. doi: 10.1111/ina.12641. Epub 2020 Jan 24. PMID: 31887240.

Oral Communications

G. Abichou, **S. H. Ngagine**, T. N. Ba, G. Wang, P. Flament, K. Deboudt, S. Dusanter, A. Tomas, M. W. Sigrist and W. Chen, 2021, 'Filter-free Measurements of Carbonaceous Particles Using Photoacoustic Spectroscopy (PAS) Operating at 880 nm', *7th International Conference on Sensors Engineering and Electronics Instrumentation Advances (SELA' 2021)*, Palma de Mallorca, Mallorca (Balearic Islands), Spain, 22-24 September 2021.

S.H. Ngagine, K. Deboudt, P. Flament, P. Augustin, M. Fourmentin, E. Dieudonné, H. Delbarre, D. Dewaele, F. Cazier, ‘Evidence of fast changes in dust composition and Mixing State during a typical Dust Pollution Event, using automated electron microscopy analysis.’, *Demi-journées des doctorant.e.s CaPPA*, Lille, 7-9 September 2021.

S.H. Ngagine, K. Deboudt, P. Flament, P. Augustin, M. Fourmentin, E. Dieudonné, H. Delbarre, F. Cazier, D. Dewaele, “Characteristics of PM₁₀ pollution events in a European highly industrialized and urbanized coastal area”, *Journee des doctorants du Pôle MTE-ULCO*, Calais, 01 July 2021. (*First Prize for the best oral presentation*).

Posters

S.H. Ngagine, K. Deboudt, P. Kulinski, F. Marteel and P. Flament, ‘Development and characterization of a sequential aerosol sampler by cascade impaction application to the study of a fine particle pollution episode’, CLIMIBIO-Journée de cloture, 24 November 2021.

Ngagine, S. H.; Flament, P.; Deboudt, K.; Augustin, P.; Fourmentin, M.; Delbarre, H.; Dieudonné, E.; Kulinski, P.; Marteel, F., ‘Characteristics of PM₁₀ pollution events in a European highly industrialized and urbanized coastal area’, *European Aerosol Conference - EAC2021*, Interactive Live Virtual Event, 30 August - 3 September 2021.

E. Dieudonné , H. Delbarre, P. Augustin, M. Fourmentin, P. Flament, K. Deboudt1, **S.H Ngagine**, F. Cazier, ‘Application of existing Doppler lidars for simultaneous air quality applications: results from comparison with PM₁₀ , PM_{2.5} and granulometric observations in a multi influenced harbor city’, *American Geophysical Union 2019 Fall meeting*, San Francisco, 9-13 December 2019.

Résumé

Titre : Hétérogénéité Chimique des Particules Atmosphériques en Milieu Urbano-Industriel lors des Evènements de Pollution

Ce travail de thèse vise à améliorer notre connaissance des sources proches et lointaines contrôlant le dépassement des seuils réglementaires de qualité de l'air, tels qu'ils peuvent être appréciés par les réseaux de mesure existants, sur le site fortement industrialisé et urbain du Grand Dunkerque. Il s'agit notamment de s'appuyer sur le calcul d'un indice d'état de mélange des particules, prenant en compte l'hétérogénéité de leur composition élémentaire, celle-ci étant liée à leur temps de séjour dans l'air et à la distance entre les sources et le site récepteur étudié.

Pour répondre à cette problématique, il a fallu dans un premier temps développer un impacteur séquentiel de particules à haute résolution temporelle, nommé TRAPS, qui répondait au besoin de suivre les changements rapides observés au sein des particules atmosphériques lors d'épisodes de pollution. Couplé à un granulomètre et après analyse individuelle des particules prélevées par microscopie électronique (MEB-EDX), le TRAPS permet de rendre compte de l'évolution physico-chimique des particules atmosphériques au cours du temps. Dans la première partie de cette thèse, des expériences menées en laboratoire et une campagne de terrain ont permis valider notre prototype, de rendre compte de la dynamique de dépôt des particules sur les zones d'impaction et de vérifier les diamètres de coupure des étages grossier et fin du TRAPS, déterminés respectivement à $1,32\mu\text{m}$ et $0,13\mu\text{m}$.

Une étude statistique des épisodes de pollution aux PM_{10} survenus sur le Grand Dunkerque a ensuite été réalisée sur 3 ans, entre 2018 et 2020. Elle nous a permis d'identifier 12 principaux types d'épisodes sur la base de leur étendue spatiale, mais aussi des conditions locales de dispersion des polluants. On a pu ainsi identifier des épisodes locaux et des épisodes régionaux observés, soit en conditions atmosphériques stationnaires ou au contraire en conditions de dispersion des polluants à plus grande échelle. Alors que 78% des jours de dépassement du seuil réglementaire des PM_{10} correspondent à des épisodes locaux, les 22% restant correspondent à des panaches de pollution d'étendue au moins régionale, avec une proportion égale de jours de dépassements en conditions de dispersion et en conditions stationnaires. Hormis les épisodes très localisés, une étude fine de la variabilité temporelle des concentrations en particules fines ($\text{PM}_{2.5}$) montre la présence systématique d'une période

d'accumulation progressive des polluants, pouvant atteindre une dizaine d'heures et caractérisée par une contribution importante de ces particules.

La dernière partie de ce travail a consisté en l'étude de la composition et l'état de mélange des particules individuelles collectés lors d'évènements particuliers de pollution sur la zone du Grand Dunkerque en 2021. La campagne a permis l'échantillonnage et la caractérisation de 5 épisodes de pollution durant lesquels le TRAPS était déployé en parallèle d'autres instruments fournissant des informations complémentaires sur la granulométrie des aérosols, la météorologie ou la dynamique atmosphérique. Près de 28 000 particules individuelles ont été caractérisées par MEB-EDX. Avec plus de 90% des échantillons associés à des valeurs de l'indice d'état de mélange chimique supérieures à 0.5, il est possible d'affirmer que les particules collectées sur la zone du Grand Dunkerque, durant ces épisodes de pollution, sont, en général, de composition très hétérogène à l'échelle de la particule individuelle (particules dites « en mélange interne »). Les résultats obtenus montrent en outre une influence de l'origine, locale ou transportée, des particules sur leur composition chimique et par là même sur l'indice d'état de mélange chimique de la population de particules échantillonnées. Une évolution croissante de l'indice d'état de mélange avec le temps de résidence des particules dans l'atmosphère lors de ces évènements est notamment observée.

Mots clés : particules atmosphériques, état de mélange, évènements de pollution, milieux urbain et industriels, impacteur en cascade rotatif, MEB-EDX

Abstract

Title: Chemical Heterogeneity of Atmospheric Particles in Urbanized and Industrialized Environments during Pollution Events.

This thesis aims at improving our knowledge of the near and distant sources controlling the exceedance of the regulatory thresholds of air quality, as detected by the air quality monitoring networks, at the strongly industrialized and urban site of the Great Dunkirk Area (GDA). This appreciation is notably based on the calculation of a mixing state index of the particles, taking into account the heterogeneity of their elementary composition, this one being related to their residence time in the atmosphere and the distance between the sources and the studied receptor site.

To do that, it was firstly necessary to develop a time resolved cascade impactor with high temporal resolution, named “TRAPS”, which answered the need to follow the rapid changes observed within the atmospheric particles during pollution episodes. Coupled with a particle size analyser and after individual analysis of the collected particles by electron microscopy (SEM-EDX), TRAPS allows to report the physicochemical evolution of atmospheric particles over time. In the first part of this thesis, laboratory experiments and a field campaign allowed to validate our prototype, to report the dynamics of particle deposition on the impaction stages and to verify the cut-off diameters of the coarse and fine stages of TRAPS, determined respectively at 1.32 μm and 0.13 μm .

A statistical study of PM₁₀ pollution episodes occurring over the GDA was then carried out over 3 years, between 2018 and 2020. It allowed us to identify 12 main types of episodes based on their spatial extent, but also on the local conditions of pollutant dispersion. We were able to identify local episodes and regional episodes observed, either in stationary or dispersive atmospheric conditions. While 78% of the PM₁₀ exceedance days correspond to local episodes, the remaining 22% correspond to pollution plumes with at least a regional extent, with an equal proportion of exceedance days in dispersion and stationary conditions. Except for very localized episodes, a detailed study of these pollution episodes shows the systematic presence of a period of pollutant accumulation, of about 10 hours, characterized by an important contribution of fine particles (PM_{2.5}) except for episodes of limited spatial coverage.

The last part of this work consisted in the study of the composition and mixing state of the individual particles collected during pollution events in the GDA in 2021. The campaign allowed the sampling and characterization of 5 pollution episodes, during which TRAPS was deployed in parallel with other instruments providing complementary information on aerosol granulometry, or atmospheric dynamics. Nearly 28,000 individual particles were characterized by SEM-EDX. With more than 90% of the samples associated with values of the mixing state index higher than 0.5, it can be said that the particles collected in the GDA during pollution episodes are in general of very heterogeneous composition at the particle scale (internal mixing). Nevertheless, the results show an influence of the local or transported origin of the particles on their chemical composition, but also on the mixing state index. An increasing evolution of this index with the particles residence time during these events is observed.

Keywords: atmospheric particles, mixing state, pollution events, urban and industrial site, rotative cascade impactor, SEM-EDX.